SOLID-STATE NMR STUDIES AT THE STRUCTURAL PHASE TRANSITION REGION OF FERROELECTRIC MATERIALS

Thesis Submitted to AcSIR for the Award of the Degree of

DOCTOR OF PHILOSOPHY

In **Chemical Sciences**

By

Anjali K

Registration Number: 10CC11J26001

Under the guidance of

Dr. T.G. Ajithkumar

and

Dr. P. A. Joy

CSIR-National Chemical Laboratory

Pune 411008, India

December 2016

सीएसआईआर - राष्ट्रीय रासायनिक प्रयोगशाला
(वैज्ञानिक तथा औद्योगिक अनुसंधान परिषद)
डॉ. होमी भाभा मार्ग, पुणे - 411 008, भारत
CSIR - NATIONAL CHEMICAL LABORATORY
(Council of Scientific & Industrial Research)
Dr. Homi Bhabha Road, Pune - 411 008, India

CERTIFICATE

This is to certify that the work incorporated in this Ph.D. thesis entitled "**Solid-state NMR studies at the structural phase transition region of ferroelectric materials**" submitted by **Ms. Anjali K** to Academy of Scientific and Innovative Research (AcSIR) in fulfillment of the requirements for the award of the Degree of **Doctor of Philosophy in Chemistry,** embodies original research work under my supervision/guidance. I further certify that this work has not been submitted to any other University or Institution in part or full for the award of any degree or diploma. Research material obtained from other sources has been duly acknowledged in the thesis. Any text, illustration, table etc., used in the thesis from other sources, have been duly cited and acknowledged.

Student
Anjali K

Research Guide
Dr. T. G. Ajithkumar
Principal Scientist
CSIR-NCL, Pune, India

Date: 01/12/2016
Place: CSIR-NCL, Pune

Research Co-Guide
Dr. P. A. Joy
Senior Principal Scientist
CSIR-NCL, Pune, India

Communication Channels
NCL Level DID : 2590
NCL Board No. : +91-20-25902000
EPABX : +91-20-25893300
: +91-20-25893400
FAX
Director's Office : +91-20-25902601
COA's Office : +91-20-25902660
SPO's Office : +91-20-25902664
WEBSITE
www.ncl-india.org

DECLARATION

I, hereby declare that all the experiments in this thesis entitled, "**Solid-state NMR studies at the structural phase transition region of ferroelectric materials**" submitted for the degree of **Doctor of Philosophy in Chemical Sciences** to Academy of Scientific and Innovative Research (AcSIR), has been carried out by me at the Physical and Materials Chemistry Division of CSIR-National Chemical Laboratory, Pune, India under the joint supervision of **Dr. T.G. Ajithkumar** and **Dr. P. A. Joy**. Research material obtained from other sources has been duly cited and acknowledged in the thesis. This work is original and has not been submitted in part or full by me for any degree or diploma to this or any other University.

Anjali

(Anjali K.)

Date: 01/12/16

CSIR-NCL

Pune, India.

Acknowledgements

I wish to place on record my profound gratitude to my research supervisor **Dr. T. G. Ajithkumar** for his guidance and advice throughout the course of this investigation. I am extremely grateful to **Dr. P.A. Joy**, my co-guide for designing the work, timely advice, and inspiring guidance extended for the successful completion of this project.

I express my sincere thanks to the former directors Dr. S. Sivaram, Dr. Sourav Pal and the present director Dr. Ashwini Kumar Nangia for their permission to work in this prestigious institution. I would like to thank Dr. P. R. Rajamohanan, Head, central NMR facility, and Dr. Anilkumar, Head, physical and material chemistry division, for providing the necessary facilities and allowing to work in their respective departments without any constraints. I would like to acknowledge Dr. V. Kumar (Director, C-MET, Thrissur) for permitting me to carry out the ferroelectric measurements from C-MET Thrissur.

I am grateful to Dr. S. Ganapathy, Dr. K. Sreekumar and Dr. R. Nandini Devi for their valuable advice and inspiration. It is my great pleasure to thank the NMR staffs, Dr. Sapna Ravindranath, Mr. Sathe, Mrs. Phalgune, Mr. Suryavanshi, Mr. Mane, Mr. Umesh and Mr. Sachin

I am extremely thankful to all my fellow research scholars, Vijay, Sreeja, Khaja, Mangesh, Pankaj, Lenin, Bindhu, Eldho, Ramsunder, Govindraj, Jayaprabha, Manjunath, Mohan, Ananth and Arun, for providing nice working environment and cooperation. My special thanks to Joyasish for his help in the dielectric measurements. I thank Divya (C-MET Thrissur) for the the P-E hysteresis measurements. I would like to thank all my friends who made my life at NCL more jovial. I record my heartfelt appreciations to Beena and Jijil for their goodwill and help extended to me for the completion of this project.

Financial assistance from UGC is greatly acknowledged.

Anjali K

Contents

List of tables

List of figures

List of Abbreviations and symbols

BLT: $Bi_{0.5}Li_{0.5}TiO_3$

BNT: $Bi_{0.5}Na_{0.5}TiO_3$

BKT: $Bi_{0.5}K_{0.5}TiO_3$

CT: Central transition

DAS: Dynamic angle spinning

DOR: Double rotation

LNT: $La_{0.5}Na_{0.5}TiO_3$

MAS: Magic angle spinning

MQMAS: Multiple quantum magic angle spinning

PCW: Powder cell for windows

QA: Quadrupolar anisotropy

RF: Radio frequency

SSNMR: Solid-sate NMR

SEM: Scanning electron microscopy

XRD: X-ray diffraction

1Q: Single quantum

3Q: 3 Quantum

C_Q: Quadrupole coupling constant

δ_{iso}: Isotropic chemical shift

Δ_{CS}: Chemical shift distribution

η: Asymmetry parameter

χ^2: Goodness of the fit

Abstract

Lead free bismuth sodium titanate ($Bi_{0.5}Na_{0.5}TiO_3$) based solid solutions are considered as an alternative for piezoelectric applications over the currently used material lead zirconate titanate ($PbZr_{1-x}Ti_xO_3$), since they have comparable properties. $Bi_{0.5}Na_{0.5}TiO_3$ has large remnant polarization (P_r =38 μ C/cm^2), high Curie temperature (T_C= 320 ^oC), high electromechanical coupling constant and its extended strain under high field is almost comparable to that of $PbZr_{1-x}Ti_xO_3$. However, $Bi_{0.5}Na_{0.5}TiO_3$ has some drawbacks such as its high conductivity and large coercive field. Substitution of K^+ for Na^+ in $Bi_{0.5}Na_{0.5}TiO_3$ is found to be effective to enhance its performance parameters. The solid solution formed between $Bi_{0.5}Na_{0.5}TiO_3$ and bismuth potassium titanate, $Bi_{0.5}K_{0.5}TiO_3$ could overcome many of the drawbacks of $Bi_{0.5}Na_{0.5}TiO_3$. In certain compositional regions of $Bi_{0.5}Na_{0.5}TiO_3$–$Bi_{0.5}K_{0.5}TiO_3$ solid solution, high piezoelectric and dielectric responses are observed.

Due to the different crystal structures of $Bi_{0.5}Na_{0.5}TiO_3$ and $Bi_{0.5}K_{0.5}TiO_3$, a structural phase transition is expected at a certain composition. In some studies, a morphotropic phase boundary (MPB) region is reported. However, there are some differing reports about the crystal structure of $Bi_{0.5}Na_{0.5}TiO_3$, structural phase transition region, existence of the MPB region and the compositional range of the MPB region in the $Bi_{0.5}Na_{0.5}TiO_3$–$Bi_{0.5}K_{0.5}TiO_3$ solid solution series. Since solid state NMR (SSNMR) is an ideal tool to study local structural distortions, the objective of the present study is to clearly locate the onset of the phase transition as well as to identify the MPB region and to correlate the local structural distortions with the dielectric properties of the solid solutions of $Bi_{0.5}Na_{0.5}TiO_3$.

A detailed analysis of the changes in the structure and properties of (1-*x*)$Bi_{0.5}Na_{0.5}TiO_3$–*x*$Bi_{0.5}K_{0.5}TiO_3$solid solutions is carried out in the present work. Since the ionic size of K^+ is larger than that of Na^+, the effect of size of the substituted ionis also studied, that will help to identify ways to improve the properties of ceramics. The effect of cation size on the structure and properties of $Bi_{0.5}Na_{0.5}TiO_3$ is studied by substituting Na^+ with a smaller ion Li^+ in the (1-*x*)$Bi_{0.5}Na_{0.5}TiO_3$–*x*$Bi_{0.5}Li_{0.5}TiO_3$ solid solutions and co-substitution of Li^+ and K^+ in (1-*x*)$Bi_{0.5}Na_{0.5}TiO_3$–(*x*/2)$Bi_{0.5}Li_{0.5}TiO_3$–(*x*/2)$Bi_{0.5}K_{0.5}TiO_3$ (where the average size of Li^+ and K^+ is comparable to that of Na^+). Similarly the effect of the contribution of the $6s^2$ lone pair of Bi on the ferroelectric properties of $Bi_{0.5}Na_{0.5}TiO_3$ is investigated by substituting Bi^{3+} with La^{3+} in the $Bi_{0.5}Na_{0.5}TiO_3$–$La_{0.5}Na_{0.5}TiO_3$ solid solution series. Since Bi^{3+} and La^{3+} have comparable ionic size, the contribution from the $6s^2$ lone pair

to the ferroelectric properties of the $Bi_{0.5}Na_{0.5}TiO_3$ can be traced by analysing the changes in structure and properties of the $Bi_{0.5}Na_{0.5}TiO_3$–$La_{0.5}Na_{0.5}TiO_3$ solid solution.

This thesis reports the studies on the structure-property correlations of the solid solutions of $Bi_{0.5}Na_{0.5}TiO_3$–$Bi_{0.5}K_{0.5}TiO_3$ (BNT–BKT), $Bi_{0.5}Na_{0.5}TiO_3$–$Bi_{0.5}Li_{0.5}TiO_3$ (BNT–BLT), $Bi_{0.5}Na_{0.5}TiO_3$–$Bi_{0.5}Li_{0.5}TiO_3$–$Bi_{0.5}K_{0.5}TiO_3$(BNT–BKT–BLT), and $Bi_{0.5}Na_{0.5}TiO_3$–$La_{0.5}Na_{0.5}TiO_3$ (BNT–LNT). The changes in the crystal structure are analysed by the Rietveld refinement of the powder XRD patterns and the local symmetry changes are probed by Raman and SSNMR spectroscopy. Variations in the microstructure are studied by scanning electron microscopy (SEM). Changes in the structure and microstructure are correlated with the changes in the dielectric properties and density of the different compositions.

Since the studied compositions have the perovskite structure, **Chapter 1** is a general introduction to perovskites and their solid solutions, including their ferroelectric properties. Also, since the work reported in this thesis is on the structure, structural phase transition and morphotropic phase boundary in lead-free ferroelectric perovskites, a review of some of the well-known solid solutions of ferroelectric perovskites, their properties at the MPB region and lead-free ferroelectric perovskites are discussed in this chapter.

Chapter 2 discusses about the synthesis of the solid solutions and details of various characterization techniques used in the present study such as XRD, Raman spectroscopy, solid-state NMR techniques and SEM. Since SSNMR is the main tool used to probe the local symmetry changes in the present work, different SSNMR techniques such as magic angle spinning (MAS) and multiple quantum MAS (MQMAS) are detailed in this chapter. Similarly, details of density, dielectric constant, and P-E hysteresis loop measurements have also been discussed in this chapter.

Chapter 3 reports the studies on (1-*x*)BNT–*x*BKT solid solution series for very close compositions in the range $0 \leq x \leq 0.36$. Different compositions in the (1-*x*)BNT–*x*BKT solid solution series are synthesised by the ceramic method and the structural changes are studied by XRD, Raman and SSNMR spectroscopy. Properties of the solid solutions, such as dielectric constant, density and P-E hysteresis loop, are also measured and the changes in the properties are correlated with the structural changes. The Rietveld refinement of XRD patterns confirmed that single phase compositions with monoclinic Cc space group are formed below $x < 0.18$ and a biphasic MPB region with monoclinic Cc and tetragonal P4bm structures is observed in the compositional region with $0.18 \leq x \leq 0.36$. Raman studies also

supported the results obtained from the XRD analysis, where major structural changes are observed after $x = 0.18$ from the Raman analysis. ^{23}Na MQMAS NMR experiments showed that only one sodium site is present in the biphasic MPB region of $Bi_{0.5}Na_{0.5}TiO_3$–$Bi_{0.5}K_{0.5}TiO_3$ solid solution. ^{23}Na quadrupolar coupling constant is found to decrease up to x= 0.15, increases above this composition up to $x = 0.22$ and then decreases again at higher compositions. The microstructure analysis showed the presence of fused and less porous grains in the MPB region. Some of the Raman parameters and ^{23}Na quadrupolar coupling constant showed deviation above $x = 0.15$, indicating local symmetry changes above this composition on substitution. These observations lead to the conclusion that the onset of the MPB region of $Bi_{0.5}Na_{0.5}TiO_3$–$Bi_{0.5}K_{0.5}TiO_3$ starts above $x = 0.15$ due to the local symmetry changes which is well correlated with the changes in properties of the solid solutions.

Chapter 4 reports the studies on the structure and properties of $Bi_{0.5}Na_{0.5}TiO_3$ obtained by substituting Na^+ by the smaller ion Li^+ in the solid solution series $(1\text{-}x)Bi_{0.5}Na_{0.5}TiO_3$–$xBi_{0.5}Li_{0.5}TiO_3$, in the range $0 \leq x \leq 0.20$. Different compositions of (1-x)BNT-xBLT are synthesised by a citrate-gel method and the changes in structure are studied by XRD, Raman and SSNMR spectroscopy. Changes in the density and the dielectric properties with Li^+ substitution are also reported in this chapter. XRD analysis showed that all the compositions are formed under monoclinic Cc space group and structural phase transition is absent in the studied compositional range. Structural distortion caused by substitution of Li^+ is less compared to K^+ substitution in the $Bi_{0.5}Na_{0.5}TiO_3$lattice. Although structural phase transition is not observed in the $Bi_{0.5}Na_{0.5}TiO_3$–$Bi_{0.5}Li_{0.5}TiO_3$ solid solution series, XRD and Raman results indicated minor structural distortion and local symmetry changes in the $Bi_{0.5}Na_{0.5}TiO_3$ lattice with Li substitution. The XRD, Raman and SSNMR parameters showed similar trend in the changes with Li^+ substitution. All the three parameters showed deviation above $x = 0.1$, indicating local symmetry changes and small distortion at this composition which is correlated with the variations in the microstructure, density and dielectric constant of the $Bi_{0.5}Na_{0.5}TiO_3$–$Bi_{0.5}Li_{0.5}TiO_3$ solid solution series.

Chapter 5 reports the studies on the Li^+ and K^+ co-substituted $(1\text{-}x)Bi_{0.5}Na_{0.5}TiO_3$–$(x/2)Bi_{0.5}Li_{0.5}TiO_3$–$(x/2)Bi_{0.5}K_{0.5}TiO_3$ solid solutions, where the average size of Li^+ and K^+ is comparable to that of Na^+. Although no phase transition is observed in the solid solution series with substitution, changes in the XRD, Raman and SSNMR parameters indicated small distortion and local symmetry changes in the crystal lattice. A small increase in the dielectric

constant is observed which is due to the minor distortions in the crystal lattice due to substitution.

Chapter 6 reports the studies on the $Bi_{0.5}Na_{0.5}TiO_3$–$La_{0.5}Na_{0.5}TiO_3$ solid solutions in the compositional range $0 \leq x \leq 0.4$. The main motive of this study is to understand the contribution of Bi^{3+} $6s^2$ lone pair towards the ferroelectric properties of $Bi_{0.5}Na_{0.5}TiO_3$, by replacing Bi^{3+} by La^{3+} having the same ionic size. All the compositions in the $Bi_{0.5}Na_{0.5}TiO_3$–$La_{0.5}Na_{0.5}TiO_3$ solid solution series are formed under monoclinic Cc space group with only minor changes in the lattice parameters. The changes in the Raman and SSNMR parameters indicated that the local symmetry increased with La substitution due to the reduced effect of $6s^2$ lone pair contribution to the crystal lattice. The decrease in the dielectric constant indicated decrease in the polarization. The deviation observed in the structural parameters around $x = 0.1$ is also observed in the density and dielectric constant of the solid solutions.

Chapter 7 is an overall summary of the work presented in the thesis and important findings of the study have been discussed. The effect of the different substituents (Li^+, K^+, La^{3+}) on the structure and properties of the $Bi_{0.5}Na_{0.5}TiO_3$ solid solutions are compared in this chapter. The deviation observed around $x = 0.1$ in the quadrupolar coupling constant, density and dielectric constant of all the four solid solutions are discussed and correlated with the local symmetry changes. The importance of solid state NMR studies to obtain information on local structural changes and the close correlation between local symmetry changes and the properties of the solid solutions is highlighted. Based on the present results, the need for further detailed studies on the structure-property-processing correlations on the different compositions is discussed at the end of this chapter.

Chapter 1

Introduction

1.1. Perovskites

Perovskites are inorganic compounds of the general formula ABX_3, where A and B are cations and X is anion, usually oxygen.[1] Some examples for perovskites are $AgMgF_3$, $CsPbI_3$, $KCuF_3$, $BaTiO_3$, $LaMnO_3$, $LiNbO_3$ etc. After the discovery of the dielectric and ferroelectric properties of $BaTiO_3$ in the 1940s, many studies were carried out to improve the properties of $BaTiO_3$ which led to the discovery of many perovskites with the overall composition ABO_3.[2]

The mineral calcium titanate ($CaTiO_3$) is known as the *perovskite*, which was discovered by Gustav Rose in 1839 and was named after the Russian mineralogist Count Lev Alekseevich Perovski (1792-1856).[3] The studies on the perovskite mineral led to many different materials with different chemical elements but the atomic arrangement the same as that of the perovskite mineral and they are said to have the perovskite structure.

Table 1.1: Properties of perovskites.[3]

Materials	**Properties**
$BaTiO_3$, $Pb(Mg_{1/3}Nb_{2/3})O_3$	Capacitors
$Pb(ZrTi)O_3$, $LiNbO_3$	Piezoelectric
$SrTiO_3$	Insulator
$MgSiO_3$	Major constituent of earth
$LaCrO_3$	Metallic conductor
$K(Ta,Nb)O_3$	Pyroelectric, electro-optic
$LiNbO_3$	Electro-optic
$LaAlO_3$, $YAlO_3$	Host material for rare earth luminescent ions
$(La,Sr)BO_3$, B= Mn, Fe, Co	Mixed conduction, catalyst
$LaGaO_3$	Oxide-ion conduction
$(La, A)MnO_3$, A = Ca, Sr, Ba	Ferromagnetism, giant magnetoresistance, spin polarized electrons
$SrRuO_3$	Ferromagnetism
$BiFeO_3$	Magnetoelectric coupling, high Curie temperature

The perovskite family is large and they are the most abundant mineral on earth. Perovskites are used in various technologies such as for energy production in solar solid oxide fuel cell technology (SOFC), environmental containment (radioactive waste encapsulation), communications (dielectric resonator material) and catalysis.[3] They possess interesting magnetic properties including colossal magnetoresistance, some of them show superconductivity, ionic conductivity and ferroelectricity. Table 1.1 shows perovskites with different properties.

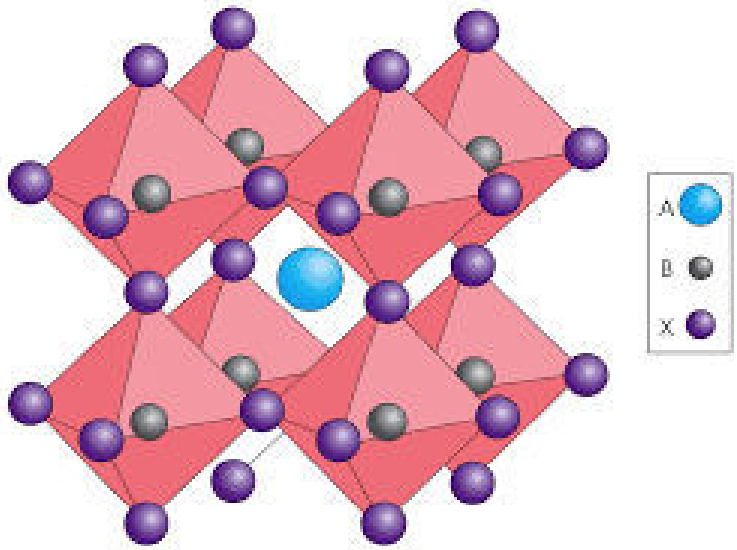

Figure 1.1: Perovskite structure with BX_6 octahedra and A cation in the center.[4]

The ABX_3 perovskite crystal structure consists of a network of BX_6 octahedra with the A cation enclosed inside the BX_6 octahedral network. The A cation has a 12-fold co-ordination and the B cation has a 6-fold co-ordination to the anions (X). The crystal structure of perovskite is shown in Figure 1.1. The ideal perovskite has a cubic structure (space group $Pm\bar{3}m$) with unit cell dimension of ~4 Å. The ideal cubic perovskite structure is not very common and the mineral perovskite itself is slightly distorted. These distortions are very significant for the magnetic and electric properties of perovskites.

The first synthetic perovskites with different compositions were made and their structures were studied by Goldsmith *et al* in 1924-26.[5] Cubic or pseudo-cubic structures were reported for earlier synthesized perovskites. But as the work on these systems progressed more and more structures were proposed for the perovskite family. Goldsmith observed that the structure of the

materials depends on the radius of the ions and the radius ratio (r_c/r_a), (r_c and r_a are radius of cation and anion, respectively) determines the co-ordination number of the cations. In a perfect cubic perovskite, the radii of the ions are related by

$$r_A + r_X = \sqrt{2}\,(r_B + r_X) \tag{1.1}$$

where r_A, r_B, r_X are the ionic radii of the A–site cation, B site cation and the anion, respectively. Goldsmith[5] introduced the concept of tolerance factor (t) which describes the deviation from the ideal perovskite packing. Tolerance factor, 't', gives the measure of the degree of distortion from the ideal perovskite structure.

The tolerance factor t for a perovskite is defined as,[5]

$$t = \frac{(r_A + r_X)}{\sqrt{2}(r_B + r_X)} \tag{1.2}$$

For an ideal cubic perovskite, the tolerance factor t = 1. If the perovskite structure is closer to cubic, the tolerance factor, t, will be close to 1. $CaRbF_3$ and $SrTiO_3$ possess ideal cubic structure. In $SrTiO_3$, Sr^{2+} and O^{2-} ions form a cubic close packed lattice with Ti^{4+} ions occupying the octahedral holes created by oxygen. The perovskite structure is very flexible, the A and B ions can be varied leading to large number of compounds with perovskite or related structures. Most of the perovskites have distorted structures. The size of A cation will be around 1.2–1.6 Å in radius and B cation radius will be around 0.6–0.7 Å. The structure possesses a neutral overall charge and generally attained by a charge distribution of $A^{1+}B^{5+}O_3$, $A^{2+}B^{4+}O_3$ or $A^{3+}B^{3+}O_3$. Mixed compositions such as $A^{2+}B_{2/3}{}^{3+}B_{1/3}{}^{6+}O_3$, $A^{2+}B_{1/3}{}^{2+}B_{2/3}{}^{5+}O_3$, $A^{2+}B_{1/2}{}^{3+}B_{1/2}{}^{5+}O_3$, $A^{2+}B_{1/2}{}^{2+}B_{1/2}{}^{6+}O_3$, $A^{3+}B_{1/2}{}^{2+}B_{1/2}{}^{4+}O_3$, $A_{1/2}{}^{2+}A_{1/2}{}^{4+}BO_3$, $A_{1/2}{}^{3+}A_{1/2}{}^{1+}BO_3$ are also possible in the perovskite structure.

Three main factors are responsible for the distortion of the cubic perovskite structure: size effect, deviation from the ideal composition and the Jahn-Teller effect. The reason for the distortion in a perovskite structure cannot be allocated to a single effect, many factors act on the structure.

For an ideal cubic perovskite the tolerance factor t = 1. Tolerance factor t will be less than 1 if the size of the A cation is smaller than the ideal value. Hence, to fill the space, [BO_6] octahedra will tilt. However, the structure will be cubic if the tolerance factor is in the range 0.89 < t < 1.[5,6] Crystals with lower t values possess lower symmetry. For example $GdFeO_3$ with t = 0.81 is orthorhombic.[7] The ilmenite structure is more stable if t is less than 0.8. If the A cation is large or the B cation is small, the tolerance factor will be larger than 1, then the hexagonal variants of the perovskite structure are stable. For example, in $BaNiO_3$, the close packed layers are stacked in a hexagonal manner, leading to a face sharing of the [NiO_6] octahedra.[8]

Many perovskites accommodate large concentration of oxygen vacancies (ABO_{3-y}), either in ordered or in random arrangement. The oxygen vacancies are either ordered to generate superstructures such as brownmillerite structure ($Ca_2Cr_2O_5$) or they stay disordered as in $BaCoO_{2.22}$, which is a highly oxygen deficient cubic material.[9] Ca_2FeCoO_5, $La_{1-x}A_xMnO_{2.5}$ (x=0.2 - 0.4 for A= Sr, Ba and x=0.2 - 0.3 for A=Ca,), Sr_2GaMnO_5, $SrCaMnGaO_{5+y}$, Ca_2MnAlO_5 etc belong to the brownmillerite structure. These materials possess good ionic conductivity and are used in solid oxide fuel cells.

The distortion in some perovskites is due to the Jahn-Teller active ions at the B position. For example in $LnMnO_3$ (Ln = La, Pr or Nd), the $3d^4$ electrons in Mn^{3+} are distributed as t_{2g}^3 and e_g^1. The one electron in the e_g orbital causes elongation of the [MnO_6] octahedra.[10]

The perovskite crystal structure is flexible and allows including cations such as NH_4^+ (NH_4ZnF_3). Complex inorganic-organic hybrid compounds such as $CH_3NH_3PbX_3$ where X is Cl, Br, I or a combination of these were also synthesized. Pb and Sn based perovskite halides [$CH_3NH_3(Pb,Sn)(I,Br)_3$] are used in solar cell applications due to their semiconducting and light absorbing properties.[11] In this hybrid structures the high conductivity of inorganic semiconductor component and strong light matter interaction of organic component are combined. They possess small excitation binding energies, low effective masses and their optical gaps are optimal for solar energy absorption which allows them for efficient charge carrier generation, transport and collection. Mostly these perovskites have cubic structure at room temperature. In their crystal structure A site is occupied by a small organic cation (methyl ammonium), B site is occupied by divalent ions (Pb or Sn) and halogens on the X site. The organic cation possesses a dipole moment which leads to the molecule based symmetry breaking and different structural varieties

are possible. As a result close to equilibrium many different structures are locally stable which differ in energy only by few meV/ formula. This leads to an electronic structure characterized by an anionic valence band (halogens) and a cationic conduction band (Sn or Pb).

1.2. Solid solutions

Solid solution is defined as a homogeneous crystalline phase which possesses various compositions without changing its structure.[12] It is the complete dissolution of one end member to the other to form a single phase allowing for continuous variability. The properties of materials can be control by changing compositions in the solid solution series. Solid solutions are of two types; substitutional solid solution and interstitial solid solution. In substitutional solid solution, an atom or an ion replaces an atom or ion of the same charge in the parent structure. In interstitial solid solutions, the introduced atom or ion occupies an empty site in the crystal lattice.

Perovskites show not only the structural flexibility but also show compositional flexibility. Chemical substitution is possible in all three sites of the perovskite structure, such as $A_{1-x}A'_xBO_3$, $AB_{1-x}B'_xO_3$, $ABO_{3-y}X_y$. Most of these A–site and B–site substituted complex perovskite structures such as $A_{1-x}A'_xBO_3$ and $AB_{1-x}B'_xO_3$ show relaxor behavior due the lack of ordering.[13] Two types of substitution are possible in the A site, isovalent ($Pb_{1-x}Ca_xTiO_3$) and aliovalent. In aliovalent substitution, electrical neutrality is maintained either by changing the oxidation state of the B cation or by the formation of oppositely charged vacancies. An example for aliovalent substituted compound is $La_xSr_{1-x}FeO_{3-n}$. These crystal structures allow the transport of oxygen ion in the perovskite lattice. Most of the technologically important perovskites belong to the $AB_{1-x}B'_xO_3$ family. Examples are $Pb(Zr,Ti)O_3$ which is used in transducers and actuators, $Ba(Mg,Nb)O_3$ used in high frequency applications, $Pb(Mg,Nb)O_3$ and $Pb(Zn,Nb)O_3$ exhibit high piezoelectric constants. B–site substitution can be either with a homovalent ion [$Pb(Zr,Ti)O_3$] or with a heterovalent ion. Examples for heterovalent substitution are $Pb(Sc_{1/2}Ta_{1/2})O_3$, $Ba(Mg_{1/3}Nb_{2/3})O_3$, $Pb(Mg_{1/3}Nb_{2/3})O_3$, $Ba(Zn_{1/3}Nb_{2/3})O_3$, $Pb(Zn_{1/3}Nb_{2/3})O_3$.

1.3. Ferroelectricity

Dielectric materials are non-conducting ceramic materials which can prevent the flow of current in an electric circuit. The first studies on the properties of dielectrics were published by Faraday

in 1837.[14] He observed that the capacitance depends on the nature of the material separating the conducting surface. The dielectric permittivity or dielectric constant (ε_r) is defined as the ratio of the capacitance C of the capacitor filled with a dielectric to the value C_o of the same capacitor under vacuum.

$$\varepsilon_r = \frac{C}{C_0} \tag{1.3}$$

Polarization of the dielectrics occurs when the positive and negative charges are separated by an applied electric field. The field induced separation and alignment of the electric charges are responsible for the electric energy storage capacity of the dielectrics under the influence of an electric field. The material shows high dielectric permittivity if large number of dipoles is aligned in the direction of the applied electric field.

Table 1.2: Centrosymmetric and noncentrosymmetric point groups.

Crystal system	**Polar (acentric)**	**Nonpolar (centric)**
Triclinic	1	
Monoclinic	2, m	
Orthorhombic	mm2	222
Trigonal	3, 3m	32
Hexagonal	6, 6mm	$\bar{6}$, $\bar{6}$m2
Tetragonal	4, 4mm	$\bar{4}$, 422, $\bar{4}$2m
Cubic	None	23, $\bar{4}$3m, 432

Ferroelectric materials lack centre of symmetry. Table 1.2 shows a list of noncentrosymmetric point groups. Materials whose crystal structures possess these noncentrosymmetric point groups show ferroelectricity. Ferroelectric materials lose their spontaneous polarization above a critical temperature. This happen either due to a change in structure with temperature or due to the hoping of small ions which result the cancelation of the net polarization. The critical temperature above which the material becomes paraelectric (non-polar dielectric) is known as the Curie temperature (T_C) of a ferroelectric material.

The temperature dependence of dielectric constant (ε) in some ferroelectrics can be represented by the Curie-Weiss law

$$\varepsilon = \varepsilon_0 + c/(T - T_0) \quad (1.4)$$

where C is Curie constant and T_0 is Curie-Weiss temperature

In perovskites, when structural phase transition to lower symmetry occurs, the cubic non-polar paraelectric phase changes to a ferroelectric phase. This transition enlarges the size of the BX_6 octahedra and as a result the B cation is displaced from the centre of the oxygen anions. These displacements create a dipole moment in the unit cell, which leads to spontaneous polarization.

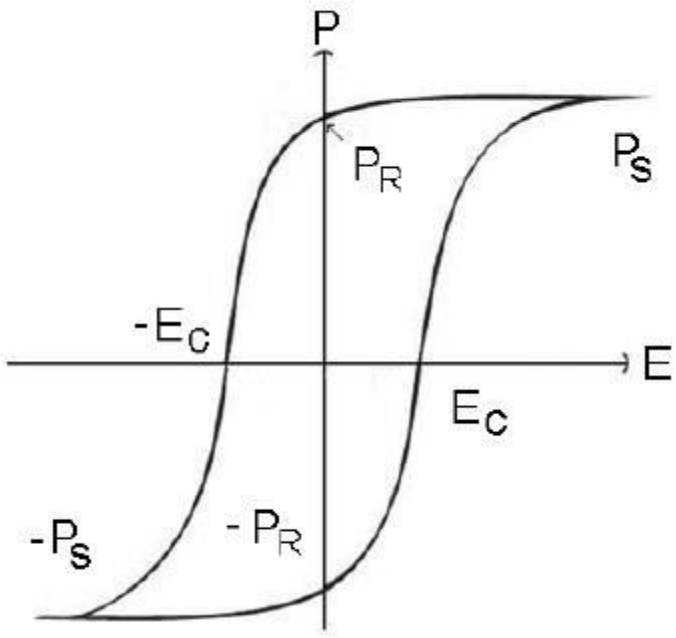

Figure 1.2: Ferroelectric hysteresis loop showing remnant polarization P_R, coercive field E_C and saturation polarization P_S.[16]

When a ferroelectric material is cooled below T_C, areas of uniform polarization called ferroelectric domains are formed and hence the macroscopic polarization of the crystal is zero. When the applied electric field is greater that the coercive field (E_c), all the domains will switch their polarization in the direction of the applied electric field to minimize the energy. Once it reached its saturation polarization, further increase in the field will no longer increase the polarization. Most of the domains continue their polarization in the direction of the field after the

removal of the applied electric field. This results in a remnant polarization in the material. The polarization will also switch to the opposite direction, when the field is applied in the opposite direction. This results the characteristic polarization versus hysteresis loop of a ferroelectric material.

Ferroelectric materials are dielectrics with extremely large permittivity and they possess spontaneous electric polarization which is reversible in an applied electric field.[15] Since the polarization is reversible, in the presence of an external electric field, ferroelectric materials show dielectric hysteresis loop (Figure 1.2), which shows the variation of polarization as a function of electric field.[16]

Pierre and Jacques Curie discovered piezoelectricity. They observed that when a mechanical stress is applied, an electric potential is developed in some materials such as quartz, tourmaline and zincblende.[17] Piezoelectricity is defined as the phenomena in which charge is produced when a mechanical stress is applied, on the other hand mechanical deformation in response to an applied electrical field. The piezoelectric effect is explained with the following equations

$$D_i = d_{ijk}\aleph_{jk} \tag{1.5}$$

And the inverse

$$x_{ij} = d_{kij}E_k \tag{1.6}$$

$\aleph_{jk}$is the applied stress, D_i is the charge density developed on the surface of the material, E_k is the applied electric field in the k direction and x_{ij} is the strain developed in the piezoelectric material. d_{ijk} and d_{kij} are the piezoelectric charge coefficients with units of pC/N and pm/V respectively. The piezoelectric coefficients for direct and converse effects are thermodynamically identical; hence the third rank tensor d_{ijk} and d_{kij} are simplified and denoted as follows

$$D_i = d_{im}\aleph_m \tag{1.7}$$

$$x_m = d_{mi}E_i \tag{1.8}$$

where the values of i = 1, 2 or 3 and the values of m = 1, 2,3 are linear components and 4, 5, or 6 are shear components of the strain.

The piezoelectric constant d_{im} is defined as the polarization generated by unit mechanical stress applied to a piezoelectric material. The first subscript in d belongs to the direction of polarization generated at zero electric field. The second subscript is the direction of the applied stress or the induced strain. Some important d terms are defined below.

d_{33} – The polarization induced in direction 3 (parallel to the direction of polarization of the ceramics) per unit stress applied in direction 3

d_{31} – The polarization induced in direction 3 per unit stress applied in direction 1 (perpendicular to the direction of polarization)

d_{15} – The polarization induced in direction 1 per unit stress applied in direction 5 (perpendicular to the direction of polarization)

The essential requirement for piezoelectricity is absence of centrosymmetry so that dipole moment can be produced by the application of stress. Out of the 21 acentric point groups 20 are piezoelectric. All ferroelectric materials are piezoelectric.

The electromechanical coupling constant, k of a piezoelectric material express its efficiency to convert mechanical stress to electrical energy or vice versa, between electric potential and mechanical displacement.

$$k = \sqrt{\frac{\text{mechanical energy generated}}{\text{electrical energy applied}}} \tag{1.9}$$

$$k = \sqrt{\frac{\text{electrical energy generated}}{\text{mechanical energy applied}}} \tag{1.10}$$

In most desired case k = 1, which indicate complete energy transfer without any heat dissipation. The electromechanical constant depends on the geometry and dimension of the measured sample.

The polarization in a piezoelectric material is coupled to the strain, consequently the changes in ferroelectric polarization is associated with a change in strain of the sample. The compressive and tensile nature of strain depends on the direction of the applied electric field and polarization. If the applied field is anti-parallel to the polarization, the strain will be compressive

till the coercive field is reached. At the coercive field (E_c), the polarization switches and the strain changes from compressive to tensile.

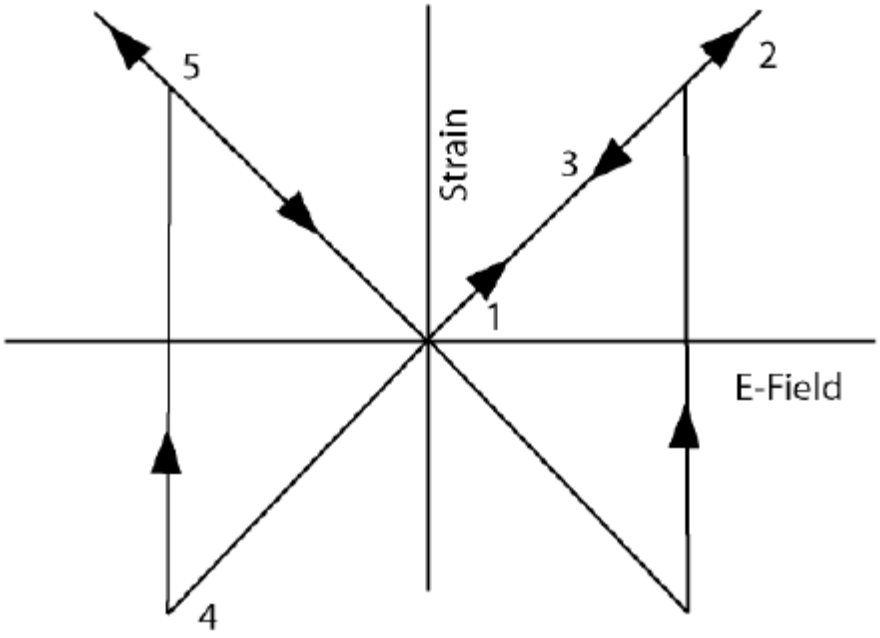

Figure 1.3: The mechanism of bipolar piezoelectric effect in ferroelectrics as a result of domain switching.[16]

Pyroelectricity is the generation of temporary polarization with a change in temperature. In pyroelectric materials the direction of polarization cannot be reversed by an applied electric field. Here the polarization is temperature dependent.

$$\Delta P_s = \pi \Delta T, \quad \pi \text{ is pyroelectric coefficient.} \tag{1.11}$$

Pyroelectric crystals are a special class of piezoelectric materials. A preexisting spontaneous polarization along atleast one crystallographic direction is enclosed in the crystal structure of a pyroelectric material. Upon heating, pyroelectric crystals undergo mechanical deformation due to thermal expansion. This results in a change in the extend polarization. Out of the 20 piezoelectric point group, 10 are pyroelectric. Examples of pyroelectric materials are $BaTiO_3$, triglycine sulfate, Rochelle salt, tourmaline, würtzite. Except $LiTaO_3$, most of the pyroelectric materials lose their pyroelectricity upon heating the samples to a few hundreds ^oC. $LiTaO_3$ is pyroelectric till 609 ^oC. This property of $LiTaO_3$ is made use in scanning micro calorimeter to sense in the sub micro caloric range. $LiTaO_3$ is also used in microenthalpimeter for monitoring catalytic process.

1.4. Ferroelectric perovskites

Ideal cubic perovskites have tolerance factor close to 1 and they are paraelectric.[19] A stable perovskite structure possess a tolerance factor (t) in the range of $0.85 < t < 1.05$. Perovskites with $t < 1$ usually have a distorted structure and most of them are ferroelectric.[19] Some perovskites, their tolerance factor and structure are listed in Table 1.3. Some of the widely used ferroelectric perovskites for technology are $BaTiO_3$, $PbTiO_3$ and $KNbO_3$.

Table 1.3: Perovskites and their properties.[19]

Perovskite	**Tolerance factor**	**Structure at 20^{o}C**	**Type**	**T_C (^{o}C)**
$BaTiO_3$	1.06	Tetragonal	Ferroelectric	135
$SrTiO_3$	1.00	Cubic	Paraelectric	
$CaTiO_3$	0.97	Tetragonal	Paraelectric	
$PbTiO_3$	1.02	Tetragonal	Ferroelectric	490
$PbZrO_3$	0.96	Orthorhombic	Antiferroelectric	235
$NaNbO_3$	0.94	Monoclinic	Ferroelectric	-200
$KNbO_3$	1.04	Tetragonal	Ferroelectric	412
$KTaO_3$	1.02	Cubic	Ferroelectric	-260
$BiScO_3$	0.83	Rhombohedral	Ferroelectric	370
$BiFeO_3$	0.87	Tetragonal	Ferroelectric	850

The first reported perovskite ferroelectric material was $BaTiO_3$ in 1941 with high dielectric constant and ferroelectric behavior.[19,20] Compared to Rochelle salt and potassium dihydrogen phosphate (KH_2PO_4), $BaTiO_3$ possess high Curie temperature (T_C = 120 ^{o}C), which made them more approving for practical applications.[19] The room temperature crystal structure of $BaTiO_3$ is tetragonal. $BaTiO_3$ crystal structure is shown in Figure 1.4.

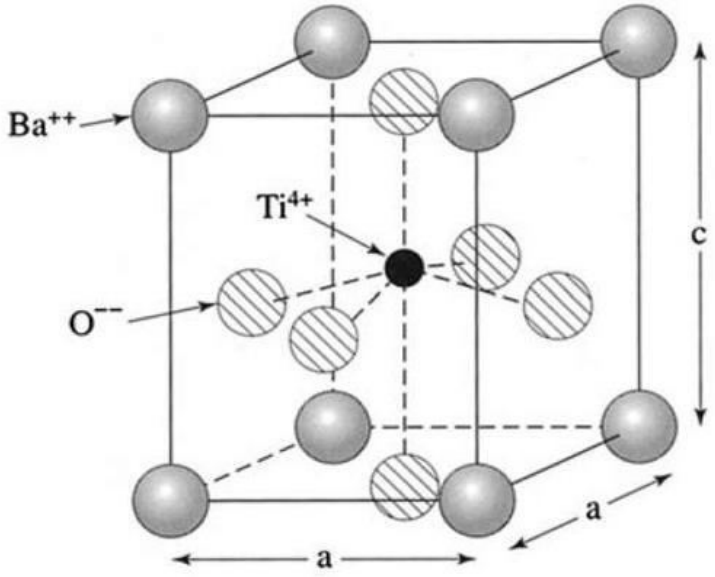

Figure 1.4: Tetragonal $BaTiO_3$ Unit cell.[12]

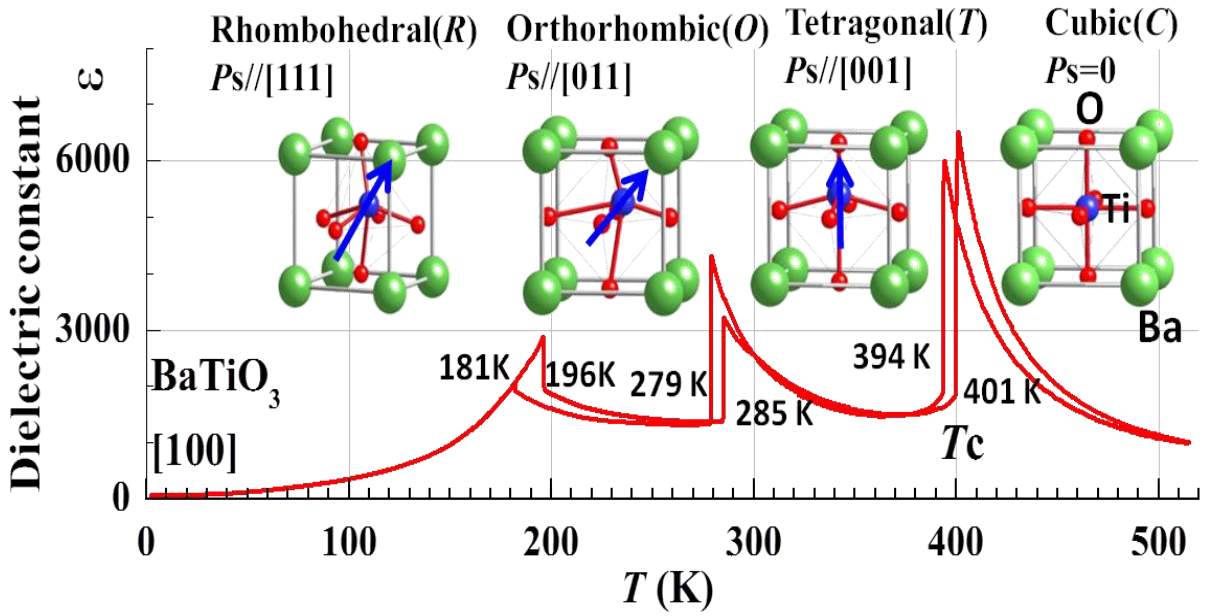

Figure 1.5: Temperature dependence of the dielectric constant of $BaTiO_3$.[22]

In $BaTiO_3$ crystal, the Ti ion present at the centre of the TiO_6 octahedra is displaced by about 6% of the Ti-O distance from the centre of the octahedra. The position of the Ba ion is also displaced slightly in the same direction. The relative displacements of ions in the crystal structure create a dipole moment. The orientation of the dipole can change by the application of

an external electric field.[22] The phase transition of $BaTiO_3$ is shown in Figure 1.5. Above 135 ^oC, $BaTiO_3$ possess a cubic paraelectric phase, it transforms to a tetragonal ferroelectric structure below 135 ^oC. It shows a second phase transition from tetragonal to orthorhombic structure at 5 ^oC. At -90 ^oC, it exhibit a third phase transition from orthorhombic to rhombohedral structure.[23] Unlike $BaTiO_3$, $PbTiO_3$ shows only one phase transition to the tetragonal phase at 490 ^oC.

Most of the properties of perovskites depend on temperature. For example the temperature dependence of dielectric constant of $BaTiO_3$ is evident from Figure 1.5. At each phase transition point, a hike in dielectric constant is observed. This property can be used in making capacitors. But, due to the temperature dependence of these properties, it is difficult to make use of this property in various technological applications. The solid solution of end member perovskites allow to control the temperature dependence of properties and these materials can provide wide range of properties.

1.5. Relaxor ferroelectrics

Relaxor ferroelectrics are different from normal ferroelectrics. The characteristic features that make relaxors different from normal ferroelectrics are,

1) In the dielectric constant versus temperature graph, the relaxor materials show a relatively broad maximum where as normal ferroelectrics show a sharp peak. In normal ferroelectrics, the Curie temperature (T_C) is independent of the applied frequency, while in relaxor ferroelectrics it is frequency dependent. The temperature of maximum dielectric constant (T_{max}) in relaxors increase with measured frequency.
2) The increase in dielectric constant in normal ferroelectrics is due to the rise in lattice polarization near T_C while in relaxors it is due to the rise in local polarization and nanosized domains which nucleate and grow below a certain temperature called the Burns temperature (T_B). T_B is higher than T_{max}
3) The macroscopic ferroelectric phase transition will not happen when it is cooled below the temperature of maximum permittivity. In relaxors the macroscopic polarization and birefringence will not grow spontaneously upon cooling. A macroscopic polar phase can be induced in relaxors by applying an electric field at a temperature lesser than the

depolarization temperature (T_d). In the absence of an electric field, if the material is heating at T_d, the induced macroscopic polarization disappears.

$Pb(Mg_{1/3}Nb_{2/3})O_3$ (PMN) is a well know relaxor ferroelectric material which has got much attention due to its interesting nanostructural and dielectric properties.[24-26] The crystal chemistry and the consequential nanostructure contribute to the physical properties of relaxor ferroelectrics. In lead-based complex relaxor perovskites, $Pb(B'_yB''_{1-y})O_3$, the B' and B" are randomly distributed along the crystallographically equivalent octahedral sites.[27,28] The disordered arrangement of the B' and B" atoms create chemical inhomogeneity in the material which result in different local Tcs and the phase transition is spread out to a wide range of temperatures. In relaxors T_{max} represent the main Curie temperature.[28]

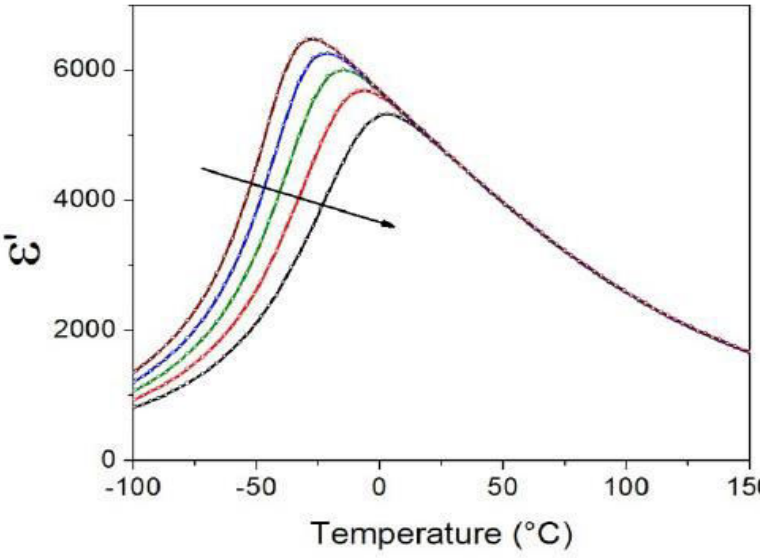

Figure 1.6: Real part of permittivity as a function of frequency and temperature for a relaxor ferroelectric showing a broad diffuse maximum.[28]

1.6. Structural phase transition and morphotropic phase boundary

Morphotropic phase boundary (MPB) is defined as the structural phase boundary formed in a pseudo binary solid solution made with two structurally dissimilar end members. Many of the technologically useful ferroelectric materials exhibit their maximum piezoelectric response at this phase transition region.[29] Near MPB region, a sudden change in crystal structure is observed and the dielectric properties and electromechanical properties become maximum. Compositions near MPB region are used in electrostrictive actuators and sensors due to their large dielectric

and piezoelectric constant. The term MPB was previously used to describe the phase transition due to the changes in composition. Later it has been redefined as the phase transition due to changes in composition or due to mechanical pressure. Jaffe *et al* proposed the term morphotropic phase boundary (MPB) to define boundary between two phases.[30]

Various physical properties of perovskites can be tuned by substituting with suitable cations in the A and B crystallographic site. In the case of PMN (lead magnesium niobate) relaxor ferroelectrics, the substitution of $(Mg_{1/3}Nb_{2/3})^{4+}$ by Ti^{4+} in $PbTiO_3$ results in a long range polar order, consequently a transition from relaxor to ferroelectric state happens.[31,32] When Ba^{2+} is substituted with Pb^{2+} in $BaTiO_3$, the ferroelectric phase transition temperature is increased up to 300 ^oC and the tetragonality of the structure also is increased. The well-known perovskite solid solutions are PZT (lead zirconate titanate) and PMN-PT (lead magnesium niobate-lead titanate).

Ferroelectric properties of $PbTiO_3$ are known since the early 1950s.[34,35] Many of its properties are analogous to that of $BaTiO_3$.[36] Its room temperature crystal structure is tetragonal and it undergoes a paraelectric to ferroelectric phase transition at its Curie temperature (T_C = 490 ^oC). Among the perovskite solid solutions, $PbZrO_3$-$PbTiO_3$(PZT) solid solution has widespread application in technology.[37-39] The $PbZrO_3$-$PbTiO_3$ phase diagram is shown in Figure 1.7.

Modified PZT ceramics possess relatively high T_C and large d_{33} values which make them useful in various applications. In the low temperature PZT phase diagram, two regions of different symmetry are observed.[40] The Zr-rich region lies in the rhombohedral symmetry and the Ti- rich region lies in the tetragonal symmetry that is shown in Figure 1.7. PZT system shows maximum piezoelectric response in the MPB region that is the boundary between two phases where x = 0.47 in $PbZr_{1-x}Ti_xO_3$.[41] The maximum piezoelectric properties of PZT are observed in MPB region.

Further studies on PZT ceramics proved that a monoclinic phase exist in the MPB region which links the tetragonal and rhombohedral phases.[42] Guo *et al*[43] and Noheda *et al*[40] proposed that the high piezoelectric response in PZT is due to the existence of monoclinic phase. The long range monoclinic structure originates due to the local displacements in the rhombohedral and

tetragonal structure. In the rhombohedral phase, the polarization axis is <111> and in the tetragonal phase polarization is in the <100> axis. Consequently, the polarization in the monoclinic phase possibly takes a range of directions within the {110} planes. Monoclinic distortion of the unit cell occurs when the polar axis rotate in the monoclinic plane. Consequently, large atomic displacement occurs in the crystal and this result in high piezoelectric response of the material.[43]

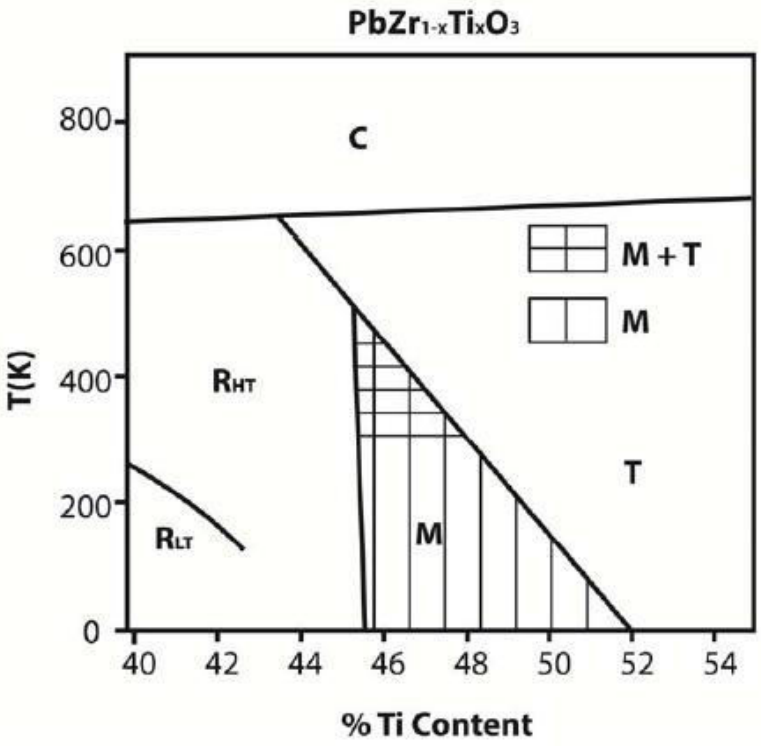

Figure 1.7: Phase diagram of (1-*x*)$PbZrO_3$-*x*$PbTiO_3$ solid solution near MPB region (M – monoclinic, T-tetragonal, R_{HT} – High temperature rhombohedral, R_{LT} – Low temperature rhombohedral, C- Cubic).[33]

Generally, complex structured materials are used for MPB compositions with high piezoelectric response. For example, the phase transition region in materials such as lead zirconatetitanate ($PbZr_{(1-x)}Ti_xO_3$, PZT), and lead magnesium niobate-lead titanate ((1-*x*)$PbMg_{1/3}Nb_{2/3}O_3$-*x*$PbTiO_3$, PMN-PT) are complex structured and the preparation of their solid solution is a difficult and overpriced process. In recent times, scientist started investigating the possibility of MPB region in simple structured ferroelectric oxides. Ahart *et al*[44] showed the presence of large MPB region in lead titanate ($PbTiO_3$) under pressure. Nowadays more studies

are going on to improve the properties of MPB region and to develop engineering specific simple structured nonlinear materials with large nonlinear dielectric and piezoelectric properties.

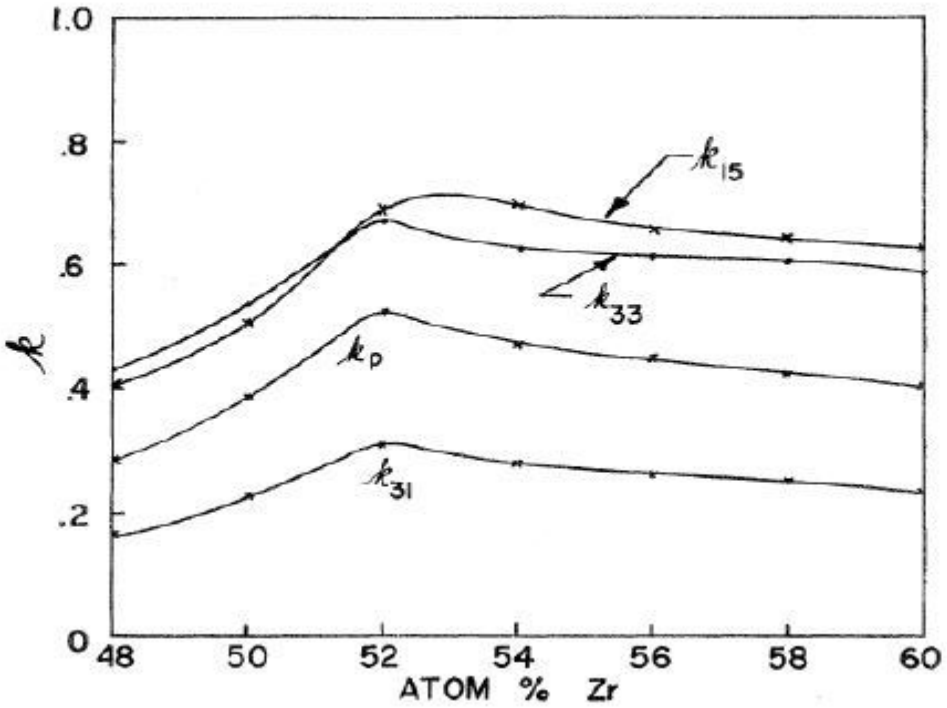

Figure 1.8: Piezoelectric coupling in PZT, showing peak near MPB region.[45]

Lead magnesium niobate (PMN) is a relaxor ferroelectric with a low Curie point (T_C = −10 °C). PMN possesses a broad and diffused phase transition below the Curie point. It exhibits high dielectric constant and less temperature dependence of the dielectric constant close to room temperature. The dielectric constant is dependent on frequency and with frequency the Curie point can shift to higher temperatures.[46] The phase diagram of PMN-PT near the MPB region is shown in Figure 1.9. (1-*x*)$Pb(Mg_{1/3}Nb_{2/3})O_3$-*x*$PbTiO_3$ solid solution for $x < 0.20$ shows relaxor behavior, showing very high maximum dielectric constant (~30,000). When compared to the dielectric constant of $BaTiO_3$ (10,000), which is currently used in multilayer capacitors, PMN-PT solid solution gives high dielectric constant value for composition with *x* between 0.05 and 0.10. Since the dielectric permittivity in this compositional region is very high, the PMN-PT solid solutions are very good candidates for high charge density capacitors.

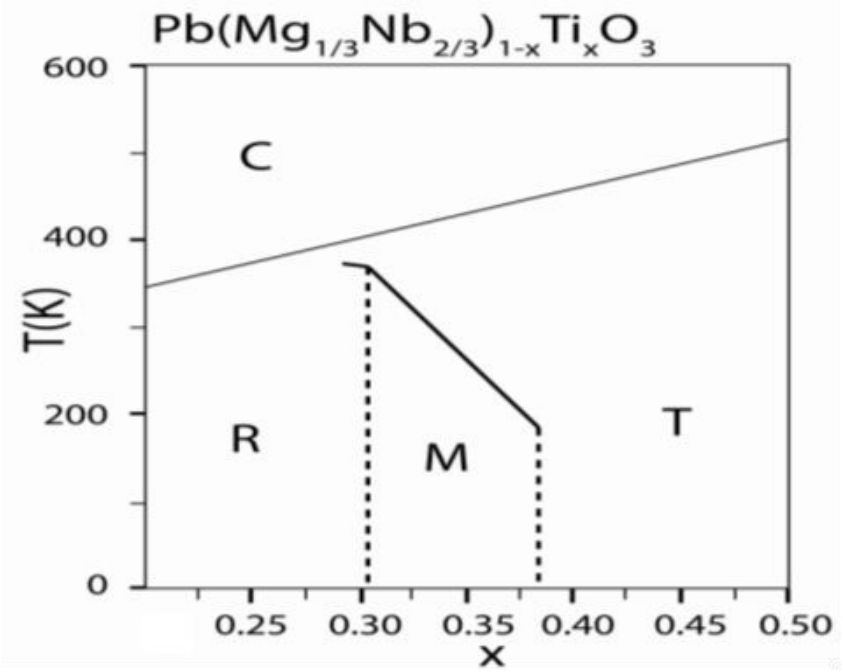

Figure 1.9: Temperature versus composition phase diagram of the (1-*x*)$Pb(Mg_{1/3}Nb_{2/3})O_3$-$PbTiO_3$(C-cubic, R- rhombohedral, M-monoclinic, T- tetragonal).[46]

Electromechanical properties of few important perovskite single crystals are given in table 1.4.[47] Here Type II is modified PZT with high electromechanical coupling and type III is modified PZT with low loss at high electric fields.

Table 1.4: Electromechanical properties of single crystals.[47]

Material	**PZT type II ceramics**	**PZT type III ceramics**	**PZN-0.045PT crystals**	**PMN-0.33PT crystals**
Dielectric constant (RT)	2050	100	5000	8000
Dielectric loss	0.018	0.003	0.01	0.01
T_C (^oC)	340	300	155	166
Electromechanical coupling coefficient (K_{33})	0.73	0.64	0.92	0.94
Piezoelectric coefficient (d_{33} , pC/N)	400	225	2200	2200

Even though PMN-PT solid solution shows high piezoelectric response, it has some disadvantages such as low T_C and lower rhombohedral to tetragonal transition temperature (T_{RT}). Since T_C is very low, thermal depoling may happen to the ceramics at high operating temperature. Hence the operating temperature has to be kept low always. The operating temperature range of piezoelectric materials is 2/3 of the lowest phase transition temperature so that the depoling can be avoided. The low depoling temperature of PMN-PT solid solution makes the material's application difficult in devices.

1.7. Lead-free ferroelectric perovskites

The high performance piezoelectric material PZT was discovered in 1952, and still it is commonly used in most of the piezoelectric applications. Although PZT is widely used, the PbO used for the preparation of PZT ceramics is highly toxic and it causes serious environmental and health issues.[48] During the preparation and sintering of PZT, PbO is released into the atmosphere and that will enhance the pollution. Therefore, there is an urgent need to develop lead-free high performance piezoelectric materials. Alkali metal based bismuth sodium titanate, $Bi_{0.5}Na_{0.5}TiO_3$ (BNT), bismuth potassium titanate, $Bi_{0.5}K_{0.5}TiO_3$ (BKT), potassium sodium niobate, $KNaNbO_3$ (KNN), etc. are among the initially developed lead-free piezoelectric materials.[49-51] However, these systems have some drawbacks such as i) sintering temperature range is narrow, ii) piezo properties are low, iii) due to the presence of alkali metals, they are highly corrosive, and iv) difficult to maintain stoichiometry due to the high volatility . Recently developed barium zirconate titanate – barium calcium titanate compositions, $Ba(ZrTi)O_3$-$(BaCa)TiO_3$ (BZT – BCT) possess high piezoelectric properties.[52,53] However, research is still going on for the development of lead-free piezoelectric materials and how to use them in practical applications.

The lead-free piezoelectric materials such as barium titanate (BT), bismuth sodium titanate (BNT), bismuth potassium titanate (BKT), sodium niobate ($NaNbO_3$), potassium niobate ($KNbO_3$), potassium sodium niobate (KNN), bismuth based layered structures, $(Bi_2O_2)^{2+}$ $(A_{n-1}B_nO_{3n+1})^{2-}$(BLSF) etc were developed in the 1950's, but did not get much attention due to their less piezoelectric properties compared to that of PZT.[49-51] The first lead-free polycrystalline piezoelectric ceramics discovered was $BaTiO_3$, possessing a piezoelectric constant (d_{33}) of approximately 190 pC/N.[54] It can be synthesized by the conventional solid state

processing. The very low Curie temperature (T_C = 120 ^oC)of $BaTiO_3$ made its practical application limited.[55]

Table 1.5: Piezoelectric properties of BNT–BKT based solid solution.

Sr. No	Composition	d_{33}(pC/N)	Ref.
1	$(Bi_{1/2}Na_{1/2})TiO_3$ (hot pressed)	94-98	56
2	$(Bi_{1/2}K_{1/2})TiO_3$ (hot pressed)	69	57
3	$(1-x)Bi_{0.5}Na_{0.5}TiO_3$-$xBi_{0.5}K_{0.5}TiO_3$	140-192	58
4	$(Na_{1-x}K_x)_{0.5}Bi_{0.5}TiO_3$	192	59
5	$Bi_{0.5}Na_{0.5}TiO_3$-Ba(Zr,Ti)O_3+2mol% of CuO	156	60
6	$85(Bi_{1/2}Na_{1/2})TiO_3$-$12(Bi_{1/2}K_{1/2})TiO_3$-$3BaTiO_3$	158	61
7	$[(Bi_{0.98}La_{0.02}Na_{1-x}Li_x)_{0.5}]_{0.94}Ba_{0.06}TiO_3$	212	62
8	$BiNaTiO_3$-$BiKTiO_3$-$BiLiTiO_3$	230	63
9	$Bi_{0.5}Na_{0.5}TiO_3$-$Bi_{0.5}K_{0.5}TiO_3$-$Bi_{0.5}Li_{0.5}TiO_3$	147-231	64
10	$Bi_{1/2}Na_{1/2}TiO_3$-$Bi_{1/2}K_{1/2}TiO_3$-$Bi_{1/2}Li_{1/2}TiO_3$ - $BaTiO_3$	163	65

BNT (bismuth sodium titanate, $Bi_{0.5}Na_{0.5}TiO_3$) is a ferroelectric material having large remnant polarization (P_r =38 $\mu C/cm^2$) and a high Curie temperature (T_C = 320 ^oC). It possesses high electromechanical coupling constant and its extended strain under high field is almost comparable to that of PZT. Thus, BNT based solid solutions are good substitutes for PZT, if its drawbacks can be overcome. BNT has some drawbacks such as high conductivity and large coercive field. The solid solution formed between BNT and BKT (bismuth potassium titanate, $Bi_{0.5}K_{0.5}TiO_3$) can overcome some of the drawbacks of BNT. BNT–BKT based lead–free solid solutions are studied for their possible technological applications. The first report on BNT was by Smolenskii *et al* in 1960.[66] Piezoelectric constant (d_{33}) approximately equal to 94-98 pC/N was reported for BNT ceramics synthesized by hot pressing method.[56] Popper *et al* synthesized BKT in 1957.[67] BKT ceramics obtained by hot pressing method has a d_{33} value of 69 pC/N, less than that of BNT.[57] Solid solution between BNT and BKT were synthesized and studied by Elkechai *et al* in 1996.[68] BNT and BKT have different crystal structures and the ferroelectric properties of the solid solutions are found to be higher in the MPB region, with the piezoelectric

constant in the range 140-192 pC/N.[58] The main advantage of BNT–BKT solid solution is its high Curie temperature (T_C) which is larger than 280 °C, so that it can be used in a wide temperature range. However, this solid solution has some drawbacks such as i) low piezo properties, ii) due to the presence of alkali metals, it is highly corrosive, iii) narrow sintering temperature range, and iv) difficult to maintain stoichiometry due to the volatile nature. The piezo electric properties of BNT–BKT solid solution can be further improved by making solid solutions with BT, BZT etc. Piezoelectric properties of some BNT–BKT based solid solutions are compared in Table 1.5.[56-65]

1.8. Objectives of the present work

In the $Bi_{0.5}Na_{0.5-x}K_xTiO_3$ (BNKT) solid solution series (or commonly represented as (1-*x*)BNT–*x*BKT), it has been shown that the dielectric and piezoelectric properties are enhanced, with maximum electromechanical coupling constant in the region $x = 0.16–0.20$.[58] The density and microstructure of the material also show some unusual trend near this compositional region.[58] This region is technologically very important, since all the ferroelectric and piezoelectric properties are maximum.

There are various contradicting reports about the crystal structure, structural phase transformation, the existence of MPB region, and the compositional range of the MPB region of the (1-*x*)BNT–*x*BKT system. The room temperature crystal structure of BNT is reported as rhombohedral, with space group, R3c. However, high resolution single crystal X-ray diffraction studies by Gorfman and Thomas[69] proved that the actual room temperature symmetry of BNT is lower than rhombohedral. The authors achieved best fit with C–centered monoclinic lattice (space group Cc). Later, it has been reported that structure of polycrystalline BNT can also be best modeled using the monoclinic Cc space group rather than the previously accepted rhombohedral R3c space group. The room temperature crystal structure of BKT is tetragonal (P4bm) and therefore, an MPB region is expected in the BNT–BKT solid solution series as observed for PZT with different symmetries for the end members.

The presence of the MPB region is reported in the compositional range of $0.16 \leq x \leq 0.2$ in (1-*x*)BNT–*x*BKT by Yang *et al*[58] from XRD analysis and electrical property measurements. In the MPB region, the crystal structure is shown to transform from rhombohedral (R3c) to

tetragonal (P4mm). It is observed that at $x = 0.16$ the (211) peak in the XRD pattern begins to split. The peak splits out to (211) and (112) for the compositions $x = 0.18$ and 0.2 where the phase transforms from rhombohedral to tetragonal. Maximum density, relatively low grain size and compact microstructure with low porosity are obtained in this compositional region. Moreover, piezoelectric and dielectric properties are found to be maximum in this region. Kreisel *et al* investigated the BNKT system using XRD and Raman spectroscopy.[70] The authors have observed that the crystal structure is rhombohedral for small K^+ concentrations ($x < 0.25$) and pseudo-cubic for $0.25 \leq x \leq 0.4$. They have analysed the phonon characteristics of (1-x)BNT–xBKT and observed a high frequency shift on increasing the substitution. Izumi *et al* proposed that MPB region does not exist at all and only a structural distortion occurs due to the local distortion in the A site in the crystal lattice.[71] It was observed that the lattice parameters increase monotonically as a function of K^+ concentration. It has been argued that compositions in the region $0.2 < x < 0.4$ is a mixture of rhombohedral and tetragonal domains, which leads to cubic-like XRD patterns. Sasaki *et al* reported that the rhombohedral and tetragonal phases co-exist in the region $0.16 \leq x \leq 0.2$ by observing the split in the XRD pattern and the peaks of electromechanical coupling factor, dielectric constant, piezoelectric constant and elastic compliance were obtained in this region.[72] Chen *et al* observed presence of rhombohedral and tetragonal phases in the composition for $x = 0.18$.[73] Elkechai *et al* found that rhombohedral and tetragonal phases co-exist in the compositional region $0.16 \leq x \leq 0.2$.[68] Xie *et al* argued that the MPB exists only at $x = 0.2$, below and above which the structure is rhombohedral and tetragonal, respectively, and there is no co-existence of mixed phase in any compositional region.[74]

Since there are many contradicting reports on the structure, phase transition and MPB region of the BNT–BKT series, it is felt that detailed structural studies are required to understand the structural changes on substitution of Na^+ by K^+. Moreover, most of the reported studies are performed on few compositions of the solid solutions. Since Raman spectroscopy and solid-state NMR studies can give information on local structural environment, these two techniques, along with Rietveld refinement of powder X-ray diffraction pattern, are used for the structural characterizations. The objective of the present work is to investigate the structural changes associated with the substitution of Na as well as Bi in $Bi_{0.5}Na_{0.5}TiO_3$ (BNT), and to correlate with the associated changes in the microstructure and dielectric properties.

In BNKT, the smaller cation Na^+ is replaced by the larger cation K^+ and the objective is to investigate i) whether a real MPB region exists, ii) what is the actual MPB concentration region, iii) whether the structural transformation is a direct transformation from rhombohedral or monoclinic to tetragonal iv) whether an intermediate triclinic or pseudo cubic phase exist, v) if the MPB region does not exist, what could be the reason for the high dielectric and piezoelectric properties at a particular concentration region. Therefore, structural studies, along with the dielectric properties, are made on very close compositions in $(1-x)Bi_{0.5}Na_{0.5}TiO_3–xBi_{0.5}K_{0.5}TiO_3$, for $\Delta x = 0.01$ in the proposed MPB region and $\Delta x = 0.02$ above and below the MPB region.

The ionic radii of Li^+, Na^+ and K^+ are 0.92 Å, 1.39 Å and 1.64 Å, respectively. The average size of Li^+ and K^+ is comparable to the size of Na^+. To investigate the role of cation size on the structure and properties of the BNT–BKT series, substitution of Na^+ in BNT by the smaller cation Li^+ in $Bi_{0.5}Na_{0.5-x}Li_xTiO_3$ or $(1-x)Bi_{0.5}Na_{0.5}TiO_3–xBi_{0.5}Li_{0.5}TiO_3$ (BNT–BLT series) and co-substitution of Li^+ and K^+ for Na^+, $(1-x)Bi_{0.5}Na_{0.5}TiO_3–(x/2)Bi_{0.5}Li_{0.5}TiO_3–(x/2)Bi_{0.5}K_{0.5}TiO_3$ (BNT–BLT–BKT series) have been attempted. The structure and dielectric properties of the substituted solid solution series are studied and the changes in the structure and local symmetry are correlated with the dielectric properties.

To understand the role of Bi $6s^2$ lone pair towards the piezoelectric properties of BNT, substitution of La^{3+} for Bi^{3+} in $Bi_{0.5-x}La_xNa_{0.5}TiO_3$ solid solution series is investigated. The piezoelectric properties of BNT may be either due to the distorted TiO_6 octahedra as in $BaTiO_3$ or due to the lone pair of Bi^{3+} ion, as in $BiFeO_3$ or both. Since the ionic radius of La^{3+} is almost the same as that of Bi^{3+} and the $6s^2$ lone pair is absent in La^{3+}, the studies on La^{3+} substituted BNT are expected to give information about the effect of lone pair on the ferroelectric properties. In the present study the crystal structure, local symmetry changes, microstructure and properties of $Bi_{0.5-x}La_xNa_{0.5}TiO_3$ solid solution series are investigated.

Changes in structure and lattice parameters are expected by the substitution of different ions (Li^+, K^+, La^{3+}) in the BNT lattice. These changes are reflected in the XRD pattern of the solid solution series. The studies on the XRD pattern of all the composition provide valuable information about the structural changes and deviation in lattice parameters with substitution. Rietveld refinement analysis of the XRD patterns of all the compositions provides information about the symmetry changes with substitution. The XRD data mainly provide information on

long range order of the material, whereas Raman and SSNMR spectroscopy are highly useful in probing local symmetry changes. The effect of substitution and the changes in symmetry are expected to be observed in the Raman spectra of the solid solution. The regions belong to different vibrations can be identified in the Raman spectra and the changes in different bonds with substitution are visible in the respective regions. The deconvolution of Raman spectra provides the changes in peak position and the changes in the area under the peak with substitution which give information regarding the local symmetry changes. The changes in local symmetry can also be studied using SSNMR by probing the quadrupolar nuclei ^{23}Na, ^{7}Li, ^{139}La. The SSNMR spectra of these nuclei will show changes in quadrupolar broadening with substitution. The deconvolution of the NMR spectra with substitution give the quadrupolar coupling constant which is related to the symmetry of the material. The changes in the local symmetry will be reflected in the quadrupolar coupling constants. The properties of the solid solution will change with substitution that is associated with the local symmetry changes and structural changes of the solid solution. Hence the structural studies using XRD, Raman and SSNMR will give a clear picture of substitution effects in the solid solutions and can also explain the changes in properties with substitution.

Chapter 2

Experimental Methods

2.1. Introduction

Different methods of synthesis and characterization techniques are used in the present work. This chapter briefly describes the methods of synthesis and the various techniques used for characterization of the materials such as powder X-ray diffraction, solid-state NMR, Raman spectroscopy, dielectric measurements and scanning electron microscopy.

2.2. Materials used

The following chemicals are used for the synthesis of different metal oxide compositions.

1. Bismuth oxide, Bi_2O_3 (Aldrich, 99.9%)
2. Sodium carbonate, Na_2CO_3 (Sd fine, 99.5%)
3. Potassium carbonate, K_2CO_3 (BDH, 99%)
4. Titanium oxide, TiO_2 (Aldrich, 99.9%)
5. Bismuth nitrate, $Bi(NO_3)_3.5H_2O$ (Sd fine 98%)
6. Sodium Nitrate, $NaNO_3$ (Merck, 99%)
7. Lithium Nitrate, $LiNO_3$ (Aldrich, 99.999%)
8. Potassium Nitrate. KNO_3 (Merck, 99%)
9. Lanthanum Nitrate, $La(NO_3)_3.6H_2O$ (Aldrich, 99.999%)
10. Citric Acid, CH_2COOH-$C(OH)COOH$-CH_2COOH (Sd fine, 99.7%)
11. Titanium isopropoxide, $Ti[OCH(CH_3)_2]_4$(Aldrich, 99%)
12. Isopropyl alcohol, $(CH_3)_2CHOH$ (Merck, 99.5%)

2.3. Synthesis methods

Various methods are available for the preparation of inorganic oxides and the method chosen depends on the form of the desired product. The most common methods used for the synthesis of metal oxides are solid state or ceramic method and wet chemical methods such as sol-gel, co-precipitation and combustion.[75-78] The ceramic method and sol-gel method are used for the synthesis of the metal oxides studied in this work. All the chemicals were used as-received without any further purification. Distilled water is used for each synthesis. Initial calcination of the samples were done in a muffle furnace (30–1000 ^oC, Kumar instruments, India) and the high

temperature heating of the samples, in the range 1000–1200 ^{o}C, were done in a programmable furnace with controlled heating and cooling arrangements (Model HT1600, Nabertherm, Germany). Alumina and platinum crucibles were used for heating the samples at high temperatures.

2.3.1. Ceramic method (Solid state method)

Solid state method is the simplest and the most common method for the synthesis of oxide ceramics. Stoichiometric amounts of binary oxides, corresponding to the composition of the final product, are taken and mixed together (usually grind them in a mortar and pestle to get a uniform distribution, or mix in a ball mill) and then heat in a furnace for several hours in a suitable container (usually silica/alumina/zirconia/platinum crucible).[12] This method of synthesis generally requires very high temperatures, usually in the range 500–2000 ^{o}C, and prolonged heating. The binary compositions possess high coordination number, depending on the size and charge of the metal ion involved and this varies between 4 and 12. High temperature is required to overcome the lattice energy of the cations so that the cations can leave their position in the lattice and diffuse to a different site to form a new composition. The heating temperatures of the solids are not higher than their melting temperatures and hence the reaction occurs in the solid state. The solid state reactions take place only at the interface between two solids. After the surface layer has reacted, the reactants diffuse from the bulk to the interface to continue the reaction. At high temperatures the reactions at the interface are more feasible and the diffusion of the solids is faster than that at room temperature. In order to minimize the distance for the reactants to diffuse, the reactants are ground to small particle size and are mixed well to maximize the surface contact area. The solid state synthesis method is used for both industrial and laboratory purposes. It has been used for the synthesis of several materials such as metal oxides, sulfides, nitrides, aluminosilicates, etc.

In the present work, different compositions in the (1-x)$Bi_{0.5}Na_{0.5}TiO_3$–x$Bi_{0.5}K_{0.5}TiO_3$ solid solution series were prepared by the ceramic method. The corresponding metal oxides and carbonates (Bi_2O_3, TiO_2, Na_2CO_3, K_2CO_3), taken in the stoichiometric ratio, were mixed thoroughly using an agate mortar and pestle. For example, for the synthesis of $Bi_{0.5}Na_{0.5}TiO_3$, 2.6136 g of Bi_2O_3, 0.5945 g of Na_2CO_3 and 1.7919 g of TiO_2 were taken (in the molar ratio

1:1:2), corresponding to a total weight of 5.00 g of the final product. The mixed powders were initially calcined at 850 ^{o}C and further calcined at 1000 ^{o}C and then at 1150 ^{o}C, with intermediate grindings, until the final composition, free of any impurities or the starting components, are formed.

2.3.2. Citrate-gel method

The citrate-gel method is a type of sol-gel method. The advantages of sol-gel method are the low calcination temperature and short time required for the synthesis of metal oxide ceramics.[79-80] The sol-gel method is a wet chemical method and it is a two-step process, consisting of i) formation of a suitable precursor in the form of a gel, ii) calcination of the dried gel to get the final product. In citrate gel method for the synthesis of metal oxide, citric acid is used as a complexing agent along with the metal salts. In this method, for the synthesis of metal oxides, stoichiometric ratio of the constituent metal salts are dissolved in a solvent and mixed well. Citric acid solution is added to the mixed metal solution by keeping an appropriate citric acid to metal ion ratio. Then the mixed solution is kept in a water bath for evaporation of the solvent. The dried gel obtained after the evaporation of the solvent is calcined at a suitable temperature for obtaining the metal oxide.

In the present work, different compositions of (1-x)$Bi_{0.5}Na_{0.5}TiO_3$–x$Bi_{0.5}Li_{0.5}TiO_3$, (1-x)$Bi_{0.5}Na_{0.5}TiO_3$–(x/2)$Bi_{0.5}Li_{0.5}TiO_3$–(x/2)$Bi_{0.5}K_{0.5}TiO_3$ and (1-x)$Bi_{0.5}Na_{0.5}TiO_3$–x$La_{0.5}Na_{0.5}TiO_3$ solid solution series were synthesized by the citrate-gel method. Stoichiometric amounts of the corresponding metal nitrate solutions were prepared by dissolving, bismuth nitrate in dilute nitric acid and other nitrates in water. Then the individual metal nitrate solutions were mixed together. Titanium isopropoxide ($Ti[OCH(CH_3)_2]_4$) was dissolved in isopropyl alcohol by stirring for 30 minutes. Then citric acid was dissolved in titanium isopropoxide solution. The ratio of citric acid to total metal nitrate content was taken as 3:1. The mixed solution of the metal nitrates was added to the titanium isopropoxide solution with constant stirring and kept on a water bath for the evaporation of the solvent. The solution becomes more and more viscous due to the continuous removal of solvent during evaporation. The gel formed after the complete removal of solvent was dried and calcined at appropriate temperatures to obtain the corresponding metal oxides. The details of the synthesis of individual compounds are discussed in the respective chapters.

2.4. Characterization techniques

Powder X-ray diffraction, solid-state NMR and Raman spectroscopy are the main characterization techniques used in this work. The primary characterization of the material was done by powder X-ray diffraction and more information on the crystal structure was obtained by Rietveld refinement of the XRD patterns. Further structural information was obtained from the analysis of the Raman and solid-state NMR spectra.

2.4.1. Powder X-ray diffraction

Powder X-ray diffraction technique is mainly used for phase identification of polycrystalline materials as well as to elucidate their crystal structure parameters.[12,81,82] The diffraction patterns obtained during the interaction between the crystalline phase and X-rays are characteristic of that crystalline material, which helps as a fingerprint for the identification of the particular material.

The wavelength of the X-ray is similar to the inter atomic separation (~1 Å) of the crystals. Hence, crystals having regularly repeating structures diffract X-rays. Peaks in the XRD patterns are obtained when the Bragg condition is satisfied, given by the Bragg's law,

$$2d \sin\theta = n\lambda \qquad (2.1)$$

where, d is the inter-planar spacing, θ is the angle of diffraction, called the Bragg angle, λ is the wavelength of X-rays and n is the order of diffraction which is usually 1. When Bragg's law is satisfied, the diffracted beams are in phase and the interference is constructive.

The atoms or ions in crystals act as secondary point sources and scatter the X-rays. The oscillating electric field associated with X-rays cause the vibration of the electrons in the atom. The emitted radiations from the vibrating charge are in phase with the incident X-ray beam. The efficiency of scattering of a given atom in a given direction is termed as atomic scattering factor.

$$\text{Atomic scattering factor, } f = \frac{\text{Amplitude of wave scattered by an atom}}{\text{Amplitude of wave scattered by an electron}} \qquad (2.2)$$

The structural factor F is defined as the resultant wave scattered by all the atoms of the unit cell. It is obtained by adding all the waves from the individual atoms. If a unit cell contains n (1, 2, 3, etc.) number of atoms with fractional co-ordinates (U_n, V_n, W_n), with scattering factors f_1, f_2,…., f_n.

$$F_{hkl} = \sum_1^n f_n \, e^{2\pi i(hU_n + kV_n + lW_n)} \quad (2.3)$$

(h, k, l) is a set of three numbers used for labeling lattice planes known as Miller indices. F_{hkl} is the expression for any scattered wave from the crystal system. The intensity of the X-ray peak depends on the structure factor and the diffraction angle is determined by the crystal lattice type and the diffraction plane.

In the present work, powder XRD analysis was carried out on a PANalytical X'pert pro powder X-ray diffractometer using Cu-K_α radiation (λ = 1.5418 Å), with Ni filter. The $K_{\alpha 2}$ component was not removed from the incident X-rays and, hence both the $K_{\alpha 1}$ and $K_{\alpha 2}$ components are present in the XRD patterns. A voltage of 40 kV was applied to the X-ray tube. The samples were scanned in the 2θ range of 10-80 degrees. A scanning rate of 2 ^{o}/min was used for general characterization. A computer program Powder Cell for Windows (PCW) version 2.4 was used for the simulation of XRD patterns.[83] The space group, lattice parameters and atomic positions of the corresponding phases, taken from the literature, are used as inputs for the simulation of the XRD patterns using the PCW software and the simulated patterns are compared with the experimental patterns to identify the phases. The structural analysis of the material was further carried out with Rietveld refinement of the XRD patterns. The XRD patterns were recorded at a slow scan rate of 1.16 ^{o}/min, for Rietveld refinement analysis.

2.4.1.1. Rietveld refinement

Hugo Rietveld developed the Rietveld refinement of powder XRD patternsfor the structural analysis of polycrystalline materials.[84,85] An XRD pattern contains information regarding the atomic positions, lattice spacing and symmetry of the crystal structure which can be determined from the intensity, width and position of the reflections.[86] The XRD patterns are generally recorded in a specific 2θ range with small increments (0.01 ^{o} to 0.05 ^{o}) for Rietveld refinement analysis.

A least square approach is used in the Rietveld refinement to obtain the best fit between the experimental and simulated patterns. This is done by minimizing the residual S_y given by the equation

$$S_y = \sum_i w_i \, (y_i - y_{ci})^2 \quad (2.4)$$

Where y_i is the observed intensity at the i'th step, w_i is the statistical weight assigned to y_i as $w_i = \frac{1}{y_i}$ and y_{ci} is the calculated intensity at the i'th step.

The Rietveld method deals with strongly overlapping reflections in a reliable fashion as the overlapping peaks are shown distinctly, thus enabling precise determination of the structure of the crystals. The Rietveld refinement produces a key feedback during the refinements between improving structural understanding and improving allocation of experimental intensity to overlapping individual Bragg reflections. The refinable parameters adjust during the Rietveld refinement process until the residual is minimized. The refinement is continued until the best fit of the entire calculated pattern to the entire observed pattern is obtained. The goodness of the fit is indicated by residual factors (R-factors). The residual factors are

$$\text{R-structure factor, } R_{F^2} = \frac{\sum I_k^{1/2} - I_{ck}^{1/2}}{\sum I_k^{1/2}} \tag{2.5}$$

$$\text{R-Bragg factor, } R_B = \frac{I_k - I_{ck}}{\sum I_{ck}} \tag{2.6}$$

$$\text{R-pattern, } R_p = \sqrt{\frac{\sum (y_i - y_{ci})}{\sum y_i}} \tag{2.7}$$

$$\text{R-weighted pattern, } R_{wp} = \sqrt{\frac{\sum w_i ((y_i - y_{ci})^2}{\sum w_i y_i^2}} \tag{2.8}$$

$$\text{R-expected, } R_e = \sqrt{\frac{M - m}{\sum w_i y_i^2}} \tag{2.9}$$

Where I_k is the intensity of the k'th Bragg reflection and I_{ck} is the calculated intensity of the k'th Bragg reflection, M is the number of steps in the pattern and m is the number of refinable parameters. The most meaningful R is R_{wp} since its numerator is the residual which is being minimized. The goodness of the fit is also indicated by the χ factor, which is given by

$$\chi^2 = {R_{wp}}\Big/{R_e} \tag{2.10}$$

The General Structure Analysis System (GSAS-EXPGUI) software is used in the present work for the Rietveld refinement analysis of the powder diffraction data.[87] The recorded raw XRD data without data smoothening and $K_{\alpha 2}$ stripping was used for the refinement. A good starting model is required for the refinement. The non-linear relationship between the adjustable parameter and the intensities may lead to a false minimum, if the starting model is not close to

the correct model. Hence the known crystal parameters of the corresponding compounds were used for the refinement. In the present work a reported procedure is followed for the Rietveld refinement of the XRD pattern. Initially the scaling factor and the background functions were refined until the intensity of the pattern is almost matched. Then the refinement of the lattice parameters were carried out that approximately fixed the positions of the peaks. After that the profile and symmetry parameters were refined using the pseudo-Voigt function. Finally the atomic co-ordinates were refined. The refinement is continued until the best fit to the experimental pattern is obtained.

2.4.2. Solid-state NMR

Solid-state NMR spectroscopy is a non destructive method for probing the local structural changes in a material.[88] It is also used for studying the structure of the material and dynamics of the ions present in the material. The interactions present in NMR active nuclei are Zeeman interaction (H_Z), J- coupling interaction (H_J), chemical shift (H_{CS}), dipolar interaction (H_D) and for nuclei I > ½, the quadrupolar interaction (H_Q).[88] The total Hamiltonian for NMR interactions is given as

$$H= H_z + H_J + H_{CS} + H_D + H_Q \quad (2.11)$$

The J-coupling and the through space dipolar interaction are the most important interactions in the liquid state NMR whereas it is negligible in solid-state NMR. The rapid molecular motion present in the liquids average out all the NMR interactions and a high resolution spectra with only isotropic chemical shift are observed in the liquid state NMR. The close-packed atoms within the structure of solids limit the random molecular motions and broad, less resolved NMR spectra due to the anisotropy in dipolar, quadrupolar and chemical shift interactions are observed.

The charge distribution in a spin ½ nuclei is spherically symmetric whereas a nuclei with I >½ possess a non symmetrical distribution of nuclear charge. Nuclei with I >½ have a quadrupolar moment which indicates a non symmetric charge distribution. The electric field gradient (EFG) created by the surrounding electron cloud at the site of the nuclei and the external or internal magnetic field, interact with quadrupolar moment which is termed as the quadrupolar

interactions. The strength of the quadrupolar interaction depends on the quadrupole moment of the nuclei and the strength of the electric field gradient.

Various techniques such as magic angle spinning (MAS), double rotation (DOR), dynamic angle spinning (DAS), multiple quantum magic angle spinning (MQMAS) are developed for removing the anisotropic interactions and improving the resolution in the solid-state NMR spectra.[89]

2.4.2.1. Magic angle spinning experiments

Mechanical rotation of the sample at the magic angle 54.74 ^{o} with respect to the static magnetic field average out the anisotropic interactions and produce isotropic-like spectra with resolved chemical shift in the case of spin half nuclei. MAS experiments require high sample rotation speed to achieve significant enhancement in resolution and sensitivity. The rate of spinning speed must be fast in comparison to the anisotropy of the interaction being spun out. (Fast means around a factor of 3 or 4 greater than the anisotropy). Slower spinning of the sample produce spinning side bands which are spaced by the rotation frequency along with the line at the isotropic chemical shift. The only line which does not change its position with the spinning speed is isotropic chemical shift line. For quadrupolar nuclei with ($I > 1/2$), with a large quadrupolar interaction, MAS in not enough to obtain high resolution. For half-integer spin quadrupolar nuclei like ^{23}Na ($I = 3/2$), ^{7}Li ($I = 3/2$) and ^{139}La ($I=7/2$) which are probed in the present work, the MAS spectra is broadened when the quadrupolar interaction is high. To obtain high resolution, techniques like MQMAS, (discussed in section 2.4.2.2) are used to probe if multiple sites are present.

For a spin 1/2 nuclei, the $\pi/2$ pulse gives maximum intensity and that is usually used for recording MAS spectra. In the case of half-integer quadrupolar nuclei, the $\pi/2$ intensity of the spectrum is dependent on the quadrupolar coupling constant and to obtain quantitative evaluation of the site population, a MAS spectra is recorded with rf pulse width of $\pi/18$. The $\pi/18$ pulse is determined by recording the static spectra of the reference samples (0.1 M solution of NaCl, LiCl and $La(NO_3)_3$) in a rotor at the required rf power. A series of spectra with gradually increasing pulse width and adequate relaxation delay are recorded. A sinusoidal variation in

intensity is obtained when it is plotted against the pulse width. The $\pi/18$ pulse was calculated from the π pulse which was obtained from the null point.

2.4.2.2. Multiple quantum magic angle spinning

Multiple quantum magic angle spinning (MQMAS) is a two dimensional NMR experiment which is used for obtaining high resolution in half integer spin quadrupolar nuclei. In MQMAS experiments the narrowing of the central transition is obtained by the correlation of the phase evolutions of the symmetric multiple quantum (MQ) and single quantum (1Q) transitions under MAS. ^{23}Na multiple quantum magic angle spinning (MQMAS) experiments were carried out to get the resolved spectra and to check the possibilities of multiples sites.

Various schemes exist for recording 2D MQMAS spectra. The 3QMAS NMR experiments were done with the pulse sequence which includes a Z-filter pulse (low RF power) and has the advantage of having a symmetrical coherence transfer pathway. The pulse sequence and the coherence diagram are given in Figure 2.1, where d1 is the recycle delay, which is the delay between the two scans, d0 is the delay between the excitation and conversion pulses and d4 is the Z-filter delay. The triple quantum excitation is done with the first pulse p1 and the second pulse p2 is used for the coherence transfer from triple quantum to zero quantum. The third pulse p3 is the z-filter pulse which is used for the selective excitation of the central transition.

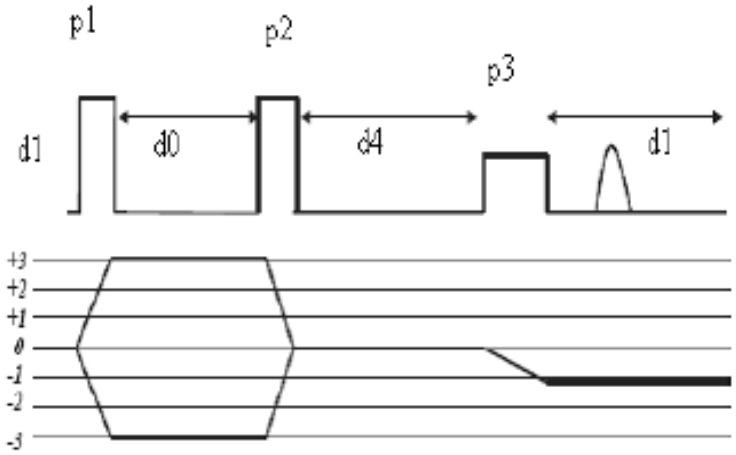

Figure 2.1: Pulse sequence and coherence diagram of 3QMAS experiment.

All the pulses p1, p2 and p3 need to be optimized before starting the experiment. Trial values for the pulses are used initially to record the one dimensional slice of the MQMAS experiment and the intensity is monitored systematically for different values of p1, p2, p3. Then the 2-dimmensional experiment is carried out with these optimized pulses. The experiment set up was first done with Sodium sulphite (Na_2SO_3) which has 3 different sodium sites with known quadrupolar and chemical shift values. The F1 dimension is multiple quantum dimensions and F2 is single quantum dimension in the MQMAS spectrum. Sharp parallel spectral ridges tilted by a slope (quadrupolar anisotropy, QA) obtained when it is processed with conventional 2D Fourier transformation. Projection of such raw data does not need high resolution spectra. In the F1 dimensionthe isotropic high resolution spectra is obtained with the shearing transformation. Hence the point which has the frequency (v_1, v_2) will lie at a frequency $(v_1\text{-}QA.v_2)$. In the present work, ^{23}Na MQMAS spectra were recorded to investigate if there were multiple sodium environments in the system. .

2.4.2.3. Line shape of the central transition of half-integer quadrupolar nuclei

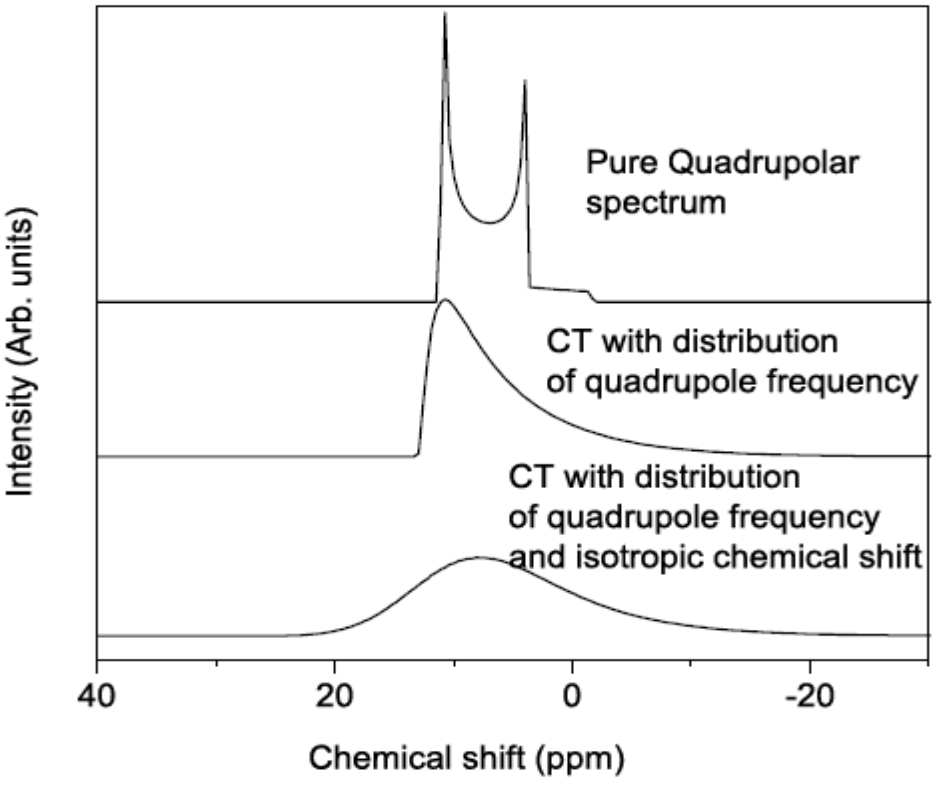

Figure 2.2: Line shape of central transition of the half integer quadrupolar nuclei.[91]

The line shape of the half integer quadrupolar nuclei depends on different NMR parameters such as quadrupole coupling constant and isotropic chemical shift. The central transition line shape of the half integer quadrupolar nuclei is shown in the Figure 2.2. If only quadrupolar interactions of the surrounding electric field are present, the characteristic line shape of the quadrupolar nuclei is with two horns which are shown in the Figure 2.2. If there is a distribution of the quadrupolar frequencies a trailing edge is developed towards the right of the spectrum. If both quadrupolar and isotropic chemical shift distribution is present, the spectra broadens and a complicated lines shape is seen. The Gaussian isotropic model (GIM) included in the NMR computer simulation program DMFIT[90] is used for the simulation of the spectra of such quadrupolar nuclei.

2.4.2.4. Deconvolution of NMR spectrum

Deconvolution of the experimental NMR spectra is done by estimating the chemical shift and quadrupole parameters and the structural information contained in the spectra can be extracted. The DMFIT program developed by Massiot *et al*[90] has incorporated the deconvolution models for the experimental NMR spectra which accurately defines the experiment and the spin system in reasonable computational costs. In the present study ^{23}Na and ^{139}La spectra is associated with a quadrupolar distribution, hence the simplest and physically consistent Gaussian isotropic model of Czjzek model is used for the simulation.[92] This model include the Gaussian isotropic model, that incorporate a Gaussian distribution of isotropic chemical shift and a distribution of the electric field gradient that gives a mean isotropic shift (δ_{iso}), a chemical shift distribution (Δ_{CS}) and a mean quadrupolar product ($C_Q^* = C_Q(1 + \eta^{2/3})^{1/2}$) for each site where η is the asymmetry parameter.[91]

The procedure for fitting the NMR spectra using the DMFIT software is as follows: First a suitable model with appropriate line shape is selected and guess parameters are given for isotropic shift (δ_{iso}) the distribution of isotropic chemical shift (Δ_{CS}) and quadrupole coupling constant (C_Q) in the model. Then do the iteration of the different NMR parameters and amplitude to get a good match between the experimental and simulated spectra. Repeat the procedure a number of times till the best match between the experimental and simulated spectra is obtained. The same procedure is carried out for the spectra of all the samples

All the NMR spectra were recorded on Bruker AV 300 MHz and AV 700 MHz spectrometers operating at field strengths of 7.05 T and 16.4 T, respectively. In the present work ^{23}Na, ^{7}Li, and ^{139}La nuclei are probed and their spectral characteristics are studied. A 4 mm MAS probe was used to carry out the experiments in the 300 MHz spectrometer. This probe can attain a maximum spinning rate of 15 kHz. The high field experiments on 700 MHz were done with a 1.3 mm MAS probe at a spinning rate of 60 kHz.

The ^{23}Na NMR studies were carried out using the AV 300 MHz spectrometer. Sodium resonance frequency (ϑ_{Na}) at 7.05 T is 79.3 MHz and the chemical shifts are referenced to the chemical shift of 0.1 M NaCl solution. ^{23}Na MAS and MQMAS experiments were carried out at a spinning speed of 10 kHz. ^{7}Li NMR experiments were also done on the AV 300 NMR spectrometer at a spinning speed of 10 kHz and the resonance frequency (ϑ_{Li}) is 116.5 MHz. ^{7}Li spectra were referenced to the chemical shift of 0.1 M LiCl solution. ^{139}La MAS NMR spectra were recorded on high field AV 700 MHz spectrometer at a spinning speed of 60 kHz and a resonance frequency (ϑ_{La}) of 98.8 MHz. 0.1 M $La(NO_3)_3$ solution was used as the reference for chemical shift.

2.4.3. Raman spectroscopy

Raman spectroscopy is a non-destructive molecular spectroscopy and uses the vibrational transitions to get more insight to the disorder and strain present in the system. The vibrational Raman spectra has shorter characteristic length scale, hence it is used to probe the local symmetry changes.[93] Raman selection rules are sensitive to local and global symmetry changes. A strong laser beam in the ultraviolet or visible region (v_0) is used in Raman spectroscopy for irradiating the sample. The scattered light is observed in a back scattering geometry. There are two types of scattered light, Rayleigh scattering and Raman scattering. If the scattered rays have the same frequency (v_0) of the incident light, it is called Rayleigh scattering. In Raman scattering the scattered rays have either lower (v_0- v_m) or higher frequency (v_0 + v_m) compared to the incident radiation, where v_m is the vibrational frequency of the molecule. The lines (v_0- v_m) and (v_0 + v_m) are known as Stokes and anti-Stokes lines respectively. Hence the vibrational frequency of different bonds in the material can be measured in Raman spectroscopy in terms of

the frequency shift ($v_0 \mp v_m$) of the incident radiation. The basic requirement for Raman activity is that the vibrational transition should proceed with a change in polarizability.[94]

In crystalline solids, instead of molecular vibrations, phonon characteristics are studied. The Raman active phonons will have a non-zero value for the first derivative of the polarizability with respect to the vibrational normal coordinate. The basic requirement to have an active phonon in a crystal is lack of centre of symmetry.

In the present study, phase transitions and local symmetry changes are studied using Raman spectroscopy. The experiments were done on a Lab RAM HR spectrometer (HORIBA JOBIN YVON, Model No.HR 800) using 633 nm He-Ne laser. A group theoretical analysis of monoclinic (Cc) BNT and tetragonal (P4bm) BKT Raman modes by correlation method was carried out.[95] In correlation method, the first step is to find the molecules per Bravais space cell. The Bravais space cell is used to derive the irreducible representation for the lattice vibrations. If the crystallographic unit cells contain more than one Bravais cells that many vibrations are needed to represent the lattice vibrations of the crystal. This problem can be eliminated by dividing the number of molecules per unit crystallographic cell (Z) by the number of lattice points (LP). Hence the number of molecules in the Bravais space cell (Z^B) is given as

$$\mathrm{Z^B} = \frac{\mathrm{Z}}{\mathrm{LP}} \tag{2.12}$$

Second step is to find the site symmetry which is the sub group of the full symmetry of the Bravais unit cell of each atom in the Bravais cell. Then, the site group is correlated to the factor group. The site symmetry of each atom gives the symmetry species corresponds to the atom displacements in the site. These displacements will become the lattice vibrations in the crystal. The correlation table can be identified from the site species for these displacements and each species of the site group can be related to the factor group. This correlation unambiguously identifies the species of the lattice vibration in the crystal and allows the prediction of Raman and infrared activity.

The deconvolution of the Raman spectra was done with Orgin8 software. The deconvolution of spectra with Orgin software consists of three main steps 1) background correction, 2) selection of peak centre and 3) iteration to the best fit. At first the background correction of the spectra was done by creating a straight line as baseline and generate anchor

points manually and then fit them to the input function. The spectra consist of three main regions; hence initially fitting was tried with three peaks. But the simulated patterns were not matching with the experimental pattern. The best fit for BNT was obtained when 7 peaks are used.

2.4.4. Scanning electron microscopy

Scanning electron microscopy (SEM) is commonly used for studying microstructure and morphology of the materials.[96] SEM provides high resolution surface imaging with three dimensional characteristics. In a typical SEM instrument thermionically emitted electrons from tungsten or lanthanum hexaboride (LaB_6) cathode are accelerated towards an anode; alternatively electrons can be emitted via field emission also. The energy of electron beam is ranging from a few 100 eV to 50 keV. The electron beam then crosses pairs of scanning coils in the objective lens. The lens will deflect the beam over a rectangular area of the sample surface. A scintillator photomultiplier device is used for detecting the electrons and the resulting signal is a two dimensional intensity distribution that can be viewed and saved as a digital image.

In the present study the microstructure analysis of the BNT based solid solution series was carried out using a FEI Quanta 200 3D ESEM. Samples were in the pellet form and they are fixed on to the disk holder by carbon tape before inserting to the SEM sample chamber.

2.4.5. Density measurements

Density measurements of the sample pellets were done using a pycnometer which is based on Archimedes principle.[97] The density measurement procedure is as follows: the weight of pycnometer (m_0) together with the inserted pellet (m_s) was measured and then the pycnometer was filled with water and the total weight (m_T) is measured which is equal to $m_0 + m_1 + m'_{H_2O}$.

The weight of water filled in pycnometer, $m'_{H_2O} = m_T - (m_0 + m_s + m'_{H_2O})$

The volume of the added water (V'_{H_2O}), is obtained from the equation

$$V'_{H_2O} = \frac{m'_{H_2O}}{\rho_{H_2O}} \tag{2.13}$$

The volume of the pellet (V_s) is the difference between the volume of the water that fills the empty pycnometer V and the volume V'_{H_2O}.

$$V_s = V - V'_{H_2O} = \frac{(m_{H_2O} - m'_{H_2O})}{\rho_{H_2O}} \quad (2.14)$$

Density of the measured object ρ_s can be calculated as

$$\rho_s = \frac{m_s}{V_s} \quad (2.15)$$

2.4.6. Dielectric measurements

The dielectric measurements of the pellets were carried out using impedance bridge (General Radio 1608-A Impedance Bridge). It is an independent impedance measurement system, which contains six bridges for the measurement of capacitance, resistance, impedance, conductance, etc. Two different modes are present in it, parallel and series. The pelletized samples with silver paste coating on both sides were used for the measurement. The silver paste coating on the polished surfaces of the pellets is done for electrical contact and they are sandwiched between the two electrodes of the sample holder. In the present study, the parallel capacitance at 1 kHz was measured in the impedance bridge. The value of the dielectric constant (ε_r) is calculated from the equation given below.[98]

$$\varepsilon_r = \frac{C_p h}{\varepsilon_0 A} \quad (2.16)$$

Where C_p is the capacitance of the sample at a given temperature, h is the sample thickness, A is the surface area of the conducting plate and ε_0 is the permittivity of air.

2.4.7. Polarization Vs electric field hysteresis loop measurements

Polarization Vs Electric field (P-E) hysteresis loop is obtained at 2 kV using a Piezoevaluation system (Model 2000, aix ACCT, Germany). Pelletized samples coated with silver paste on both polished flat surfaces were used for the measurement. P-E loop measurements are based on a Sawyer-Tower circuit which uses a high frequency ac field and the current is integrated into charge by virtue of a linear capacitor connected in series to the sample.[99] The voltage across the capacitor is proportional to the polarization of the sample. The X and Y axes of the oscilloscope convert the voltage to the P-E hysteresis loop. The saturation polarization (P_s) and the coercive field (E_c) are also obtained from this measurement.

Chapter 3

Studies on (1-x)$Bi_{0.5}Na_{0.5}TiO_3$–$xBi_{0.5}K_{0.5}TiO_3$ Series

3.1. Introduction

The solid solution of $Bi_{0.5}Na_{0.5}TiO_3$ (BNT) and $Bi_{0.5}K_{0.5}TiO_3$ (BKT), bismuth sodium potassium titanate ($Bi_{0.5}Na_{0.5-x}K_xTiO_3$), is a lead-free alternative for the well-known piezoelectric composition lead zirconium titanate, $Pb(Zr_{1-x}Ti_xO_3)$, with superior properties.[1] The crystal structure of BNT is earlier reported as rhombohedral with the R3c space group but later on it has been confirmed that the structure is monoclinic with the space group Cc.[72] The structure of BKT is tetragonal with the P4bm space group. Hence a structural phase transition is expected when Na in BNT is replaced by K. A morphotropic phase boundary (MPB) region is reported in the compositional range $0.16 \leq x \leq 0.20$.[68] As discussed in chapter 1 (Section 1.7), there are contradicting reports in the literature on the crystal structure, structural phase transformation, existence of the MPB region, and the compositional range of the MPB region of the $Bi_{0.5}Na_{0.5}TiO_3$–$Bi_{0.5}K_{0.5}TiO_3$ solid solution series, known as the (1-x)BNT–xBKT system.

All the reported studies on the structural aspects of the BNT–BKT solid solution series have been carried out using only few compositions in the MPB region. Therefore, to understand the structure-property correlations in this complicated system, detailed structural studies of the solid solution (1-x)BNT–xBKT, where $0 \leq x \leq 0.36$, with small compositional variations (Δx in steps of 0.02 for $x < 0.1$ and $x > 0.2$ and in steps of 0.01 for $0.10 \leq x \leq 0.20$) have been carried out by Rietveld refinement of the powder XRD patterns. Further, for understanding the role of short range ordering and the associated local structural changes due to the substitution of the smaller Na^+ ion by the larger K^+ ion, Raman and solid state NMR spectroscopic studies have been carried out. Raman spectral studies on BNT is reported in the literature.[100-102] Kreisel *et al* have reported the Raman spectra of few compositions in the BNT-BKT solid solution series.[70]

In the present study, we have carried out a detailed Raman spectral analysis on the structural phase transition region of the (1-x)BNT–xBKT series. Since the crystal symmetry of the end members are different, Raman modes of BNT and BKT will be different. Therefore, corresponding changes are expected in the Raman modes of the different compositions of (1-x)BNT–xBKT.[70] Similarly, solid state NMR (SSNMR) is the best tool to probe the local structural disorder in non-magnetic compositions, since it can provide information on the local structure. SSNMR studies on the (1-x)BNT–xBKT solid solution series are not reported in the literature. In this work, we have used MAS and MQMAS[103]

techniques and the spectra obtained are fitted using the DMFIT[90] program. The changes in the structural parameters obtained from XRD, Raman and NMR studies are correlated with the changes in the microstructure, density, dielectric constant, and ferroelectric polarization. Very good correlations are observed between the changes in the local structure and the properties of the solid solution series.

3.2. Synthesis

Table 3.1: Compositions in the (1-x)BNT–xBKT series and the corresponding sample codes.

x	**Composition $(1-x)Bi_{0.5}Na_{0.5}TiO_3$-$xBi_{0.5}K_{0.5}TiO_3$, (1-*x*)BNT–*x*BKT**	**Sample code**
0	BNT	BNT
0.02	0.98BNT–0.02BKT	0.02BKT
0.04	0.96BNT–0.04BKT	0.04BKT
0.06	0.94BNT–0.06BKT	0.06BKT
0.08	0.92BNT–0.08BKT	0.08BKT
0.10	0.90BNT–0.10BKT	0.10BKT
0.11	0.89BNT-0.11BKT	0.11BKT
0.12	0.88BNT–0.12BKT	0.12BKT
0.13	0.87BNT-0.13BKT	0.13BKT
0.14	0.86BNT–0.14BKT	0.14BKT
0.15	0.85BNT-0.15BKT	0.15BKT
0.16	0.84BNT–0.16BKT	0.16BKT
0.17	0.83BNT-0.17BKT	0.17BKT
0.18	0.82BNT–0.18BKT	0.18BKT
0.19	0.81BNT-0.19BKT	0.19BKT
0.20	0.80BNT–0.20BKT	0.20BKT
0.22	0.78BNT-0.22BKT	0.22BKT
0.24	0.76BNT-0.24BKT	0.24BKT
0.26	0.74BNT-0.26BKT	0.26BKT
0.28	0.72BNT-0.28BKT	0.28BKT
0.30	0.70BNT-0.30BKT	0.30BKT
0.32	0.68BNT-0.32BKT	0.32BKT
0.34	0.66BNT-0.34BKT	0.34BKT
0.36	0.64BNT-0.36BKT	0.36BKT

Different compositions in the (1-x)BNT–xBKT solid solution series were prepared by the conventional solid state reaction method using Bi_2O_3, Na_2CO_3, K_2CO_3, and TiO_2. Stoichiometric amounts of the components were taken according to following formula (1-x)BNT–xBKT where x ranging from 0 to 0.36 in steps of 0.02 (steps of 0.01 for $0.1 \leq x \leq 0.2$). The powders were mixed thoroughly using an agate mortar and pestle, and initially calcined at 850 ^oC for 6 hours. The pre-calcined powders were further calcined at 1000 ^oC and 1150 ^oC, for 12 hours each, with intermediate grindings. The final powders were uniaxially pressed into circular discs (10mm diameter × 3mm height) at a pressure of 8 MPa and sintered in air at 1150 ^oC for 2 hours, at heating and cooling rates of 5 ^oC/min. All the compositions were processed and sintered under identical conditions. The compositions and the corresponding sample codes are specified in Table 3.1

3.3. Powder X-ray diffraction

All the compositions are initially characterized by powder XRD studies to verify phase formation. Figure 3.1 shows the powder XRD patterns of selected compositions in the (1-x)BNT–xBKT series. The simulated XRD pattern of BNT using the R3c space group and crystallographic parameters taken from literature,[104] is also shown for comparison.The powder XRD pattern is simulated using the PCW software, as discussed in chapter 2 (Section 2.4.1). All the XRD patterns showed peaks similar to that in the simulated pattern, and the peaks correspond to the perovskite lattice without any impurities.

Rietveld refinement analyses of the XRD patterns of all compositions have been carried out. Figure 3.2 compares the result of the Rietveld refinement analysis[87] of BNT using the reported rhombohedral R3c and monoclinic Cc space groups. The R3c space group gave a good fit with reduced $\chi^2 = 2.26$ and $R_p = 5.91\%$. However, the monoclinic space group gave a better fit with improved $\chi^2 = 1.95$ and $R_p = 5.60\%$. These results suggested that the correct structure of BNT is monoclinic with space group Cc, as reported by Aksel *et al.*[105]

Structural refinement of different compositions for $x > 0$ is carried out using the Cc space group and it is found that χ^2 increases drastically for $x > 0.17$. Results of the Rietveld refinement analysis of selected compositions of (1-x)BNT–xBKT , for $x < 0.17$, are shown in Figure 3.3. Table 3.2 gives the results obtained from Rietveld refinements of (1-x)BNT–xBKT for $0 \leq x \leq 0.26$. The reduced χ^2 and R_P values are found to be much larger for $x > 0.17$.

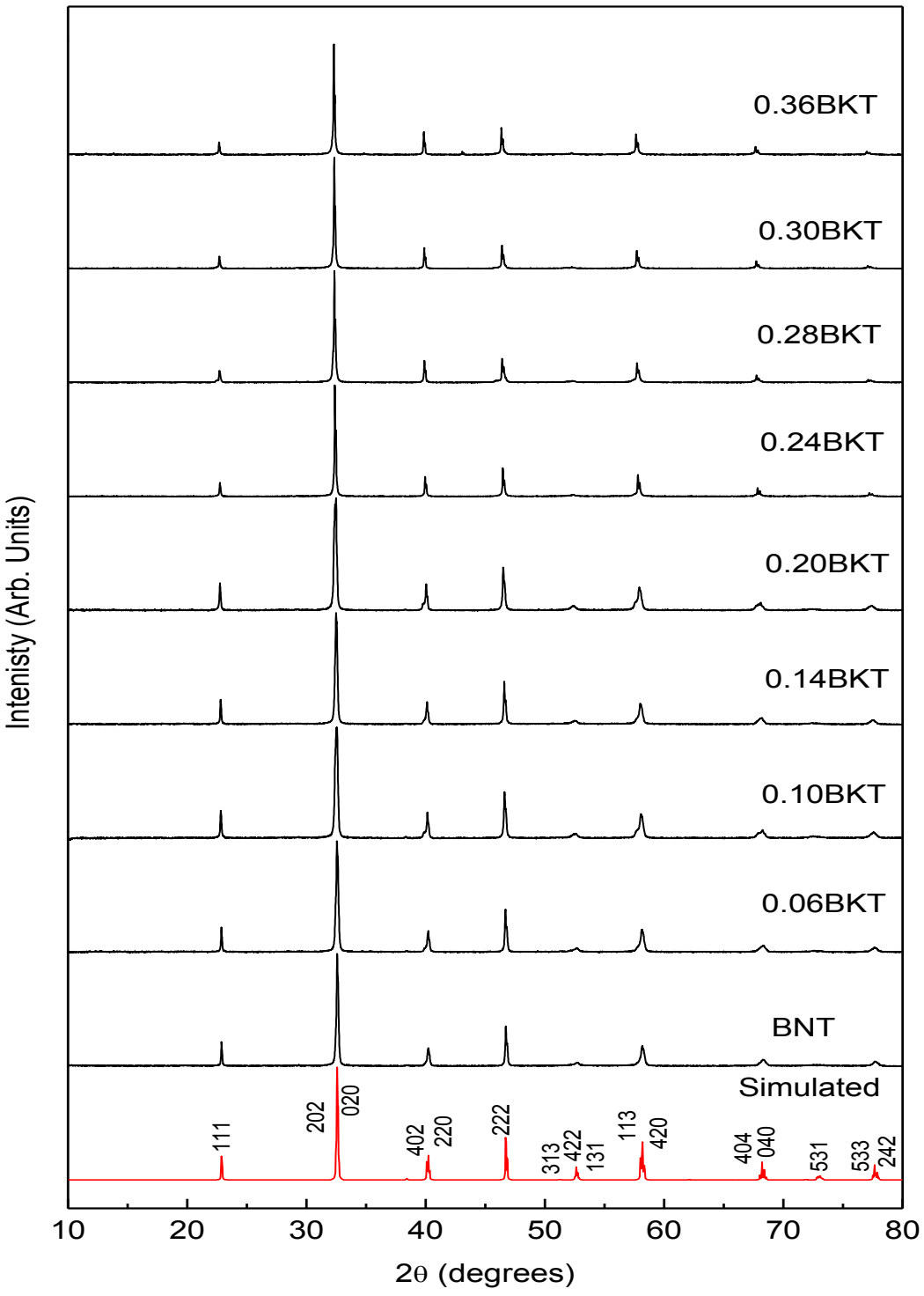

Figure 3.1: Powder XRD patterns of selected compositions in the (1-x)BNT–xBKT solid solution series. Simulated pattern of BNT is shown at the bottom for comparison.

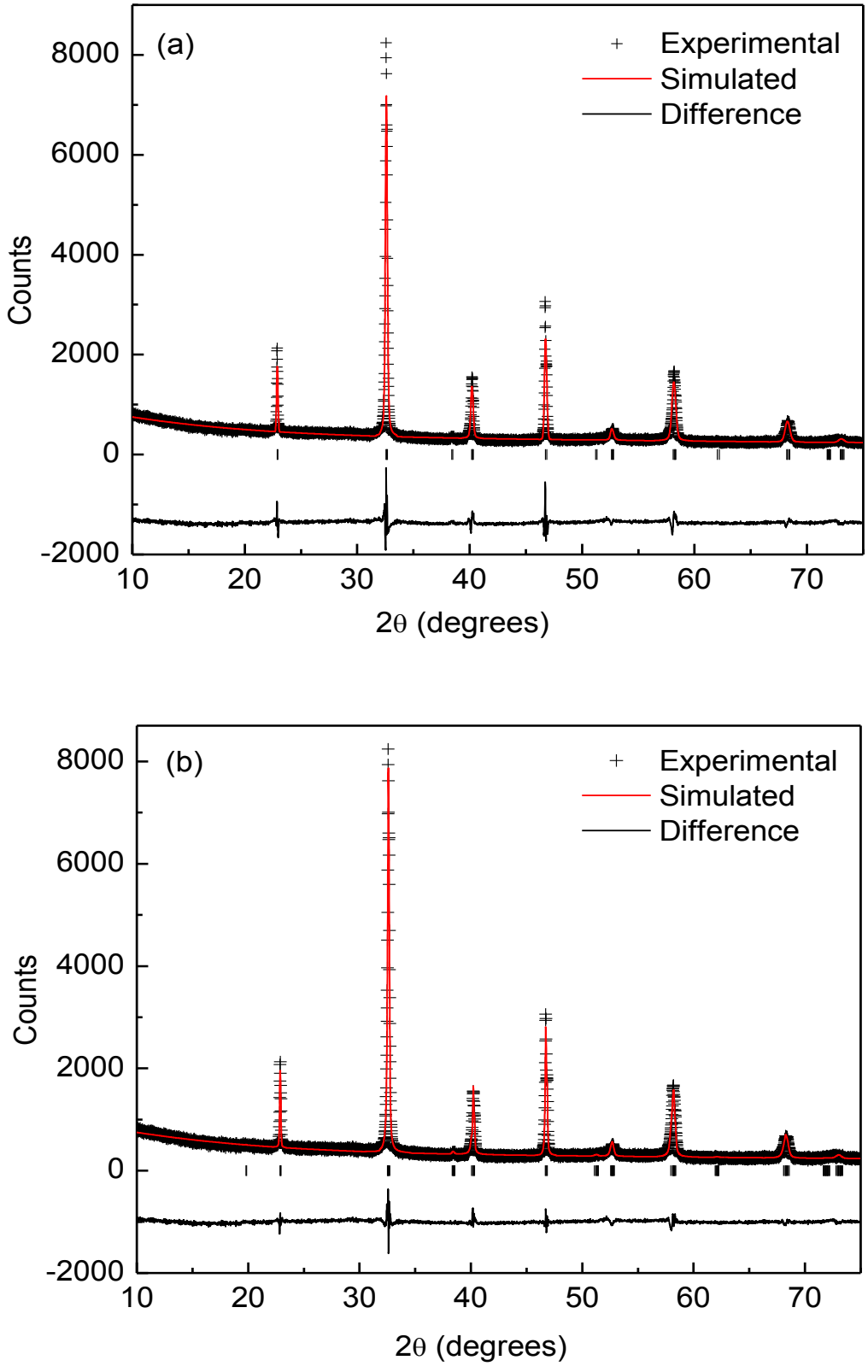

Figure 3.2: Results of the Rietveld refinement analysis of BNT using (a) rhombohedral R3c and (b) monoclinic Cc space groups.

Table 3.2: Lattice parameters, reduced χ^2 and R_P values of (1-x)BNT–xBKT obtained from Rietveld analysis.

Sample	**Cc**				χ^2	R_p (%)
	a (Å)	**b (Å)**	**c (Å)**	**β (degree)**		
BNT	9.5419	5.4781	5.5074	125.43	1.95	5.24
0.02BKT	9.5389	5.4792	5.5073	125.41	2.001	5.38
0.04BKT	9.5455	5.4815	5.5121	125.50	1.957	5.24
0.06BKT	9.5546	5.4807	5.5157	125.57	1.931	5.16
0.08BKT	9.5288	5.4829	5.5082	125.38	1.940	5.16
0.10BKT	9.5548	5.4825	5.5175	125.58	2.027	5.28
0.11BKT	9.5531	5.4849	5.5177	125.61	2.278	5.16
0.12BKT	9.5570	5.4850	5.5177	125.58	2.112	5.44
0.13BKT	9.5572	5.4841	5.5184	125.59	2.153	5.50
0.14BKT	9.5477	5.4861	5.5146	125.50	2.181	5.44
0.15BKT	9.5523	5.4884	5.5174	125.57	2.253	5.42
0.16BKT	9.5517	5.4850	5.5154	125.52	2.398	5.58
0.17BKT	9.5559	5.4892	5.5172	125.52	2.289	5.33
0.18BKT	9.5625	5.4900	5.5252	125.58	3.3	5.39
0.19BKT	9.6076	5.4922	5.5497	125.48	3.5	5.56
0.20BKT	9.5472	5.4941	5.5198	125.51	3.8	6.49
0.22BKT	9.5391	5.5014	5.5196	125.38	5.8	7.88
0.24BKT	9.5330	5.4997	5.5165	125.38	6	8.27
0.26BKT	9.5365	5.5009	5.5212	125.36	6.2	8.47

The variation of the lattice parameters indicated interesting features. Figure 3.4 shows the variation in lattice parameters, '*a', 'b', 'c'*, and the cell volume with BKT concentration. Most prominent change is observed for the lattice parameter '*b*', as shown in Figure 3.4(b). A linear increase in the lattice parameter, *b* is observed up to $x = 0.17$, with a large deviation above this concentration. These results suggest that the compositions in the range $0 \leq x \leq 0.17$ form under the Cc space group and the structure and/or space group may be different for compositions $x > 0.17$, to accommodate the larger K^+ ion in the crystal lattice. Since the ionic radius of K^+ (1.64 Å) is much larger than that of Na^+ (1.39 Å), substitution of Na^+ by K^+

expands the lattice spacing of BNT, and hence the unit cell dimensions are expected to increase.

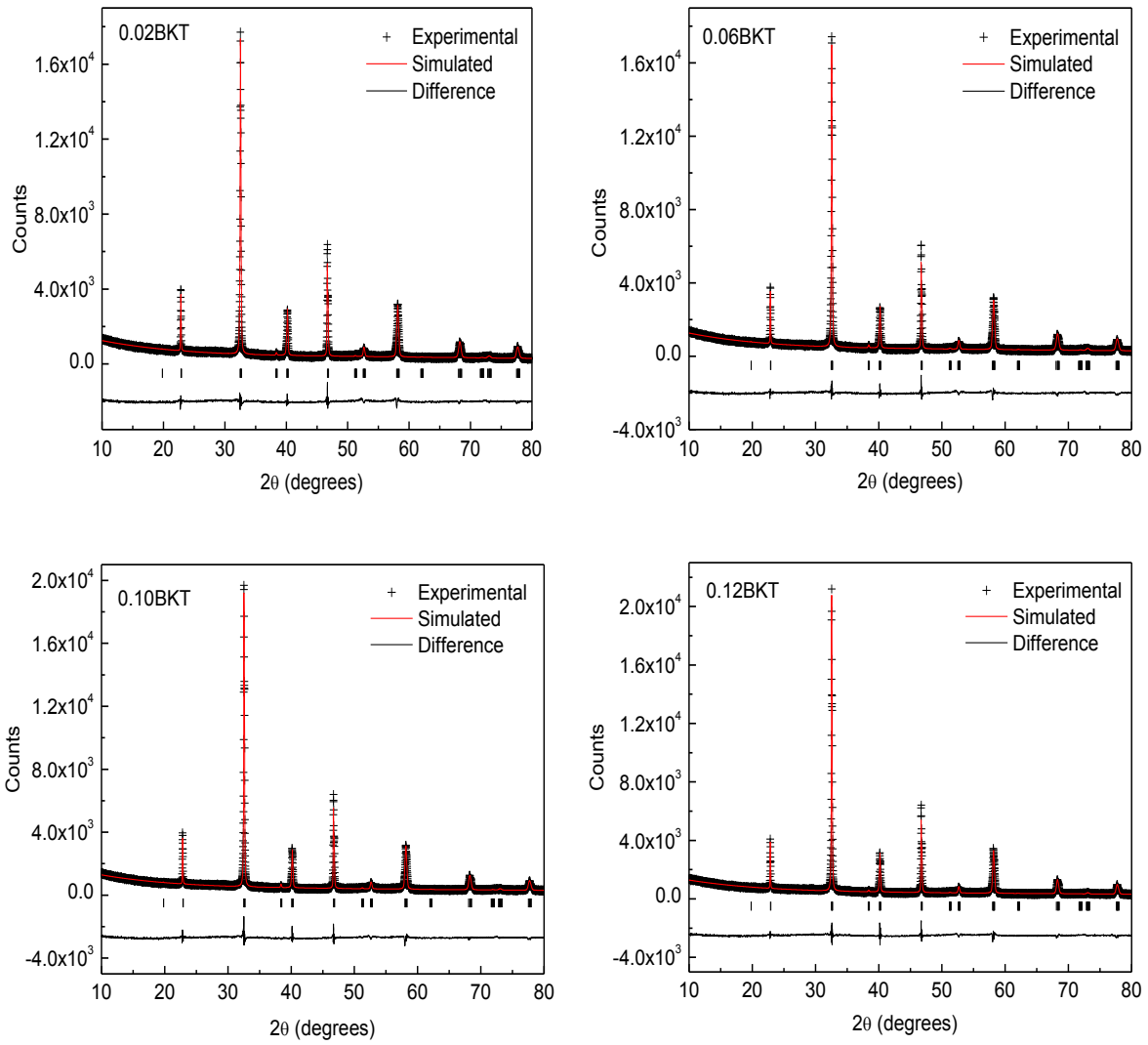

Figure 3.3: Results of the Rietveld refinement analysis of (1-x)BNT–xBKT using the monoclinic Cc space group, for 0.02BKT, 0.06BKT, 0.10BKT and 0.12BKT.

Since the XRD patterns of higher BKT concentrations ($0.18 \leq x \leq 0.36$) did not give good fit using the monoclinic Cc space group, Rietveld refinements are carried out for higher BKT concentrations ($0.18 \leq x \leq 0.36$) using the rhombohedral space group R3c reported for BNT as well as the tetragonal space groups P4bm, P4mm reported for BKT. However, all of the compositions gave larger R_P and χ^2 values, using these structural models, indicating that the tried structures are not the right models. Therefore, further refinements that were carried out with possibility of mixed phases (R3c as well as Cc with P4bm and P4mm) gave much improved fits.

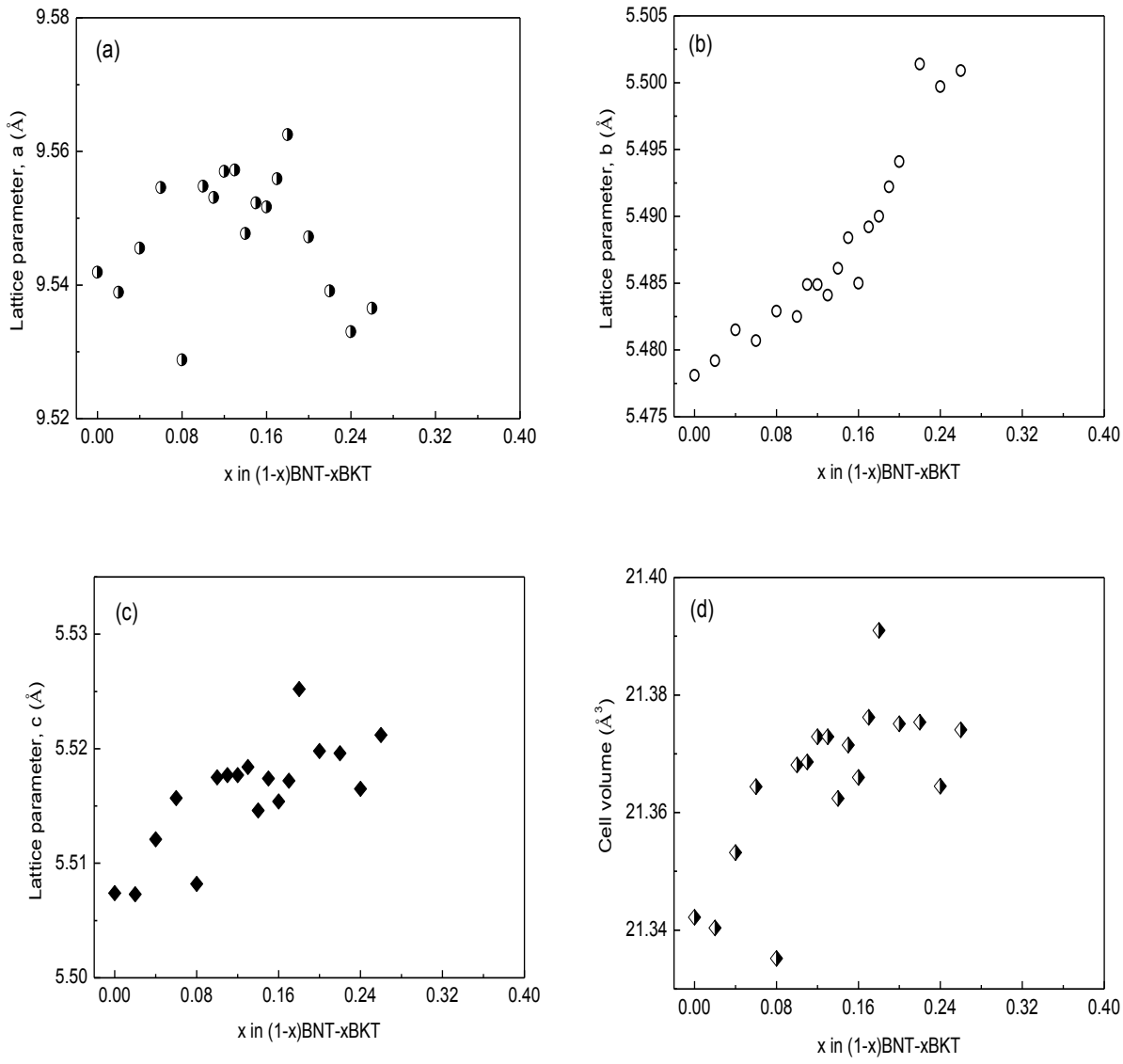

Figure 3.4: Variation of the monoclinic lattice parameters (a) '*a'*, (b) *'b'*, (c) *'c'* and (d) cell volume of (1-*x*)BNT–*x*BKT solid solution series as a function of *x*.

Better fits with relatively lower values of χ^2 and R_p are obtained for mixed phases of monoclinic Cc and tetragonal P4bm. The best fit parameters using the mixed phase analysis are given in Table 3.3. Figure 3.5 shows the results of the Rietveld refinement for $x = 0.24$ using the monoclinic Cc space group alone and mixed phase of monoclinic Cc and tetragonal P4bm space groups. Figure 3.6 shows the Rietveld refinement of selected compositions in the BNT–BKT solid solution series for $0.18 \leq x \leq 0.36$.

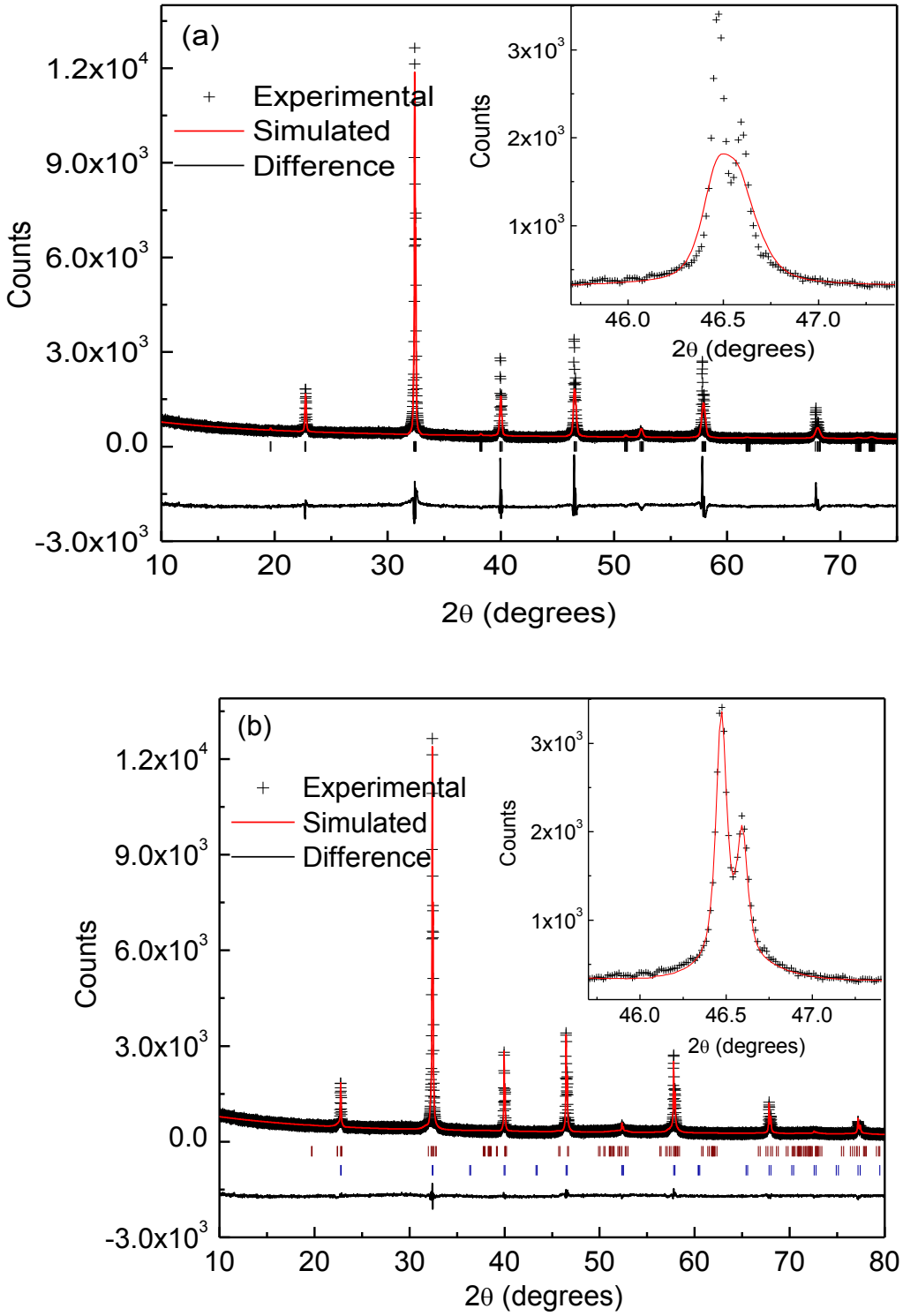

Figure 3.5: Results of the Rietveld refinement analysis of 0.24BKT using (a) Cc space group and (b) mixed phases of Cc and P4bm space groups. Insets show the goodness of the fit using the two different models.

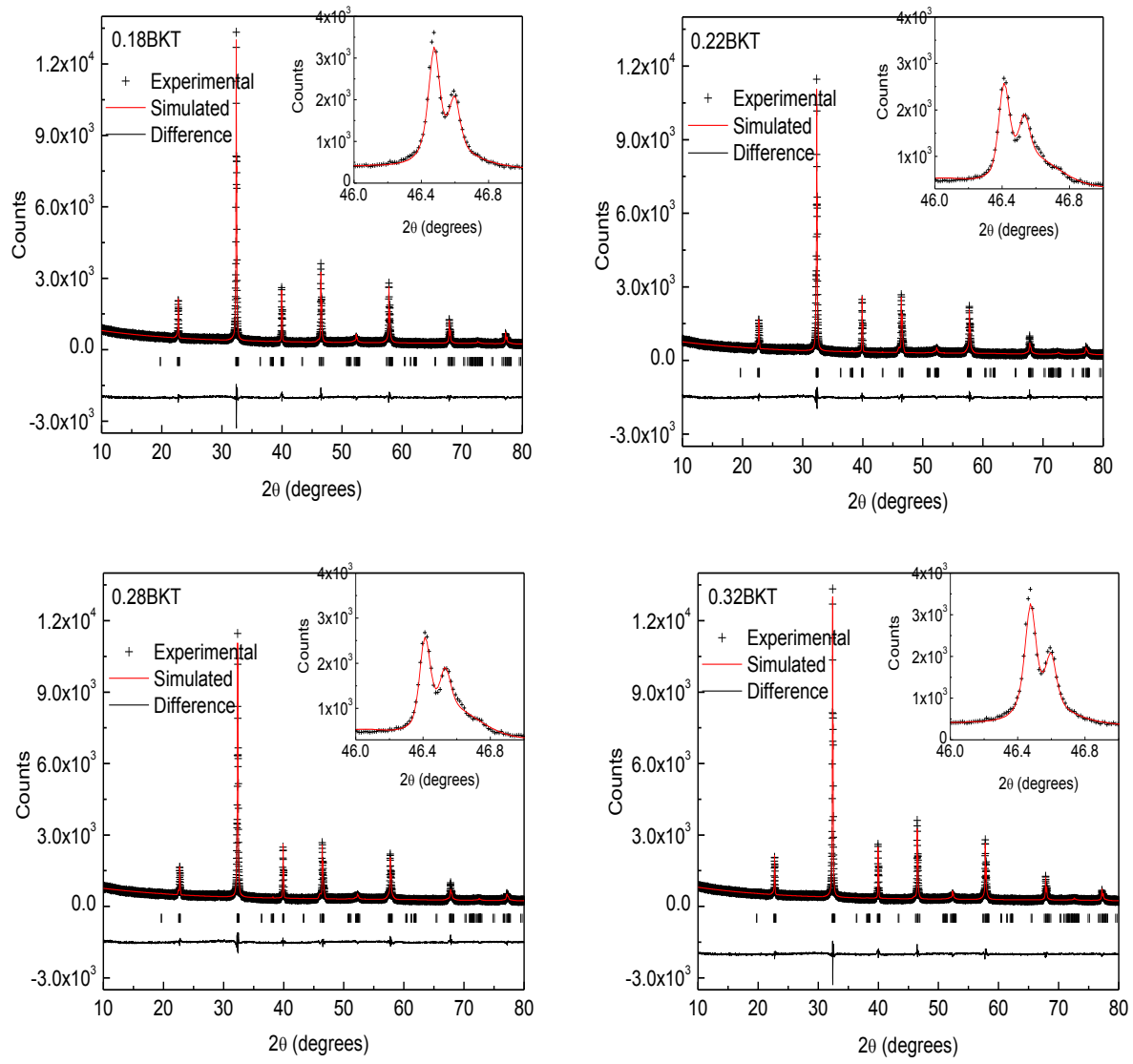

Figure 3.6: Results of the Rietveld refinement analysis of (1-x)BNT–xBKT using mixed phases of monoclinic Cc and tetragonal P4bm space groups, for 0.18BKT, 0.22BKT, 0.28BKT and 0.32BKT.

Thus, the XRD analysis results show that for the compositional region studied in the BNT–BKT solid solution series ($0 \leq x \leq 0.36$), the structures are different for lower and higher values of x. Single phase compositions (monoclinic Cc space group) are formed for $x < 0.18$ and compositions in the range $0.18 \leq x \leq 0.36$, are found to be a mixture of monoclinic and tetragonal phases. There is no compositional region separating the two different structures, contrary to the previous report[72] of observing a tetragonal structure alone above $x = 0.18$.

Table 3.3: Lattice parameters, reduced χ^2 and R_P values of (1-x)BNT–xBKT ($0.18 \leq x \leq 0.36$) with mixed phases of monoclinic Cc and tetragonal P4bm space groups.

Sample	Cc				P4bm			χ^2	R_p(%)
	a (Å)	b (Å)	c (Å)	β (degrees)	a (Å)	b (Å)	c (Å)		
0.18BKT	9.57445	5.4942	5.5197	125.52	5.5245	5.5245	3.9360	2.030	5.28
0.19BKT	9.5696	5.5036	5.5233	125.50	5.5176	5.5176	3.9075	2.110	5.46
0.20BKT	9.5718	5.5038	5.5208	125.51	5.5180	5.5180	3.9061	2.257	5.67
0.22BKT	9.5472	5.4726	5.4964	124.63	5.5205	5.5205	3.9047	1.818	4.96
0.24BKT	9.7896	5.4661	5.5444	125.87	5.5204	5.5204	3.9039	1.706	5.00
0.26BKT	9.5937	5.4819	5.4919	125.14	5.5216	5.5216	3.9045	2.577	5.53
0.28BKT	9.6114	5.4941	5.5101	125.07	5.5211	5.5211	3.9018	2.055	5.65
0.30BKT	9.5409	5.4951	5.5068	124.87	5.5225	5.5225	3.9050	2.106	5.27
0.32BKT	9.6355	5.4988	5.4978	125.19	5.5206	5.5206	3.9070	2.424	6.18
0.34BKT	9.5722	5.4993	5.5154	124.73	5.5227	5.5227	3.9069	2.269	5.71
0.36BKT	9.5735	5.4943	5.5229	124.72	5.5219	5.5219	3.9082	2.398	5.92
0.38BKT	9.5645	5.5012	5.5205	124.78	5.5219	5.5219	3.9071	2.392	5.86

3.4. Raman spectroscopy

The structural refinement data of BNT confirmed that the room temperature crystal structure of polycrystalline BNT is monoclinic (Cc), as reported by Aksel *et al.*[105] Although Raman data of BNT are available in the literature, the reported factor group analysis is based on the rhombohedral structure.[100-101] Therefore, a group theoretical analysis of Raman modes of BNT is carried out by the correlation method[95] for the monoclinic Cc space group. The Raman modes present in BNT can be characterized to C_s symmetry with the site symmetry of C_1. In the monoclinic (Cc) structure of BNT, all the 6 atoms are (Bi, Na, Ti, 3O) present in the 4(a) Wyckoff positions with C_1 site symmetry. The factor group analysis of monoclinic BNT gives 27 Raman active modes.[106-107] The irreducible representation for BNT obtained by the correlation method is given in Table 3.4. The room temperature crystal structure of BKT is tetragonal (P4bm). The Raman modes present in BKT can be characterized to C_{4v} factor group and the site symmetries present in this are $C_4(2)$, $C_2v(2)$, $C_S(4)$, $C_1(8)$. For tetragonal (P4bm) BKT, the Wyckoff positions are Bi/Na (2b), Ti (2a), O (2a), O (4c) with site symmetries Bi/Na (C_{2v}), Ti (C_4), O (C_4), O (C_s). The factor group analysis of tetragonal BKT gives 16 Raman active modes.[108-109] The irreducible representation is given in Table 3.5.

Table 3.4: Irreducible representation of BNT. [a] Wyckoff notation, [b] Site symmetry.

BNT space group Cc (C_s^4)

	Site			C_s factor group representation	
Atom	**a**	**b**	**Site representation**	**A′**	**A″**
Bi/Na	4a	C_1	6A	3	3
Ti	4a	C_1	6A	3	3
O	4a	C_1	6A	3	3
O	4a	C_1	6A	3	3
O	4a	C_1	6A	3	3

$$\tau_{BNT} = 15A' + 15A''$$

$$\tau_{acoust} = 2A' + A''$$

$$\tau_{BNT}^{Raman} = 13A' + 14A''$$

Table 3.5: Irreducible representation of BKT. [a] Wyckoff notation, [b] Site symmetry, [c] site element used for the correlation between site group and factor group.

BKT space group P4bm C_{4v}^2

	Site				C_{4v} factor group representation				
Atom	**a**	**b**	**c**	**Site representation**	**A_1**	**A_2**	**B_1**	**B_2**	**E**
Bi/K	2b	C_{2v}	σ_d	$2A_1+2B_1+2B_2$	1			1	2
Ti	2a	C_4		2A+2E	1	1			2
O	2a	C_4		2A+2E	1	1			2
O	4c	C_s	σ_d	8A′+4A″	2	1	1	2	3

$$\tau_{BKT} = 5A_1 + 3A_2 + B_1 + 3B_2 + 9E$$

$$\tau_{acoust} = A_1 + E$$

$$\tau_{BKT}^{Raman} = 4A_1 + B_1 + 3B_2 + 8E$$

Since the Raman active vibrational modes of BNT and BKT crystals are different, theoretically it is possible to distinguish both the space groups using polarised Raman

spectroscopy. It is observed in other perovskites that the disorder in the A site will lead to broadening of the Raman bands and break down of the selection rules.[70] Some Raman modes in BNT and BKT are IR active which results in the broadening of the bands in the polycrystalline samples.[70] In the present work, the changes in the Raman spectra of the (1-x)BNT–xBKT solid solution series are studied in a more quantitative way.

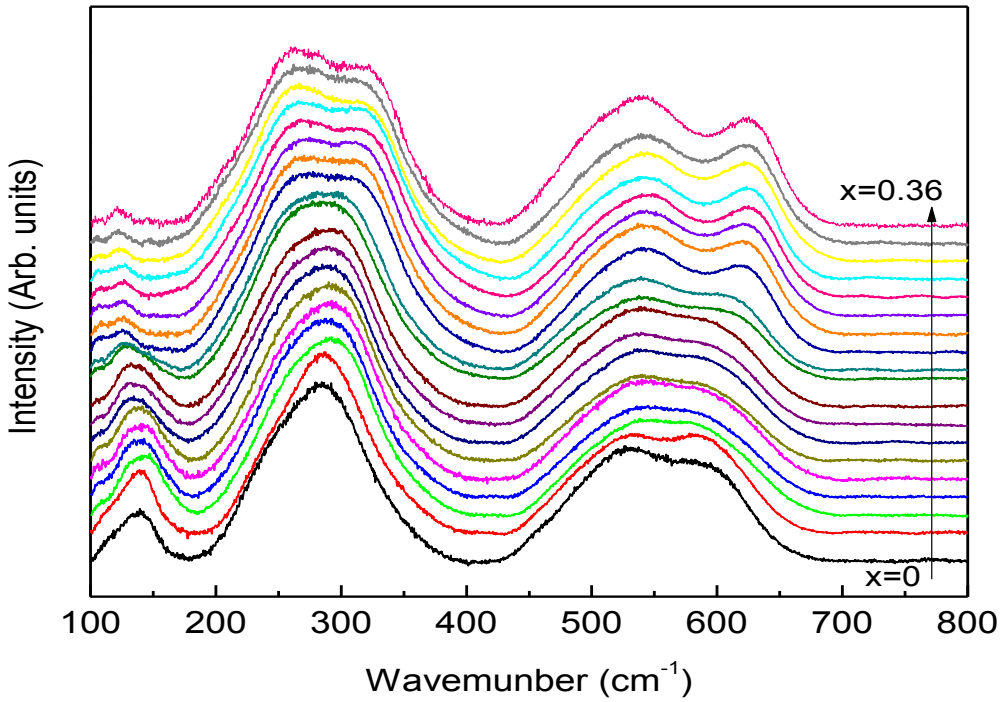

Figure 3.7: Raman Spectra of different compositions in the (1-x)BNT–xBKT series for $0 \leq x \leq 0.36$ ($\Delta x = 0.02$).

Figure 3.7 shows the Raman spectra of different compositions in the (1-x)BNT–xBKT solid solution series. The Raman spectra obtained for BNT and other compositions in the (1-x)BNT–xBKT solid solution are similar to that already reported.[70,110] Three different regions are observed in the Raman spectra and each region is related to different kinds of vibrations. The region below 180 cm^{-1} is related to the A-O vibration (A = Bi^{3+}, Na^{+}, K^{+}) in the ABO_3 perovskite structure and the region between 180 and 400 cm^{-1} belongs to the Ti-O vibrations. The high frequency region above 400 cm^{-1} is associated with the vibrations of the TiO_6 octahedra. On increasing the BKT concentration, several characteristic features are observed in the Raman spectra of the different compositions. These changes are expected since BNT and BKT have different crystal structures and hence, different Raman modes. On increasing the BKT concentration, a small downward shift is observed for the peak at ~135 cm^{-1}. Changes in the peak profile/intensity are observed for the bands above 200 cm^{-1} for x

>0.16. The band centred around 280 cm^{-1} shows splitting for higher BKT concentrations (x > 0.18) which indicate changes in the crystal structure. Corresponding changes are observed for the band in the 400-700 cm^{-1} region also. Relatively broad spectra are observed for all the compositions in the (1-x)BNT–xBKT solid solution series. This is due to the effect of substitution of Na^+on the A site by the larger K^+ ion and also due to the overlapping of the different Raman modes.

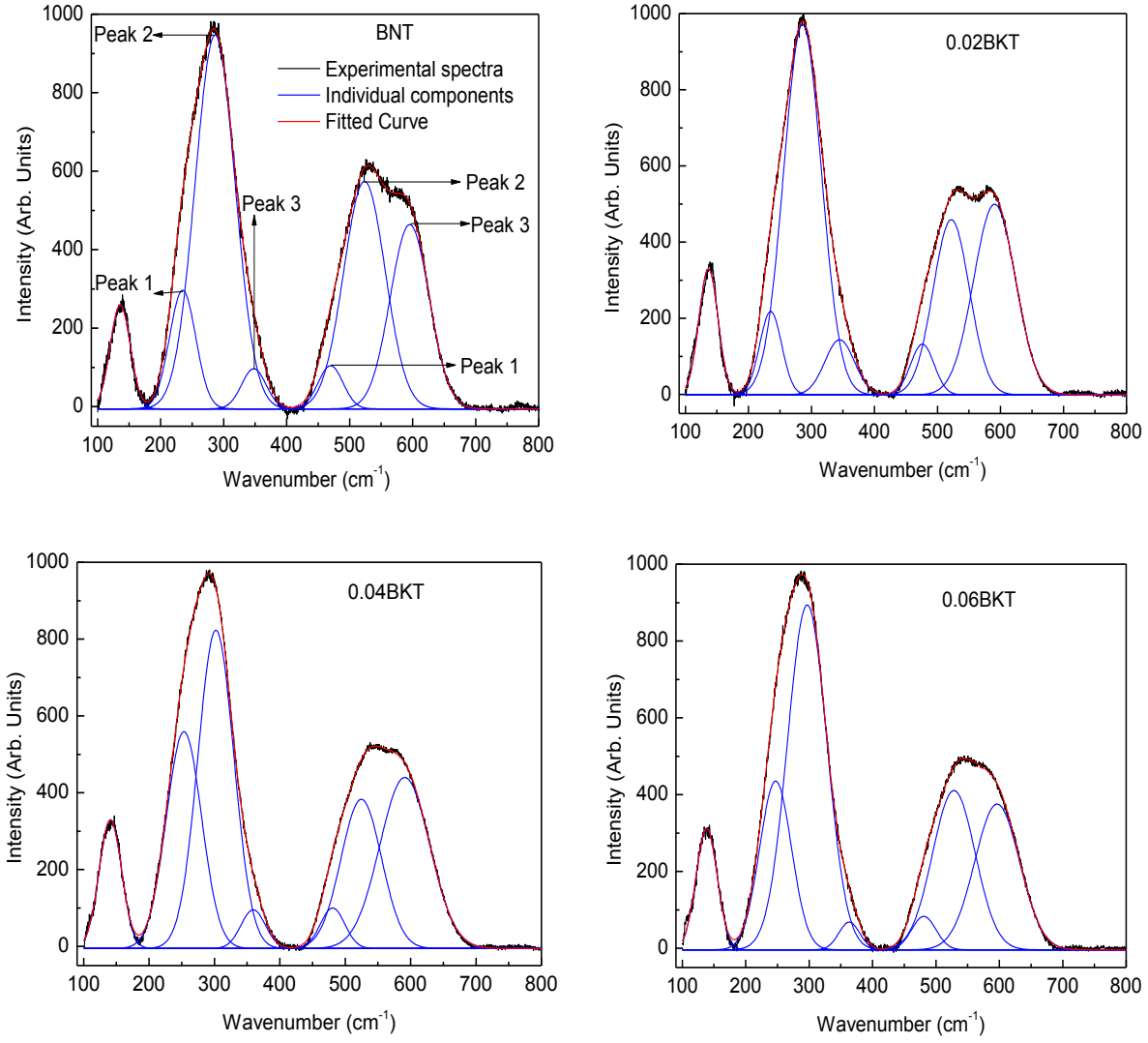

Figure 3.8: Deconvoluted Raman spectra of BNT, 0.02BKT, 0.04BKT, 0.06BKT, in (1-x)BNT–xBKT. The black, red and blue curves correspond to experimental spectra, fitted curves and the individual components, respectively.

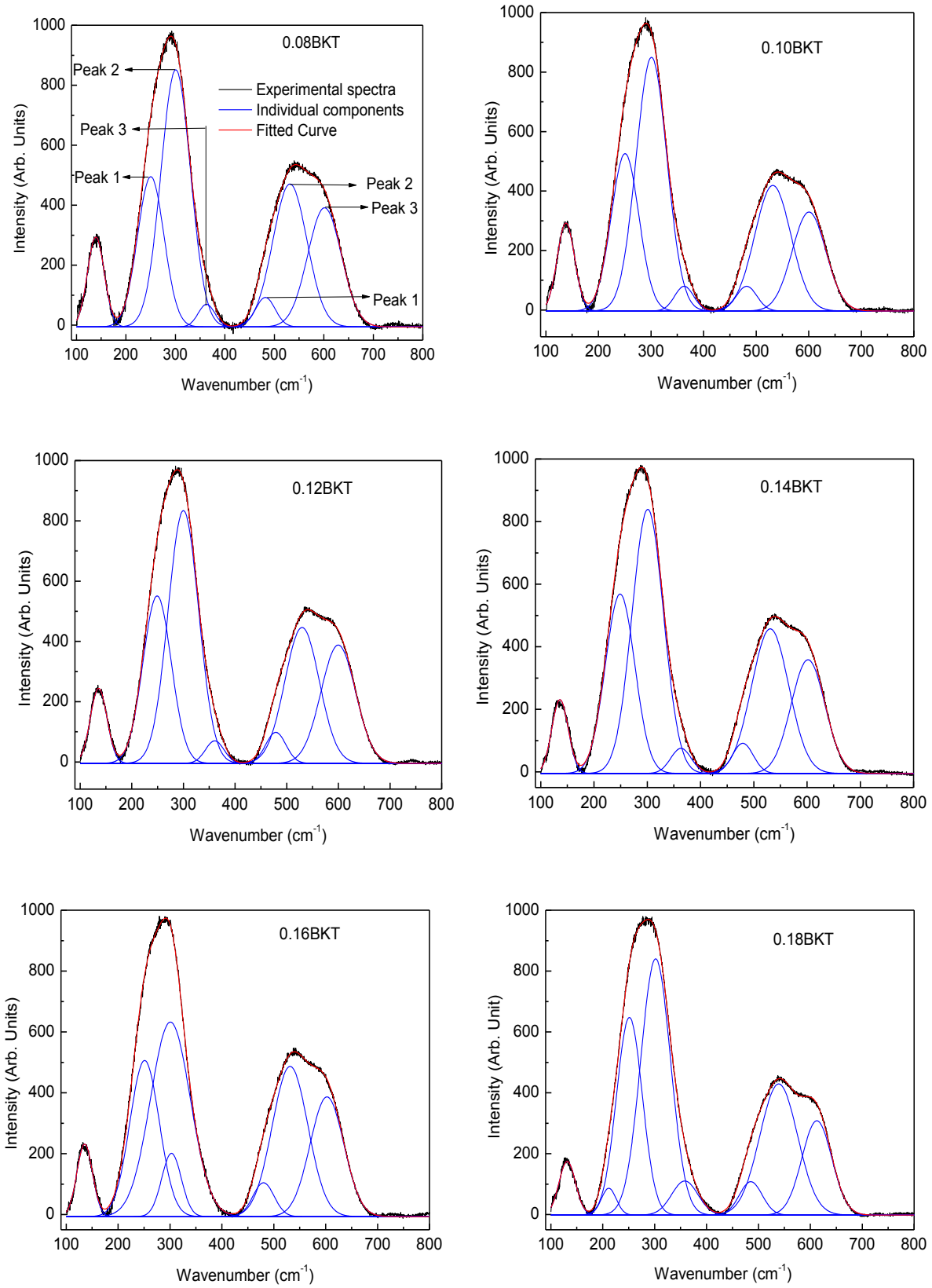

Figure 3.9: Deconvoluted Raman spectra of 0.08BKT, 0.10BKT, 0.12BKT, and 0.14BKT, 0.16BKT, 0.18BKT in (1-x)BNT–xBKT. The black, red and blue curves correspond to experimental spectra, fitted curves and the individual components, respectively.

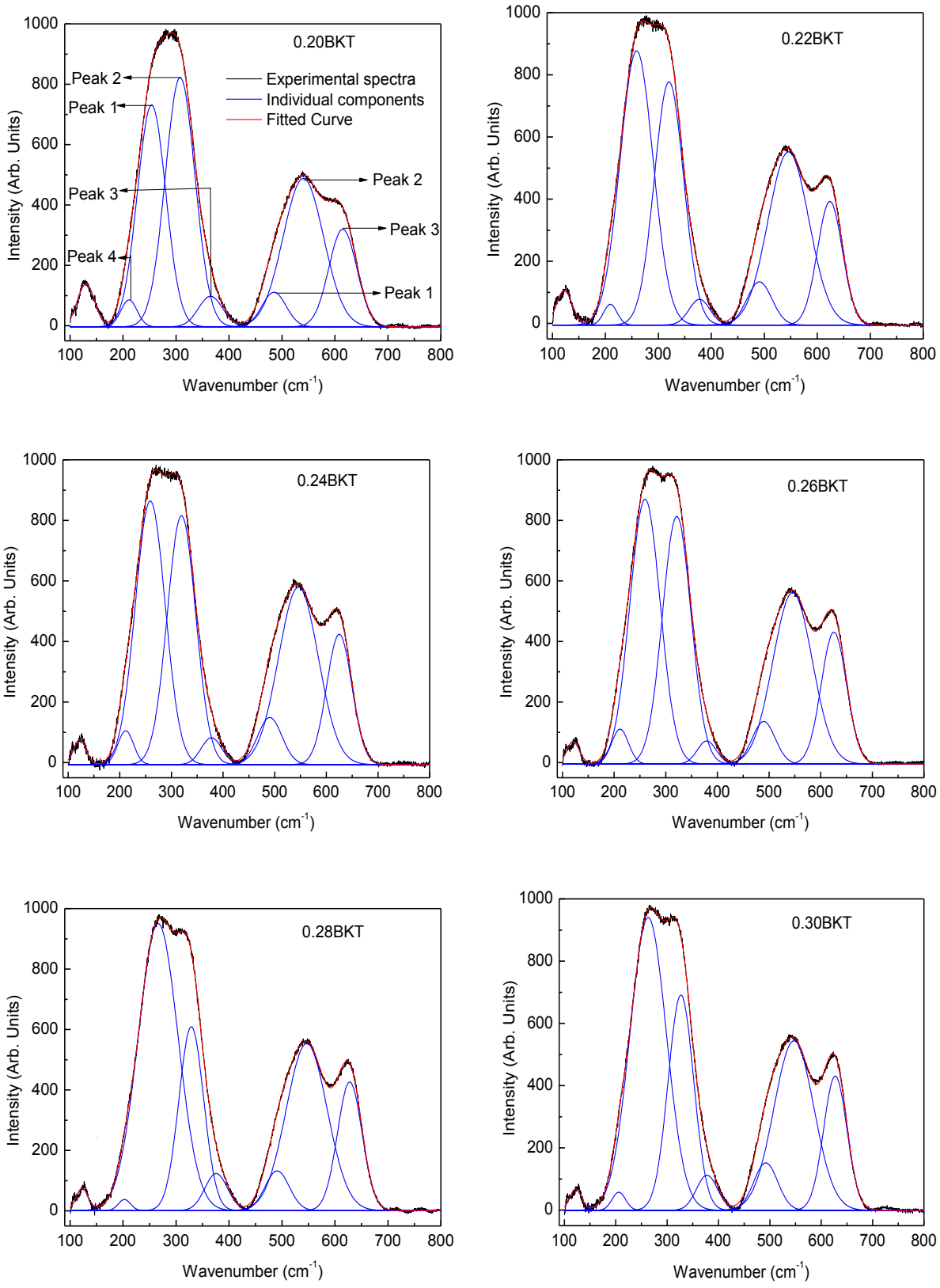

Figure 3.10: Deconvoluted Raman spectra of 0.20BKT, 0.22BKT, 0.24BKT, 0.26BKT, 0.28BKT, and 0.30BKTin (1-x)BNT–xBKT. The black, red and blue curves correspond to experimental spectra, fitted curves and the individual components, respectively.

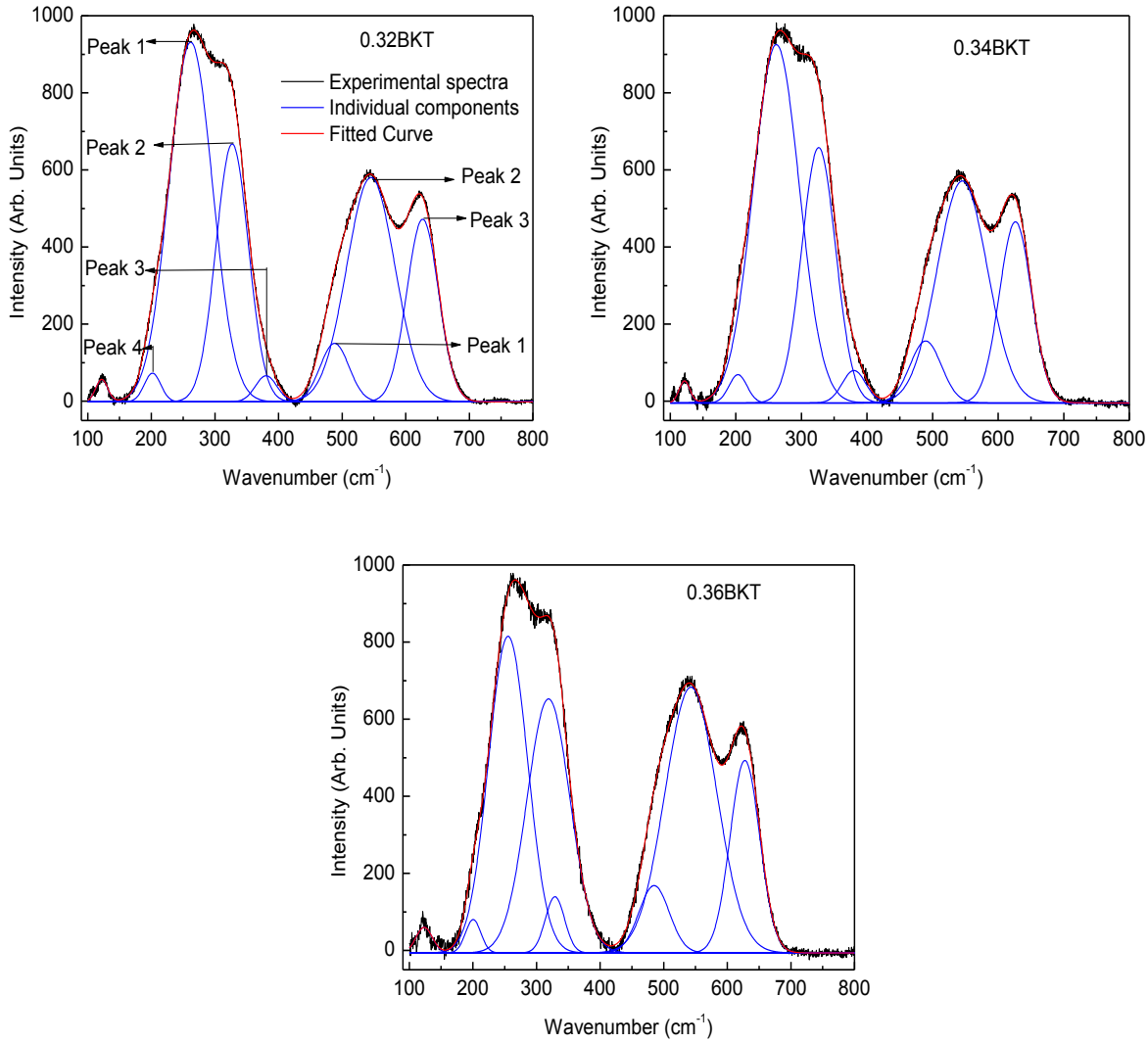

Figure 3.11: Deconvoluted Raman spectra of 0.32BKT, 0.34BKT, and 0.36BKT in (1-x)BNT–xBKT. The black, red and blue curves correspond to experimental spectra, fitted curves and the individual components, respectively.

To obtain more information, the Raman spectra of the different compositions of (1-x)BNT–xBKT are deconvoluted into Gaussian peaks. Figures 3.8, 3.9, 3.10 and 3.11show the deconvoluted Raman spectra of different compositions of the BNT–BKT solid solutions. For BNT, the spectrum is deconvoluted into 7 peaks. The band below180 cm^{-1} is fitted with one peak. The bands in the regions 180-400 cm^{-1} and 400-700 cm^{-1} are deconvoluted into three components each. The three components may be related to TiO_6 octahedra closer to Bi alone, closer to Na alone and surrounded by both Bi and Na. A fourth component is required to fit the spectra in the region 180-400 cm^{-1} for $x > 0.18$. This could be due to the additional Raman mode for the P4bm space group.

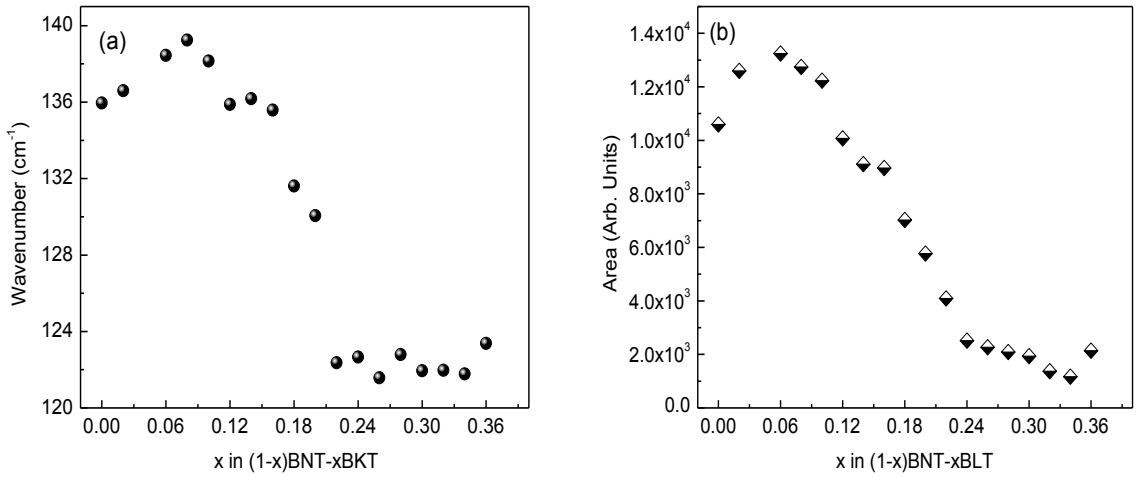

Figure 3.12: Changes in the (a) peak position and (b) area under the peak of the band below 180 cm^{-1} in the Raman spectra as a function of x in (1-x)BNT–xBKT.

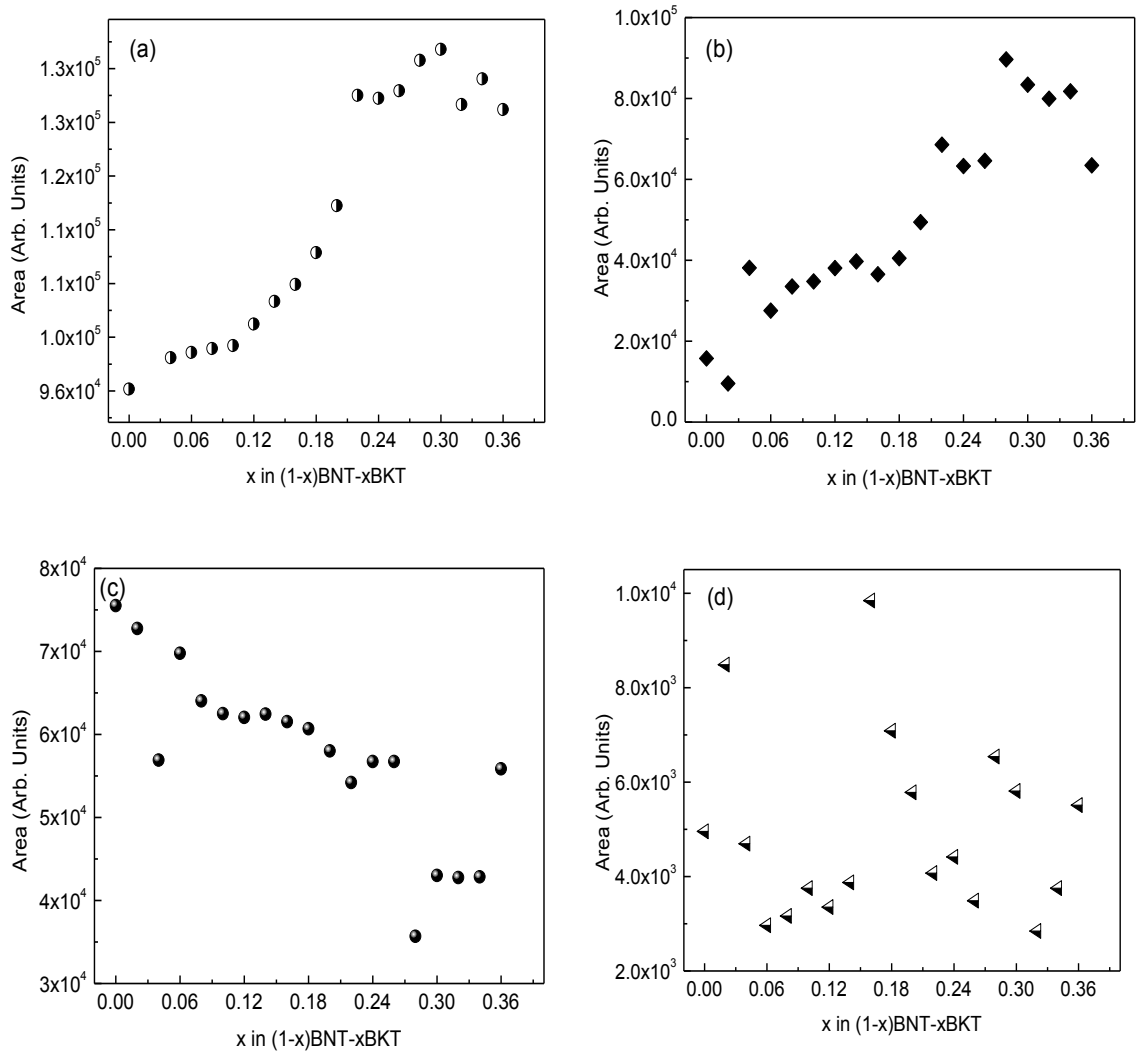

Figure 3.13: Total area and area under the individual peaks of the Raman band in the 180–400 cm^{-1} region as a function of x in (1-x)BNT–xBKT., (a) total area, (b) area under the 1st peak, (c) area under the 2nd peak, (d) area under the 3rd peak.

Figure 3.12 shows the position and area under the peak related to the A-O band below 180 cm^{-1}. A small increase in the position of the band with increasing BKT concentration is observed for $x < 0.1$, followed by a linear decrease up to $x = 0.16$ with increasing the BKT concentration and a sharp drop for $0.16 < x < 0.22$. The peak position is unchanged for higher BKT concentrations ($x > 0.22$). The area under the peak also shows similar changes, where the area initially increases, then decreases drastically after $x = 0.1$, and remains almost constant for $x > 0.24$. This peak belongs to the (Na^+-O/K^+-O) vibration since the band due to Bi-O vibration cannot be observed in this region due to the higher mass of Bi^+ ion.[100] The changes in the nature of this peak (position and area) with increasing K^+ concentration could be due to the changes in the local structural distortions at lower concentrations, structural change from monoclinic to tetragonal at intermediate concentrations in the MPB region and increase in the A site disorder at higher level of substitution.

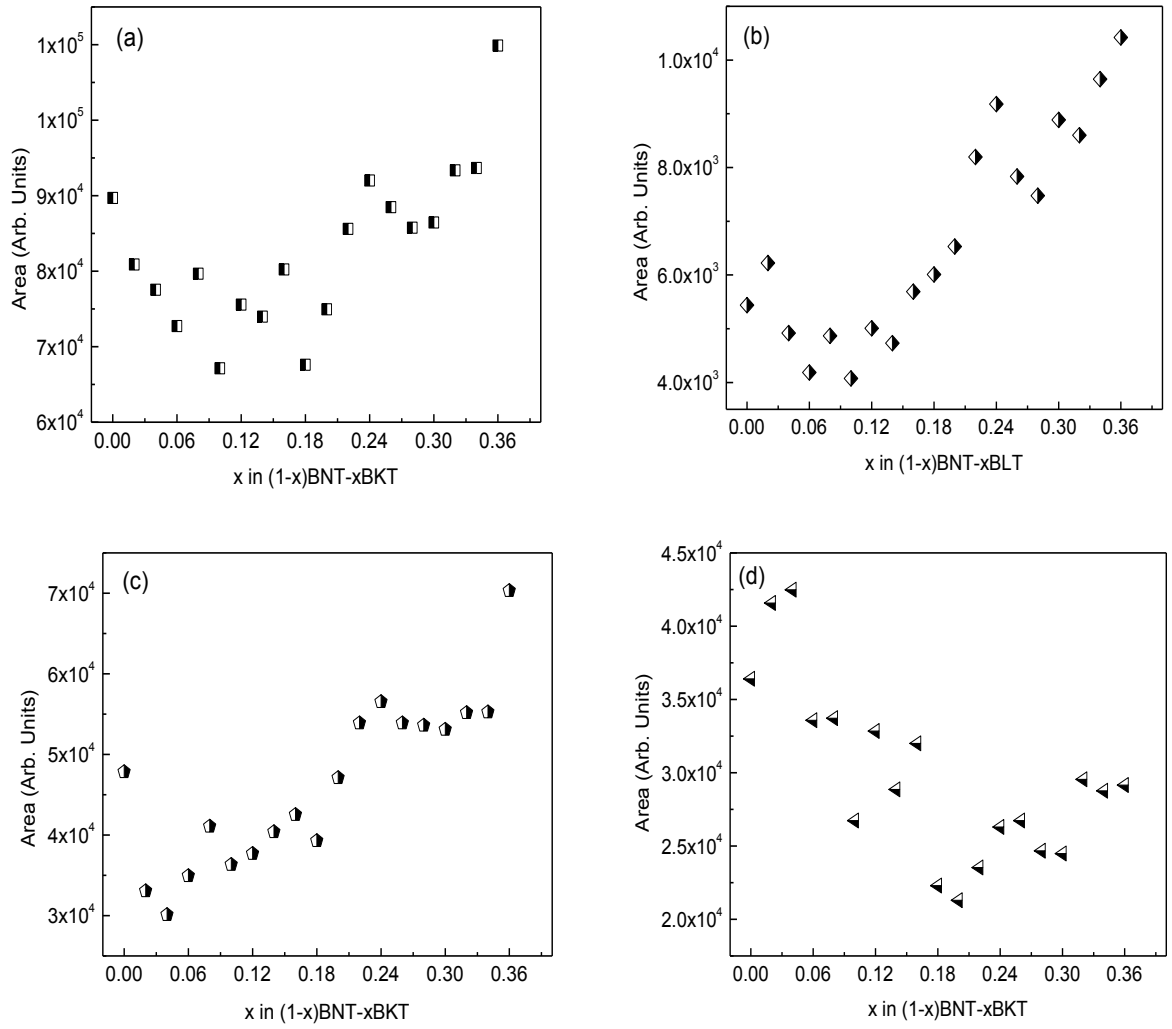

Figure 3.14: Total area and area under the individual peaks of the Raman band in the 400–700 cm^{-1} region as a function of x in (1-x)BNT–xBKT., (a) total area, (b) area under the 1st peak, (c) area under the 2nd peak, (d) area under the 3rd peak.

The broad band observed in the 180–400 cm^{-1} region is associated with the Ti-O vibrations. This band is deconvoluted into 3 components up to x = 0.18, with an additional component for x > 0.18, in the low frequency region which is a clear indication for structural changes after x = 0.18. The additional component for 0.18 < x < 0.36 suggests some changes in the Ti-O bond for $x \geq 0.18$. Figure 3.13(a) shows the changes in area under the band in the 180-400 cm^{-1} region as a function of BKT concentration. On increasing the BKT concentration, the area increases gradually and at higher concentrations the area becomes almost constant. However, different regions can be identified in the graph, such as slow increase up to x = 0.1, relatively larger slope from x = 0.1 to 0.18, large jump between x = 0.18 and 0.24 and remains almost constant for x > 0.24. Associated changes are observed for the area under the different components. Even though the area under the peak 1(Figure 3.13 (b)) increases, under peak 2 (Figure 3.13 (c)) decreases and under peak 3 (Figure 3.13 (d)) remains almost constant, some visible changes are observed in the regions observed under the total area.

The broad band in the 400-700 cm^{-1} region in the Raman spectra is associated with TiO_6 vibrations and the oxygen octahedra. Not much significant changes are observed in the characteristics of this band on increasing the BKT concentration. However the effect of substitution is clearly observed where a higher frequency shift of the peak is observed on increasing the BKT concentration. This region in the spectra is deconvoluted into three components and the changes in the total area under the peak as well as the area under the individual peaks are shown in Figure 3.14. The total area initially decreases up to x ~0.16 and then increases almost linearly. The area under the peak 1decreases up to x = 0.1 and then increases linearly, area under peak 2 increases up to x = 0.24 and then becomes independent of x, area under peak 3 decreases up to the region x = 0.2–0.24 and then increases. Figure 3.15 shows that there is a continuous shift in the position of the individual peaks to higher wave number under the band in the 400-700 cm^{-1} region. However, a close analysis shows anomalies in the peak positions at concentrations where anomalies are observed under the area under the peaks. The positions of all three peaks remain the same for compositions $x \geq$ 0.24. A sharp change in the positions of the peaks is observed for $0.16 \leq x \leq 0.24$, and the positions remain almost the same for compositions in the range $0.08 \leq x \leq 0.16$. All these observations are in line with the observed structural changes.

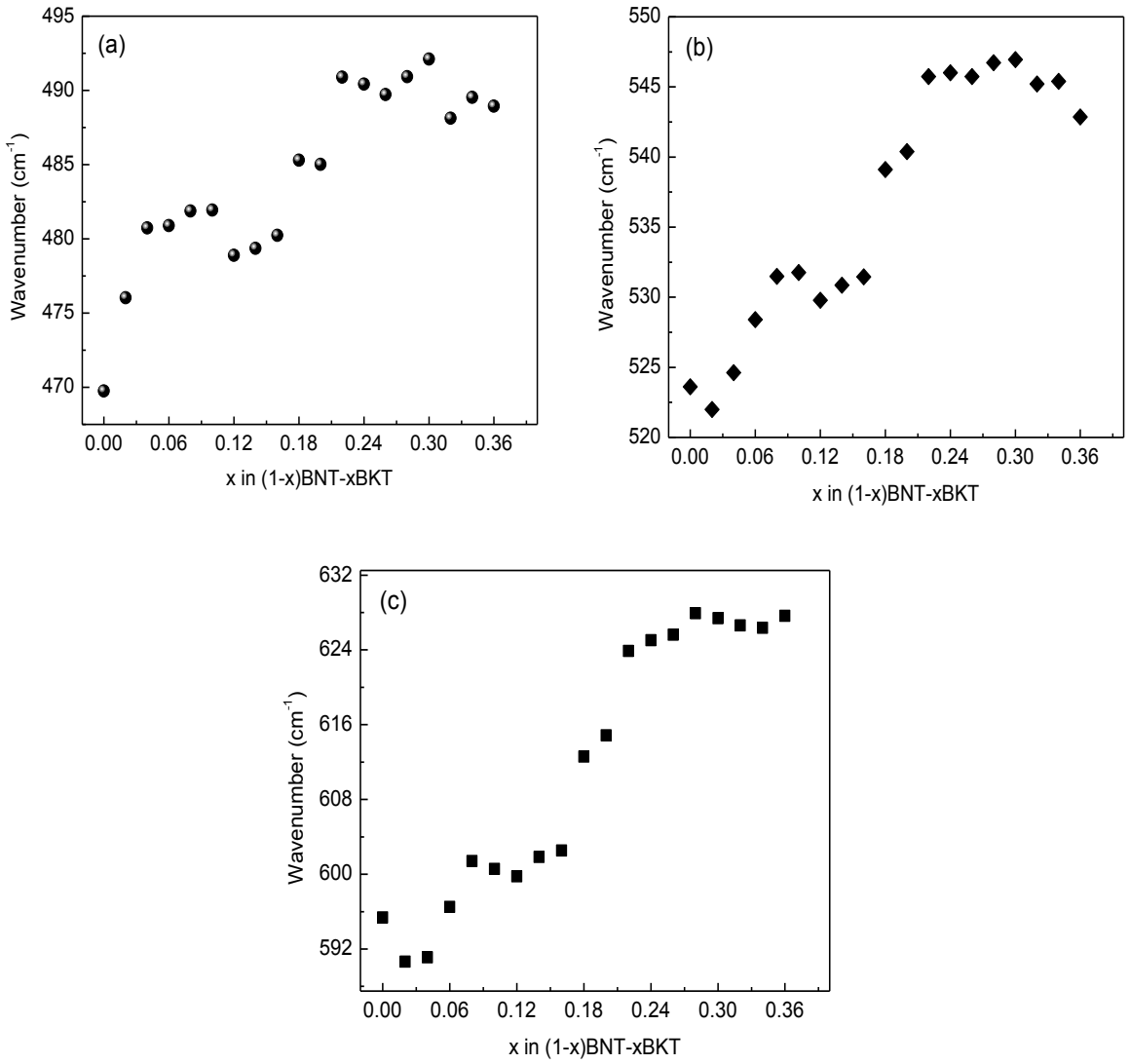

Figure 3.15: Changes in the individual peak positions of the Raman band in the 400–700 cm^{-1} region as a function of x in (1-x)BNT–xBKT.(a) 1st peak, (b) 2nd peak, (c) 3rd peak.

The analysis of the Raman spectra of different compositions, thus, confirms changes in the local structure for $x < 0.18$ and major structural changes for $x > 0.18$ in the (1-x)BNT–xBKT series. An additional band is observed after this composition in the 180-400 cm^{-1} region which corresponds to the Ti-O vibrations. This additional mode observed is a clear indication for symmetry change after $x = 0.18$. Moreover, there is a sudden downward shift after $x = 0.18$ in the band position centered ~135 cm^{-1}. Corresponding changes are observed for the band in the 180-400 cm^{-1} region. This indicates that substitution of Na by K at the A-site of the perovskite lattice directly affects the Ti-O bonds. Similarly, an upward shift in the frequency is observed after $x = 0.18$ in the peaks present in the region between 400-700 cm^{-1}. Since the bands in this region corresponds to TiO_6 vibrations, the upward frequency shift indicates changes in the symmetry of TiO_6 octahedra after $x = 0.18$. Co-

existence of the monoclinic Cc and tetragonal P4bm structures are observed from the XRD studies which correlates very well with the results from the present Raman studies.

3.5. Solid-state NMR spectroscopy

SSNMR studies on the (1-x)BNT–xBKT solid solution series have not yet been reported in the literature. We have carried out ^{23}Na MAS NMR and MQ MAS NMR studies on different compositions in the (1-x)BNT–xBKT series to understand the local symmetry changes on the formation of the solid solution and especially across the MPB region. Figure 3.16(a) shows the ^{23}Na MAS spectra of different compositions in the BNT–BKT series and Figure 3.16(b) shows the zoomed central transition. An immediate observation is the shift in the position of the peak with increasing x and the variation of the peak position as a function of x is shown in the inset of Figure 3.16(b). There are four different compositional regions identified in the inset figure. The chemical shift varies only a little up to $x = 0.06$, sharp increase in the shift is observed for $0.06 \leq x \leq 0.16$, large increase in the chemical shift is observed for $0.16 \leq x \leq 0.24$, and the chemical shift remains almost constant for $x > 0.24$. From the spectra of different compositions, it is clear that their linewidths are different which is due to the changes in their quadrupolar coupling which also result in an apparent change in the peak maxima. The changes in the quadrupolar coupling are due to the changes in the symmetry on replacing the smaller ion Na^+ by the larger K^+ ion.

To extract the NMR parameters, all the ^{23}Na MAS spectra were fitted using the DMFIT program.[9] From the lineshape of the ^{23}Na spectra, it is clear that this system has a distribution of quadrupolar coupling constants as described in chapter 2 (Section 2.3.2.3). The Gaussian isotropic model (GIM) of the 'Czjzek' distribution is the simplest and physically consistent model[90] to simulate a spectrum which has a distribution of quadrupolar coupling constants. The 'Czjzek' model in the DMFIT program incorporates the Gaussian isotropic model which includes a Gaussian distribution of isotropic chemical shift and a distribution of electric field gradient which gives a mean isotropic shift (δ_{iso}), a chemical shift distribution (Δ_{cs}) and a mean quadrupolar product $C_Q^* = C_Q(1+\eta^{2/3})^{1/2}$, where η is the asymmetry parameter. The use of 'Czjzek' model allows a quantitative decomposition of the spectra and the extraction of the quadrupole coupling. After selecting the 'Czjzek' model, guess parameters for the isotropic shift (δ_{iso}), the distribution of isotropic chemical shift (Δ_{cs}) and the quadrupolar coupling C_Q^* are used to generate an approximate line shape. Then, the simulated lineshape was iterated by changing the NMR parameters and the amplitude until a

good match with the experimental spectra is obtained. Figure 3.17 shows the experimental and simulated spectra for selected compositions (x = 0, 0.11, 0.2, 0.36) in the (1-x)BNT–xBKT series. It can be seen that the experimental and the simulated spectra match very well for all the compositions.

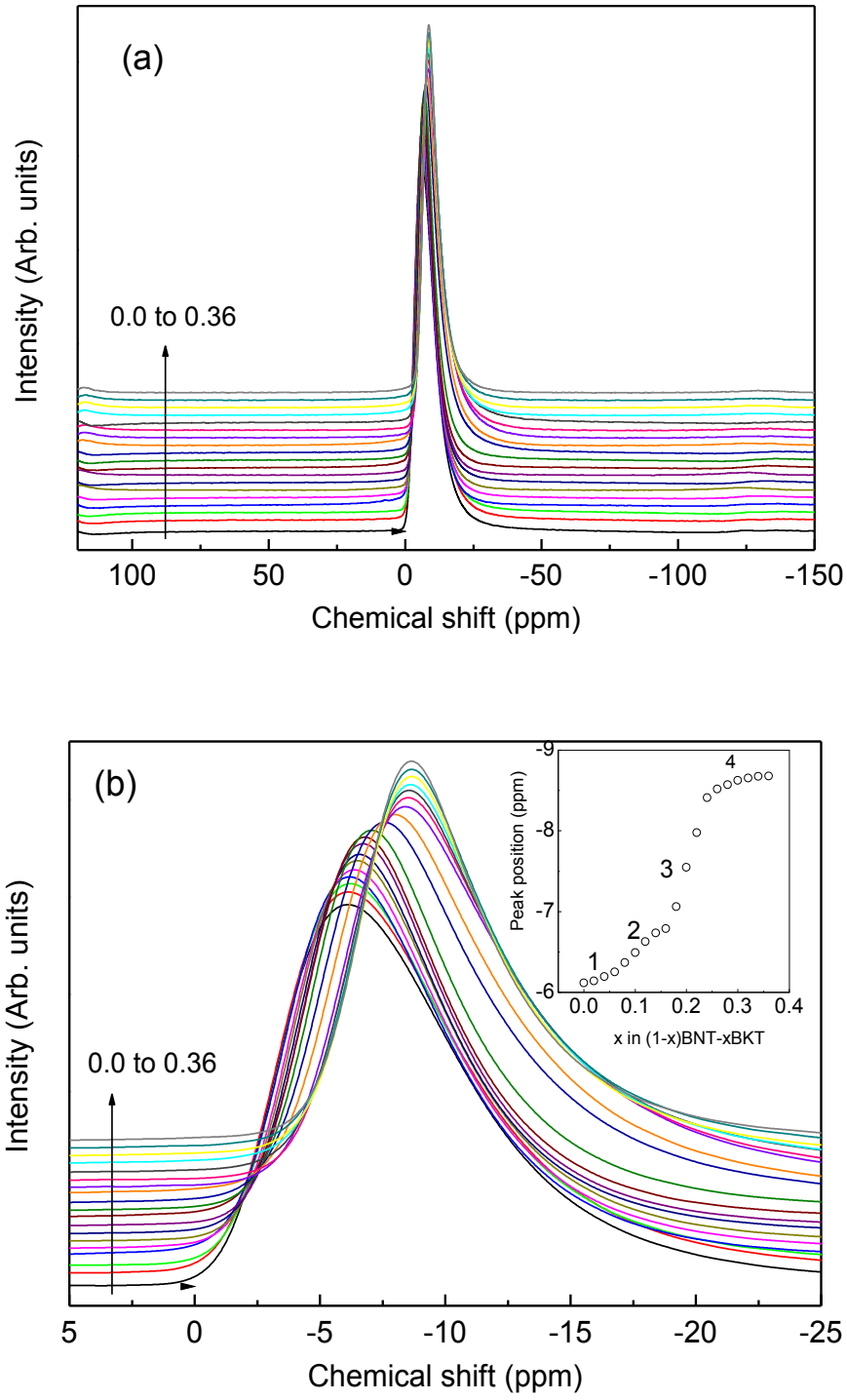

Figure 3.16: (a) ^{23}Na NMR spectra of the different compositions in the (1-x)BNT–xBKT series, (b) Zoomed view of the central region. Spectra are shown for $\Delta x = 0.02$.

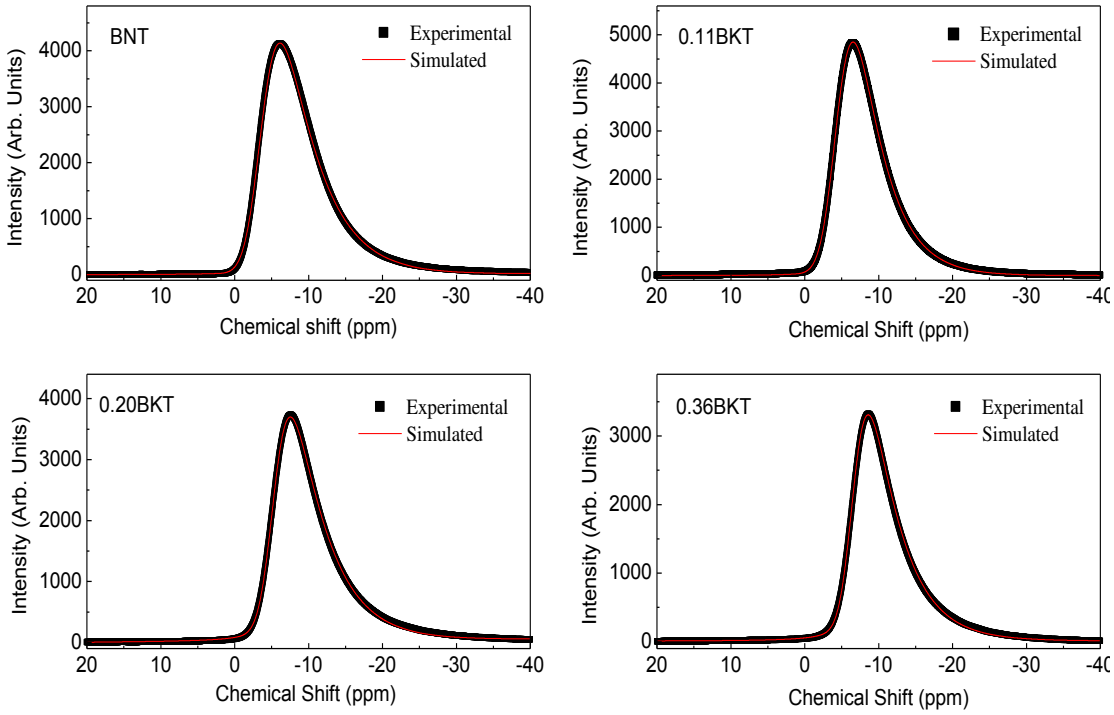

Figure 3.17: Comparison of the experimental and simulated ^{23}Na NMR spectra of BNT, 0.11BKT, 0.20BKT, and 0.36BKT in the (1-x)BNT–xBKT series.

Figure 3.17 shows the variation of the quadrupolar coupling, C_Q^*, with concentration of BKT in the (1-x)BNT–xBKT series. C_Q^* decreases initially with increasing BKT concentration and then increases in the concentration range $0.15 \leq x \leq 0.24$, after reaching a minimum value for $x = 0.15$ and further decreases above $x = 0.24$. The variation of C_Q^* in the region $x < 0.15$ shows two distinct regions, a non-linear region below $x < 0.1$ and a linear region for $0.1 < x < 0.15$. Quadrupolar coupling constant is known to be related to the crystal symmetry of a material.[91] Since the C_Q^* decreases initially, it is possible that the rhombohedral distortion decreases with increasing BKT concentration and that the distortion may be minimum around $x = 0.15$ and also that phase separation and the MPB region starts above this value of x. This implies that the rhombohedral/monoclinic unit cell of BNT is unstable above $x = 0.15$, because of the larger size of K^+ compared to that of Na^+, and forms the tetragonal unit cell at higher levels of substitution. Thus, from the NMR results, it can be considered that the compositional region $0.15 \leq x \leq 0.24$ may correspond to the MPB region. XRD studies showed the onset of the MPB region as $x = 0.18$. Since solid state NMR studies probe the local symmetry changes, compared to the long range ordering probed by XRD, it is possible that the onset of the MPB region is $x = 0.15$.

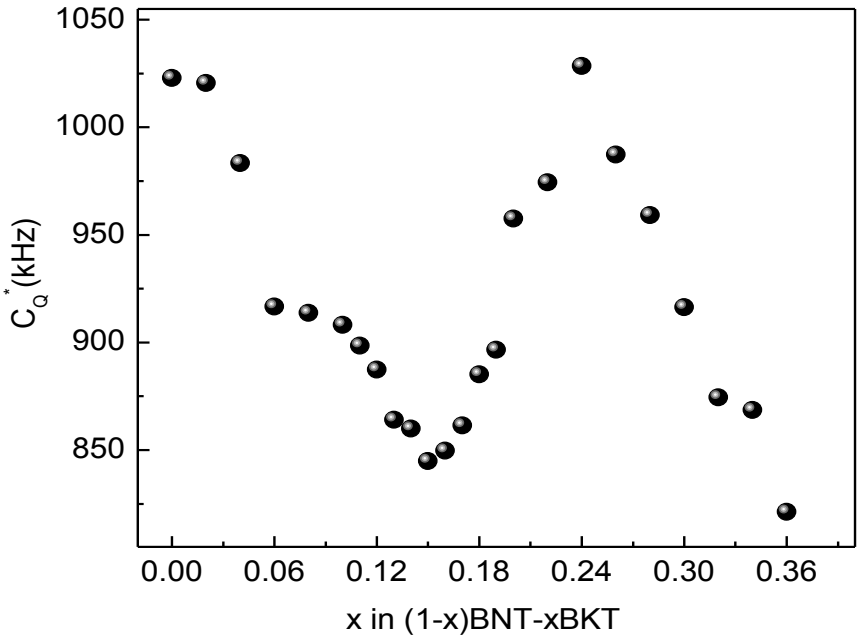

Figure 3.18: Variation of ^{23}Na C_Q^* of (1-x)BNT–xBKT series as a function of x.

XRD studies showed a biphasic MPB region in the (1-x)BNT–xBKT series, for $x \geq$ 0.18, with monoclinic (Cc) and tetragonal (P4bm) structures. To verify whether more than a single sodium site is present or not, ^{23}Na MQMAS NMR investigations are carried out on a few compositions of (1-x)BNT–xBKT solid solution. Figure 3.19 shows the MQMAS spectra of four different compositions of (1-x)BNT–xBKT.

If there were more than one sodium site present in the crystal structure, it would have been evident as a separate contour in the MQMAS spectrum. Since more than one contour is absent in the MQMAS spectra, it is clear that only a single sodium site is present in the crystal structure of different compositions in the (1-x)BNT–xBKT solid solution, even in the MPB region. The MQMAS spectra are contours which are centered around -6 to -7 ppm in the x axis and narrows down towards the right hand side as expected for a system with a distribution of quadrupolar coupling.[111]The y co-ordinate of contour is dependent on the strength of the quadrupolar coupling C_Q^* with the contour shifting down when C_Q^* is more. From the MQMAS spectrum of 0.11BKT shown Figure 3.19(b), it can be seen that the y coordinate of the contour is less than that of BNT shown in Figure 3.19(a) as expected since the C_Q^* for this composition is less than that of BNT. Similar trend is seen for the MQMAS spectra of other compositions shown. The y co-ordinate of the contour of the spectrum of 0.36 BKT shown in Figure 3.19(d) has the least value since this has the lowest C_Q^*.

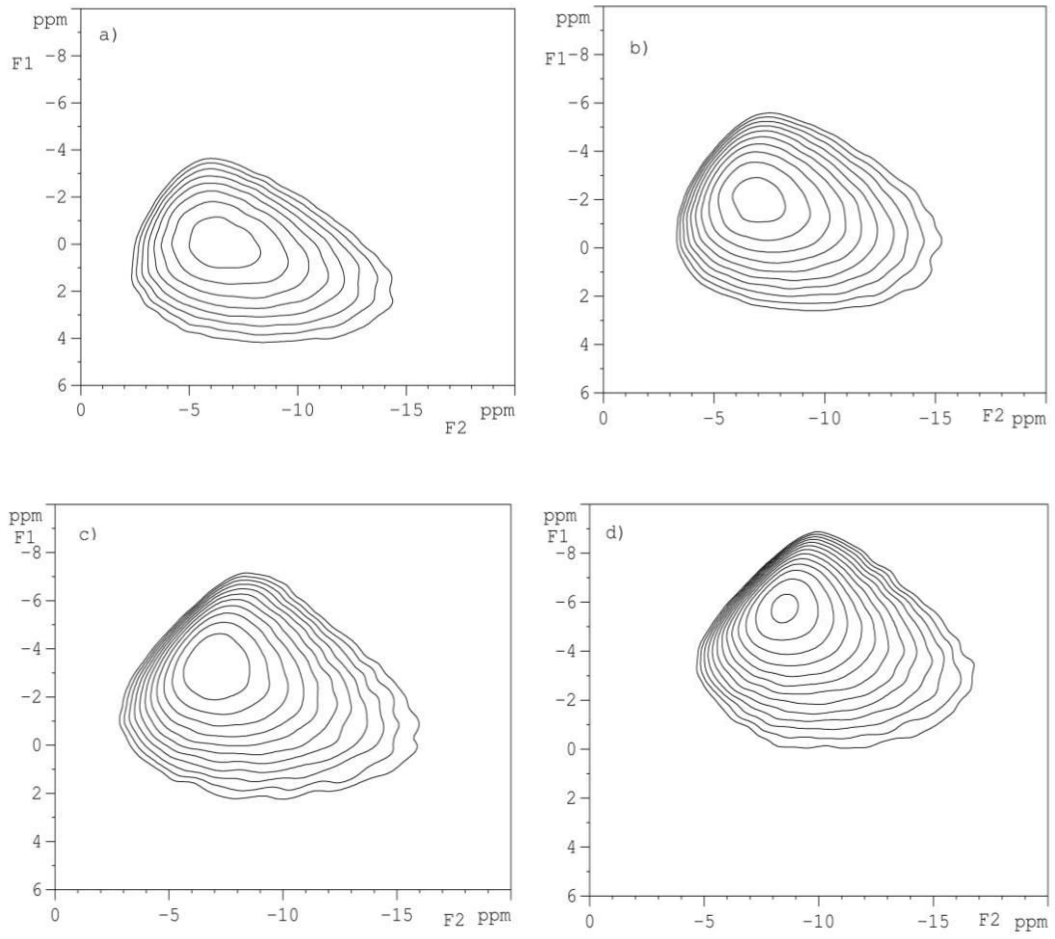

Figure 3.19: ^{23}Na MQ MAS NMR spectra of different compositions in the (1-x)BNT–xBKT series; a) BNT, b) 0.11BKT, c) 0.20BKT, and d) 0.36BKT.

From the ^{23}Na SSNMR studies it may be concluded that the MPB region starts from x = 0.15 compositions and the distortion in the crystal lattice is maximum in the composition range $0.22 \leq x \leq 0.24$. Only one sodium site present in the MPB region of BNT–BKT solid solution although both monoclinic and tetragonal phase co-exist in the MPB.

3.6. Scanning electron microscopy

SEM images of different compositions of (1-x)BNT–xBKT are shown in Figure 3.20. Table 3.6 shows grains size and density of different compositions in the (1-x)BNT–xBKT series. Very large grains of size ~10 μm are observed for BNT (x = 0) with large inter and intra-granular pores. The grain size and porosity are decreased with increasing BKT concentration. Individual grains of size in the range 1–5 μm are clearly seen for the composition x=0.14. Further increase in the BKT concentration leads to the formation of fused grains, with decreasing porosity, for compositions in the range $0.16 \leq x \leq 0.24$. These compositions correspond to the MPB region as evidenced from the XRD studies. For compositions with x

>0.24, individual and well-crystallized small grains are observed. Thus, there is a direct correlation between the phase content in the BNT–BKT system obtained from XRD analysis and the microstructure of the sintered products

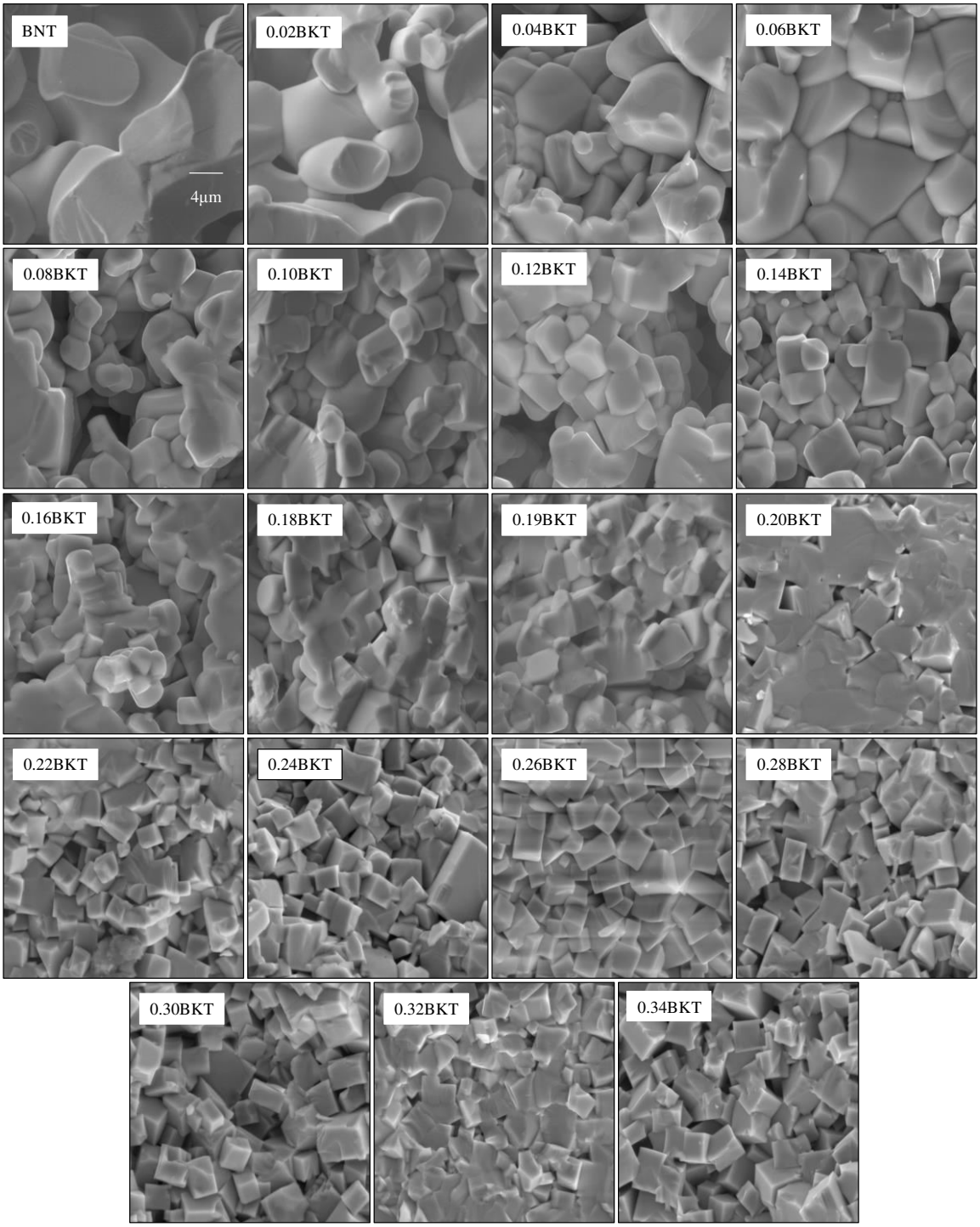

Figure 3.20: SEM images of different compositions in the (1-x)BNT–xBKT system. The scale shown is common for all images.

Table 3.6: Density and grains size of different compositions in the (1-x)BNT–xBKT series.

Sample	Grain size (µm)	Density (g/cm^3)	Theoretical Density (g/cm^3)
BNT	11.4	4.66	6.00
0.02BKT	10.0	4.68	6.00
0.04BKT	9.7	4.77	6.00
0.06BKT	9.7	4.78	6.00
0.08BKT	8.5	4.81	6.01
0.10BKT	5.7	4.81	6.01
0.12BKT	5.7	4.83	6.01
0.14BKT	4.5	4.85	6.01
0.16BKT	5.1	4.90	6.02
0.18BLT	3.7	4.94	5.93
0.19BKT	3.7	4.97	5.97
0.20BKT	3.4	5.10	5.97
0.22BKT	3.1	5.18	5.98
0.24BKT	3.7	5.20	5.93
0.26BKT	3.4	5.07	5.99
0.28BKT	2.8	5.04	5.97
0.30BKT	3.1	5.00	5.99
0.32BKT	2.8	5.00	5.98
0.34BKT	3.4	5.00	5.97

3.7. Density

Figure 3.21 shows the variation of sintered density of (1-x)BNT–xBKT with BKT concentration. The density is relatively low, compared to that in the previous reports,[58,112] and this is due to the very lower pressure (8 MPa) used in the present work for compaction of the pellets. For example, Yang *et al* reported a maximum density of 5.66 g/cm^3 for x = 0.18 for powders compacted at a pressure of 100 MPa and sintered at 1150 ^oC.[58] Similarly, Otonicar *et al* reported a sintered density of 5.86 g/cm^3 for BNT powders compacted at a pressure of 750 MPa and sintered at ~1100 ^oC.[112] In the present work, the sintered density of BNT is (4.6615 g/cm^3) is very low compared to the theoretical density 5.9970 g/cm^3, due to the very low

compaction pressure used (8 MPa). A comparison of theoretical density and measured density is shown in Table 3.6

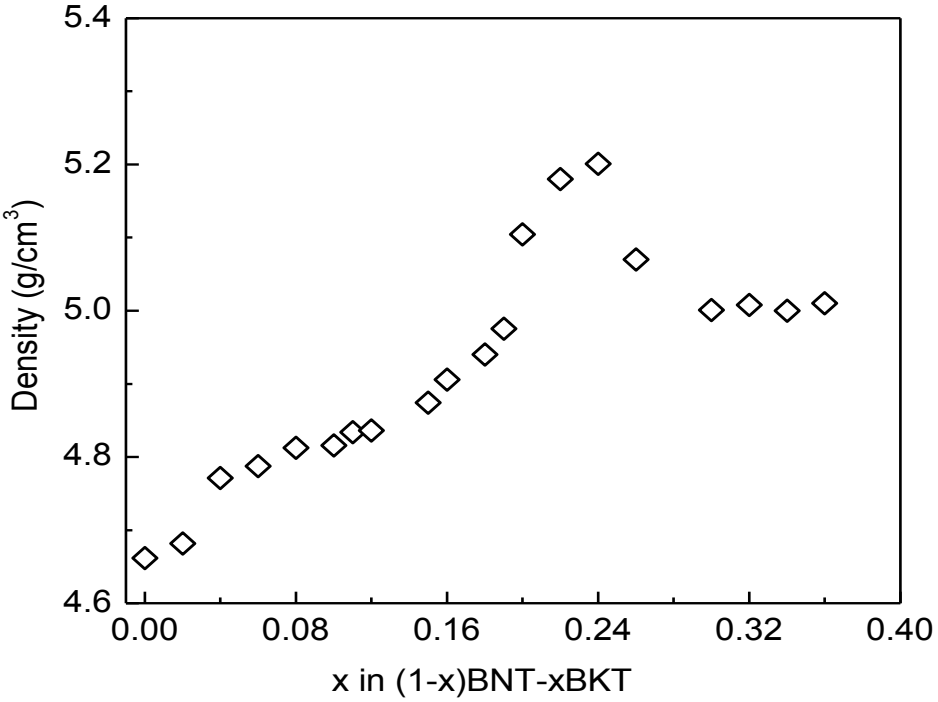

Figure 3.21: Variation of the sintered density of (1-x)BNT–xBKT solid solution as a function of x.

The density of (1-x)BNT–xBKT initially increases almost linearly with increasing x, suggesting the formation of an ideal solid solution. A large increase in the density is observed above $x = 0.18$ and the density reaches a maximum value in the region $0.22 \leq x \leq 0.24$. The density is decreased above $x = 0.24$ and reaches almost constant value for $x > 0.26$. The changes in the density correlate very well with the features observed in the microstructure, where the grain size and porosity decreases with increasing x up to $x = 0.18$, fused grains with increasing grain size are observed for compositions in the range $0.22 \leq x \leq 0.24$ and well crystallized grains are observed for $x \geq 0.24$.

3.8. Dielectric constant

Figure 3.22 shows the variation of the dielectric constant of (1-x)BNT–xBKT as a function of x, measured at a frequency of 1 kHz. It is observed that, on increasing the BKT concentration, the dielectric constant initially increases almost linearly up to $x = 0.17$. A large increase in the dielectric constant is observed above $x > 0.17$ and the value reaches a maximum in the compositional range $0.20 \leq x \leq 0.26$, with the highest value of $\varepsilon_r = 1800$ obtained for $x = 0.24$.

A sharp drop in the dielectric constant is observed above x = 0.24 and the dielectric constant decreases almost linearly above x = 0.26.

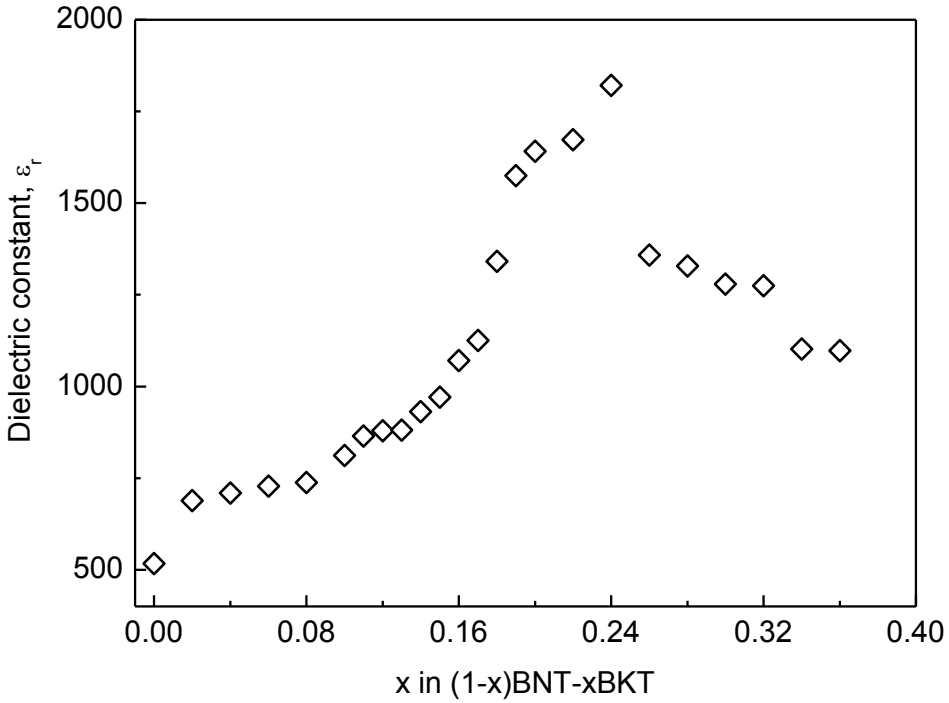

Figure 3.22: Variation the of dielectric constant of (1-x)BNT–xBKT as a function of x.

For BNT, dielectric constant is obtained as 516, comparable to that reported (536).[112] Otonicar *et al* have reported a maximum dielectric constant ε_r = 1140 for x = 0.2 where only few compositions in the BNT–BKT series are studied (0.17, 0.2 and 0.22, 0.24) in the MPB region.[112] Yang *et al* reported a maximum dielectric constant ε_r = 893 at x = 0.18 in the MPB region of BNT–BKT solid solution.[58] Sasaki *et al* could achieve a dielectric constant ε_r = 1100 at x = 0.20 in the BNT-BKT solid solution.[72] The changes in the dielectric constant with increasing x are almost similar to the variation of the density (Figure 3.20), suggesting the correlation with the dielectric constant and microstructure. Even though the densities of the present sintered compacts are much less than that reported due to the differences in the compaction pressure used, comparable or larger values of the dielectric constant are obtained for different compositions in the present work.

Figure 3.23 shows the temperature dependent dielectric constant of different compositions of BNT–BKT solid solution. The dielectric constant of the ceramics is initially increased with temperature, reached a maximum at a particular temperature and then

decreased. Only one peak is observed for compositions with low K^+ content ($x \leq 0.10$). For higher BKT content ($0.12 \leq x \leq 0.20$), an additional peak is observed at a lower temperature.

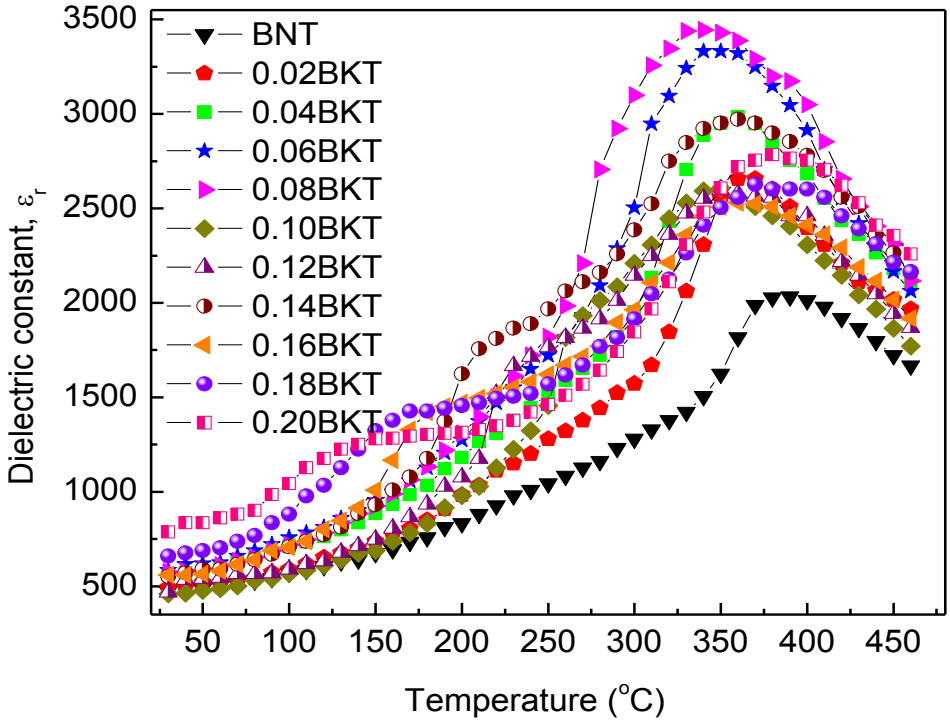

Figure 3.23: Variation of the dielectric constant of different compositions of (1-x)BNT–xBKT as a function of temperature.

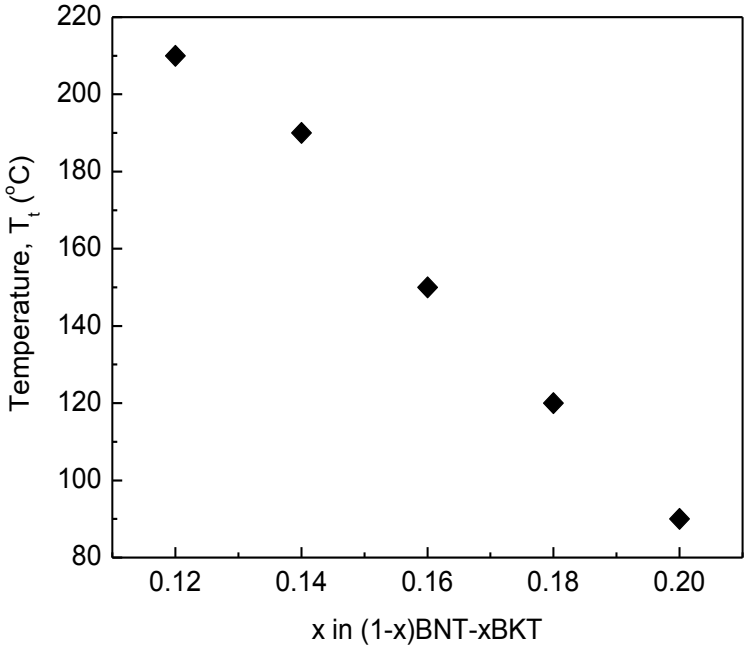

Figure 3.24: The first transition temperature (T_t) of (1-x)BNT–xBKT solid solution as a function of x.

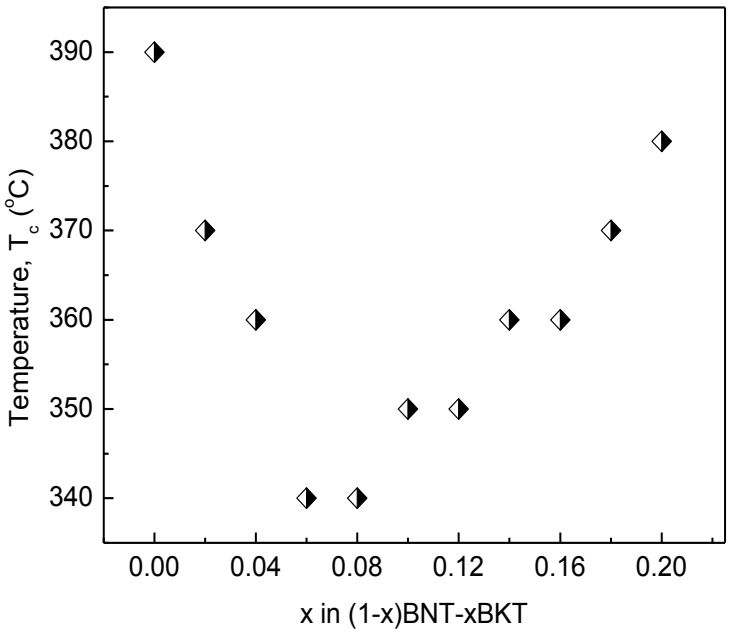

Figure 3.25: Curie temperature (T_C) of (1-*x*)BNT–*x*BKT solid solution as a function of *x*.

Previous report on the temperature dependent dielectric constant concluded that the first peak (T_t) at the lower temperature is due to the rhombohedral ferroelectric to tetragonal antiferroelectric phase transition and the second peak (T_C) is due to the transition from tetragonal antiferroelectric phase to cubic paraelectric phase.[58] The first peak at T_t showed a low temperature shift with increasing BKT concentration as shown in Figure 3.24. The changes in T_C as a function of BKT concentration is shown in Figure 3.25. For low K^+ concentration ($x \leq 0.08$) T_C decreases with increasing BKT concentration and for higher K^+ concentrations ($0.08 \leq x \leq 0.20$) T_C increases. The observations in the present investigation are slightly different from already reported studies. Yang *et al* reported that T_t shifts to low temperature and T_C shifts to high temperature with BKT concentration.[58] Elkechai *et al* studied the temperature dependent dielectric permittivity of selected compositions of BNT–BKT in the frequency range 100 kHz to 1 MHz and observed a similar behaviour characterized by a large maximum of permittivity without frequency dispersion.[68] They observed a small shoulder at the low temperature side (T_t) for compositions with low BKT concentration which diminished and shifted towards the low temperature side with increase in BKT concentration. This shoulder at T_t disappeared at $x = 0.1$ composition. T_C of BNT–BKT solid solution showed a slight decrease till $x = 0.1$ composition and then it increased.

At higher BKT concentrations, more cations co-occupy in a single unit cell lattice, hence more chemical compositions are possible in the unit cell. As a result, the crystal

structure become inhomogeneous in the nanometer level and the relaxor behaviour of the ceramics is increased. Consequently the T_C of the material is shifted to higher temperatures with BKT concentration. The low temperature shift in the T_C at low BKT concentrations ($x \leq 0.08$) is due to the local symmetry changes due to the non-uniform distribution of the substituted ion in the crystal lattice. The studies on dielectric properties of the BNT–BKT solid solution showed that the substitution of larger K^+ ion in the BNT lattice caused distortions in the unit cell which leads to changes in the dipole moment. This will induce strain in the crystal lattice and a raise in the relaxor behaviour, as suggested.[58]

3.9. Polarization

The P-E hysteresis loops of BNT–BKT solid solution are measured in the voltage range of ±2000 V. The P-E hysteresis loops of different compositions ofthe BNT–BKT solid solution series are shown in Figure 3.26. For a direct comparison of the changes with composition, the P-E loops of selected compositions are compared in Figure 3.27.

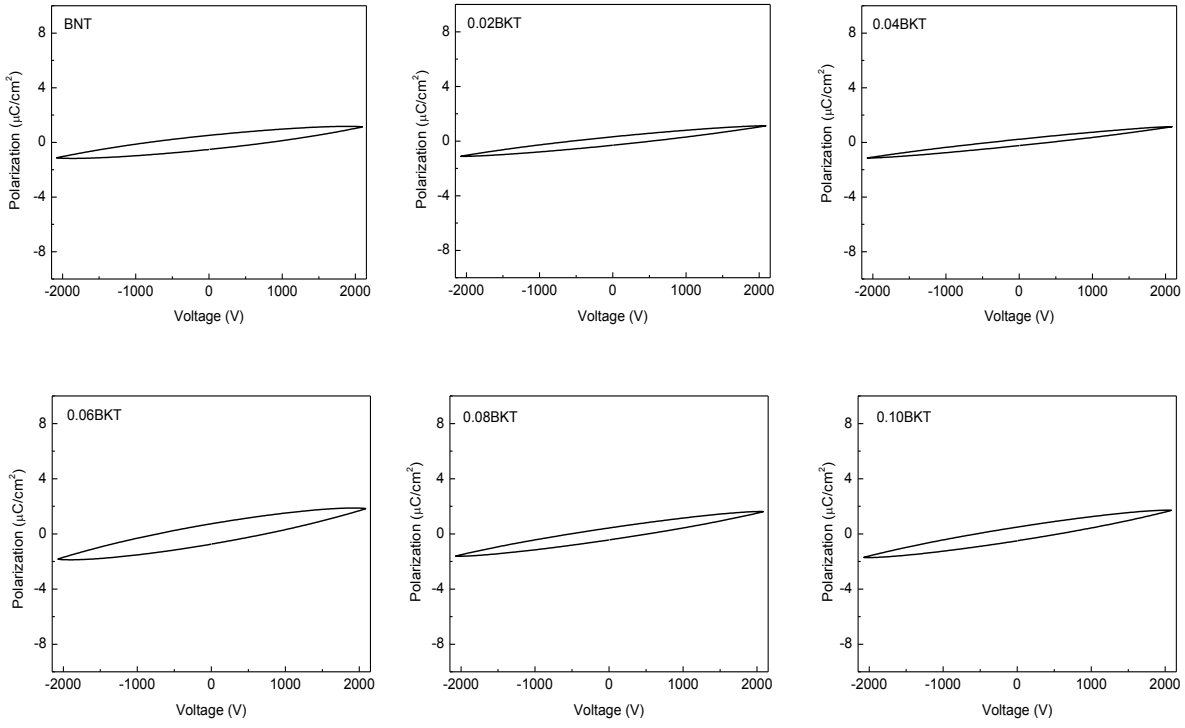

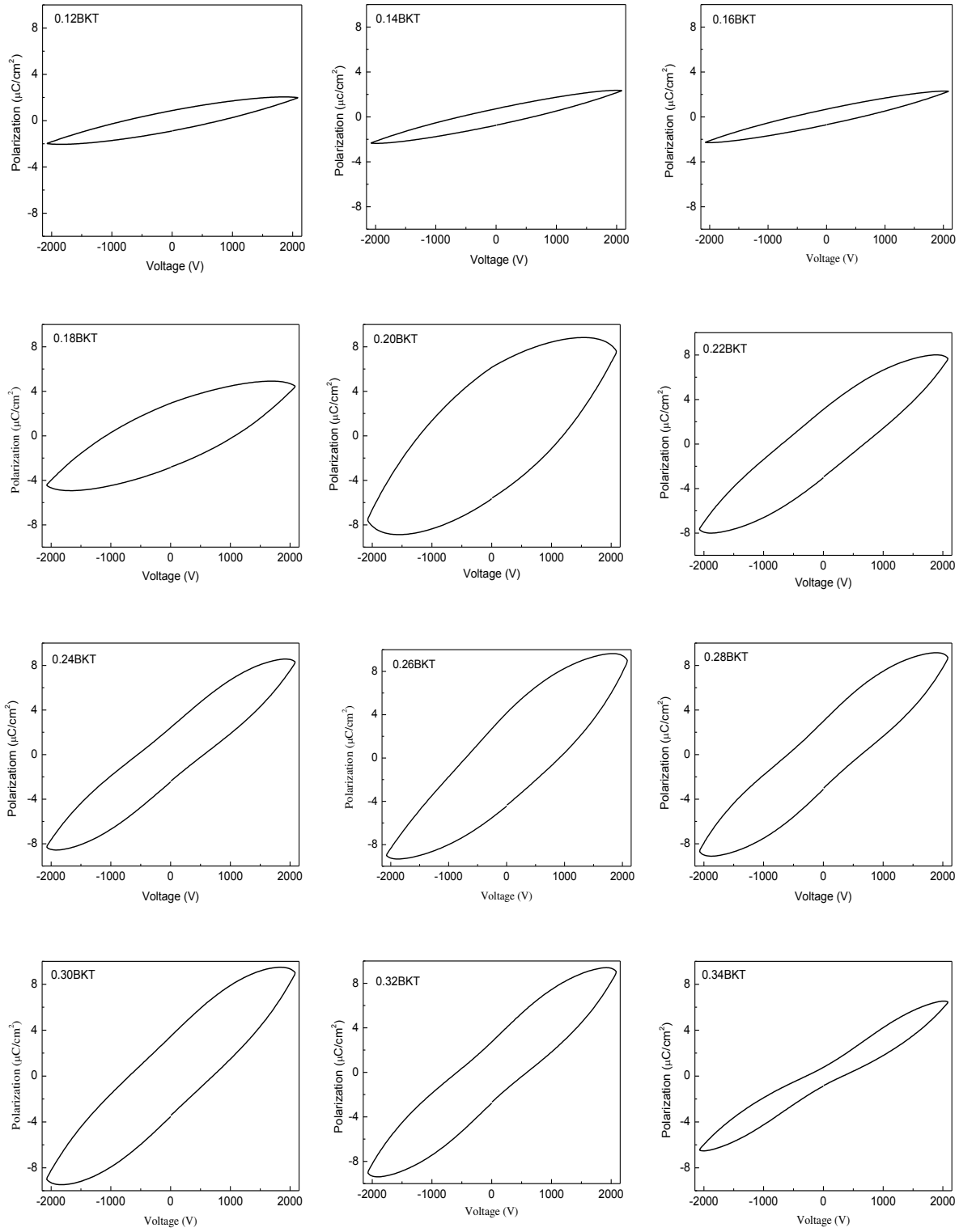

Figure 3.26: P-E hysteresis loop of different compositions in (1-x)BNT–xBKT.

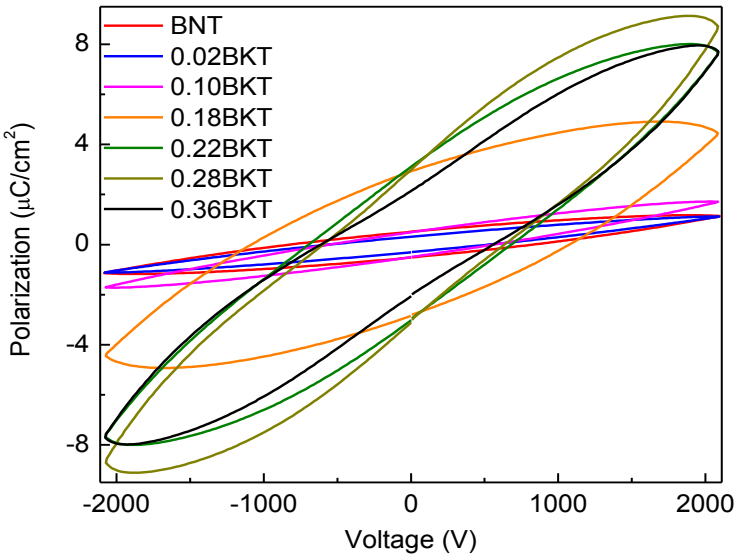

Figure 3.27: Comparison of the P-E hysteresis loops of selected compositions of (1-x)BNT–xBKT.

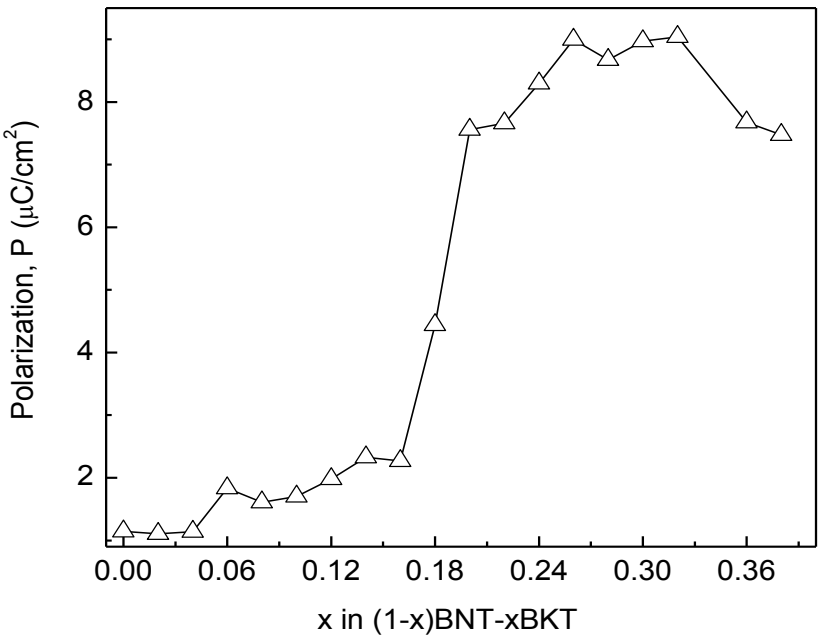

Figure 3.28: Polarisation at 2000 V as a function of x in (1-x)BNT–xBKT.

Polarization is not saturated for all compositions due to the low electric field used for the measurement. However, it is seen that the polarization and the width of the loop increase with increasing BKT content. Figure 3.28 shows the variation of polarization at the maximum measured field of 2000 V, as a function of x in (1-x)BNT–xBKT. On increasing the BKT concentration, the polarization increases almost linearly up to $x = 0.16$, and a large increase in the polarization is observed between $x = 0.16$ and 0.20. Polarization reaches a maximum in the compositional range $0.22 \leq x \leq 0.28$. The coercive field is found to be maximum for the

compositions x = 0.18 and 0.20, even though the polarisation is not saturated, and hence no meaning for the measured coercive field.

3.10. Structure-property correlations

The present results show that the changes in the crystal structure, phase content, microstructure, sintered density, dielectric constant and polarization of the (1-x)BNT–xBKT system follow exactly similar trend. Linear variations of the lattice parameter, density, dielectric constant and polarization are observed for $0 \leq x \leq 0.17$ and maximum values of density, polarization and dielectric constant are obtained in the range $0.20 \leq x \leq 0.24$, where the microstructure shows fused grains. These results indicate the direct correlation between the changes in the structural, microstructural and performance parameters with increasing BKT content in the (1-x)BNT–xBKT system.

From the Raman and ^{23}Na NMR spectral studies on different compositions in the (1-x)BNT–xBKT series, close correlations between the local structural variations and the properties of the system have been obtained. For example, Figure 3.29 shows comparison of the variation of the dielectric constant and the area under the band in the 200-400 cm^{-1} region of the Raman spectra, as a function of BKT content.

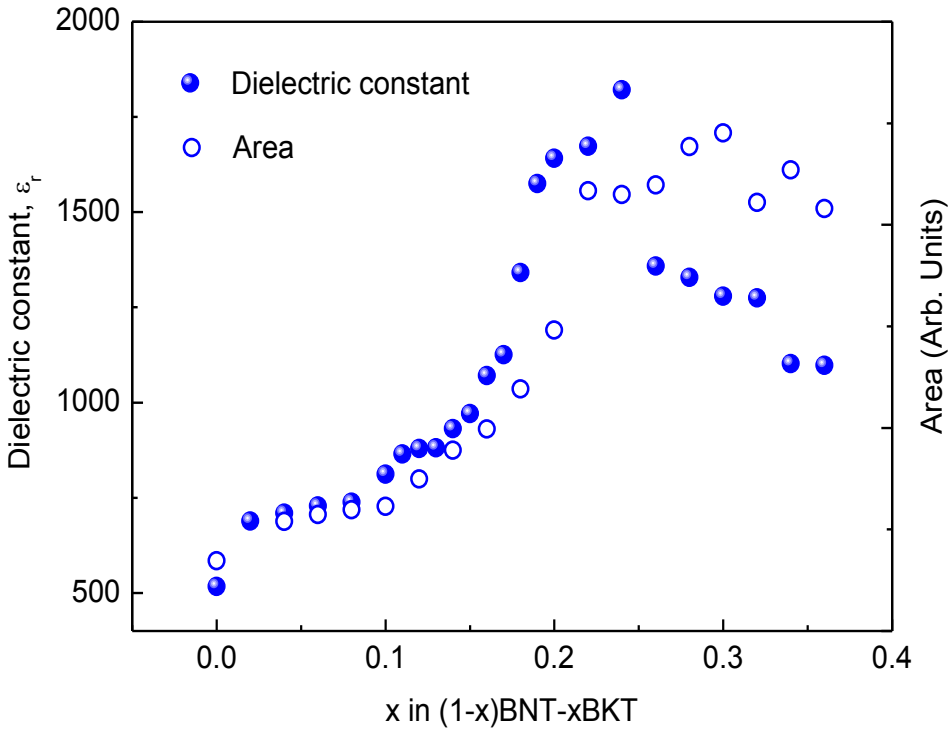

Figure 3.29: Comparison of the dielectric constant and the area under the Raman band in the 200-400 cm^{-1} region as a function of x in the (1-x)BNT–xBKT series.

The Raman band in this frequency region corresponds to the Ti-O vibrations in the perovskite structure. Both parameters show almost similar variation, below x = 0.2. Since Raman spectra is sensitive to local structural variations, the similar changes observed for both parameters in the same compositional region, suggests the role of minor variations in the local structure in determining the ferroelectric properties of the material.

In fact, better correlation is obtained from the NMR studies. Since SSNMR spectrum is known to be very sensitive to local structural variations, additional information is obtained from the ^{23}Na NMR spectral studies. Figure 3.30 compares the changes in the ^{23}Na quadrupolar coupling constant obtained from the NMR studies and the position of the Raman band below 180 cm^{-1}. This band in the Raman spectra corresponds to the Na/K-O vibrations. Corresponding changes are observed for both parameters in different compositional regions. The quadrupolar coupling constant increases above x = 0.15 and a corresponding large drop is observed in the position of the Raman peak.

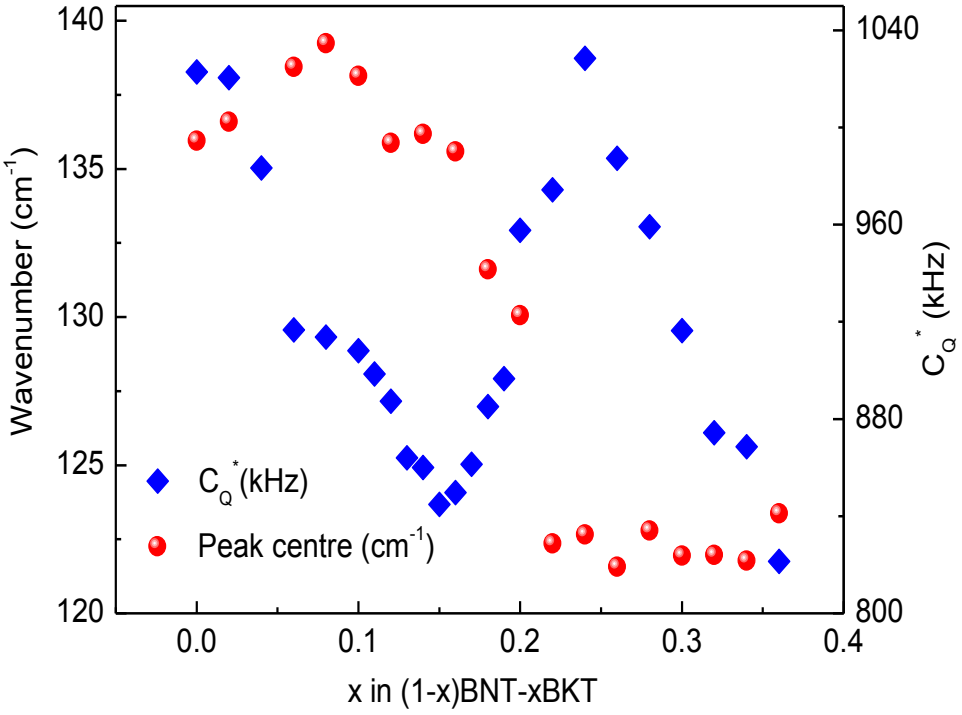

Figure 3.30: Comparison of the position of the Raman peak below 180 cm^{-1} and the ^{23}Na quadrupolar coupling constant from NMR spectra, as a function of x in (1-x)BNT–xBKT.

The XRD analysis showed structural phase transition above x = 0.18 in the BNT–BKT solid solution[11] and the SSNMR and Raman parameters showed deviation after x = 0.15 composition. A large increase in the quadrupolar coupling constant is observed above x =

0.15. Raman analysis also suggests changes in the parameters above x = 0.15. These indicate onset of local symmetry changes for x > 0.15 which are not detectable by the XRD analysis since it measures only the long range order of a system. Thus, the results suggests that the onset of the MPB region is x = 0.15. Thus, the NMR studies suggest that the MPB region corresponds to $0.15 \leq x \leq 0.24$ in the (1-x)BNT-xBKT solid solution series. A close observation of different parameters suggests corresponding changes. For example, large increase in the dielectric constant and polarization is observed for x > 0.15, suggesting the importance of the local structural changes in determining the properties of the system. Thus, solid state NMR studies, along with other characterization techniques, appear to be an important tool in predicting the structure-property correlations of the functional ceramic systems.

3.11. Conclusions

Structural, microstructural, density and dielectric properties of the lead-free ferroelectric compositions in the solid solution series (1-x)$Bi_{0.5}Na_{0.5}TiO_3$–$xBi_{0.5}K_{0.5}TiO_3$, are studied to understand the correlation between the structure and properties of the system. From Rietveld refinement analysis of the powder XRD patterns, it is found that the crystal structure is monoclinic for x < 0.18. A biphasic MPB region exists for $x \geq 0.18$ with monoclinic and tetragonal structures. Some of the Raman spectral parameters showed a deviation after x = 0.15 suggesting the importance of changes in the local symmetry and structural distortion. More information on the importance of local structural changes is obtained from solid state NMR studies. The quadrupolar coupling of ^{23}Na NMR showed large deviation above x = 0.15, confirming changes in the local symmetry above this composition. The properties of the solid solution showed corresponding changes. Thus, there is a direct correlation between the structure, microstructure, and density of the compositions with the dielectric constant, where the properties vary linearly for x < 0.15, deviates above x = 0.15 and reached a maximum in the compositional region $0.22 \leq x \leq 0.28$ where the material shows maximum density. The long range order of the (1-x)BNT–xBKT solid solution is obtained from XRD studies which confirmed the existence of a biphasic MPB region above x = 0.18 composition. However the local symmetry changes and distortions studied by Raman spectroscopy and SSNMR evidenced the structural changes above x = 0.15 composition which can correlate with the microstructure and properties of the BNT–BKT solid solution. From the studies, it is concluded that the structural phase transition starts around x = 0.15, the MPB region corresponds to $0.15 \leq x \leq 0.24$ as evidenced from solid state NMR studies and better

performance parameters are obtained in the MPB region of the (1-x)BNT-xBKT solid solution series.

Chapter 4

Studies on (1-*x*)$Bi_{0.5}Na_{0.5}TiO_3$–*x*$Bi_{0.5}Li_{0.5}TiO_3$ Series

4.1. Introduction

Several studies have been reported in the literature on the modifications of $Bi_{0.5}Na_{0.5}TiO_3$ (BNT) in order to improve its piezoelectric properties. Most of these studies are centered on the substitution of A or B site of the ABO_3 perovskite lattice by other metal ions of comparable size, ionic character etc. There are few studies reported in the literature on the substitution of Na^+ by Li^+ in BNT. Lu *et al* synthesized $Bi_{0.5}(Na_{1-x}Li_x)_{0.5}TiO_3$ solid solution series by the ceramic method and observed that the compositions in the range $0 \leq x \leq 0.20$ have perovskite structure with rhombohedral symmetry.[113] The maximum piezoelectric constant d_{33} and planar electromechanical coupling factor K_p are obtained as 110 pC/N and 0.18 at $x = 0.15$, respectively. The unsubstituted BNT has lower piezoelectric coupling constant d_{33} (80pC/N) and planar electromechanical coupling factor K_p (0.14). The mechanical quality factor Q_m was found to decrease with increasing Li^+ content. Said and Maaoui investigated the relaxor behavior of $Bi_{0.5}(Na_{1-x}Li_x)_{0.5}TiO_3$ solid solution series.[114] The ceramics showed relaxor type behavior, with diffuse phase transition and high Curie temperature, for low Li^+ substitution in the range $0 \leq x \leq 0.20$. The variation of permittivity with temperature is found to follow the equation $\frac{1}{\varepsilon} - \frac{1}{\varepsilon_m} = C(T - T_m)^\gamma$ where γ is close to 1.5. The authors explained the relaxor behavior as due to the cation disorder in the A site. Lin *et al* studied Li and K co-substituted $Bi_{0.5}(Na_{1-x-y}K_yLi_x)_{0.5}TiO_3$ solid solution series and observed that small amount of Li^+ substitution improved the sintering condition and the piezoelectric properties.[115] The properties of Li^+ and K^+ co-substituted BNT solid solution series have also been studied by other researchers.[116-118]

There are only few reports in the literature on the $Bi_{0.5}(Na_{1-x}Li_x)_{0.5}TiO_3$ or (1-x)$Bi_{0.5}Na_{0.5}TiO_3$–$xBi_{0.5}Li_{0.5}TiO_3$ (BNT–BLT) solid solution series. Detailed structural characteristics of this solid solution series are not yet reported. Therefore, the objective of the present work is detailed structural characterization using Rietveld analysis of the XRD patterns, Raman spectroscopy and solid state NMR studies and then to correlate dielectric properties with the structural changes. Since the size of Li^+ (0.92 Å) is smaller than Na^+ (1.39 Å) (values for 8–fold coordination)[119] the substitution of Li^+ for Na^+ in BNT may cause structural changes and phase transition. This is investigated by the Rietveld refinement analysis of the XRD patterns[87] of different close compositions in the (1-x)BNT–xBLT series. Similarly, local structural changes

are studied by Raman spectroscopy and solid-state NMR analysis. The solid solutions contain two quadrupolar nuclei, ^{7}Li and ^{23}Na, and probing these two by NMR is expected to give additional information about the local structural changes. The effect of substitution of Li^+ on the dielectric properties, density and microstructure of the solid solution are also examined to find correlation, if any, with the associated structural changes.

4.2. Synthesis

Different compositions in the (1-x)BNT–xBLT solid solution series were prepared by the citrate gel method for x ranging from 0 to 0.20 in steps of 0.02. The compositions and the corresponding sample codes are specified in Table 4.1.

Table 4.1: Compositions in the (1-x)BNT–xBLT series and the corresponding sample codes.

x	**Composition (1-*x*)$Bi_{0.5}Na_{0.5}TiO_3$-*x*$Bi_{0.5}Li_{0.5}TiO_3$, (1-*x*)BNT–*x*BLT**	**Sample code**
0	BNT	BNT
0.02	0.98BNT–0.02BLT	0.02BLT
0.04	0.96BNT–0.04BLT	0.04BLT
0.06	0.94BNT–0.06BLT	0.06BLT
0.08	0.92BNT–0.08BLT	0.08BLT
0.10	0.90BNT–0.10BLT	0.10BLT
0.12	0.88BNT–0.12BLT	0.12BLT
0.14	0.86BNT–0.14BLT	0.14BLT
0.16	0.84BNT–0.16BLT	0.16BLT
0.18	0.82BNT–0.18BLT	0.18BLT
0.20	0.80BNT–0.20BLT	0.20BLT

Solutions of stoichiometric amounts of bismuth nitrate ($Bi(NO_3)_3.5H_2O$), sodium nitrate ($NaNO_3$) and lithium nitrate ($LiNO_3$) were made separately by dissolving bismuth nitrate in dilute nitric acid and the nitrates of sodium and lithium in distilled water. The separate solutions

were then mixed together. Stoichiometric amount of titanium isopropoxide ($Ti[OCH(CH_3)_2]_4$) was dissolved in isopropyl alcohol and citric acid was dissolved in this solution with continuous stirring. The ratio of citric acid to the total metal ion was taken as 3:1. The mixed metal nitrate solution was added to the titanium isopropoxide solution with constant stirring and then evaporated at 60 ^oC on a hot plate until a transparent viscous gel was obtained. The dried gel was kept at 150 ^oC for overnight heating that formed a foam. The foam was crushed using a mortar to obtain fine powder. This powder was initially calcined at 400 ^oC, followed by calcination at 850 ^oC and 1000 ^oC with an intermediate grinding. The powder samples obtained were uniaxially pressed into circular discs (10 mm diameter x 3mm height) at a pressure of 8 MPa and sintered at 1000 ^oC for 2 hours. All the samples were sintered under identical conditions with heating and cooling rates of 5 ^oC/min.

4.3. Powder X-ray diffraction

Crushed sintered pellets of (1-x)BNT–xBLT were used for XRD, Raman spectroscopy and solid-state NMR studies. The powder XRD patterns of all the compositions in the (1-x)BNT–xBLT series are shown in Figure 4.1. The simulated XRD pattern of BNT, using the structural parameters reported for the monoclinic space group Cc,[105] is also shown in the figure for comparison. All the peaks in the XRD patterns of the different compositions match with the simulated pattern of BNT, suggesting the formation of single phase compositions. No additional peaks are detected in the XRD patterns, suggesting the single phase nature of the different compositions.

Rietveld refinement analysis of all the studied compositions of (1-x)BNT–xBLT are carried out using the monoclinic Cc space group. All the compositions gave reasonable good fit with low reduced χ^2 and R_p values. Table 4.2 gives the results obtained from Rietveld refinements of (1-x)BNT–xBLT for $0 \leq x \leq 0.20$. Figures 4.2 and 4.3 show the results of the Rietveld refinement analysis of all the compositions of (1-x)BNT–xBLT.

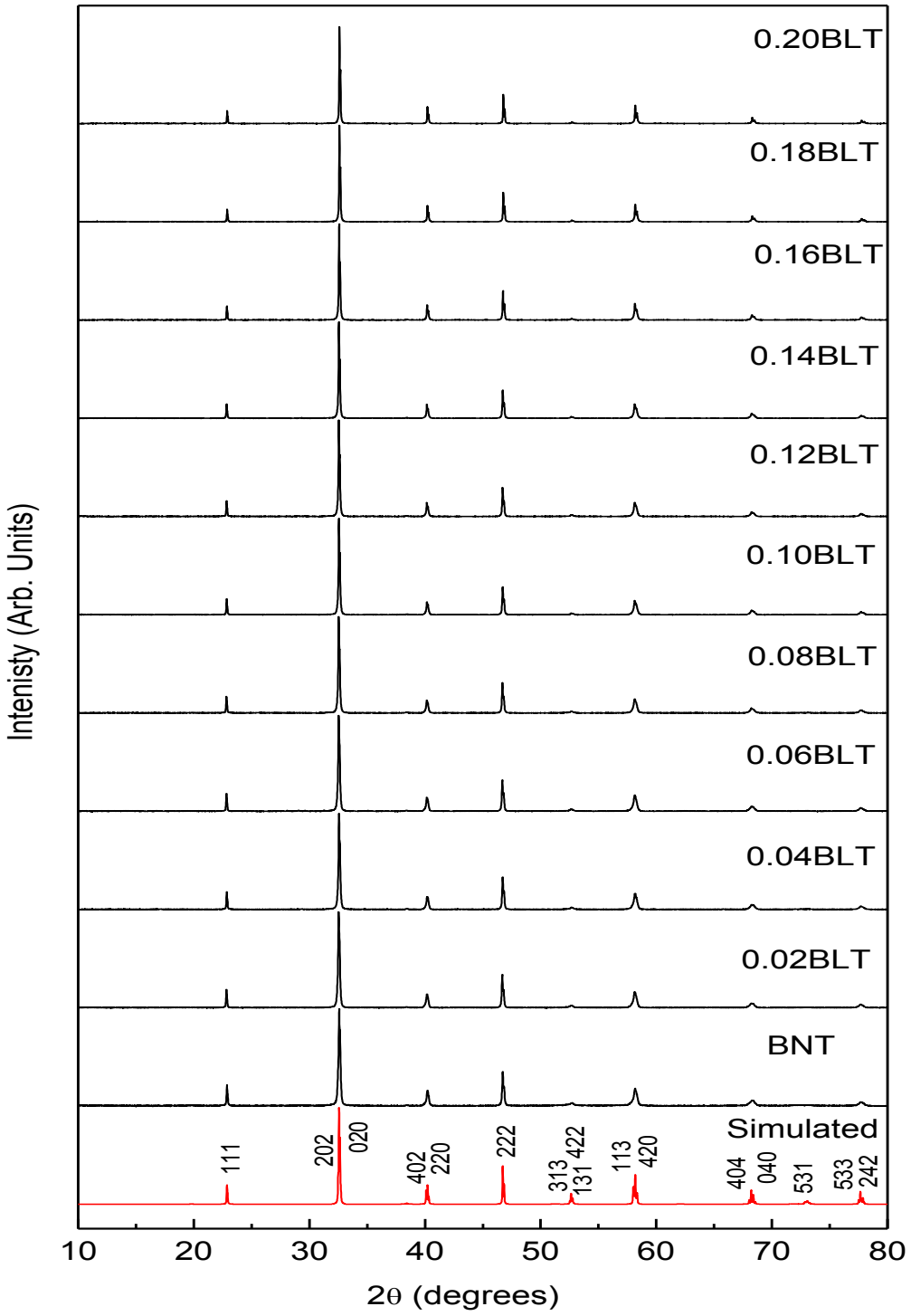

Figure 4.1: Powder XRD patterns of different compositions in the (1-x)BNT–xBLT solid solution series. Simulated pattern of BNT is shown at the bottom for comparison.

Table 4.2: Lattice parameters, reduced χ^2 and R_p values of (1-*x*)BNT–*x*BLT obtained from Rietveld analysis.

Sample	**Cc**				**χ^2**	**R_p (%)**
	a (Å)	**b (Å)**	**c (Å)**	**β (degrees)**		
BNT	9.5263	5.4829	5.5091	125.43	2.065	5.18
0.02BLT	9.5261	5.4832	5.5089	125.42	3.225	5.46
0.04BLT	9.5238	5.483	5.5077	125.40	3.121	5.49
0.06BLT	9.5249	5.4826	5.5064	125.39	3.260	5.65
0.08BLT	9.523	5.4838	5.5056	125.39	3.562	5.79
0.10BLT	9.5197	5.4834	5.503	125.36	3.664	5.91
0.12BLT	9.5159	5.4864	5.4982	125.33	3.679	5.97
0.14BLT	9.5154	5.4887	5.4955	125.32	3.322	5.65
0.16BLT	9.5101	5.4904	5.4911	125.29	3.424	5.69
0.18BLT	9.5081	5.4896	5.4897	125.28	3.789	5.92
0.20BLT	9.508	5.4897	5.4897	125.27	3.858	5.96

Figure 4.4 shows the variation of the lattice parameters with concentration of BLT and the variation of the unit cell volume with BLT concentration is shown in Figure 4.5. On increasing the BLT concentration, the lattice parameters '*a'*, '*c'* and the angle *β* are decreased whereas '*b'* is slightly increased. The ionic size of Li^+ is 0.92 Å and that of Na^+ is 1.39 Å, for 8–fold coordination. When larger Na^+ is replaced by the smaller ion Li^+, the unit cell volume is decreased. The substitution of Li^+ causes contraction of the unit cell, and hence corresponding changes are seen in the lattice parameters. The difference between the lattice parameters '*a*' and '*c*' of the maximum doped (*x* = 0.2) sample compared to that of BNT is approximately 0.02 Å. The difference in the monoclinic angle is around 0.15 degrees. Although the lattice parameter '*b*' showed a small increase, the difference is negligible (~0.006 Å). The small increase in the value of '*b*' could be due to the distortion or tilting of the TiO_6 octahedra on substitution.

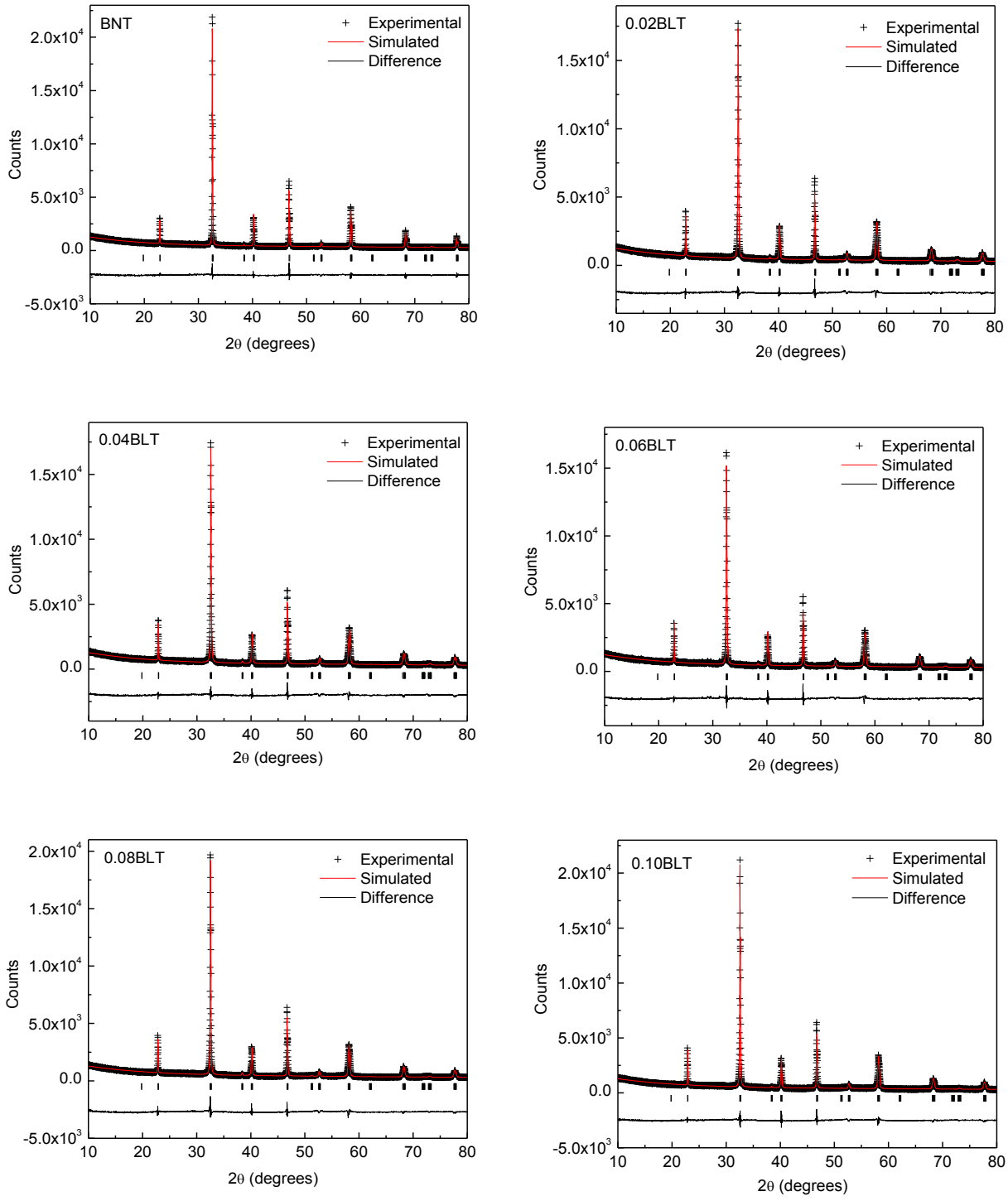

Figure 4.2: Results of the Rietveld refinement analysis of (1-x)BNT–xBLT using the monoclinic Cc space group, for BNT, 0.02BLT, 0.04BLT, 0.06BLT, 0.08BLT, and 0.10BLT.

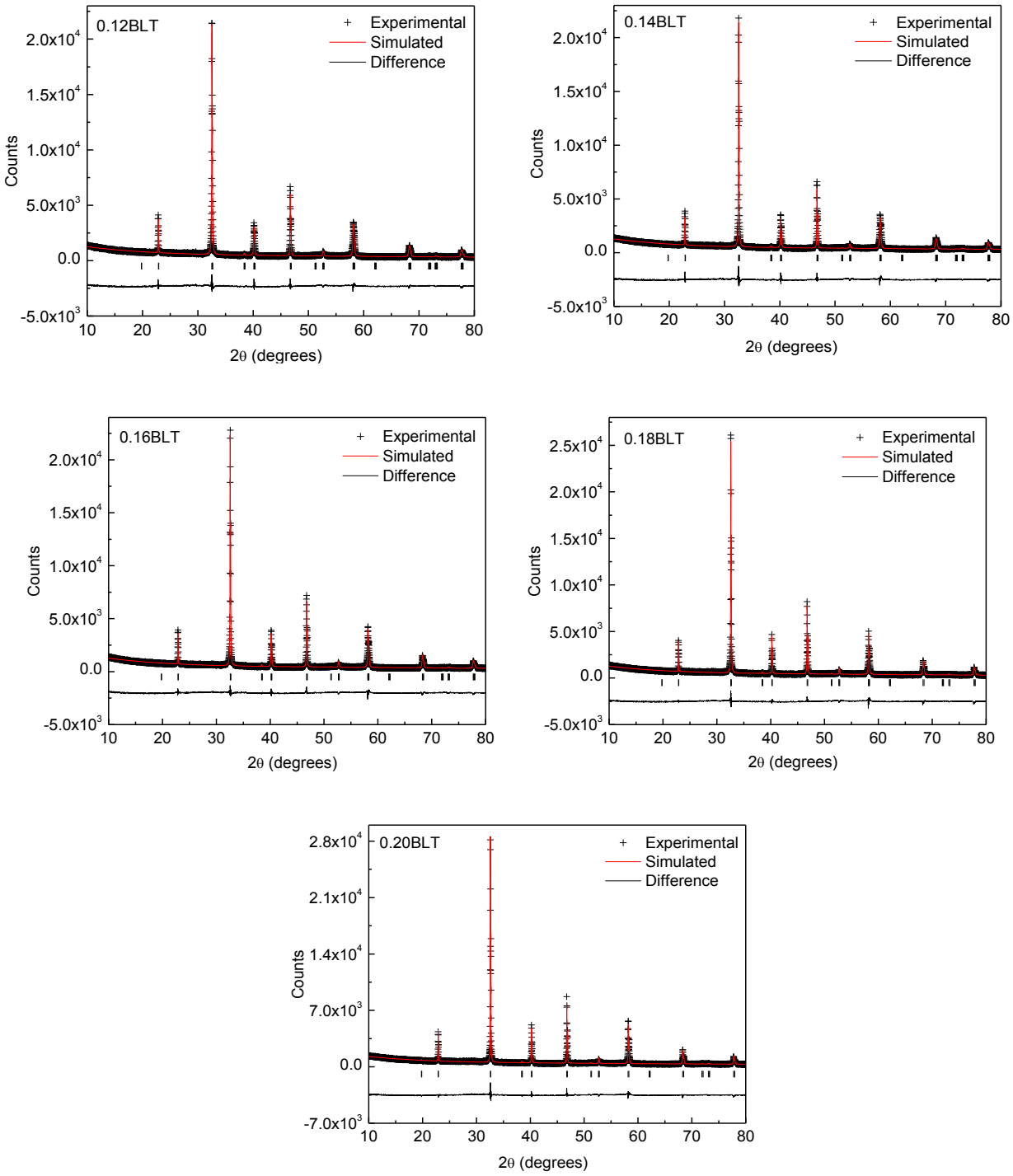

Figure 4.3: Results of the Rietveld refinement analysis of (1-x)BNT–xBLT using the monoclinic Cc space group, for 0.12BLT, 0.14BLT, 0.16BLT, 0.18BLT, and 0.20 BLT.

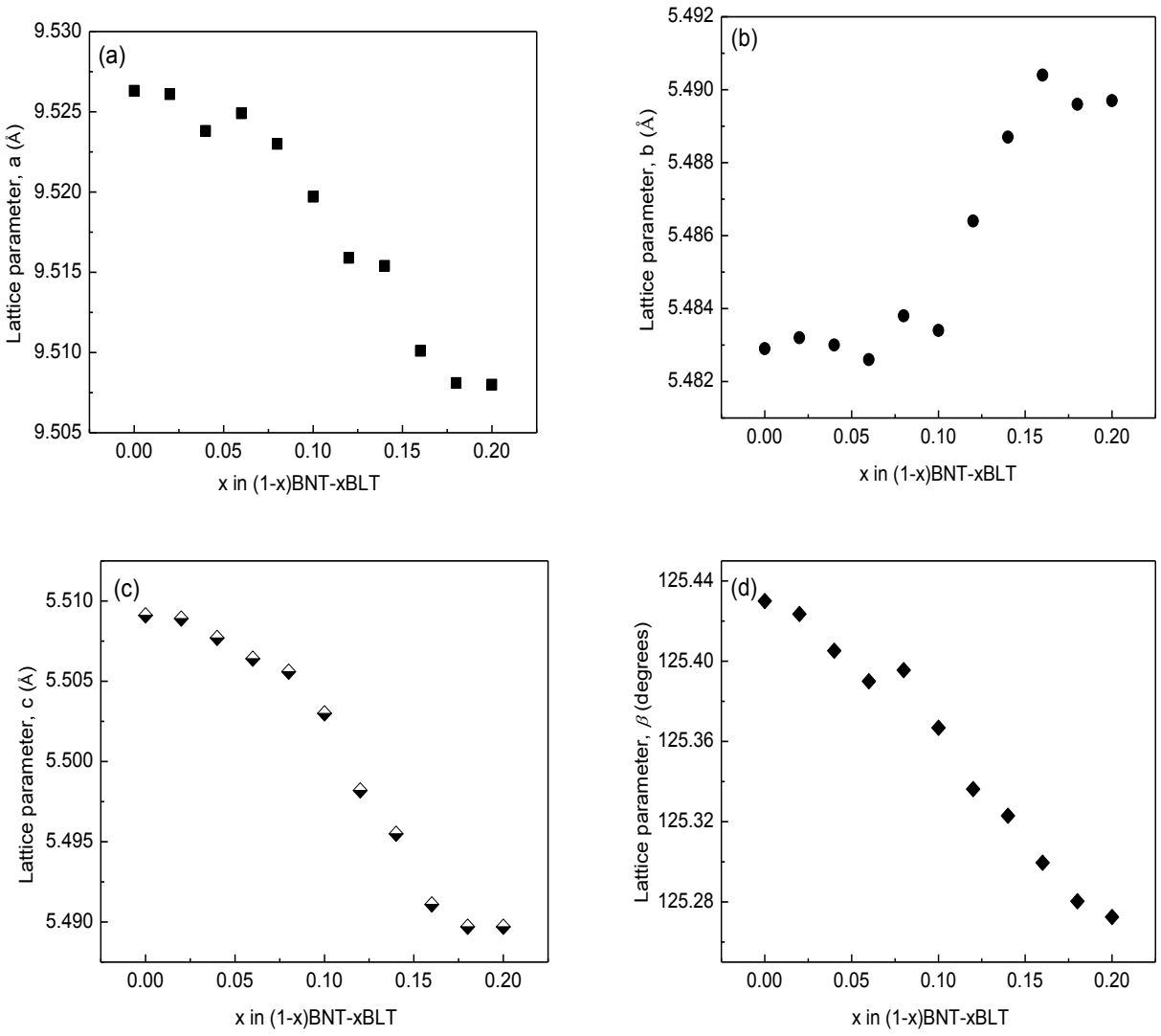

Figure 4.4: Variation of monoclinic lattice parameters (a) '*a'*, (b) '*b'*, (c) '*c'*, and (d) angle β of (1-x)BNT–xBLT solid solution series as a function of x.

It is interesting to note that the rates of decrease of the lattice parameters '*a'* and '*c'* are different above and below $x \approx 0.08$. Similarly, the lattice parameter '*b'* is almost constant till $x \approx 0.1$ and after this concentration, an increase is observed up to $x = 0.16$ and *'b'* becomes almost constant again at higher Li^+ concentrations. Similar changes are observed in the variation of the unit cell volume also. Since the change in the lattice parameters is very small, it may be concluded that there is no structural phase transformation as observed in the case of BNT–BKT. The small change in the variation of lattice parameters around $x \approx 0.1$ may be due to local structural changes, due to the in homogeneous distribution of the substituted Li ions in the lattice for $x < 0.1$. However, onset of a structural phase transition cannot be ruled out in this

compositional region, even though good fits are obtained in the Rietveld refinement analysis, using the monoclinic structure in the entire compositional region studied.

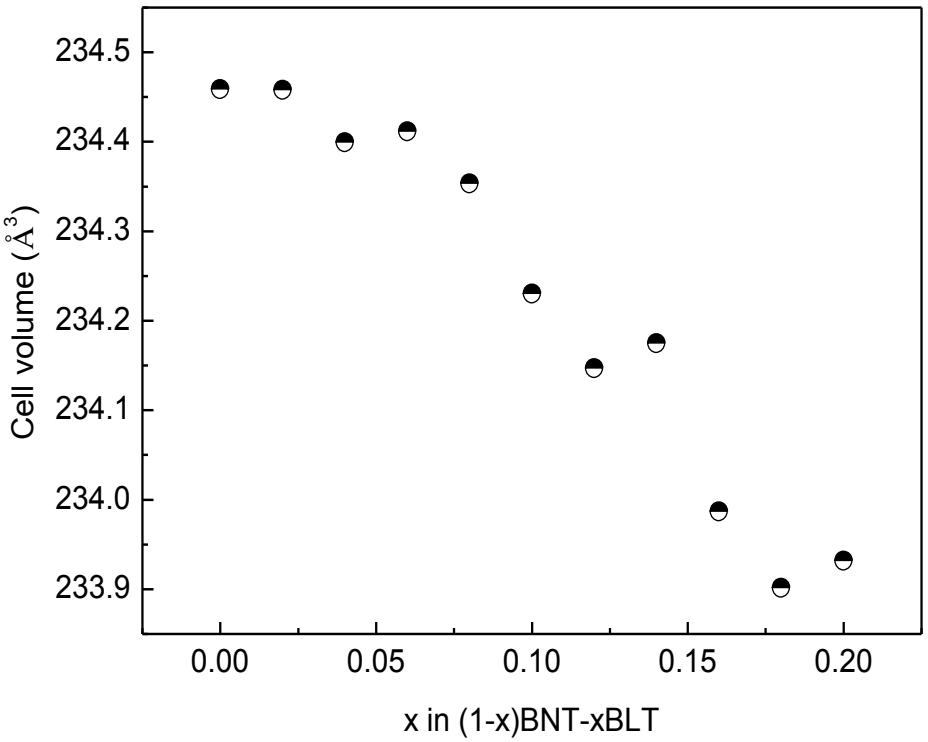

Figure 4.5: Variation of unit cell volume of (1-x)BNT–xBLT solid solution series as a function of x.

4.4. Raman spectroscopy

Structural analysis from XRD studies showed that all the studied compositions in the (1-x)BNT–xBLT series form under the monoclinic Cc space group. Also, no structural phase transformation is observed in the studied compositional range. Figure 4.6 shows the Raman spectra of different compositions of the (1-x)BNT–xBLT series. As observed in the case of the BNT–BKT series (Figure 3.7), the Raman spectra of the BNT–BLT solid solution consist of three different regions. The band below 200 cm^{-1} is due to A-O vibrations in the perovskite lattice, and in the present case it is due to Bi-O, Na-O and Li-O vibrations. The band in the 200–400 cm^{-1} region in the spectra belongs to the B-O (Ti-O) vibrations and the band in the 400–800 cm^{-1} region belongs to the vibration of the TiO_6 octahedra. As observed from the structural studies of BNT–BLT solid solution, the substitution of smaller Li^+ ion in the BNT lattice causes contraction of the unit cell volume and structural distortions. Hence, corresponding changes are expected in the Raman

spectra of BNT–BLT solid solutions. The immediate observation from the Raman spectra is the decrease in the area and the downward frequency shift of the peak centered at 135 cm^{-1}. In the BNT–BKT solid solution series, an additional band is observed in the 200–400 cm^{-1} region (Figure 3.7) which gave clear indication about the symmetry changes and phase transition. Such very prominent changes are not observed in the 200–400 cm^{-1} and 400–800 cm^{-1} region in the Raman spectra of the BNT–BLT solid solutions. Detailed analysis of the Raman spectra is carried out by the deconvolution of each spectrum and the changes in the parameters are studied**.** The Raman spectrum of BNT in the present work is almost the same as to that reported in the previous chapter on the BNT–BKT series (Figure 3.7), even though the compound is prepared by a different method in the present work.

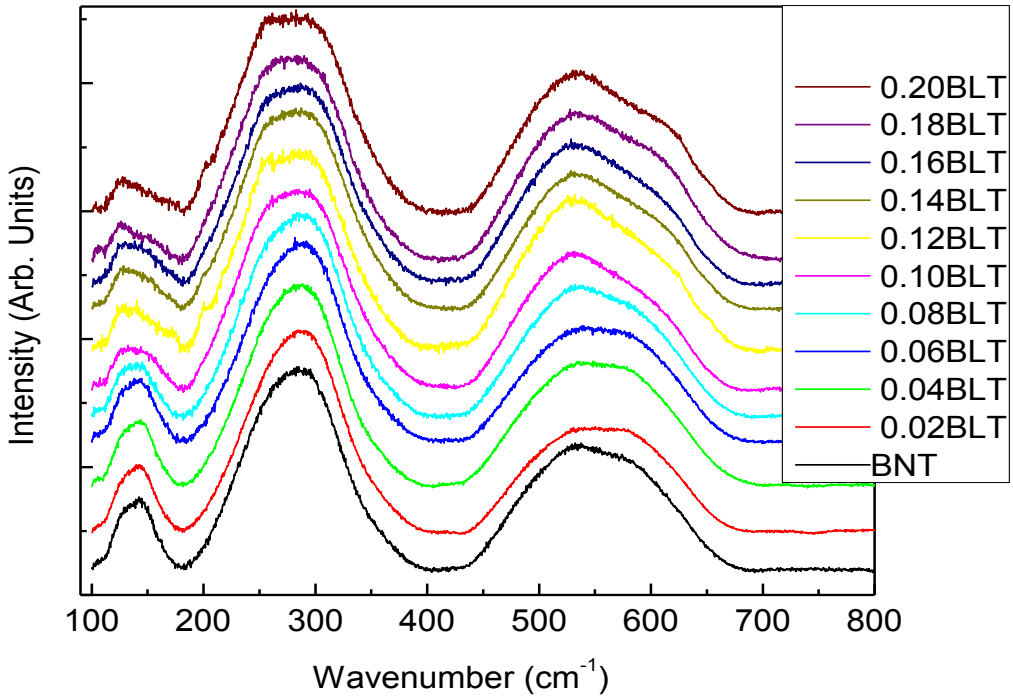

Figure 4.6: Raman spectra of different compositions of (1-x)BNT–xBLT for $0 \le x \le 0.20$ ($\Delta x = 0.02$).

Raman spectra of the different BNT–BLT compositions are deconvoluted in to seven Gaussian peaks. The band due to A-O vibrations contains only one peak. The broad bands in the 200–400 $cm^{-1}$and 400–800 cm^{-1} regions are deconvoluted in to three peaks each. Figure 4.7 and 4.8 shows the deconvoluted Raman spectra of all the compositions of BNT–BLT solids solution series.

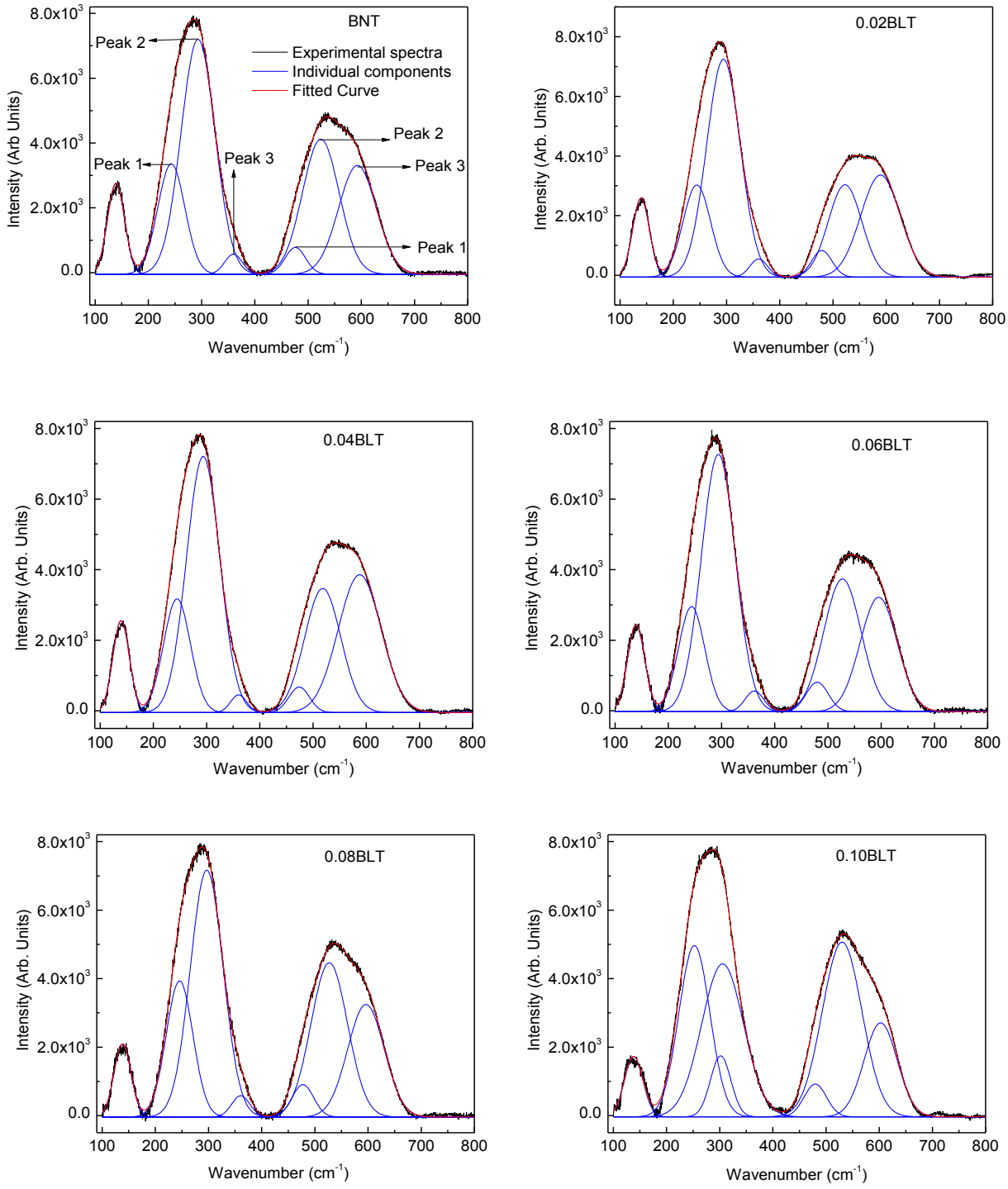

Figure 4.7: Deconvoluted Raman spectra of BNT, 0.02BLT, 0.04BLT, 0.06BLT, 0.08BLT and 0.10BLT in (1-x)BNT–xBLT. The black, red and blue curves correspond to experimental spectra, fitted curves and the individual components, respectively.

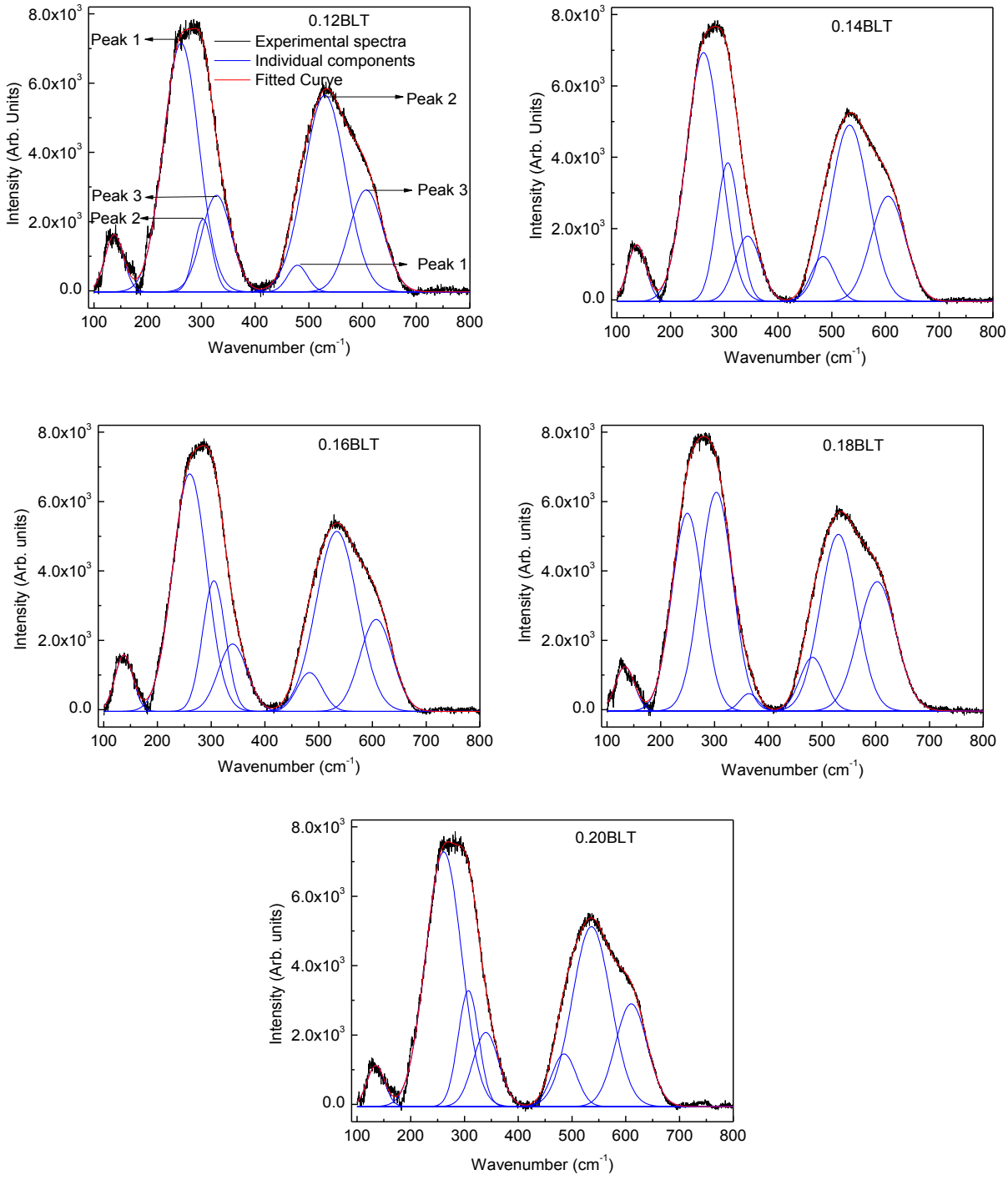

Figure 4.8: Deconvoluted Raman spectra of 0.12BLT, 0.14BLT, 0.16BLT, 0.18BLT, and 0.20BLT in (1-x)BNT–xBLT. The black, red and blue curves correspond to experimental spectra, fitted curves and the individual components, respectively.

Figure 4.9 shows the variations in the peak position and area of the band below 200 cm^{-1}. A low frequency shift is observed in the A-O band of the BNT–BLT solid solution with Li^+ substitution. There is a small shift in the position of the band up to $x \approx 0.1$ and a large decrease above this composition. However, the area under the peak decreases almost linearly. The low frequency shift may be due to the diffusion of small Li^+ ions in the crystal lattice which will weaken the Li-O bond strength and results in some local symmetry changes.

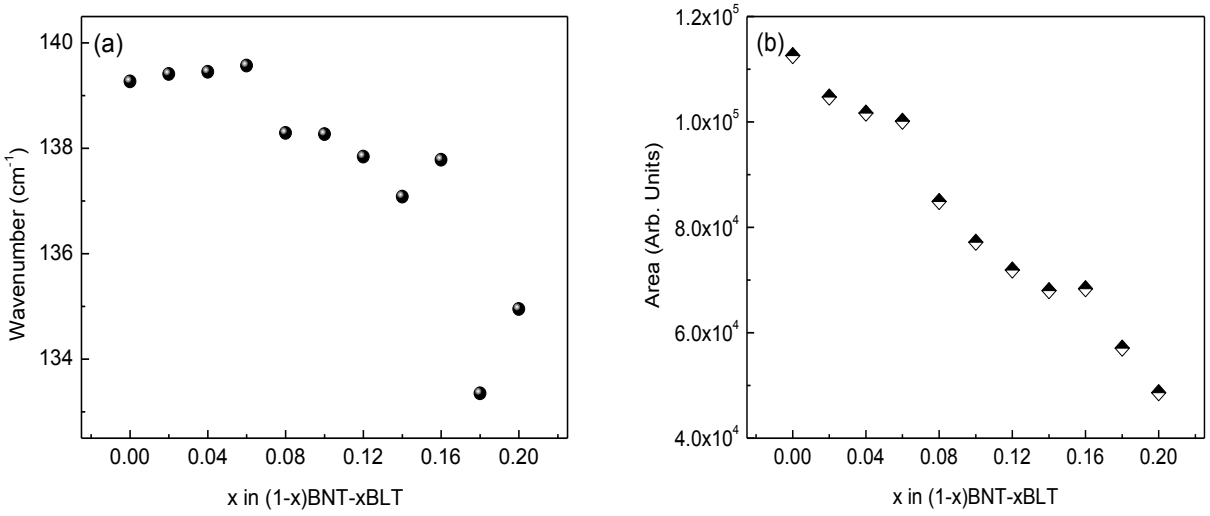

Figure 4.9: Changes in the (a) peak position and (b) area under the peak of the band below 200 cm^{-1} in the Raman spectra as a function of x in (1-x)BNT–xBLT.

The Raman band in the 200–400 cm^{-1} region is due to the Ti-O vibrations. Figure 4.10 shows the variation of the position of the individual peaks in this region with concentration of BLT. On increasing the BLT concentration, the first two components show upward frequency shift whereas the third component shows a different trend. For the first two peaks within this band, the positions of the peaks remain almost the same for $x < 0.08$ and $x > 0.12$, with a drastic increase between $x = 0.08$ and 0.12. Similar changes are observed in the case of the third peak, except for a large drop for $0.08 \leq x \leq 0.12$. Figure 4.11 shows the changes in total area and area of the individual peaks of the band in the 200–400 cm^{-1} region. The area under the peaks also show a major change between $x = 0.08$ and $x = 0.12$ as in the case of the changes in the peak positions. Since XRD studies did not show any evidence for a structural phase transition, the changes in the peak positions and area under the peaks suggest a probable local structural change in this compositional region.

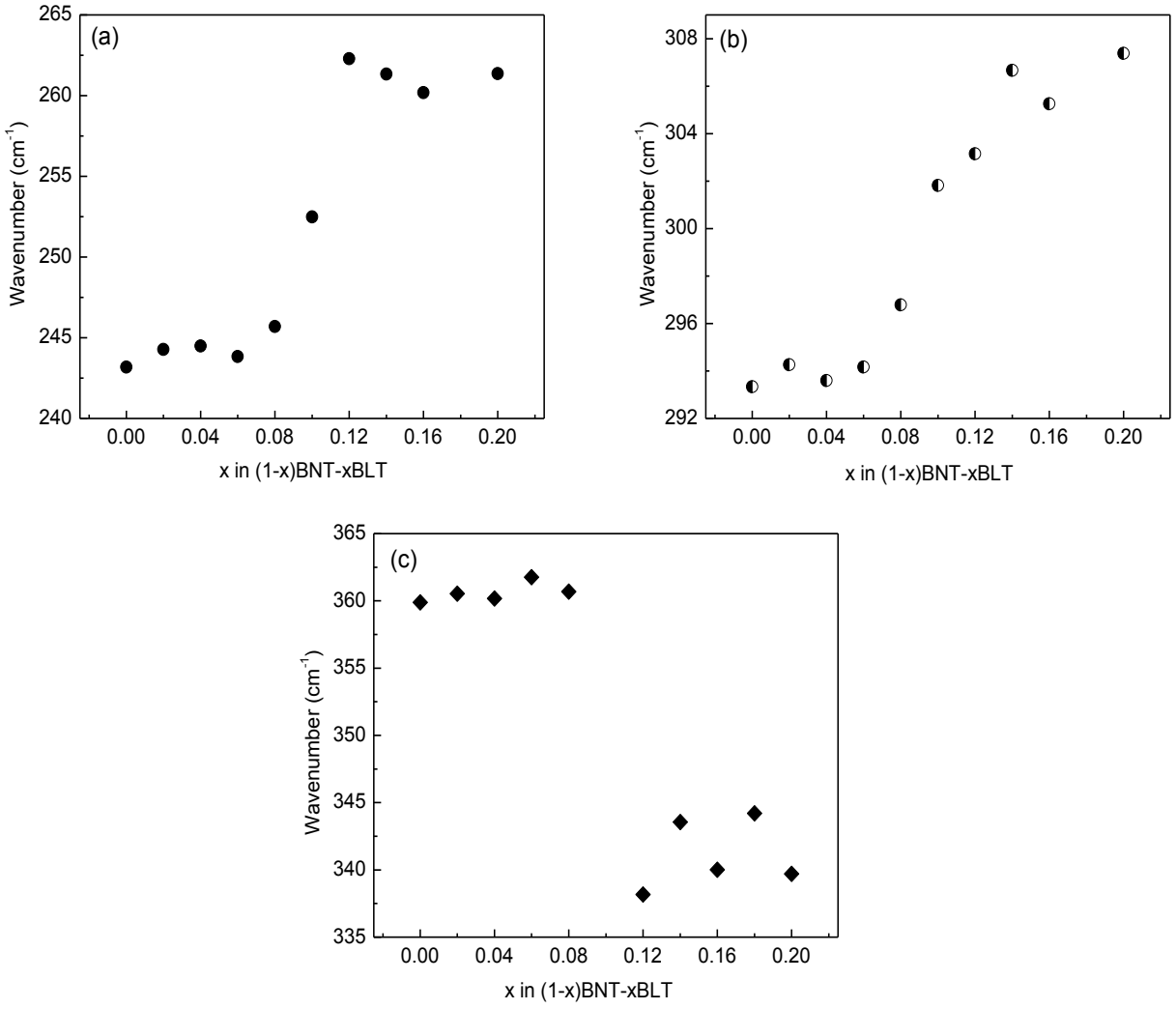

Figure 4.10: Changes in the individual peak positions of the Raman band in the 200–400 cm^{-1}region as a function of x in (1-x)BNT–xBLT. (a) 1st peak, (b) 2nd peak, (c) 3rd peak.

Figure 4.12 shows the variation in the positions of the individual peaks of the Raman band in the 400–800 cm^{-1} region. This band belongs to the vibration of the TiO_6 octahedra. A linear increase in the position of the individual peaks is observed on increasing the BLT concentration. Figure 4.13 shows the changes in total area of the band in the 400–800 cm^{-1} region and the area of the individual peaks under this band. Total area and the area under the first two peaks increase with increasing BLT concentration whereas the area of the third peak decreases with BLT concentration. The total area increases almost linearly with increasing BLT concentration, whereas the changes in the area of the individual peaks show different trends below and above $x = 0.08$.

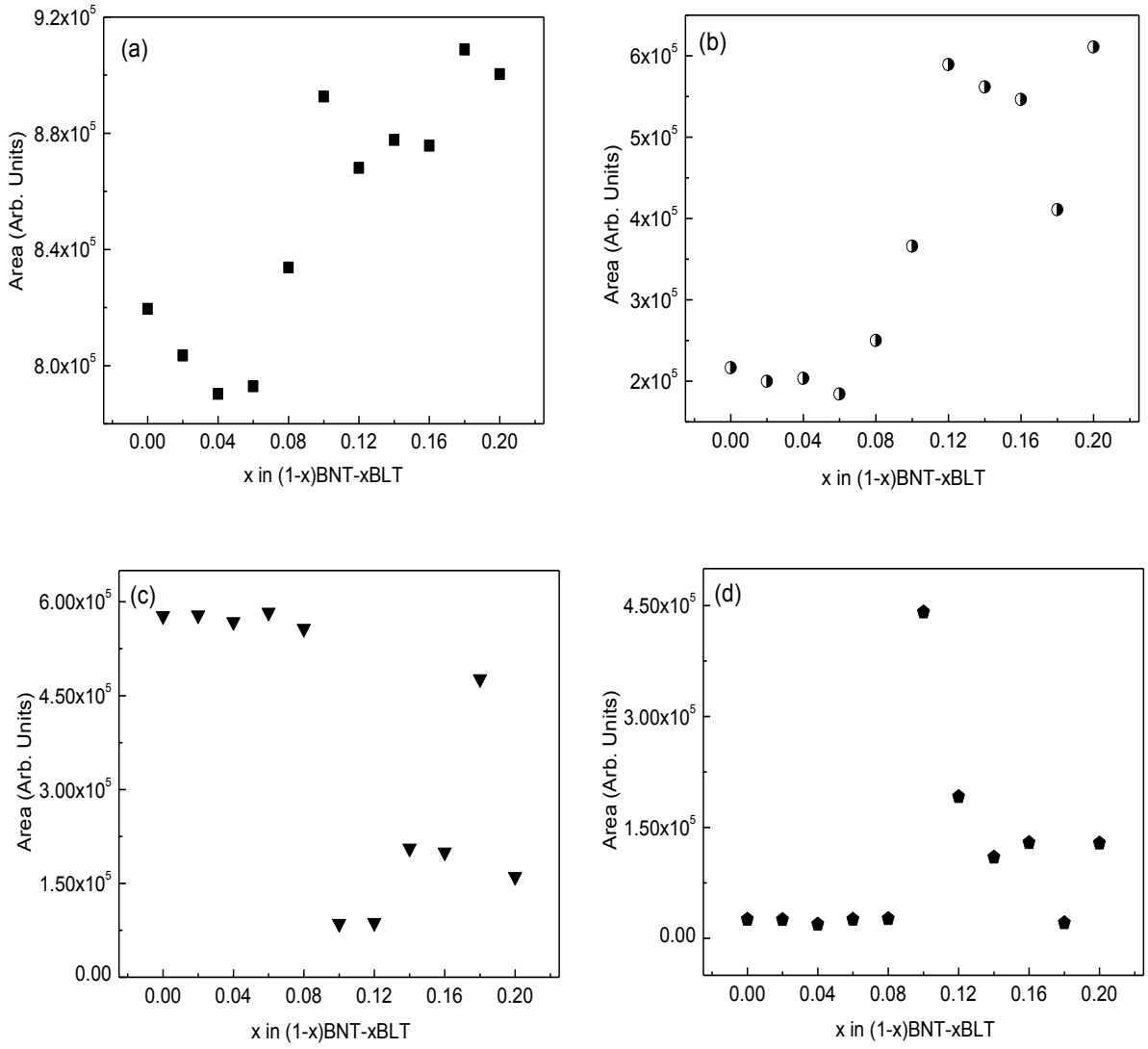

Figure 4.11: Total area and area under the individual peaks of the Raman band in the 200–400 cm^{-1} region as a function of x in (1-x)BNT–xBLT., (a) total area, (b) area under the 1st peak, (c) area under the 2nd peak, (d) area under the 3rd peak.

The area of peak 1 is independent of x for $x < 0.08$ and then increases, area of peak 2 increases up to $x = 0.8$ and then remains almost constant, area of peak 3 decreases up to $x = 0.08$ and then remains almost constant. These changes suggest some associated changes in the distortion of the TiO_6 octahedra with substitution of Li^+ for Na^+. On the other hand, drastic changes are observed for the peak positions and areas for the band in the 200–400 cm^{-1} region, indicating minor changes in the Ti-O bond length and not much distortion in the TiO_6 octahedra. Hence it may be concluded that the effect of substitution of Li^+ for Na^+ in the A site of the BNT

lattice is reflected on the changes in the Ti-O bonds. Hence, corresponding changes in the polarization is expected which may lead to minor variations in the dielectric constant.

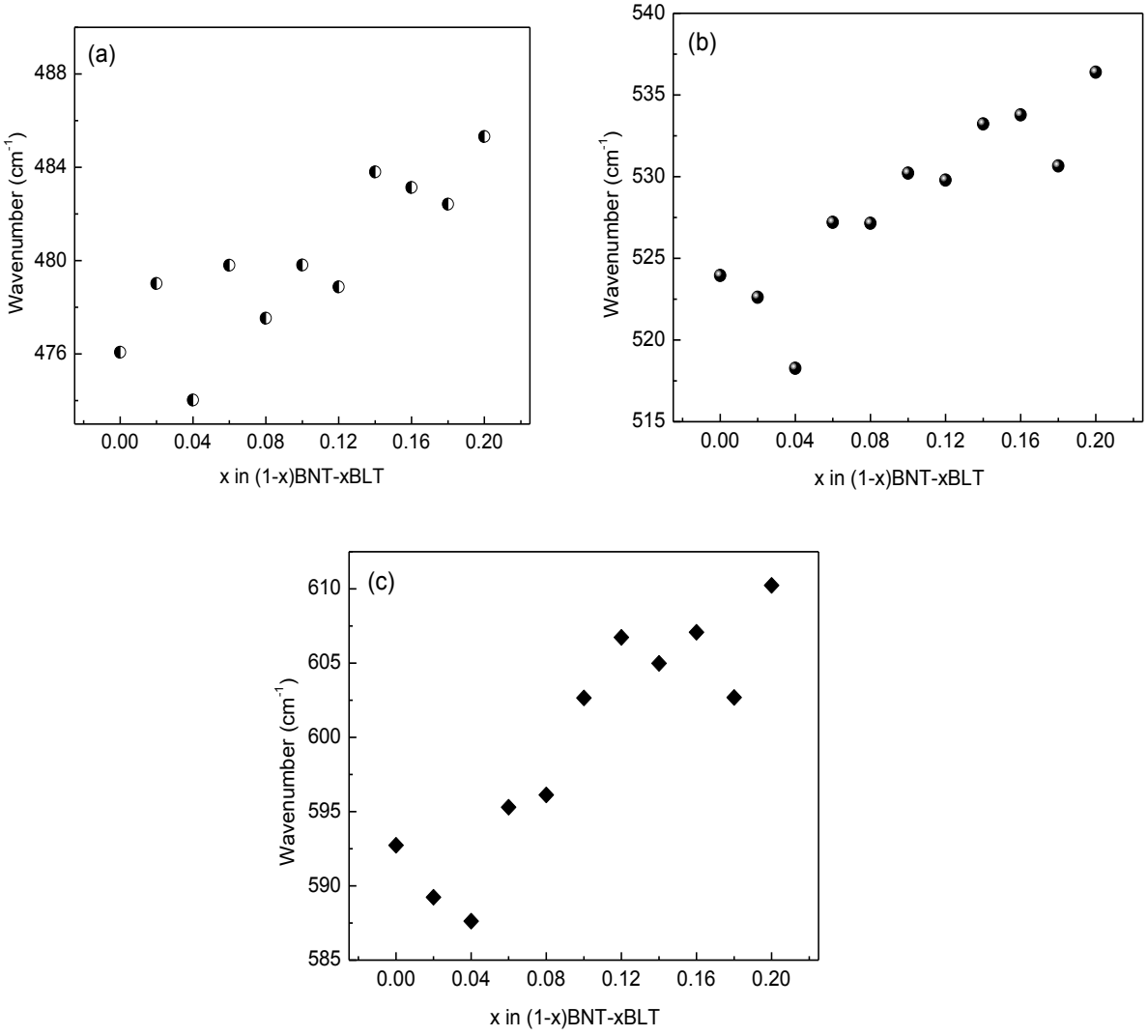

Figure 4.12: Changes in the individual peak positions of the Raman band in the 400–800 cm^{-1}region as a function of x in (1-x)BNT–xBLT.(a) 1st peak, (b) 2nd peak, (c) 3rd peak.

Thus, the Raman spectroscopic studies give crucial information on the changes in the Ti-O bond lengths and the TiO_6 octahedra on the substitution of Li for Na in BNT. Results from the XRD studies suggested minor structural changes above x = 0.08 in (1-x)BNT-xBKT and the Raman studies suggest that this is due to the minor changes in the coordination environment at the A- and B-sites in the perovskite lattice.

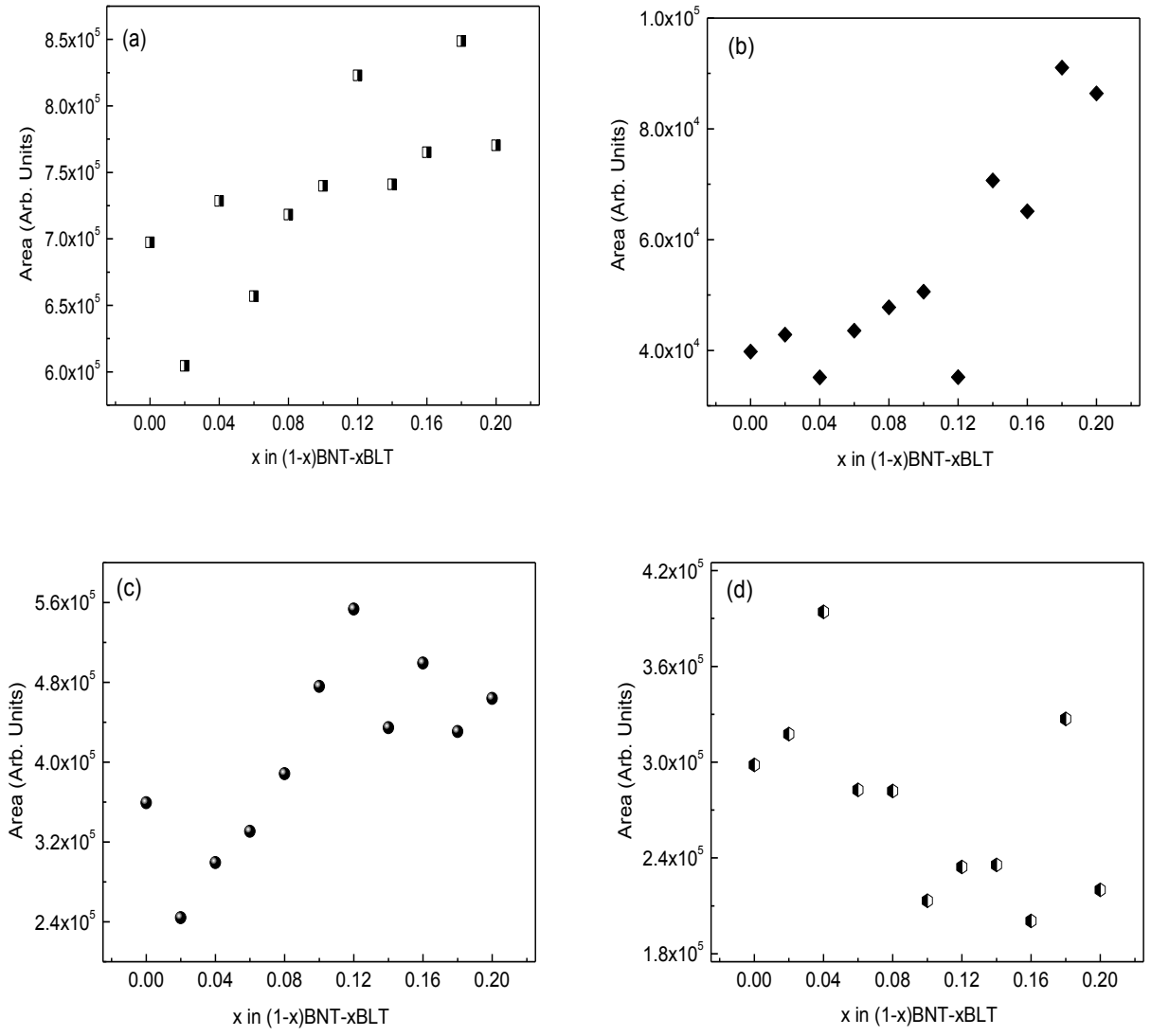

Figure 4.13: Total area and area under the individual peaks of the Raman band in the 400–800 cm^{-1} region as a function of x in (1-x)BNT-xBLT, (a) total area, (b) area under the 1st peak, (c) area under the 2nd peak, and (d) area under the 3rd peak.

4.5. Solid-state NMR spectroscopy

4.5.1. ^{23}Na NMR

Solid state NMR spectroscopy studies have been carried out to obtain more details on the local structural changes on the substitution of Na^+ by Li^+ in BNT. ^{23}Na MAS and ^{7}Li MAS NMR spectra are recorded for all the compositions of (1-x)BNT–xBLT. Figure 4.14 (a) shows the ^{23}Na MAS spectra and Figure 4.14 (b) shows the zoomed view of the central transition. A gradual increase in the broadening of the ^{23}Na MAS spectra, along with a minor shift in the peak

position, is observed with increasing BLT concentration. This broadening is likely to be due to the local symmetry change and/or distortion of the NaO_x polyhedra on substitution of the smaller Li^+ ion for the larger Na^+ ion in the BNT lattice.

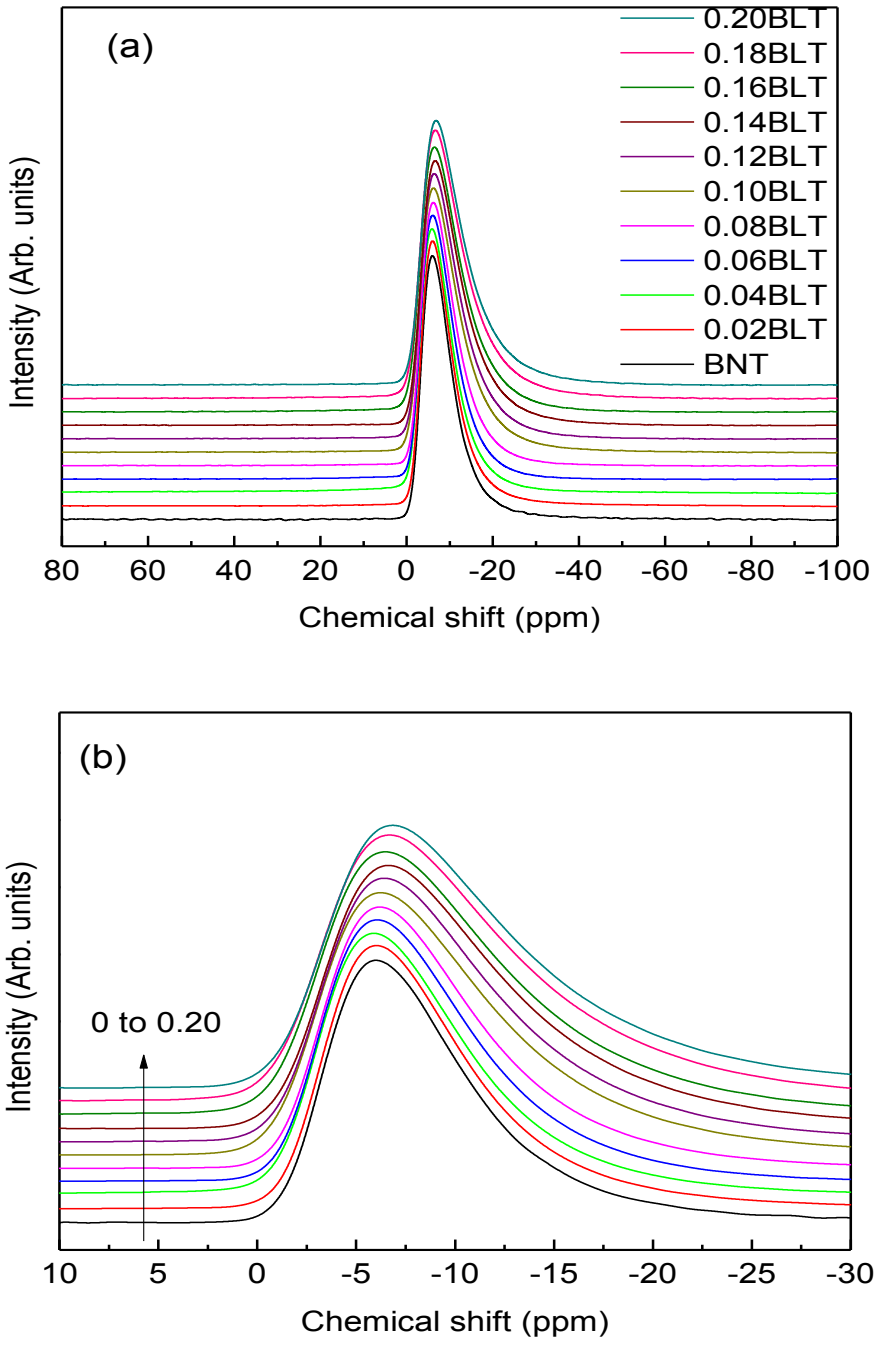

Figure 4.14: (a) ^{23}Na NMR spectra of the different compositions in the (1-x)BNT–xBLT series, (b) Zoomed view of the central region. Spectra are shown for $\Delta x = 0.02$.

Table 4.3: Parameters extracted from the ^{23}Na MAS NMR spectra.

Sample	δ_{iso} (ppm)	C_Q^* (kHz)	Δ_{CS}(ppm)
BNT	-3.21	1004	3.93
0.02BLT	-3.21	1008	3.99
0.04BLT	-3.10	1007	4.09
0.06BLT	-3.06	1038	4.31
0.08BLT	-3.08	1067	4.22
0.10BLT	-2.83	1144	4.40
0.12BLT	-3.00	1144	4.44
0.14BLT	-3.05	1175	4.46
0.16BLT	-2.89	1174	4.54
0.18BLT	-2.94	1207	4.47
0.20BLT	-3.11	1212	4.64

The NMR parameters are extracted by fitting the experimental spectra using the DMFIT program,[90] as discussed in the previous chapter (section 3.5). The line shape of the ^{23}Na MAS spectra show that it has a distribution of quadrupolar coupling constant and therefore the 'Czjzek' model in the DMFIT program, which is described in section 3.5 was used. The experimental spectra and the simulated spectra for selected compositions of (1-x)BNT–xBLT are shown in Figure 4.15 and it can be seen that both experimental and simulated spectra are matching very well. The NMR parameters obtained using the DMFIT program for all the compositions of BNT–BLT solid solution are shown in Table 4.3.

Figure 4.16 shows the variation of ^{23}Na C_Q^* of (1-x)BNT–xBLT with BLT concentration. It can be seen that the quadrupolar coupling has increased with increasing BLT concentration. As discussed in chapter 3, in the BNT–BKT solid solution series, C_Q^* decreased to a minimum at x = 0.15 and then increased to a maximum in the range $0.20 \leq x \leq 0.26$ (section 3.5, Figure 3.17). From XRD studies, an MPB region was observed in the BNT–BKT series (Section 3.3). On the other hand, in the present case of BNT–BLT series, C_Q^* is almost independent of x up to x = 0.04 and then increases almost linearly for $x > 0.04$. C_Q^* is related to the local symmetry of a material

and systems which have high C_Q^* are less symmetric.[91] Hence, in the case of BNT–BLT series, increasing C_Q^* suggests decreasing symmetry of the lattice with increasing BLT concentration. The substitution of the larger Na^+ ion with the smaller Li^+ ion in the BNT lattice causes distortion in the symmetry and the distortion increases as the concentration of Li^+ is increased.

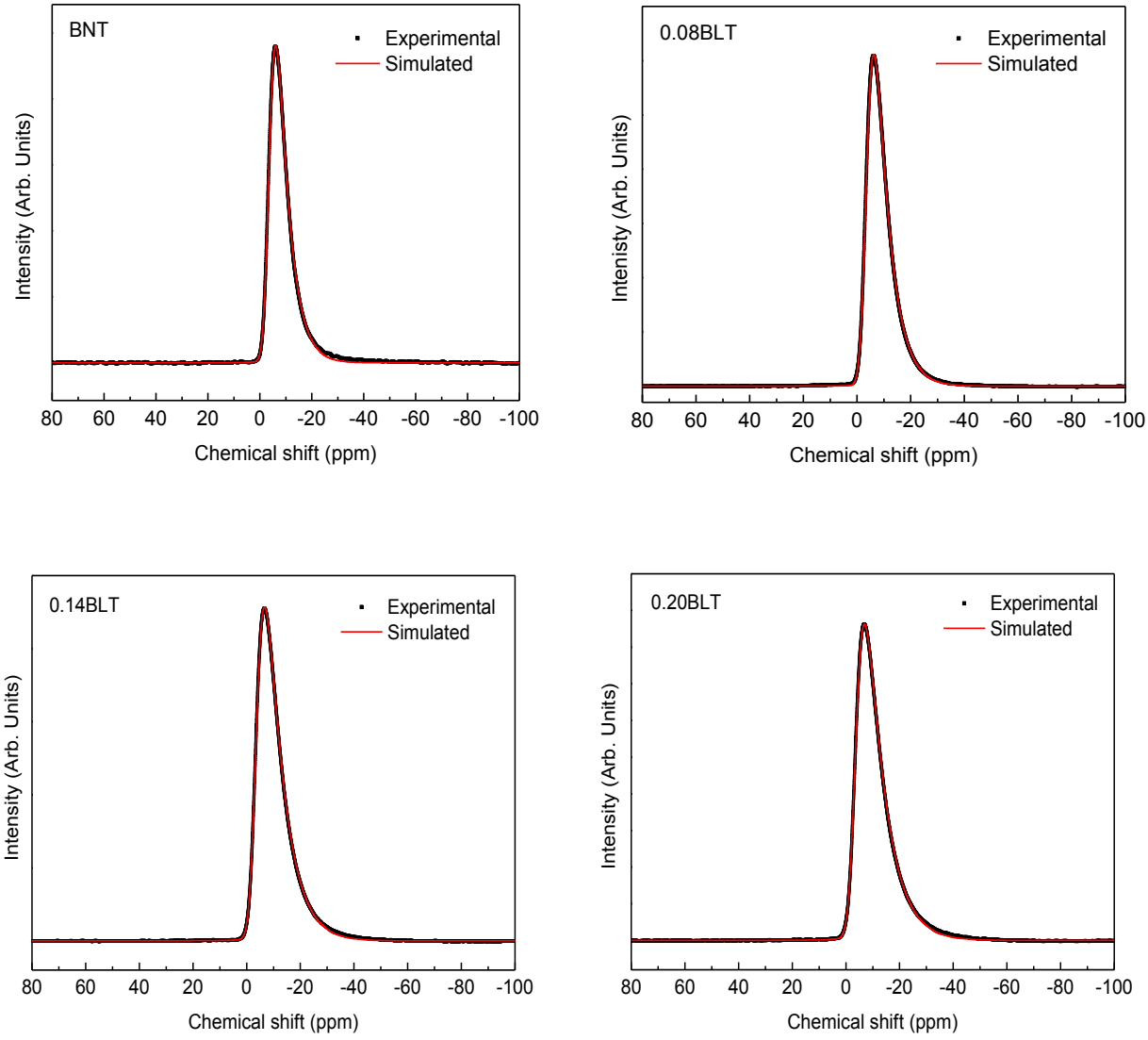

Figure 4.15: Comparison of the experimental and simulated ^{23}Na MAS NMR spectra of selected compositions (BNT, 0.08BLT, 0.14BLT, 0.20BLT) of the (1-x)BNT–xBLT series.

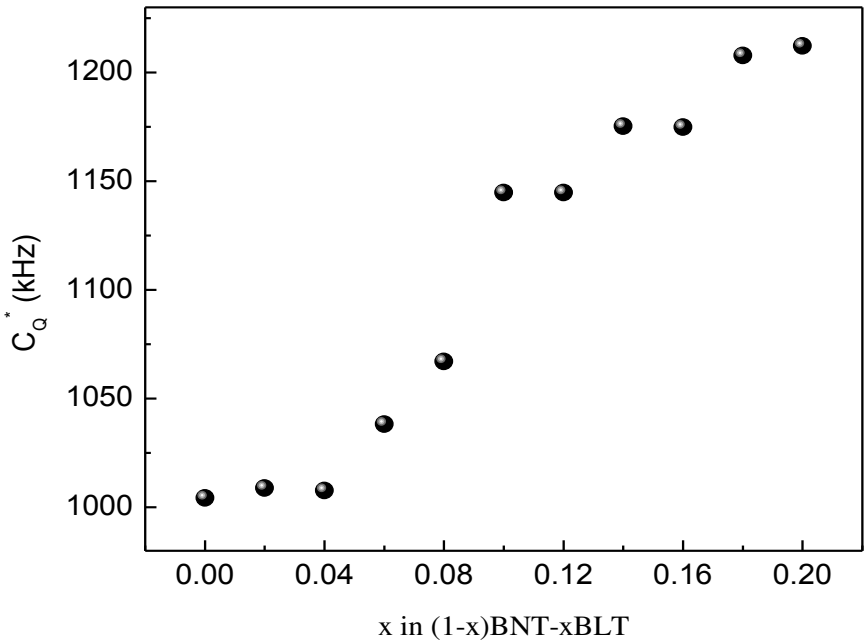

Figure 4.16: Variation of ^{23}Na C_Q^* of (1-x)BNT–xBLT series as a function of x.

4.5.2. ^{7}Li NMR

^{7}Li MAS NMR spectra including the spinning side band profile of all the compositions of BNT–BLT solid solution are shown in Figure 4.17 (a) and Figure 4.17 (b) shows the zoomed view of the central transition. From the full spectra in Figure 4.17 (a), it can be seen that as the BLT concentration increases the side bands become prominent which is due to an increase in the quadrupolar coupling constant. This is because the sidebands originate from the satellite transitions (±1/2 - ±3/2) and the center line from the central transition (+1/2 - -1/2).[91] When the quadrupolar coupling constant increases, the central transition is not very much affected and it is the satellite transition that gets broadened which reflects in the increase in the spread and intensity of the spinning sidebands. Therefore, in a powder sample, when the quadrupolar coupling is very small, there will be less number of sidebands since spreads of the satellite transitions is less. The ^{7}Li NMR parameters are extracted from the spectra using the DMFIT program.

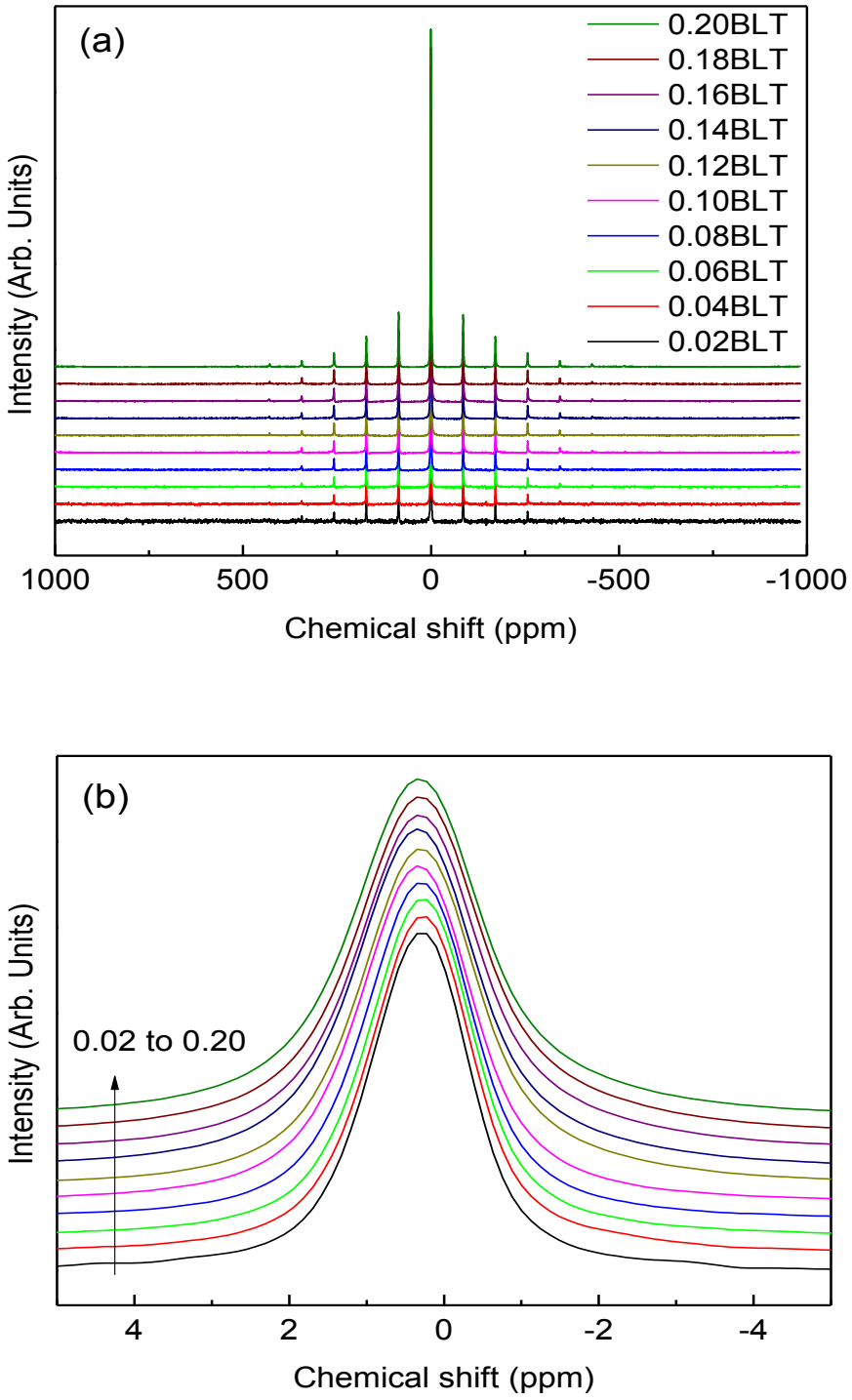

Figure 4.17: (a) ^{7}Li NMR spectra of the different compositions in the (1-x)BNT–xBLT series, (b) Zoomed view of the central region. Spectra are shown for Δx=0.02.

Table 4.4: Parameters extracted from the ^{7}Li MAS NMR spectra and G/L is the ratio of the Gaussian/Lorentzian components.

Sample	δ_{iso} (ppm)	Width (ppm)	G/L	C_Q (kHz)
0.02BLT	0.29	1.53	0.46	47.03
0.04BLT	0.30	1.59	0.46	48.03
0.06BLT	0.31	1.61	0.43	48.28
0.08BLT	0.33	1.67	0.42	48.80
0.10BLT	0.36	1.75	0.39	48.80
0.12BLT	0.31	1.82	0.33	49.80
0.14BLT	0.35	1.87	0.31	50.47
0.16BLT	0.31	1.90	0.28	50.68
0.18BLT	0.30	1.95	0.28	51.18
0.20BLT	0.34	1.97	0.27	51.35

Since the quadrupolar coupling constant of ^{7}Li is small, which is evident from the sharp lines observed from the spectra a model which includes only the first order quadrupolar interaction, the 'quad first' model in the DMFIT program, is used for fitting.[90] This model includes a Gaussian distribution of isotropic chemical shift with a mean isotropic shift (δ_{iso}), quadrupolar coupling constant (C_Q) and the Gaussian to Lorentzian ratio (G/L). The experimental and simulated ^{7}Li MAS NMR spectra of selected compositions of (1-x)BNT–xBLT are shown in Figure 4.18. The parameters extracted from the ^{7}Li MAS NMR spectra for all the compositions of BNT–BLT solid solution are listed in Table 4.4. The effect of Li^+ substitution is seen as a small increase in the quadrupolar coupling constant. The variation in C_Q of ^{7}Li spectra with BLT concentration is shown in Figure 4.19. C_Q increases with increasing BLT concentration indicating a decrease in the symmetry environment around Li^+. As observed in the variation of the Raman spectral parameters, a small deviation at x = 0.1 is observed in the C_Q indicating the probable local structural changes around this composition.

The broadening observed in the ^{7}Li spectra is a combination of Gaussian and Lorentzian line shapes and the contribution from each of the components is obtained from the DMFIT program and the Gaussian to Lorentzian ratio (G/L) is tabulated in Table 4.4. It is observed that

on increasing the BLT concentration, the G/L ratio of the ^{7}Li NMR spectra decreases which means that the line shape becomes more Lorentzian. The variations of the Gaussian and Lorentzian components with BLT concentration are shown in Figure 4.20. The Gaussian component in the spectrum indicates the spread of the chemical shift from the ideal value and the Lorentzian component is an indication of the diffusion or mobility of the ions present in the crystal lattice.[120,121]

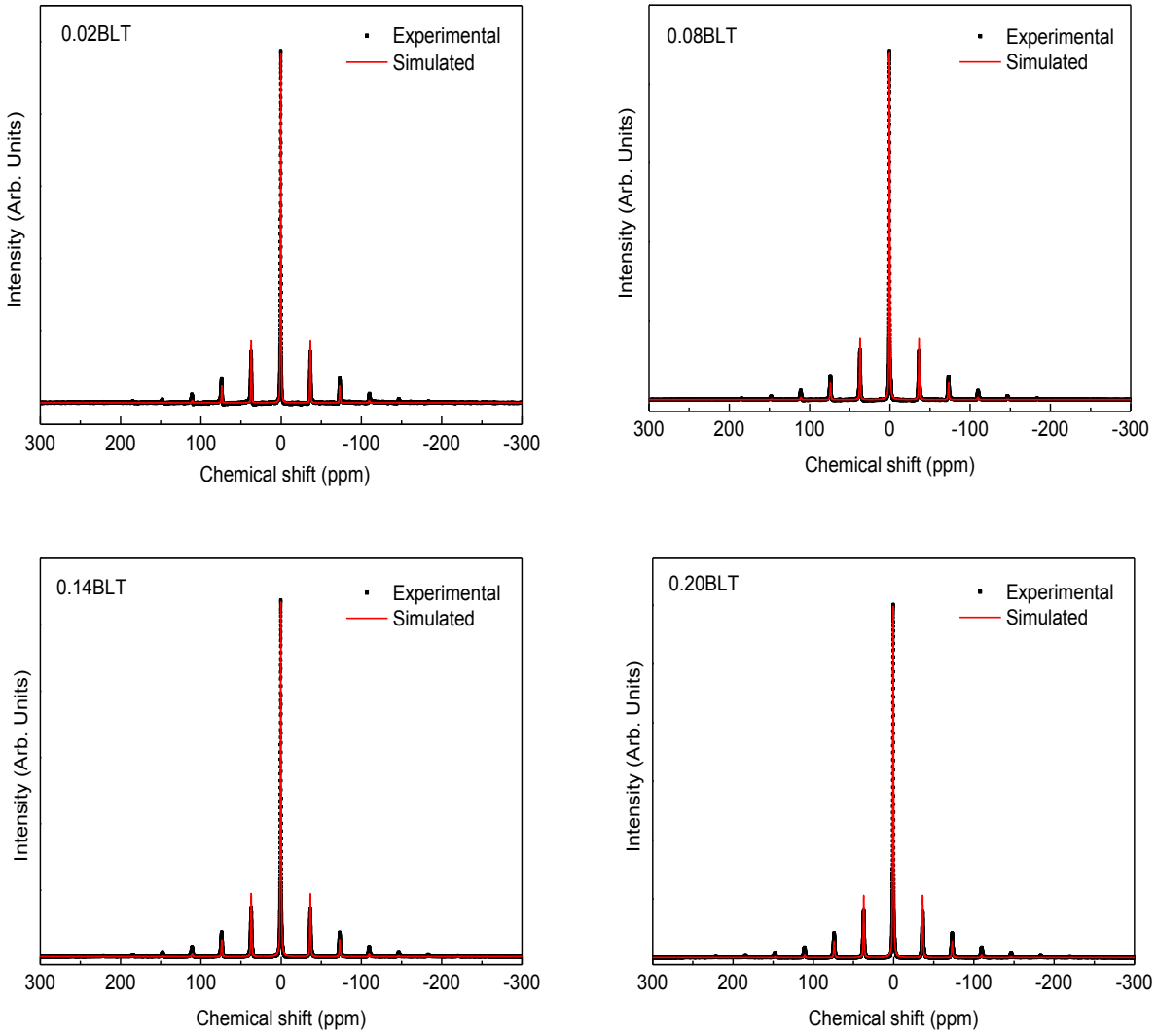

Figure 4.18: Comparison of the experimental and simulated ^{7}Li MAS NMR spectra of selected compositions (0.02BLT, 0.08BLT, 0.14BLT, 0.20BLT) of the (1-x)BNT–xBLT series.

On increasing the BLT concentration, the ^{7}Li NMR peak becomes more and more Lorentzian and the Gaussian components gradually decrease. From Figure 4.20 it can be seen

that the Gaussian component shows a large slope change at x = 0.1 and at this composition a change in the slope is observed for the Lorentzian component also. These changes indicate that the local symmetry changes around x = 0.1. The Lorentzian component specifies the diffusion or mobility of the ions present in the crystal lattice.

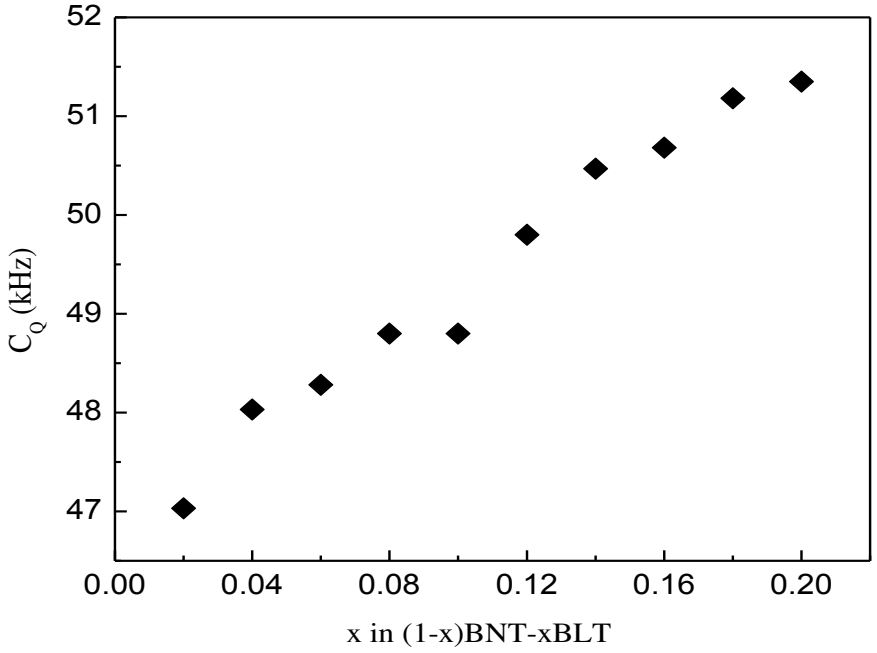

Figure 4.19: Variation of ^{7}Li C_Q of (1-x)BNT–xBLT series as a function of x.

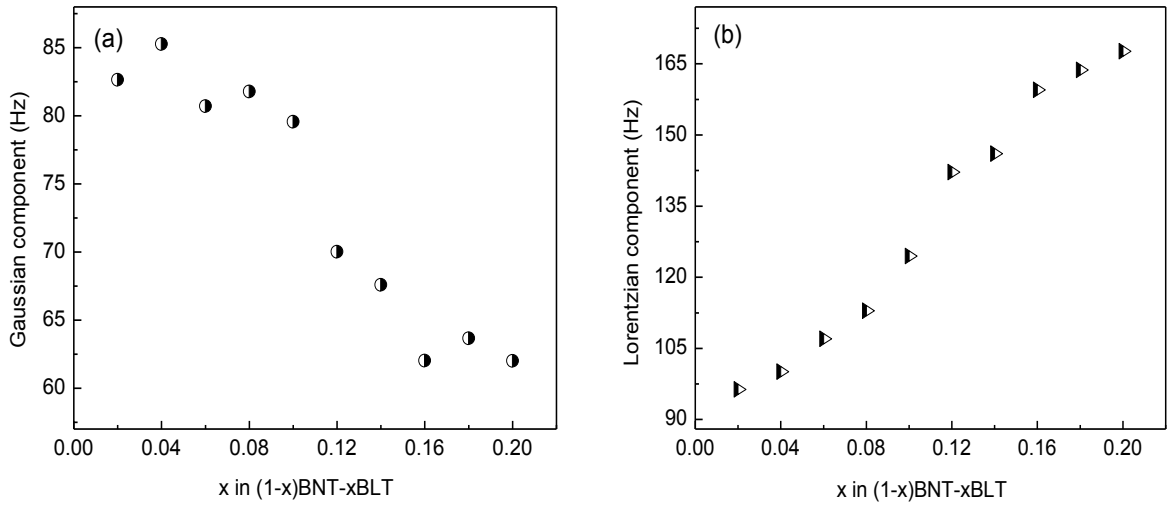

Figure 4.20: Variations of (a) Gaussian and (b) Lorentzian components of ^{7}Li spectra as a function of x in (1-x)BNT–xBLT.

The increase in the Lorentzian component indicates the increase in the Li^+ ion mobility in the crystal lattice with increasing Li content in the solid solution. This can be correlated with the downward frequency shift observed in the A-O band of the Raman spectra (Figure 4.8(a)). It is evident from the ^7Li NMR spectral analysis that the diffusion of Li^+ ion increases with BLT concentration, which lead to the weakening of the Li-O bond and a downward frequency shift of the A-O band in the Raman spectra.

4.6. Scanning electron microscopy

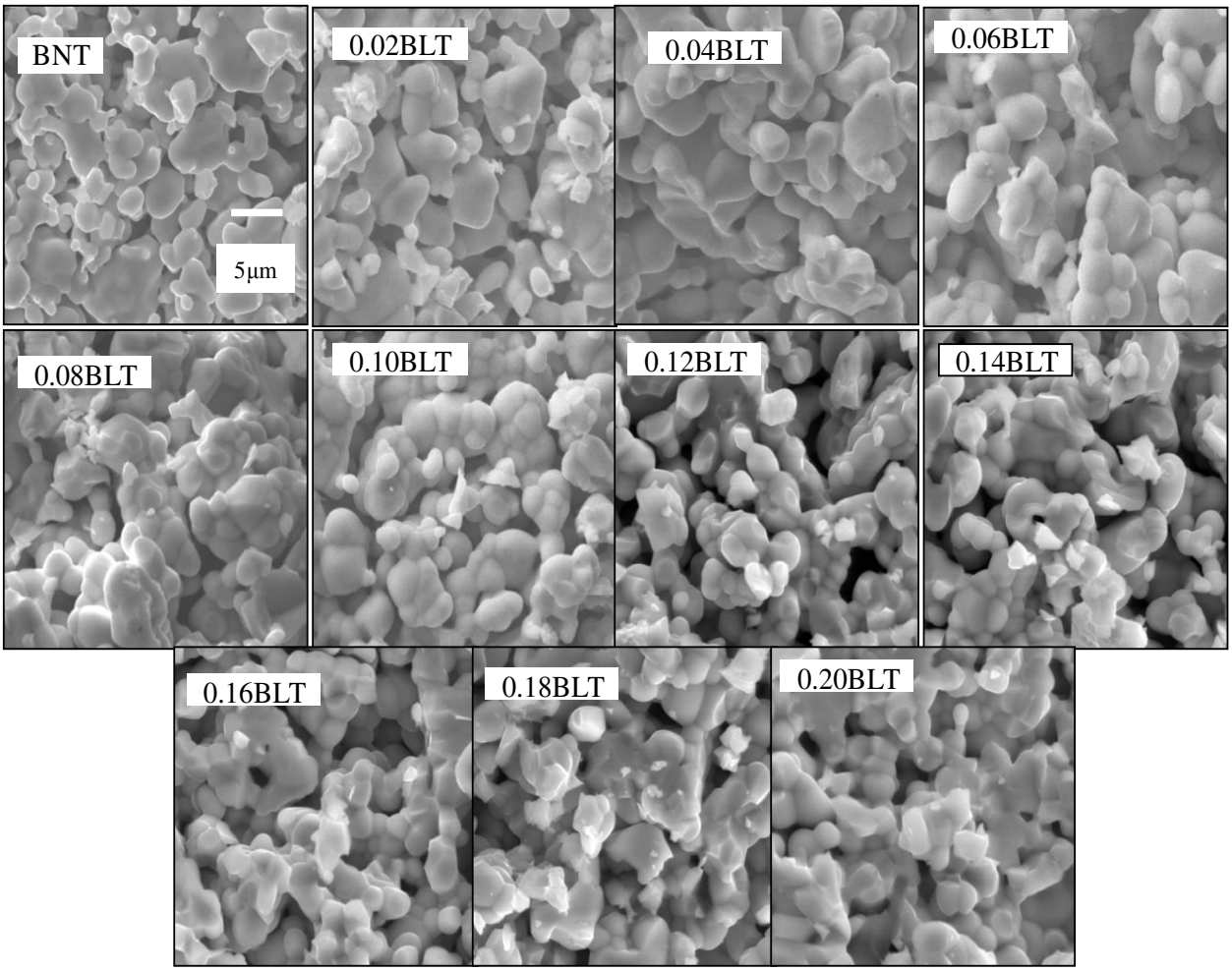

Figure 4.21: SEM micrographs of different compositions in the (1-x)BNT–xBLT series. The scale shown is common for all images.

Figure 4.21 shows the SEM micrographs of different compositions of (1-x)BNT–xBLT series. The grain size of the sintered ceramics decreases with increasing BLT concentration. The average grain size of the ceramics is compared with their density in Table 4.5. BNT possesses grains of very large size ~7.5 μm and the grain size is gradually decreases with increasing BLT concentration. The grain size of the composition with the highest BLT concentration (x = 0.20) is ~2.8μm. Fused grains with increased porosity are observed for compositions x = 0.1 and above.

Table 4.5: Density and grains size of different compositions in the (1-x)BNT–xBLT series.

Sample	**Grain size (μm)**	**Density (g/cm^3)**	**Theoretical Density (g/cm^3)**
BNT	7.5	3.52	5.97
0.02BLT	7.5	3.52	5.99
0.04BLT	5.9	3.59	5.99
0.06BLT	6.2	3.80	5.99
0.08BLT	5.6	3.87	6.02
0.10BLT	5.9	3.90	5.98
0.12BLT	5.0	3.89	5.98
0.14BLT	3.7	3.88	5.98
0.16BLT	3.4	3.90	5.97
0.18BLT	3.4	3.79	5.98
0.20BLT	2.8	3.81	6.06

4.7. Density

Figure 4.22 shows the variation of the sintered density of (1-x)BNT–xBLT compositions with Li^+ concentration. The density increases initially with BLT concentration and reached a maximum at $x \approx 0.1$, showing a small decrease in the density above this composition. It is observed from the SEM micrographs that the grain size decreases with increasing Li concentration and above $x \approx$ 0.1 the nature of the microstructure changed, where grains are fused and more pores are observed. The small decrease in the density after $x \approx 0.1$ can be correlated with the increased

porosity. The changes in the density and microstructure are also correlated with the structural changes. The measured densities are ~ 60% of the theoretical densities for all compositions. Density of BNT in the BNT-BLT series is 3.15 g/cm^3 which is relatively small when compared to the density of BNT (4.66 g/cm^3) in the BNT-BKT series (Section 3.7, Table 3.6). The relatively low density of BNT in the BNT–BLT series is due to the difference in synthetic method and the lower sintering temperature (1000 ^{o}C) used. A comparison of theoretical density and measured density of the ceramics is shown in Table 4.5. The measured densities of the ceramics are very low when compared to the literature reports. Lu *et al* synthesized BNT–BLT compositions having density close to the theoretical density.[113] They synthesized the BNT–BLT series with conventional ceramic fabrication method at a sintering temperature of 1040–1120 ^{o}C. The relatively low density of the BNT–BLT ceramics in the present study is due to the low pressure used for the compaction of the pellets (8 MPa) and the lower sintering temperature (1000 ^{o}C).

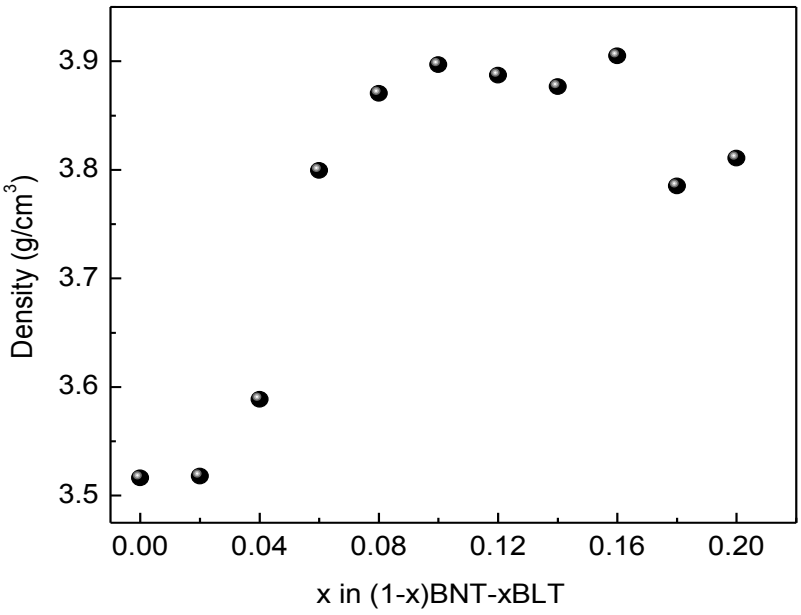

Figure 4.22: Variation of the sintered density of (1-x)BNT–xBLT solid solution as a function of x.

4.8. Dielectric constant

The dielectric constant of all the studied compositions of (1-x)BNT–xBLT, measured at 1 kHz, as a function of BLT concentration is shown in Figure 4.23. The dielectric constant shows a

small increase up to x = 0.08 which is shown in the inset of Figure 4.23 and an abrupt change in the slope is observed above x = 0.08. For $x \geq 0.12$, the dielectric constant remains almost the same. Although no structural phase transition is observed in the BNT–BLT solid solution series up to x = 0.2, the lattice parameter '*b*' showed a small but drastic increase above x = 0.1. Thus, similar changes are observed in the case of the structural parameters, density, microstructure and dielectric constant, suggesting that the changes in the structure are responsible for the dielectric properties of the BNT–BLT solid solution.

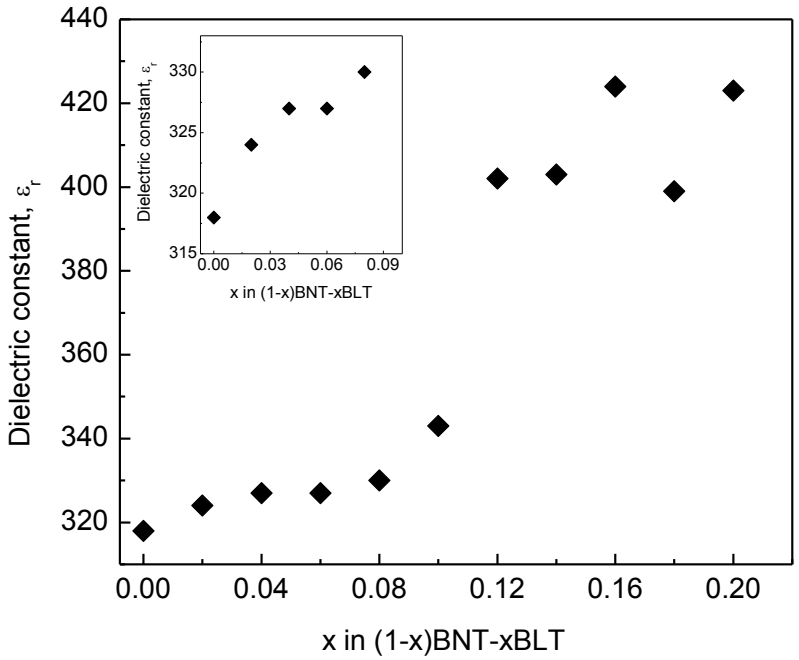

Figure 4.23: Variation of the dielectric constant of (1-x)BNT–xBLT as a function of x, inset showing zoomed figure for $0 \leq x \leq 0.1$.

The maximum dielectric constant observed for the BNT–BLT compositions is ~420. However this value is relatively small, when compared to the maximum dielectric constant observed for the BNT–BKT series which is ~1800 (Figure 3.21 and section 3.8). However, for the BNT–BKT system, maximum dielectric constant is observed in the MPB region where the monoclinic and tetragonal phases co-exist. Such a phase transition and MPB region are not observed in the case of the BNT–BLT system. Also, the distortion of the monoclinic structure is relatively larger for the BNT–BKT system due to the larger size of the K^+ ions. Moreover, the sintering temperature (1150 ^oC) used for the BNT–BKT solid solution series is larger than the sintering temperature (1000 ^oC) used for the BNT–BLT solid solution series. Hence, the

maximum density (~5.2 g/cm^3) observed in the BNT–BKT solid solution (Table 3.6) is larger than that of BNT–BLT solid solution which is ~4g/cm^3. For BNT, reported in chapter 3, synthesized by the ceramic method and sintered at 1150 ^{o}C, the dielectric constant is obtained as 516, whereas the value obtained is 318 for the sample synthesized by the citrate method and sintered at 1000 ^{o}C. Thus, the higher dielectric constant of the BNT–BKT solid solutions is due to their larger density. The observed dielectric constants of the BNT–BLT ceramics are relatively low when compared to the earlier literature reports.[113-114] Lu *et al* reported a dielectric constant~ 800 for the x = 0.20 composition in the BNT-BLT series.[113] This is due to the difference in synthesis methods, processing conditions, density, sintering temperature and the pressure used for the compaction of pellets.

4.9. Structure-property correlations

The present studies on (1-x)BNT–xBLT solid solution series show that same trends are observed for the changes in the structural parameters and properties of the system. A linear variation in some of the lattice parameters, Raman spectral parameters, NMR parameters and dielectric constant is observed for $0 \leq x \leq 0.1$ and maximum values are observed in the range $0.12 \leq x \leq 0.20$. The microstructure of the ceramics also showed changes above $x = 0.1$ where the grains are smaller, fused and porous.

A close correlation between the structure, local structure and dielectric constant of the (1-x)BNT–xBLT solid solution with BLT concentration is obtained from the XRD, Raman and SSNMR studies. Figure 4.24 shows a comparison of the variations in the lattice parameter 'b', area under the first component of the Raman band in the 200-400 cm^{-1} region and the dielectric constant of the solid solutions with increasing BLT concentration. The Raman band belongs to the Ti-O vibrations in the BNT–BLT solid solution. All the three parameters show similar variation, where the parameters are not changed till $x \approx 0.08$, a large increase up to $x = 0.12$ and again independent of x in the range $0.12 \leq x \leq 0.20$. Since the Raman parameter shows the changes in the Ti-O bond with Li^+ substitution, and similar trend is followed by the lattice parameter 'b', and the dielectric constant, it may be concluded that the changes in the local symmetry contribute to the variations in the dielectric constant with Li^+ substitution.

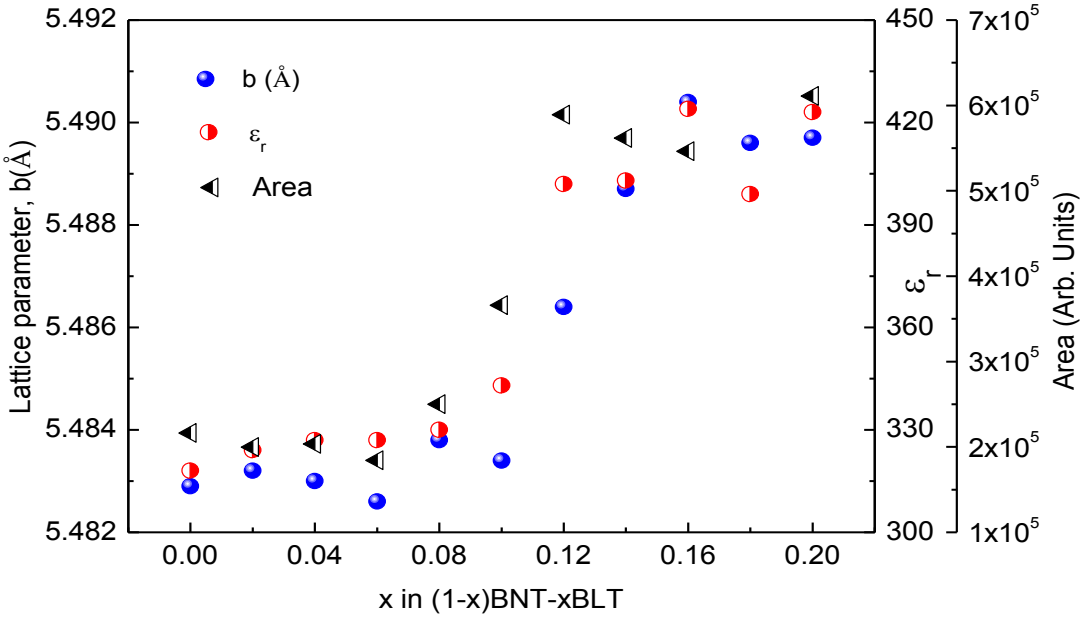

Figure 4.24: Comparison of lattice parameter '*b*', dielectric constant (ε_r) and area under the first component of the Raman band in the 200-400 cm^{-1} region, as a function of x in the (1-x)BNT-xBLT series.

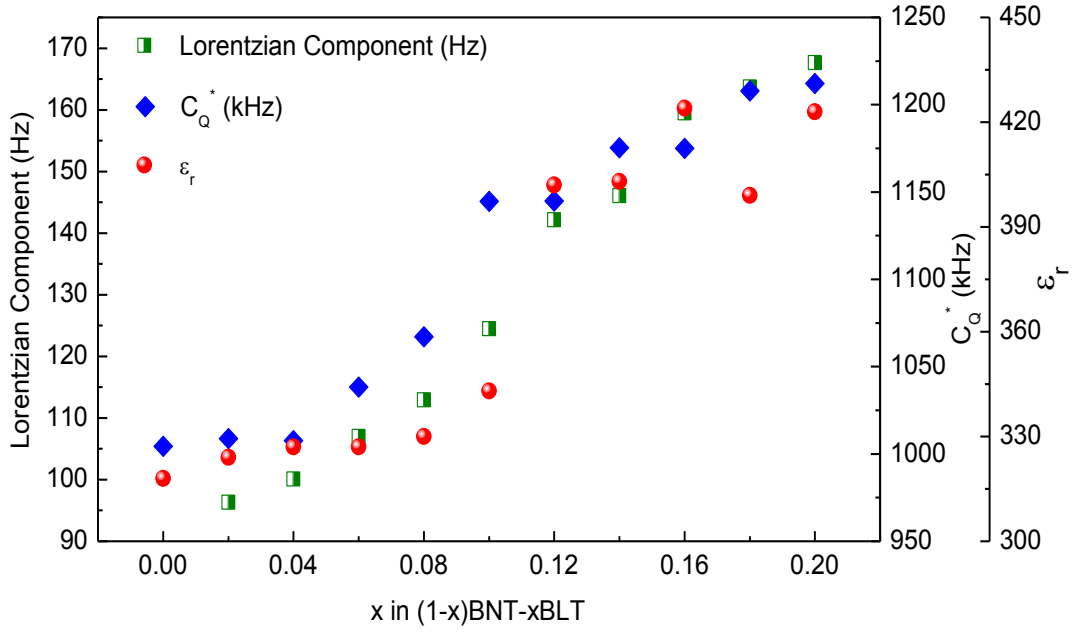

Figure 4.25: Comparison of the changes in the Lorentzian component of ^7Li NMR spectra, quadrupolar coupling constant (C_Q^*) of ^{23}Na spectra and dielectric constant (ε_r) as a function of x in the (1-x)BNT-xBLT series.

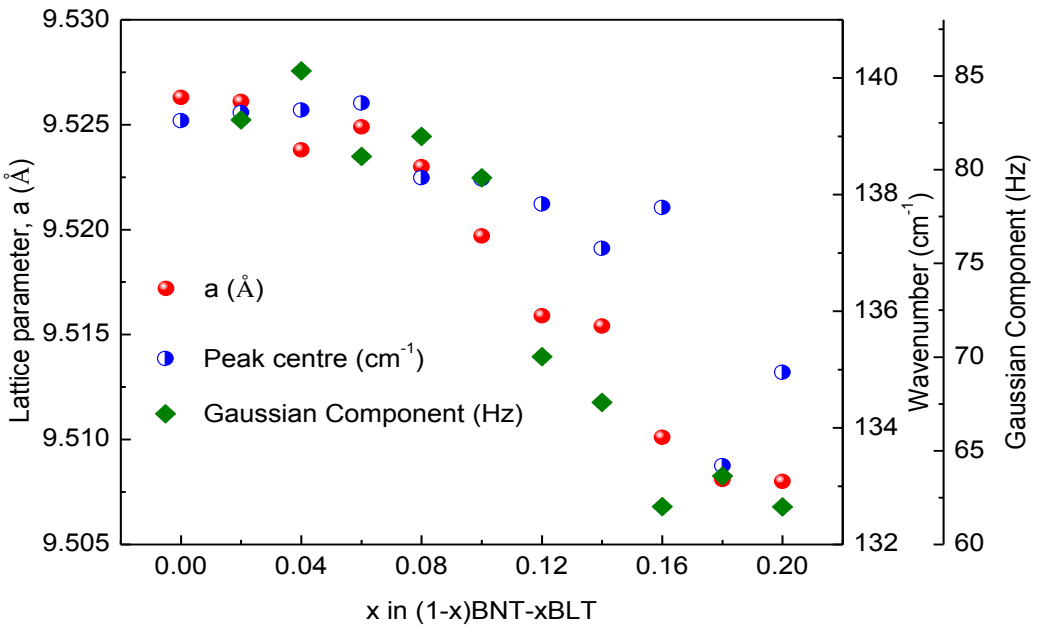

Figure 4.26: Comparison of lattice parameter '*a*', peak centre of the Raman band below 200 cm^{-1} and Gaussian component of the ^{7}Li NMR spectra.

Figure 4.25 compares the changes in the Lorentzian component of the ^{7}Li spectra, quadrupolar coupling (C_Q^*) of ^{23}Na spectra and dielectric constant (ε_r) with BLT concentration. The variations in the NMR parameters and the dielectric constant of the ceramics show similar trend with substitution. The changes in the NMR parameters specify the local symmetry changes with Li^+ substitution. This shows a clear indication that the local symmetry changes with substitution is correlated to the dielectric properties of the ceramics. This is supported by the ^{23}Na NMR results that showed an increase in C_Q^* with BLT substitution. The rise in the dielectric polarization can be contributed by the distortion of the local environment.

Figure 4.26 shows a comparison of the changes in the lattice parameter '*a*' , the peak position of Raman band below 200 cm^{-1} and the Gaussian component calculated from the simulated ^{7}Li NMR spectra. All three parameters exhibit similar changes with BLT concentration. The parameters show a linear decrease in the range $0 \leq x \leq 0.1$ and a large drop after $x = 0.1$. Similar changes in all three parameters indicate that the structural and local symmetry changes are associated to each other. The Raman band below 200 cm^{-1} belongs to the A-O vibrations. The downward frequency shift of this band specifies Li^+ diffusion in the crystal lattice. This is supported by the similar decrease observed in the Gaussian component.

Thus, the overall results indicate a direct correlation between the structure, microstructure and properties with BLT concentration in the BNT–BLT solid solution. The Rietveld refinement analysis, Raman spectroscopy and SSNMR studies confirmed the absence of any structural phase transition in the BNT–BLT solid solution series in the range $0 \leq x \leq 0.20$. However, the deviations in the variation of the lattice parameters and Raman spectral parameters indicate some effect on the substitution. It is observed from the ^{23}Na NMR studies that the structural distortion increases with BLT concentration and this can be correlated with increase in the dielectric constant. As the BLT concentration increases, the microstructure of the ceramics is changed. Smaller sized, fused and porous grains are observed for $x > 0.1$. This also correlates with the slight decrease in the density above $x = 0.1$ and the structural changes after this composition.

4.10. Conclusions

Solid solutions in the series (1-x)$Bi_{0.5}Na_{0.5}TiO_3$–$xBi_{0.5}Li_{0.5}TiO_3$, (1-x)BNT–xBLT, in the range $0 \leq x \leq 0.20$ are prepared by a citrate gel method. The phase formation was studied by powder XRD. Rietveld refinement analysis of the XRD patterns was carried out for all the compositions of the (1-x)BNT–xBLT solid solution series and the results suggest absence of any phase transformation. The changes in lattice parameters with BLT concentration indicated a small distortion and local symmetry changes in the crystal lattice. Raman spectroscopy analysis supported the results obtained from XRD studies. The changes in the Raman parameters with substitution followed the same trend as that observed in the case of crystal structure parameters. Solid state NMR studies gave more information about the local symmetry changes. Symmetry of the compositions is decreased with increasing BLT concentration as evidenced from the quadrupolar coupling. The Lorentzian component in the ^{7}LiNMR spectra is found to increase with increasing Li concentration. The SSNMR results are in agreement with the Raman studies. The downward frequency shift in the A-O vibration band in the Raman spectra and the increase in the Lorentzian component of the ^{7}Li NMR indicate rise in Li^+ diffusion with BLT substitution in the crystal lattice. Thus the XRD, Raman and SSNMR studies showed clear indication for local symmetry changes and small distortions in the BNT lattice with BLT substitution. The density and dielectric constant of the compositions increased with BLT concentration. A close correlation between the XRD, Raman, SSNMR parameters, microstructure and the properties of the ceramics are observed. Variation of all structural and spectral parameters as well as the

density, microstructure and the dielectric constant show similar changes with increasing BLT concentration, with a change around x = 0.1. This suggests local structural changes because of the distribution of Li^+ ions in the crystal lattice, indicating the close correlation between structure, microstructure, and properties of the ferroelectric compositions in the (1-x)$Bi_{0.5}Na_{0.5}TiO_3$–$xBi_{0.5}Li_{0.5}TiO_3$ solid solution series.

Chapter 5

Studies on (1-x)$Bi_{0.5}Na_{0.5}TiO_3$–(x/2)$Bi_{0.5}Li_{0.5}TiO_3$–(x/2)$Bi_{0.5}K_{0.5}TiO_3$ Series

5.1. Introduction

Studies on the correlations among the crystal structure, phase transition and dielectric and ferroelectric properties of potassium (K^+) and lithium (Li^+) substituted bismuth sodium titanate (BNT) solid solution series are discussed in the previous chapters. The ionic size of K^+ (1.64 Å) is larger and that of Li^+ (0.92 Å) is smaller than that of Na^+ (1.39 Å) in BNT and therefore structural distortions are expected because of the replacement of Na^+ by the larger or smaller ions. However, since the average size of Li^+ and K^+ (1.28 Å) is comparable to that of Na^+, partial substitution of Na^+ by equal amounts of Li^+ and K^+ is not much expected to alter the structure and properties of BNT.

There are few reports in the literature on the studies on K^+ and Li^+ co-substituted BNT solid solutions. Lin *et al* synthesized the solid solution series $[Bi_{0.5}(Na_{1-x-y}K_xLi_y)_{0.5}]TiO_3$, ($0 < x+y < 1$) by conventional ceramic method.[115] The XRD results showed that the ceramics possess perovskite structure with a little unknown phase when $y \leq 0.20$.[115] High piezoelectric coupling constant d_{33}(~180 pC/N) and higher planar electromechanical coupling factor K_p (~35.0 %) are obtained for $[Bi_{0.5}(Na_{1-x-y}K_xLi_y)_{0.5}]TiO_3$ with higher amount of K^+ and lower amount of Li^+. Lu *et al* studied the phase transition behavior of Li^+ and K^+ co-substituted BNT ceramics as a function of composition and temperature using X-ray diffraction analysis, dielectric and ferroelectric characterisation.[116] The authors observed that the low frequency permittivity showed a remarkable increase at high temperatures and the peak of maximum permittivity vanished due to the space charge polarization induced by the conductivity of the ions. The studies on ferroelectric hysteresis loops at different temperatures showed that above the depolarization temperature, antiferroelectric phase does not exist. Lin *et al* investigated the structure, electrical properties and temperature characteristics of (1-x-y)$Bi_{0.5}Na_{0.5}TiO_3$–x$Bi_{0.5}K_{0.5}TiO_3$–y$Bi_{0.5}Li_{0.5}TiO_3$ solid solution series.[117] The authors observed a morphotropic phase boundary in the compositional range $0.15 \leq x \leq 0.25$ from the XRD analysis. It is reported that the partial substitution of Li^+ and K^+ in the BNT lattice lowers the coercive field (E_c) and increase the remnant polarization (P_r) and as a result, large improvement is observed in the piezoelectric properties of the ceramics. The piezoelectric properties are maximum in the MPB region (x =0.15-0.25, y= 0.05-0.10). Ming *et al* studied the effect of Li^+ substitution and sintering temperature on the properties of $Bi_{0.5}$(Na,

$K)_{0.5}TiO_3$ solid solution.[118] The authors observed that not only the Li^+ content but also the sintering temperature has effect on the piezoelectric properties of the ceramics.

In the present work we have co-substituted equal amounts of Li^+ and K^+ ions for Na^+ in BNT, so that the average ionic size of the substituted ions is comparable to that of Na^+. The objective is to understand the changes in the crystal structure and properties, if any, due to the co-substitution. (1-x)BNT–(x/2)BLT–(x/2)BKT solid solution series, where x = 0, 0.06, 0.12, 0.18, 0.24 are synthesized and a detailed structural analysis has been carried out by Rietveld refinement of XRD patterns and Raman spectroscopy. Local symmetry changes are studied by solid state NMR by probing the two quadrupolar nuclei ^7Li and ^{23}Na.

5.2. Synthesis

Different compositions in the (1-x)BNT-(x/2)BLT-(x/2)BKT solid solution series, where x = 0, 0.06, 0.12, 0.18, 0.24, were prepared by the citrate gel method, as discussed in the previous chapter. Stoichiometric ratios of bismuth nitrate ($Bi(NO_3)_3.5H_2O$), sodium nitrate ($NaNO_3$), lithium nitrate ($LiNO_3$) and potassium nitrate (KNO_3) were taken, their individual solutions were prepared and then mixed together. Stoichiometric amount of titanium isopropoxide ($Ti[OCH(CH_3)_2]_4$) was dissolved in isopropyl alcohol and citric acid was dissolved in this solution with continuous stirring. The ratio of citric acid to the total metal ion was taken as 3:1. The mixed metal nitrate solution was added to the titanium isopropoxide solution with constant stirring and then evaporated at 60 ^oC on a hot plate until a transparent viscous gel was obtained. The dried gel was kept at 150 ^oC for overnight heating that formed a foam. The foam was then crushed using a mortar and pestle to fine powder. This powder was initially calcined at 400 ^oC, then at 850 ^oC and finally at 1000 ^oC with intermediate grindings. The powder samples obtained were uniaxially pressed into circular discs (10 mm diameter x 3 mm height) at a pressure of 8 MPa and sintered at 1000 ^oC for 2 hours. All the samples were sintered under identical conditions at a heating and cooling rate of 5 ^oC/min. The prepared compositions and the corresponding sample codes are listed in Table 5.1. Crushed and powdered sintered pellets of (1-x)BNT–(x/2)BLT–(x/2)BKT were used for XRD, Raman spectroscopy and solid-state NMR studies.

Table 5.1: Compositions in the (1-x)BNT–(x/2)BLT–(x/2)BKT series and the corresponding sample codes.

x	**Composition** **(1-x)$Bi_{0.5}Na_{0.5}TiO_3$–(x/2)$Bi_{0.5}Li_{0.5}TiO_3$–(x/2)$Bi_{0.5}K_{0.5}TiO_3$** **(1-x)BNT–(x/2)BLT–(x/2)BKT**
0	BNT
0.06	0.94BNT–0.03BLT–0.03BKT
0.12	0.88BNT–0.06BLT–0.06BKT
0.18	0.82BNT–0.09BLT–0.09BKT
0.24	0.76BNT–0.12BLT–0.12BKT

5.3. Powder X-ray diffraction

Figure 5.1 shows the XRD patterns of all the compositions of (1-x)BNT–(x/2)BLT–(x/2)BKT series. The simulated XRD pattern of BNT using the monoclinic Cc space group is shown in the figure for comparison. The XRD patterns of all the compositions of (1-x)BNT–(x/2)BLT–(x/2)BKT match very well with simulated pattern of BNT, which confirms the formation of single phase compositions. To understand the changes in the crystal structure and any associated symmetry changes, Rietveld refinement analysis of the XRD patterns of all the compositions of (1-x)BNT–(x/2)BLT–(x/2)BKT have been carried out. Low values of reduced χ^2 and R_p are obtained for all compositions using the monoclinic Cc structure of BNT. Thus, no evidence for any structural phase transition is obtained on substitution of equal amounts of Li and K in the BNT lattice, in the range $0.0 \leq x \leq 0.24$ in (1-x)BNT–(x/2)BLT–(x/2)BKT. Figure 5.2 shows the results of the Rietveld refinement analysis of all the compositions of (1-x)BNT–(x/2)BLT–(x/2)BKT. The results obtained from the Rietveld refinement analysis of (1-x)BNT-(x/2)BLT-(x/2)BKT are summarized in Table 5.2.

The lattice parameters obtained from the Rietveld refinement analysis of XRD patterns are analyzed. The lattice parameters 'a', 'b', 'c' and the monoclinic angle β showed minor changes with substitution. The changes in the lattice parameters with concentration are shown in Figure 5.3. Lattice parameters 'a' and 'b' show a small increase with increase in the

concentration of the substituents Li^+ and K^+ in the BNT lattice whereas the lattice parameter 'c' and the monoclinic angle β are slightly decreased.

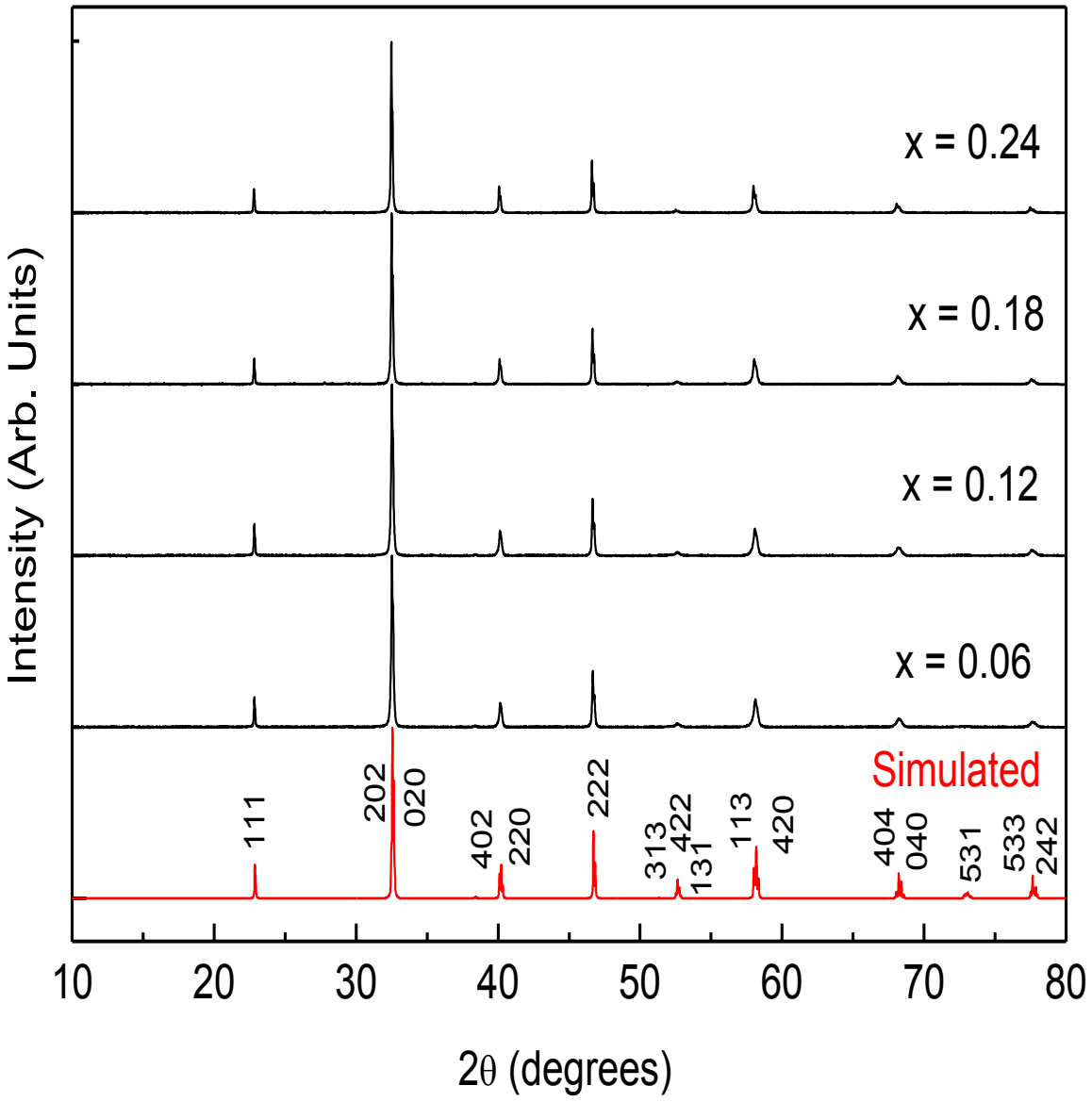

Figure 5.1: Powder XRD patterns of different compositions in the (1-x)BNT–(x/2)BLT–(x/2)BKT solid solution series. Simulated pattern of BNT is shown at the bottom for comparison.

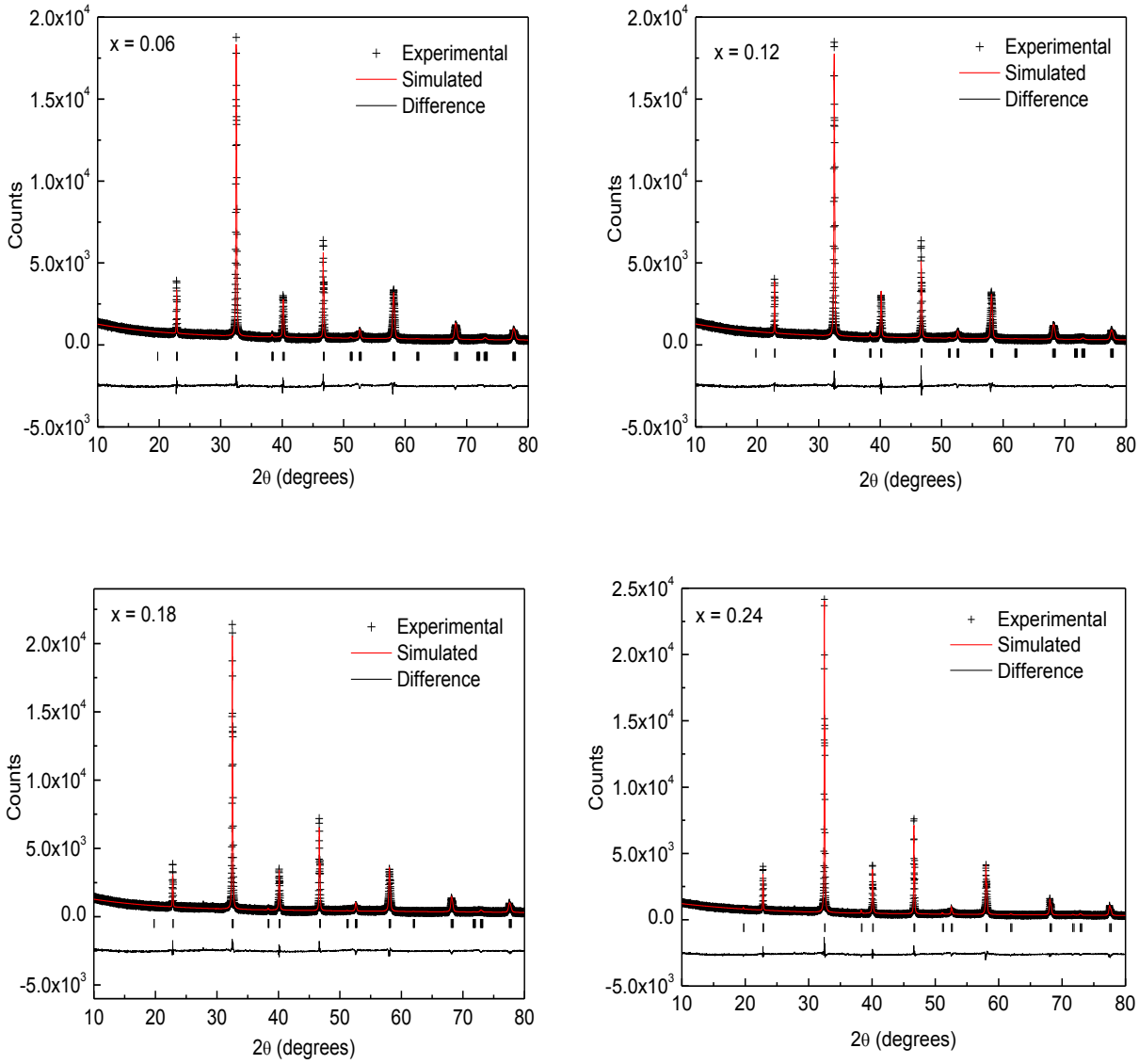

Figure 5.2: Results of Rietveld refinement analysis of (1-x)BNT–(x/2)BLT–(x/2)BKT using monoclinic Cc space group, for x = 0.06, x = 0.12, x = 0.18, x = 0.24.

A small but linear increase in the unit cell volume is observed with substitution of Li^+ and K^+, as shown in Figure 5.4. Thus, due to the comparable average size of Li^+ and K^+ with that of Na^+, only a marginal change in the lattice parameters and volume of the unit cell are observed. Although structural transformation or symmetry changes is not observed in the (1-x)BNT–(x/2)BLT–(x/2)BKT solid solution series, the changes in the lattice parameters indicate minor distortion of the BNT lattice for accommodating smaller Li^+ ion and larger K^+ ions.

Table 5.2: Lattice parameters, reduced χ^2 and R_p values of (1-x)BNT–(x/2)BLT-(x/2)BKT obtained from Rietveld analysis.

Sample	**Cc**				χ^2	R_p (%)
x	**a (Å)**	**b (Å)**	**c (Å)**	**β (degrees)**		
0	9.5263	5.4829	5.5091	125.43	2.065	5.18
0.06	9.5218	5.4885	5.505	125.34	3.620	5.67
0.12	9.5303	5.489	5.5086	125.38	3.244	5.49
0.18	9.5255	5.4927	5.5042	125.29	3.961	6.13
0.24	9.5298	5.502	5.5021	125.28	3.634	5.78

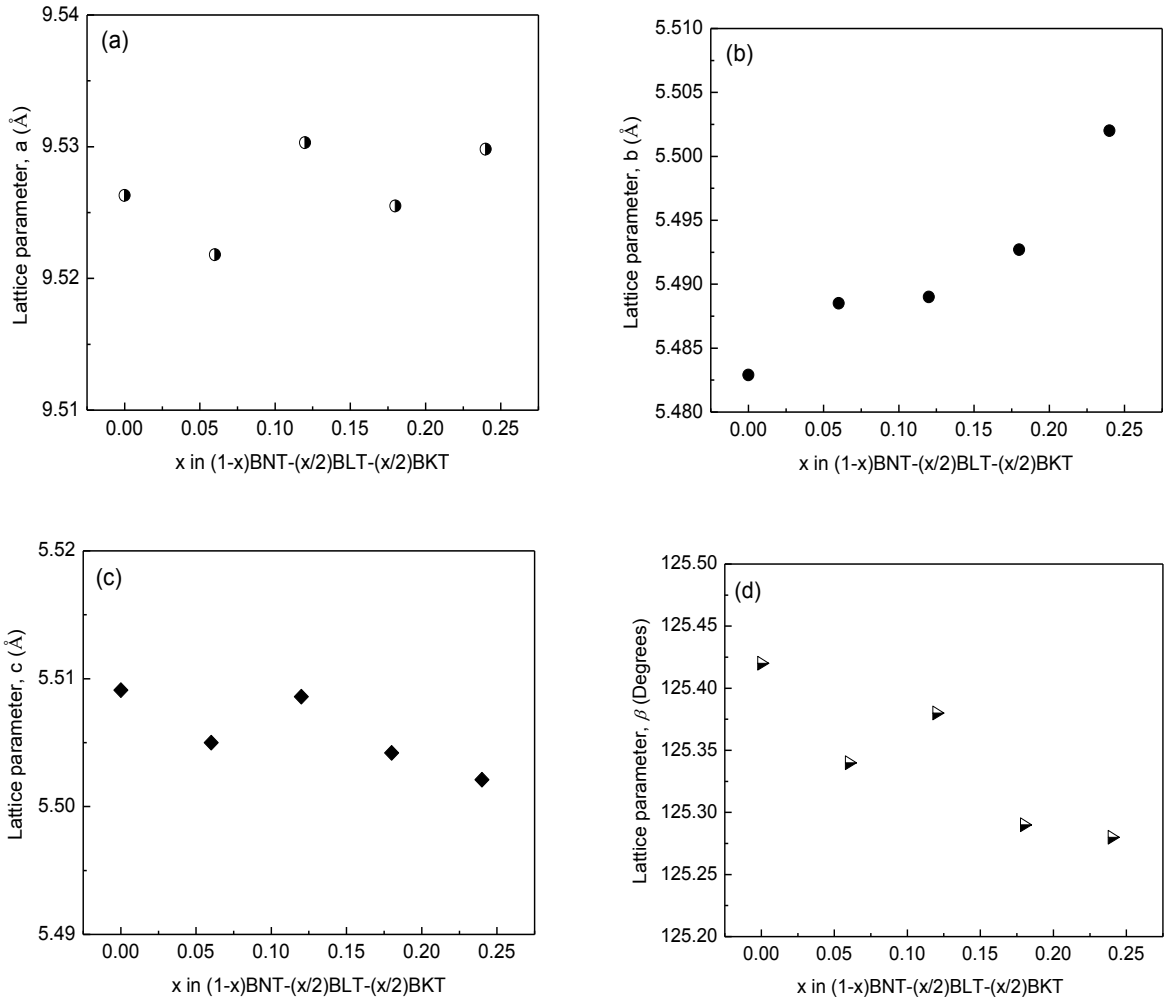

Figure 5.3: Variation of monoclinic lattice parameters (a) '*a'*, (b) '*b'*, (c) '*c'* and (d) angle β of (1-x)BNT–(x/2)BLT–(x/2)BKT solid solution as a function of x.

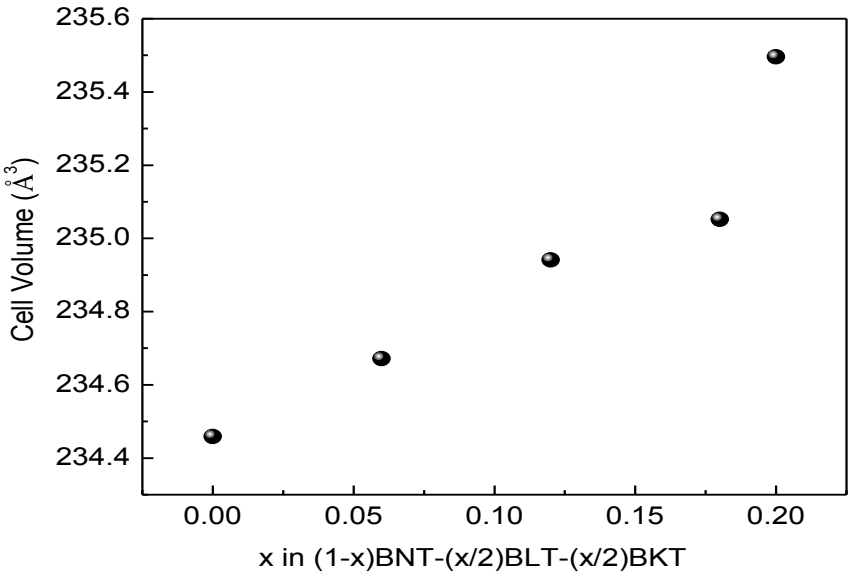

Figure 5.4: Variation of unit cell volume of (1-x)BNT–(x/2)BLT–(x/2)BKT solid solution series as a function of x.

5.4. Raman spectroscopy

Raman spectra of all the compositions of (1-x)BNT–(x/2)BLT–(x/2)BKT are shown in Figure 5.5.

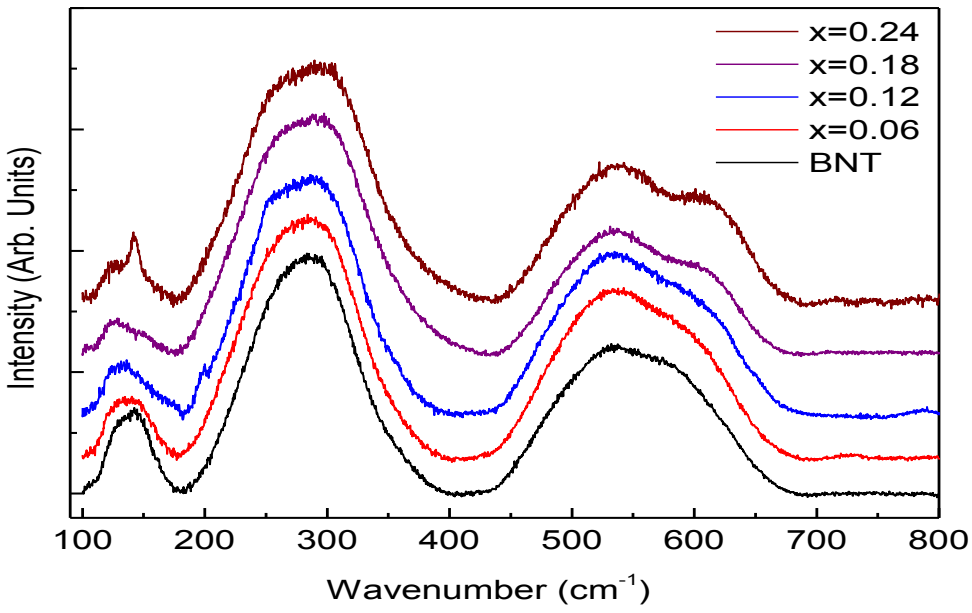

Figure 5.5: Raman spectra of different compositions of (1-x)BNT–(x/2)BLT–(x/2)BKT.

As observed in the Raman spectra of the BNT-BKT (Figure 3.7) and the BNT-BLT (Figure 4.6) series, the Raman spectra of (1-x)BNT–(x/2)BLT–(x/2)BKT series also show three different regions which are related to the three different vibrations.

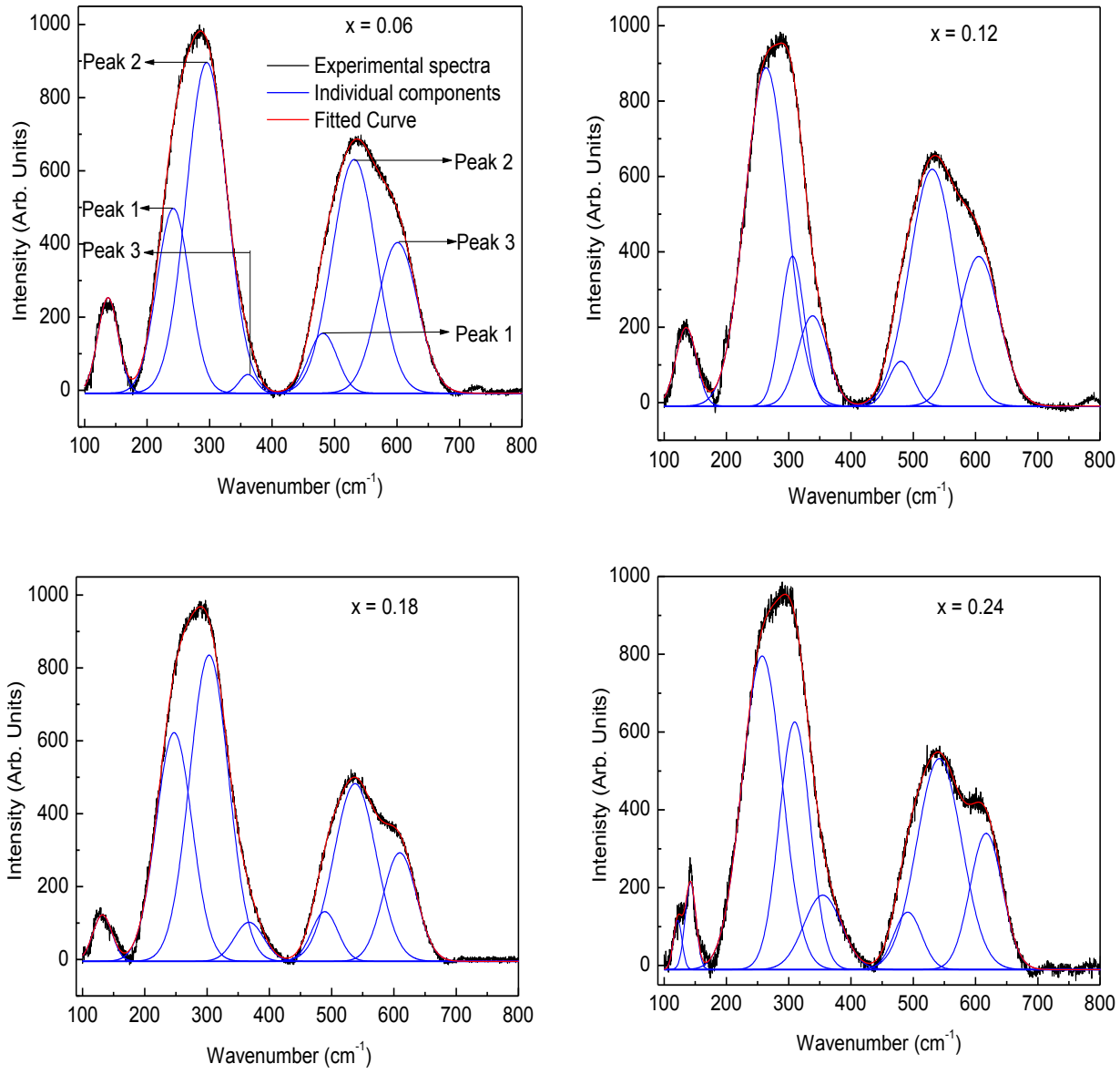

Figure 5.6: Deconvoluted Raman spectra of x = 0.06, x = 0.12, x = 0.18 and x = 0.24 in (1-x)BNT–(x/2)BLT–(x/2)BKT. The black, red and blue curves correspond to experimental spectra, fitted curves and the individual components, respectively.

The band below 180 cm^{-1} is due to the A-O vibrations, the band in the 200-400 cm^{-1} region is due to Ti-O vibrations and the band in the 400-700 cm^{-1} region is due to TiO_6 octahedra in the perovskite structure. A prominent change observed in the Raman spectra of (1-x)BNT–

(x/2)BLT–(x/2)BKT is the splitting of the band below 180 cm^{-1} for the x = 0.24 composition. Such notable changes are not seen in the 200-400 cm^{-1} and 400-700 cm^{-1} region of the Raman spectra of (1-x)BNT–(x/2)BLT–(x/2)BKT solid solution series. A detailed Raman analysis has been carried out after deconvoluting each spectrum and changes in the parameters are examined.

Raman spectra of the compositions x = 0, 0.06, 0.12, 0.18 are deconvoluted in to 7 Gaussian peaks. The band below 180 cm^{-1} of the Raman spectra of the composition x = 0.24 showed splitting and hence, for this composition, the spectrum is deconvoluted in to 8 Gaussian peaks. The band below 180 cm^{-1} of the Raman spectra of all the compositions except x = 0.24 is fitted with a single peak. The 200-400 cm^{-1} band is deconvoluted in to three peaks and the 400-700 cm^{-1} band is also deconvoluted in to three peaks. The deconvoluted Raman spectra of all the compositions of the (1-x)BNT–(x/2)BLT–(x/2)BKT solid solution series is shown in Figure 5.6.

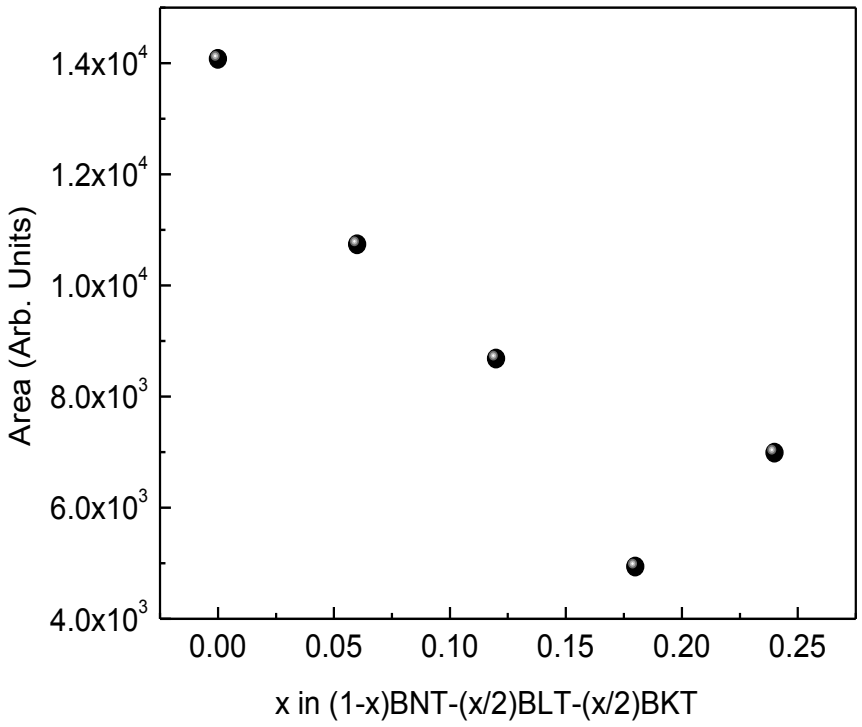

Figure 5.7: Changes in the area under the curve of the band below 180 cm^{-1} in the Raman spectra as a function of x in (1-x)BNT–(x/2)BLT–(x/2)BKT.

The Band below 180 cm^{-1} in the Raman spectra of (1-x)BNT–(x/2)BLT–(x/2)BKT belongs to the Bi-O, Na-O, Li-O, K-O vibrations. Since the atomic mass of bismuth is high, the Bi-O vibrations will be in the low frequency region and hence not visible in the Raman spectra.

Hence the observed band below 180 cm^{-1} is due to Na-O, Li-O, K-O vibrations. The 180 cm^{-1} Raman band of all the compositions except that of x =0.24 is deconvoluted to one peak. The additional Raman peak observed in the 180 cm^{-1} band of x = 0.24 is due to the A-site disorder resulting from the higher concentration of the co-substituents Li^+ and K^+ in the BNT lattice. If the crystal lattice of the unit cell is co-occupied by more cations, inhomogeneity of the crystal structure increases in the nanometer scale. This inhomogeneity leads to local disorder in the A-site of the crystal lattice in the ABO_3 perovskite structure and changes in the A-O vibration band.

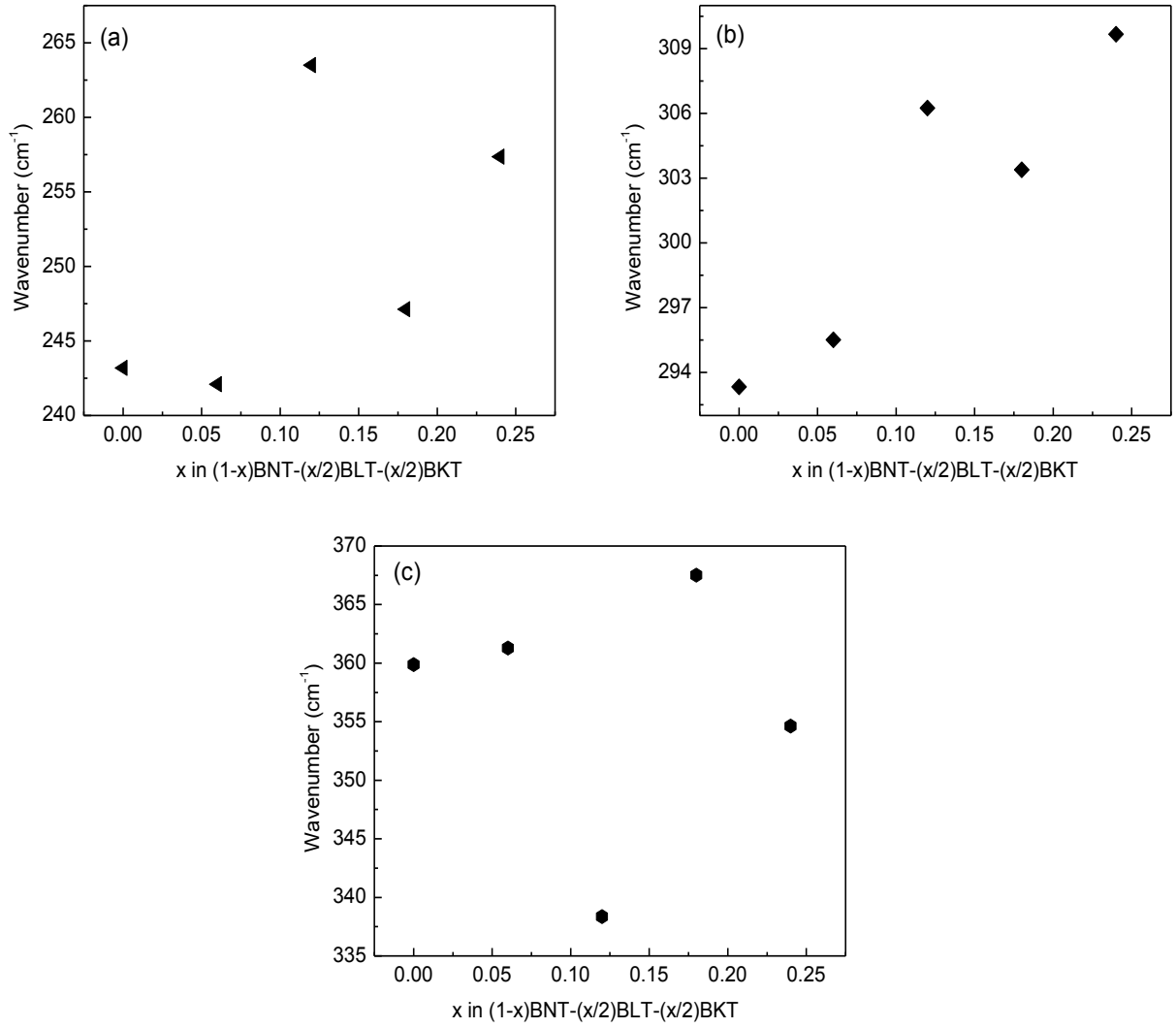

Figure 5.8: Changes in individual peak positions under the band in the 200-400 cm^{-1} region as a function of x in (1-x)BNT–(x/2)BLT–(x/2)BKT;(a) 1st peak, (b) 2nd peak, (c) 3rd peak.

The changes in the area under the band below 180 cm^{-1} with concentration of x is shown in Figure 5.7. As the concentration of the substituents increase the area under the A-O band has decreased. A small increase in area is observed for x = 0.24. The overall decrease in the area with substitution is likely to be due to the diffusion of Li^+ ions in the crystal lattice that will weaken the Li-O vibrations. When the concentration of the substituents increase, number of Li^+ ions in the crystal lattice increase which results in the weakening of the A-O vibrations and consequent decrease in the area under the A-O band.

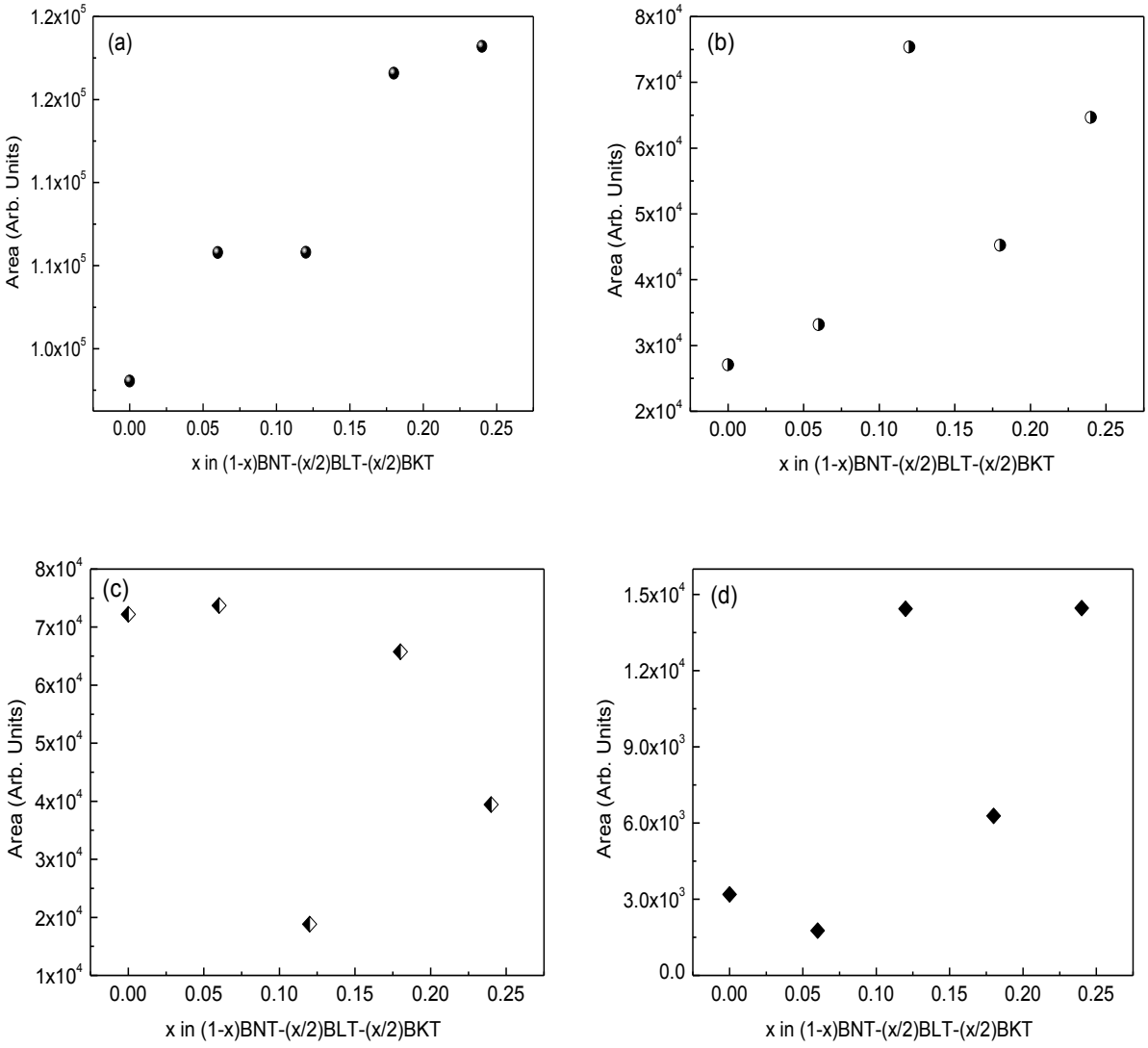

Figure 5.9: Total area and area under the individual peaks under the band in the region 200-400 cm^{-1} as a function of x in (1-x)BNT–(x/2)BLT–(x/2)BKT;(a) total area, (b) area under the 1st peak, (c) area under the 2nd peak, and (d) area under the 3rd peak.

Figure 5.8 shows the variations in the individual peak positions under the band in the 200-400 cm^{-1} region due to Ti-O vibrations, with substitution. The position of the individual peaks show only minor changes with substitution. The first and the third peak show random changes whereas the second peak shows an upward frequency shift with substitution. Figure 5.9 shows the changes in total area and the individual area under the band 200-400 cm^{-1} with substitution. Total area under the 200-400 cm^{-1} band has increased with substitution. The areas under the individual peaks also show minor changes with substitution, with an increasing (peak 1 and peak 3) or decreasing (peak 2) trend.

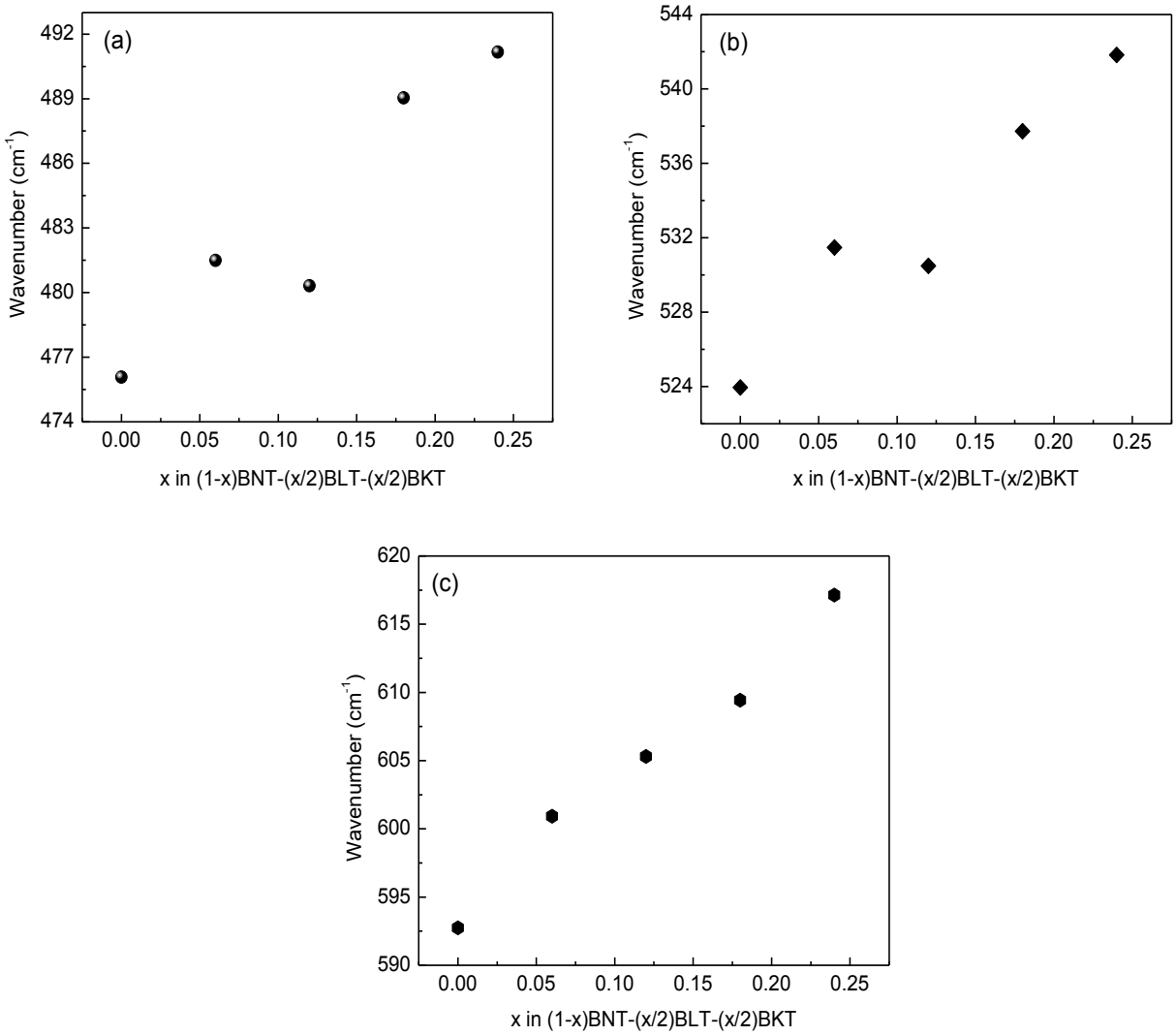

Figure 5.10: Changes in the individual peak positions of the Raman band in the 400–800 cm^{-1} region as a function of x in (1-x)BNT–(x/2)BLT–(x/2)BKT;(a) 1st peak, (b) 2nd peak, and (c) 3rd peak.

The Raman band in the 400-700 cm^{-1} region is due to the vibrations of the TiO_6 octahedra. Figure 5.10 shows the individual peak positions in the 400-700 cm^{-1} region. In this region the peak positions showed an upward frequency shift with substitution. Figure 5.11 shows the changes in total area and individual area in the 400-700 cm^{-1} region. Changes in area was observed with substitution.

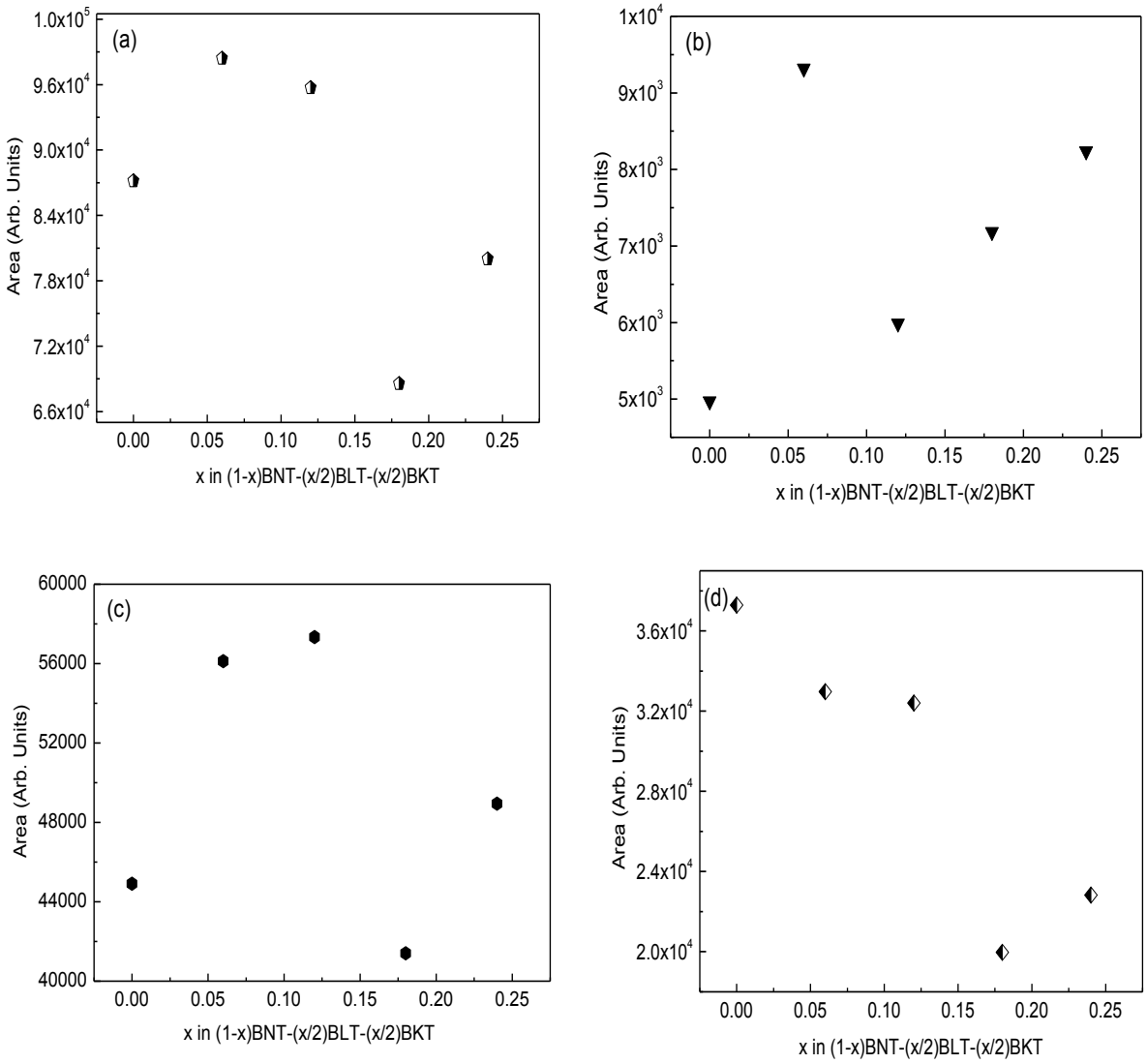

Figure 5.11: Total area and area under the individual peaks of the Raman band in the 400-800 cm^{-1} as a function of x in (1-x)BNT-(x/2)BLT-(x/2)BKT, (a) total area, (b) area under the 1st peak, (c) area under the 2nd peak, and (d) area under the 3rd peak.

As observed in the XRD analysis the substitution effect is seen in the Raman spectra of (1-x)BNT–(x/2)BLT–(x/2)BKT solid solution. The additional mode observed in the band below

180 cm^{-1} of x = 0.24 concentration indicate distortion in the crystal lattice with substitution that correlate with the XRD results. The changes in Raman parameters with substitution specified the local symmetry changes.

5.5. Solid-state NMR spectroscopy

5.5.1. ^{23}Na NMR

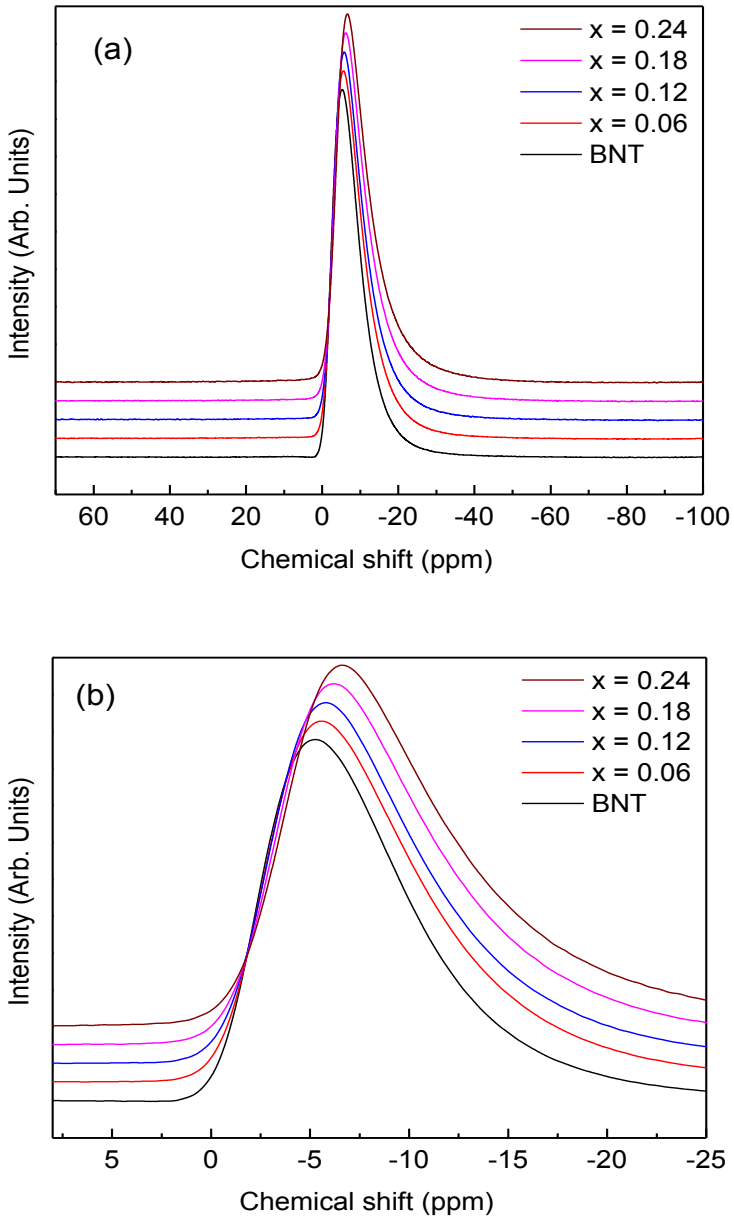

Figure 5.12: (a) ^{23}Na NMR spectra of the different compositions in the (1-x)BNT–(x/2)BLT–(x/2)BKT series, (b) Zoomed view of the central region.

Figure 5.12 (a) shows the ^{23}Na MAS NMR spectra of all the compositions and Figure 5.12 (b) shows the zoom part of the central region of the spectra. A gradual increase in the broadening of the ^{23}Na NMR spectra is observed as the concentration of the substituent is increased indicating local symmetry changes in the BNT crystal lattice. A small shift in the position of the peak is also observed.

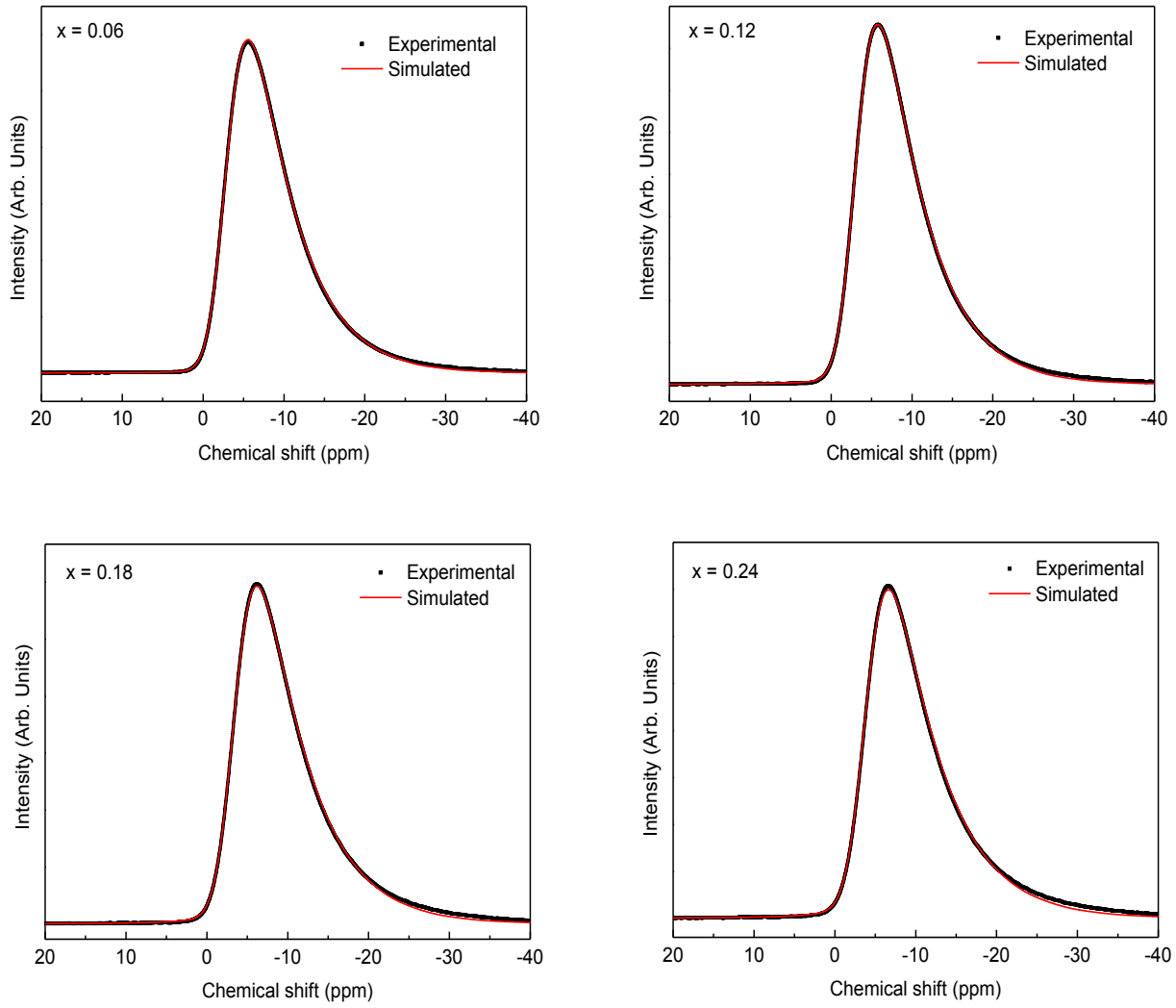

Figure 5.13: Comparison of the experimental and simulated ^{23}Na MAS NMR spectra of selected compositions (x = 0.06, x = 0.12, x = 0.18, x = 0.24) of the (1-x)BNT–(x/2)BLT–(x/2)BKT series.

The NMR parameters were extracted from the ^{23}Na MAS NMR spectra for all the compositions using the DMFIT program.[90] Since the observed ^{23}Na MAS NMR spectra has the characteristic line shape of a system which has a distribution of quadrupole coupling constant, as discussed in chapter 3 (Section 3.5) the 'Czjzek' model in the DMFIT program which uses the

Gaussian isotropic model (GIM)[90] is used for fitting. The NMR parameters, mean isotropic shift (δ_{iso}), chemical shift distribution (Δ_{CS}) and a mean quadrupolar product (C_Q^*) are extracted from the MAS NMR spectra using the DMFIT program and the parameters are listed in Table 5.3. The simulated and experimental spectra of the different compositions are shown in Figure 5.13 and it can be seen that the experimental and simulated spectra match very well.

Table 5.3: Parameters extracted from the ^{23}Na MAS NMR spectra using.

x	**δ_{iso}(ppm)**	**C_Q^*(kHz)**	**Δ_{CS} (ppm)**
x = 0	-2.31	1084	3.99
x = 0.06	-2.49	1136	3.94
x = 0.12	-2.70	1140	3.91
x = 0.18	-3.03	1168	3.98
x = 0.24	-3.43	1179	4.04

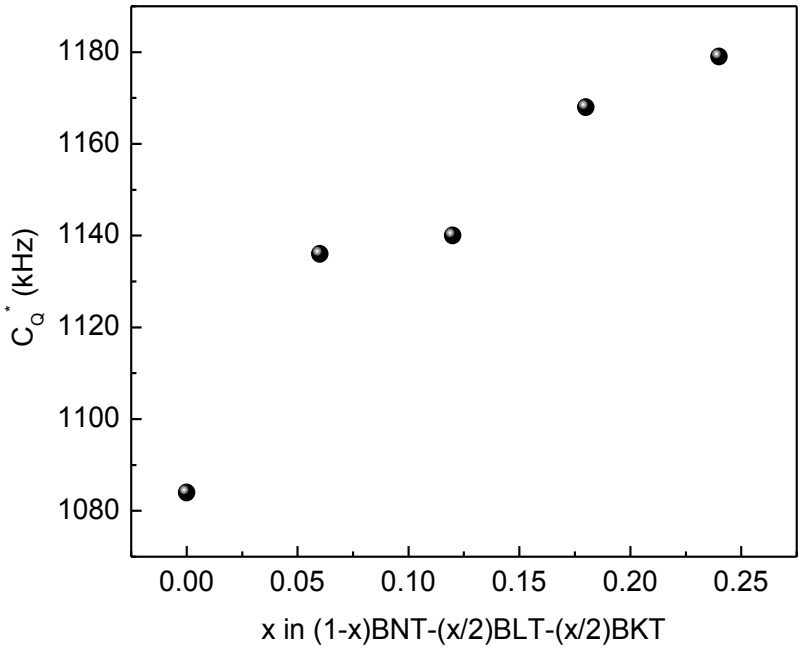

Figure 5.14: Variation of ^{23}Na C_Q^* of (1-*x*)BNT–(*x*/2)BLT–(*x*/2)BKT as a function of *x*.

The variation of the quadrupolar coupling (C_Q^*) with substitution is shown in Figure 5.14. The C_Q^* of the (1-x)BNT–(x/2)BLT–(x/2)BKT solid solution increases with substitution which is similar to that observed in the BNT–BLT solid solution series (Section 4.5.1, Figure 4.16). However, in the BNT–BKT solid solution, C_Q^* found to decrease initially with increasing BKT concentration and reached a minimum at $x = 0.15$ and then increases to a maximum in the range $0.20 \leq x \leq 0.26$ (Section 3.5, Figure 3.18). Since C_Q^* is related to the local symmetry environment, higher value of C_Q^* indicates lower symmetry.[91] The changes in C_Q^* with substitution indicate that the local symmetry changes in the BNT lattice. Therefore, in the (1-x)BNT–(x/2)BLT–(x/2)BKT solid solution series, it may be concluded that the symmetry of crystal lattice decreases with substitution.

5.5.2. ^{7}Li NMR

The ^{7}Li MAS NMR spectra, including the full side band profile, for all the composition of the (1-x)BNT–(x/2)BLT–(x/2)BKT are shown in Figure 5.15 (a). Figure 5.15 (b) shows the zoomed spectra of the central region. From the spectra it is seen that on substitution there is an increase in the prominence of the sidebands and an increase in the line broadening which can be attributed to an increase in the quadrupolar coupling constant. The NMR parameters are extracted from the spectra using the DMFIT program. The very sharp lines in the spectra suggest that the quadrupolar coupling constant of ^{7}Li in (1-x)BNT–(x/2)BLT–(x/2)BKT is small. Therefore, the 'quad-first' model in the DMFIT program which includes the first order quadrupolar interaction is used for generating the lineshape,[90] as discussed in chapter 4 (Section 4.5.2). This model includes a Gaussian distribution of isotropic chemical shift with a mean isotropic shift (δ_{iso}), quadrupolar coupling constant (C_Q) and a Lorentzian component. The experimental and simulated ^{7}Li MAS NMR spectra are shown in Figure 5.16. The NMR parameters extracted from the ^{7}Li MAS NMR spectra for all the composition of (1-x)BNT–(x/2)BLT–(x/2)BKT are shown in Table 5.4. Very small variations are observed in the quadrupolar coupling constant C_Q on substitution.

The broad peak in the ^{7}Li spectra is a combination of Gaussian and Lorentzian line shapes and the contributions from each of the components are estimated from the fitting. The Gaussian component of the spectrum indicates the spread of the chemical shift from the ideal value and the Lorentzian component is an indication of the diffusion or mobility of the ions present in the crystal lattice.[120]

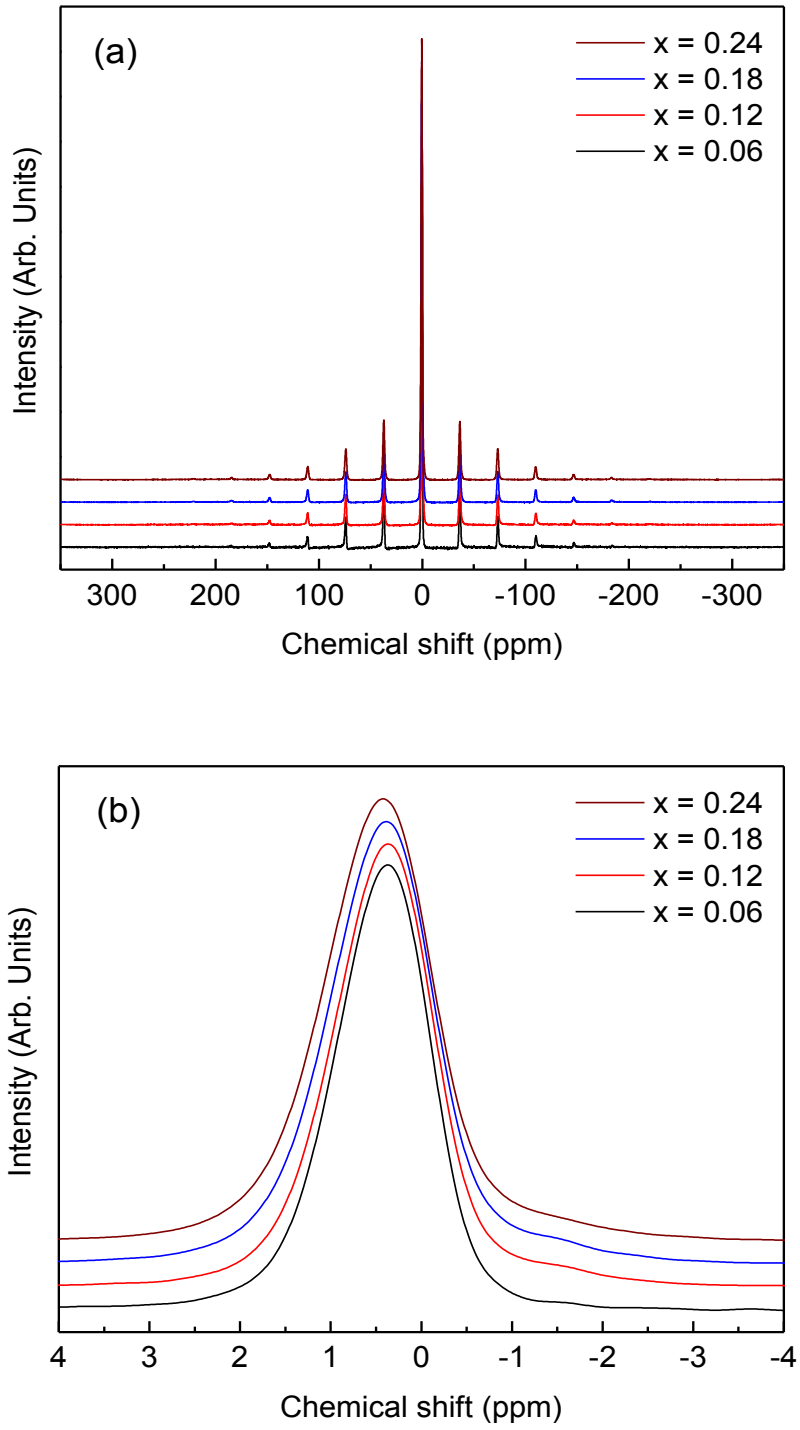

Figure 5.15: (a) ^{7}Li NMR spectra of the different compositions in the (1-x)BNT–(x/2)BLT–(x/2)BKT series, (b) Zoomed view of the central region.

Table 5.4: Parameters extracted from the ^{7}Li MAS NMR spectra using.

x	δ_{iso} (ppm)	Width(ppm)	G/L	C_Q(kHz)
x = 0.06	0.42	1.22	0.80	45.13
x = 0.12	0.41	1.28	0.68	45.33
x = 0.18	0.44	1.35	0.62	45.31
x = 0.24	0.47	1.39	0.61	45.18

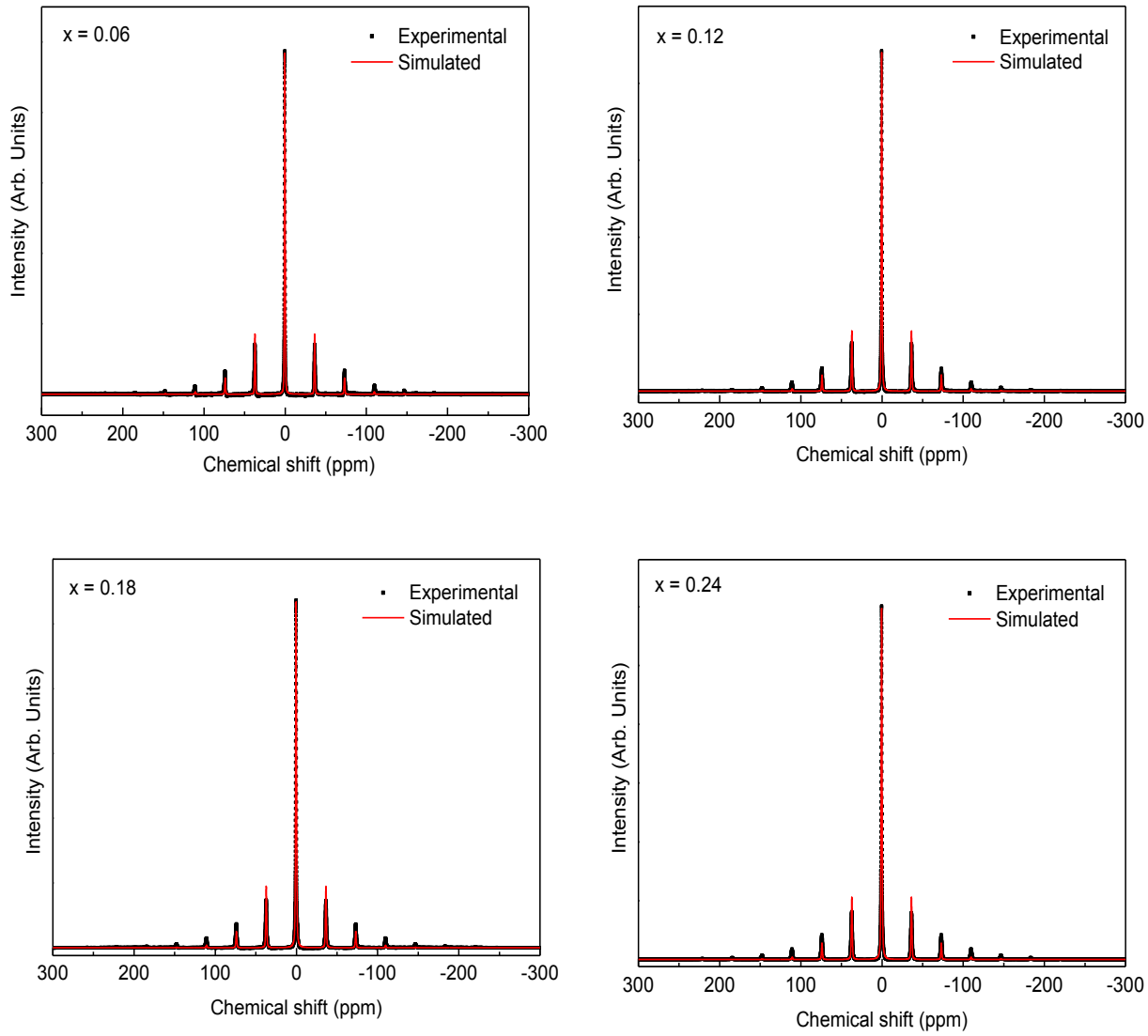

Figure 5.16: Comparison of the experimental and simulated ^{7}Li MAS NMR spectra of selected compositions (x = 0.06, x = 0.12, x = 0.18, x = 0.24) of the (1-x)BNT–(x/2)BLT–(x/2)BKT series.

The Gaussian to Lorentzian component ratio (G/L) obtained from the fit is tabulated in Table 5.4. It is observed that on increasing the BLT concentration, the G/L ratio of the ^{7}Li NMR spectrum decreases which means that the line shape becomes more Lorentzian. The variations of the Gaussian and Lorentzian components are shown in Figure 5.17. The increase in the Lorentzian component with BLT concentration indicates the rise in Li^+ ion diffusion in the crystal lattice. When the concentration of the substituents is increased, the Li^+ content in the BNT lattice is increased which results in an increase in the mobility of Li^+ ions in the crystal lattice. This can be correlated with the decrease in the area of the Raman band below 180 cm^{-1} with substitution. The decrease in the area is due to the weak Li-O vibrations due to the Li^+ ion diffusion in the BNT crystal lattice.

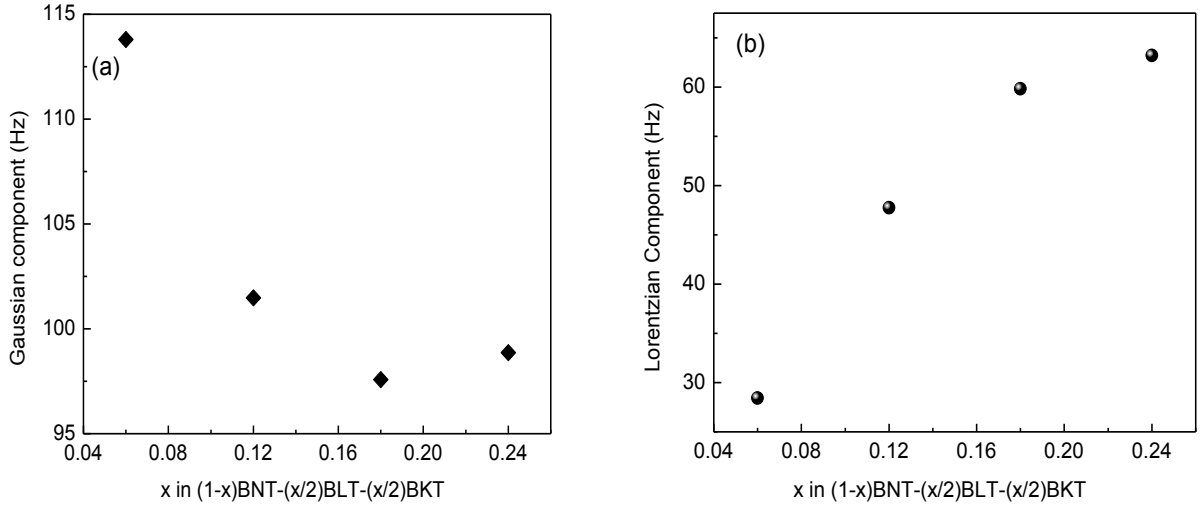

Figure 5.17: Variations of (a) Gaussian and (b) Lorentzian components of ^{7}Li spectra as a function of x in (1-x)BNT–(x/2)BLT–(x/2)BKT.

The increase in ^{23}Na and ^{7}Li quadrupolar coupling constant indicate the increased distortion in the BNT crystal lattice with substitution. The increase in Lorentzian component indicate an increase in diffusion of Li^+ ions in the BNT lattice with substitution and this can be correlated to the decrease observed in the area under the 180 cm^{-1} peak of the Raman spectra.

5.6. Scanning electron microscopy

SEM micrographs of different compositions of (1-x)BNT–(x/2)BLT–(x/2)BKT are shown in Figure 5.18.

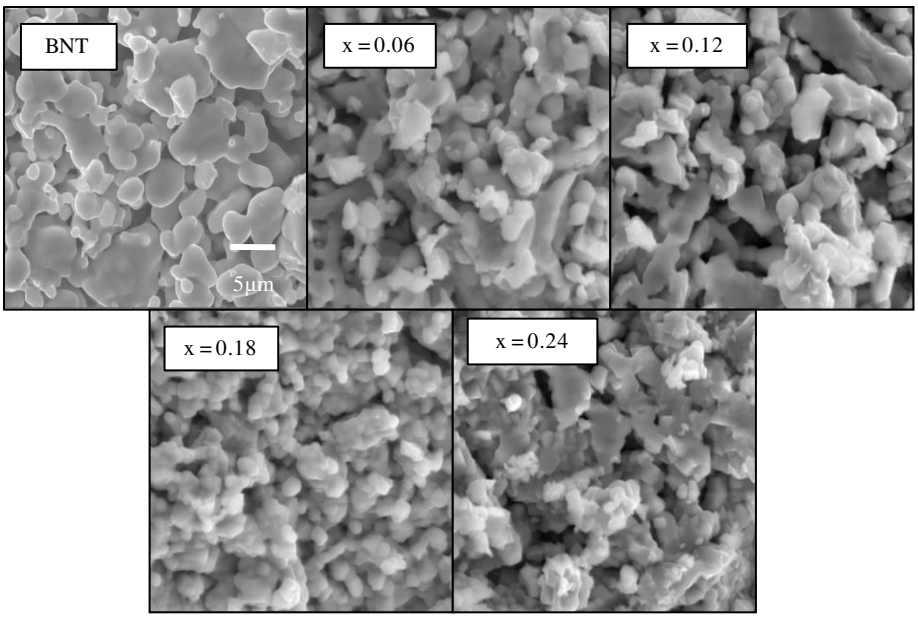

Figure 5.18: SEM images micrographs of different compositions in the (1-x)BNT–(x/2)BLT–(x/2)BKT series. The scale shown is common for all images.

Table 5.5: Density and grain size of different compositions in the (1-x)BNT–(x/2)BLT–(x/2)BKT series.

Sample	**Grain size (μm)**	**Measured Density (g/cm^3)**	**Theoretical density (g/cm^3)**
BNT	7.5	3.52	5.96
x= 0.06	2.6	3.79	5.99
x=0.12	2.2	3.83	5.99
x=0.18	1.8	3.97	5.98
x=0.24	1.2	3.83	5.97

The microstructure of the ceramics has changed with substitution. The grain size is decreased with substitution and more pores are observed in the substituted compositions. The average grain size of the ceramics and density are compared in Table 5.5. The grain size of BNT is ~7.5 μm and with substitution the grain size has decreased. The grain size of maximum substituted composition is ~1.2 μm. Compared to the microstructure of BNT, the substituted compositions have more fused and porous grains. Relatively large grains of size ~10 μm are observed for BNT in the BNT–BKT solid solution due to the high sintering temperature

(1150 ^oC) used and the difference in synthetic methods (Section 3.6). In BNT–BKT solids solution the grains are reasonably larger in size and less porous. In the BNT–BLT solid solution also relatively larger grains are observed (Section 4.6).

5.7. Density

The variation in the density as function of x is shown in Figure 5.19. The density of the ceramics has increased with substitution. It is observed from the microstructure analysis that the grain size of the ceramics decreased with substitution and this led to increase in the density. Comparison of theoretical and measured densities of the ceramics is shown in Table 5.5.

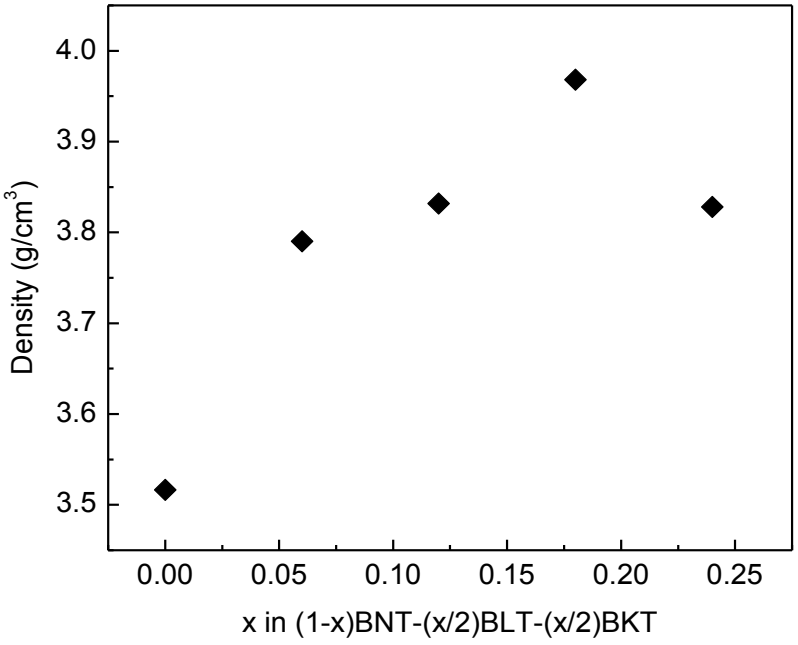

Figure 5.19: Variation of the sintered density of (1-x)BNT–(x/2)BLT–(x/2)BKT as a function of x.

Higher densities are reported for Li^+ and K^+ co-substituted BNT solid solution series (> 5.5) which is almost comparable to that of the theoretical density of the ceramics.[118] The measured density in the present work is ~ 60% of the theoretical density. This low value is due to the difference in the synthesis, processing conditions, lower compaction pressure (8 Mpa) used for making pellets and the low sintering temperature (1000 ^oC) in the present study. In BNT–BKT solid solution, the ceramics possess higher density due to the difference in microstructure nature (Section 3.7) where as the densities of the ceramics in BNT–BLT solid

solution is comparable (Section 4.7). The comparable density observed may be due to the same synthetic method and sintering temperature (1000 ^oC) used for BNT–BLT and BNT–BLT–BKT solid solution whereas higher sintering temperature (1150 ^oC) and different synthetic method changed the microstructure nature of BNT–BKT solid solution and a consequent increase in the density of the ceramics.

5.8. Dielectric constant

The dielectric constant of all the compositions of (1-x)BNT–(x/2)BLT–(x/2)BKT are measured at 1 kHz and the variation of the dielectric constant with substitution is shown in Figure 5.20. The dielectric constant of the ceramics gradually increased with the degree of substitution.

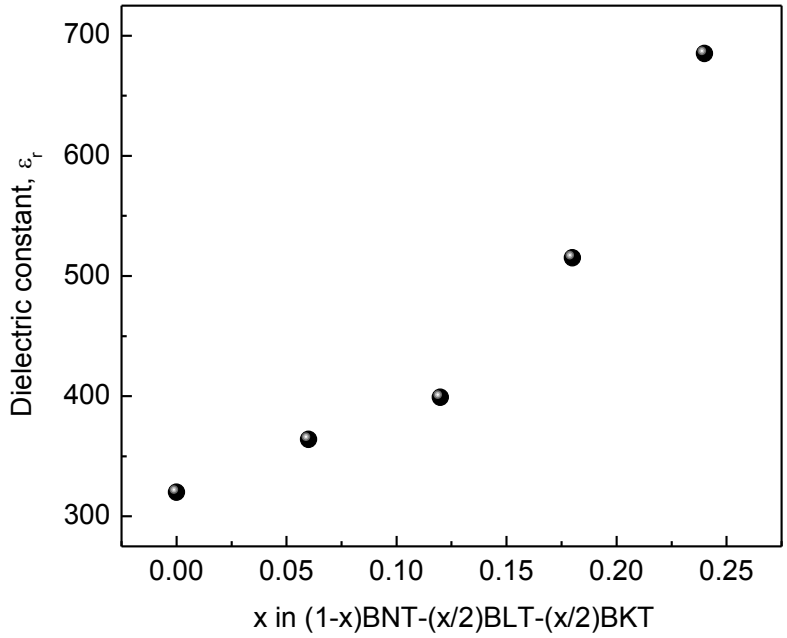

Figure 5.20: Variation of the dielectric constant of (1-x)BNT–(x/2)BLT–(x/2)BKT as function of x.

The (1-x)BNT–(x/2)BLT–(x/2)BKT solid solutions show higher values for dielectric constant compared to the BNT–BLT solid solution reported in the previous chapter (Section 4.8). The measured dielectric constant for maximum Li^+ substituted composition (x = 0.24) in (1-x)BNT–(x/2)BLT–(x/2)BKT is 685 whereas the dielectric constant of same Li^+ concentration (x = 0.12) in the BNT–BLT solid solution series is obtained as 402. Since the densities of both the solid solution series are almost comparable (~ 4 g/cm^3) and the sintering temperature and

processing conditions are the same, the difference in the dielectric constants is due to the structural distortion caused by the larger K^+ ions in the (1-x)BNT–(x/2)BLT–(x/2)BKT series. However, compared to the BNT–BKT solid solution series (Chapter 3, Section 3.8), the dielectric constant of the (1-x)BNT–(x/2)BLT–(x/2)BKT solid solution is relatively low. This could be due to the higher sintering temperature used for the BNT–BKT solid solution; and hence the compositions possess higher density. Additionally, larger distortion caused by the K^+ ion in the BNT lattice results in the formation of MPB region in the BNT–BKT solid solution series leading to a more polarized crystal structure. The reported dielectric constants for the (1-x)BNT–(x/2)BLT–(x/2)BKT compositions are larger than that obtained in the present study.[115,116,118] In all the reported studies, the synthesis methods are different and high sintering temperatures (1100-1200 ^oC) are used. Moreover, the pressure used for the compaction of the pellets is higher (160 MPa) in the literature reports, compared to the low compaction pressure used in the present study (8 MPa) which led to higher density and dielectric properties.

5.9. Structure-property correlations

Detailed XRD studies on all the compositions of (1-x)BNT–(x/2)BLT–(x/2)BKT suggested the absence of any phase transition in this solid solution series. However, the minor changes in the lattice parameters and cell volume indicated slight distortions in the crystal symmetry with substitution which led to changes in the microstructure and hence an increase in the density. The additional mode observed in the Raman band below 180 cm^{-1} for the composition x = 0.24 and the increase in the quadrupolar coupling constant of the ^{23}Na MAS NMR spectra with substitution specify the distortion and polarization in the crystal lattice. The increase in the dielectric constant is due to the increased polarization and density with substitution. ^7Li NMR studies showed an increase in the Lorentzian component with substitution that can be correlated with the decrease in the area of the Raman band below 180 cm^{-1}.

All the studies on (1-x)BNT–(x/2)BLT–(x/2)BKT showed a close correlation between the structure and the properties. Changes in some of the structural parameters and properties with Li^+ and K^+ co-substitution show similar trends. Figure 5.21 compares the changes in the lattice parameter '*b*', dielectric constant and the area under the Raman band in the region 200-400 cm^{-1}. All the three parameters increased with substitution and show similar trend in the variation with substitution indicating that the changes in the dielectric constant is related to the structural

changes. Figure 5.22 compares the density, quadrupolar coupling constant of ^{23}Na MAS NMR and the position of the 2nd peak in the Raman band in the 200-400 cm^{-1} region with Li^+ and K^+ co-substitution. All the three parameters show similar trend in the changes with substitution and increased with substitution. The changes in lattice parameter, '*b*', specifies the structural changes. 200-400 cm^{-1} region of the Raman band is associated with the Ti-O vibration and hence, the changes in the area of this band and position of individual peaks within this band, with substitution, show the changes in the Ti-O bonds. The increase in C_Q^* is an indication of a decrease in the local symmetry. The changes in Ti-O bond with substitution contribute to the symmetry changes and density of the ceramics. Hence, it may be concluded that the structural changes and the changes in the Ti-O bonds with substitution has affected the polarization of the (1-x)BNT–(x/2)BLT–(x/2)BKT solid solution that contributed to the dielectric properties. Figure 5.23 compares the changes in the Li NMR Gaussian component and the area under the peak 180 cm^{-1} in the Raman spectra. Both the parameters decreased with the co-substitution of Li^+ and K^+ in the BNT lattice and showed similar changes. As the concentration of Li^+ increased with substitution the diffusion of the Li^+ ions in the crystal lattice increased as a result the area under the 180 cm^{-1} Raman band and the Gaussian component decreased.

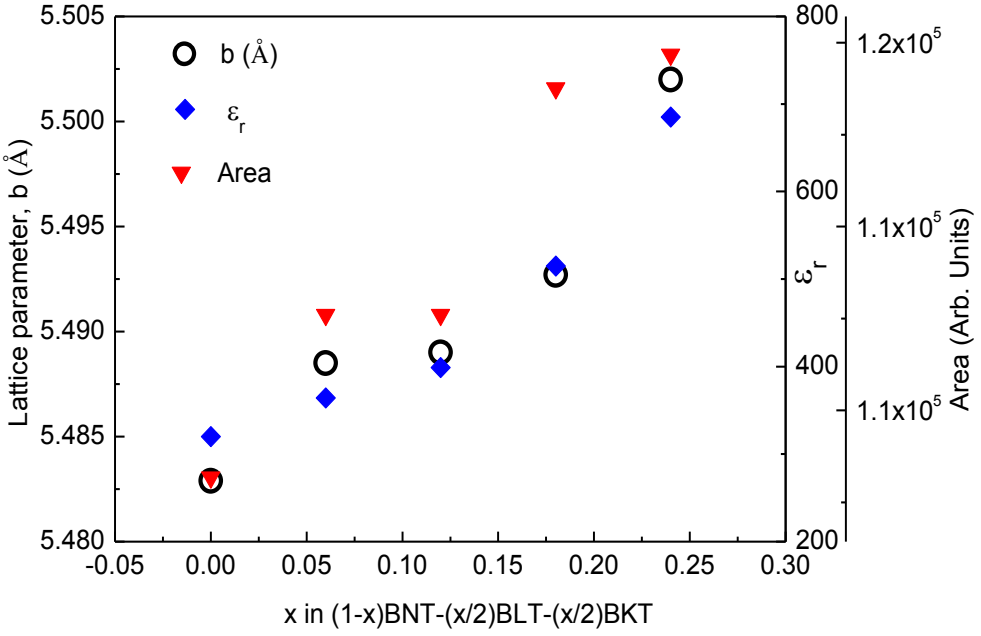

Figure 5.21: Comparison of lattice parameter '*b*', dielectric constant (ε_r) and area under the Raman band in the 200-400 cm^{-1} region.

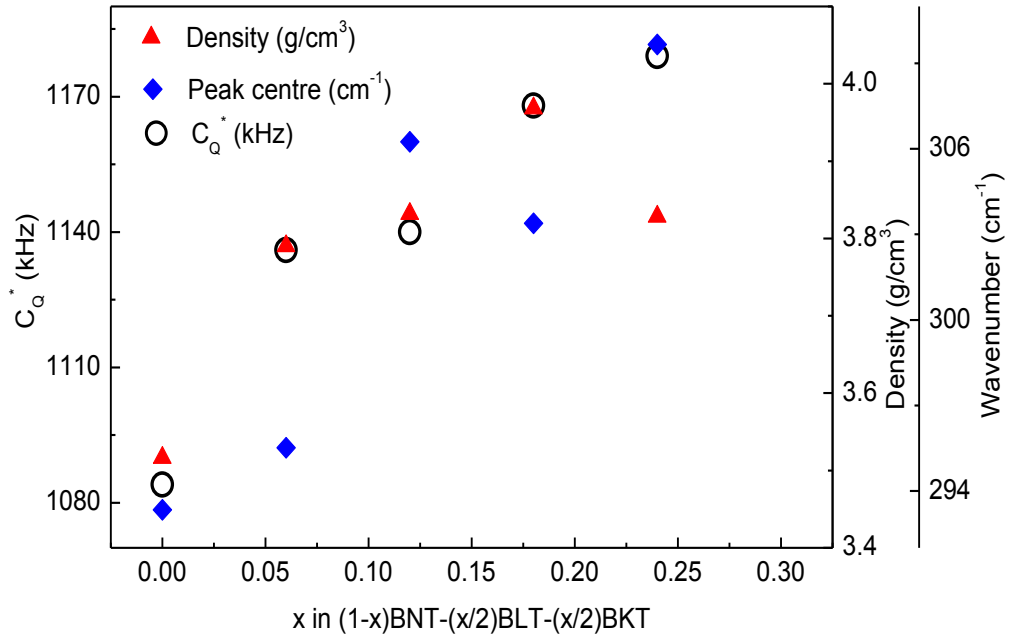

Figure 5.22: Comparison of density, quadrupolar coupling of ^{23}Na and the peak centre of the second band in the 200-400 cm^{-1}region of the Raman spectra.

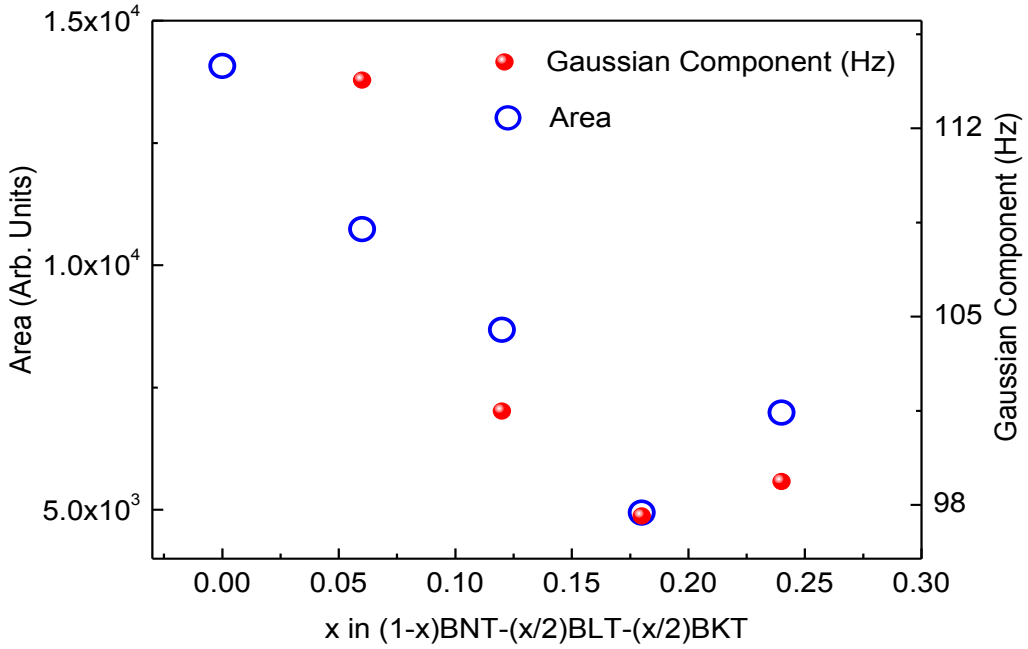

Figure 5.23: Comparison of ^{7}Li NMR Gaussian component and the area under the peak below 180 cm^{-1}in (1-x)BNT-(x/2)BLT-(x/2)BKT solid solution.

5.10. Conclusions

Rietveld refinement analysis of the XRD patterns of all the compositions of (1-x)BNT–(x/2)BLT–(x/2)BKT confirmed the formation of all the compositions under the monoclinic Cc space group of BNT, without any phase transition. The changes in lattice parameters and cell volume with substitution suggested minor distortions in the crystal lattice. Raman spectral analysis also supports the conclusions drawn from the Rietveld refinement analysis of the XRD patterns. The additional band observed below 180 cm^{-1} of the composition with x = 0.24 is an indication for distortions in the crystal lattice. The decrease in the area of the band below 180 cm^{-1} with substitution suggests Li^+ ion diffusion and local symmetry changes. Evidence for local symmetry changes is further obtained from the NMR studies of the (1-x)BNT–(x/2)BLT–(x/2)BKT solid solution. Evidence for structural distortion and decrease in the local symmetry are evident from the observed increase in the quadrupolar coupling of ^{23}Na MAS NMR. The ^7Li NMR studies proved the diffusion of Li^+ ions in the crystal lattice. The microstructure of the ceramics changed with substitution, and hence the density of the ceramics is found to be increasing with x. A corresponding increase in the dielectric constant is observed with increasing degree of substitution. This is due to the local structural changes as evidenced from the solid-state NMR studies.

Chapter 6

Studies on (1-*x*)$Bi_{0.5}Na_{0.5}TiO_3$–*x*$La_{0.5}Na_{0.5}TiO_3$ Series

6.1. Introduction

$Bi_{0.5}Na_{0.5}TiO_3$(BNT) shows excellent piezoelectric and ferroelectric characteristics, which initiated studies on its application as a lead-free piezoelectric material for various applications. BNT's extended strain under an applied electric field goes beyond that of $PbTi_{1-x}Zr_xTiO_3$ (PZT).[110] In BNT, Pb^{2+}in $PbTiO_3$ is replaced by the ($Bi_{0.5}{}^{3+}Na_{0.5}{}^{1+}$) combination. In $BaTiO_3$, ferroelectricity arises from the distorted TiO_6 octahedra, while in the case of $PbTiO_3$, in addition to the contribution from the TiO_6 octahedra, hybridization between Pb 6s and O 2p states cause large tetragonal distortion which results in high electromechanical properties.[122] Similarly, in the related ferroelectric materials containing Bi, the role of Bi^{3+} for the origin of ferroelectricity is very well established. For example, in $BiMnO_3$, the $6s^2$ lone pair of the Bi^{3+} ion is responsible for ferroelectricity.[123] The $6s^2$ lone pair of Bi^{3+} ion tends to hybridize with oxygen 2p orbital and this improves the ferroelectricity by pushing the Bi^{3+} ions towards the oxygen atom. Similarly in $BiFeO_3$, the lone pair orbital in Bi^{3+} is steriochemically active and it causes distortion in the crystal structure. The polarization caused by the $6s^2$ lone pair is responsible for the ferroelectricity in $BiFeO_3$.[124]

It is possible that in $Bi_{0.5}Na_{0.5}TiO_3$, the $6s^2$ lone pair present in the Bi^{3+} ion also contribute to ferroelectricity apart from the contribution from the distorted TiO_6 octahedra. The effective way of understanding the role of the $6s^2$ lone pair in Bi^{3+} ion is to replace Bi^{3+} with an ion which has almost comparable size and charge. Hiruma *et al* found that the rhombohedral-tetragonal phase transition temperature (T_d) decreases and the temperature at which maximum dielectric constant is observed (T_m) increases, from the studies on the substitution of La^{3+}, Nd^{3+}, Ho^{3+} and Yb^{3+} in BNT, for the cation deficient compositions $(Bi_{50}.Na_{0.5})_{(1-1.5x)}Ln_xTiO_3$, and it is found that the changes depend on the ionic size of the substituent.[125] Cheah *et al* observed that addition of La in the BNT structure caused lattice distortions and the symmetry changed from tetragonal to hexagonal in $(Bi_{50}.Na_{0.5})_{(1-1.5x)}La_xTiO_3$.[126] Also, La-substitution is found to increase the densification of BNT and suppress its ferroelectricity. Yi *et al* investigated the sintering and electrical characteristics of La-modified BNT ceramics and observed that doping reduced the grain size by suppressing the grain growth and enhancing the densification process.[127] Aparna *et al* carried out dielectric, impedance and admittance spectroscopy studies of La doped BNT, $Na_{0.5}(La_xBi_{1-x})_{0.5}TiO_3$ for x = 0, 0.1, 0.15, 0.2, in a particular temperature range (from room

temperature to 550 ^oC) and in the frequency range of 100 Hz to 1 MHz and correlated the structural phase transition with the changes in the composition, frequency and temperature.[128] The authors observed a decrease in the electromechanical coupling coefficient with La-doping. Aparana *et al*, in another study, observed that the incorporation of La^{3+} in the BNT lattice causes lattice distortion and the properties show relaxation due to the changes in the structure.[129] The authors also observed that the dielectric constant decreased with La substitution.

The main objective of the present work is to study the structural changes on substitution of Bi^{3+} in BNT by La^{3+} using Raman and solid state NMR spectroscopy as well as Rietveld refinement analysis of powder XRD patterns. Since the ionic radii of Bi^{3+} and La^{3+} are almost the same (Bi^{3+} = 1.17 Å, La^{3+} = 1.16 Å, for eight fold coordination), distortion in the TiO_6 octahedra and any structural phase transformation are not expected. Hence, any changes in the dielectric properties could be associated with the $6s^2$ lone pair present in Bi^{3+} ion.

There are various studies on the crystal structure and properties of $La_{0.5}Na_{0.5}TiO_3$. Early structural studies reported that $La_{0.5}Na_{0.5}TiO_3$ has a $R\bar{3}c$ structure with the $a^-a^-a^-$ tilt system. Later studies on the $La_{0.5}Na_{0.5}TiO_3$ crystal structure reported better refinements with space group Pnma with the $a^- b^+ a^-$ tilt system.[130] Li *et al* reported that $La_{0.5}Na_{0.5}TiO_3$ crystallizes in the tetragonal space group I4/mcm.[131] Geneste *et al* studied the structural and dynamical properties of $La_{0.5}Na_{0.5}TiO_3$ and suggested that $La_{0.5}Na_{0.5}TiO_3$ is a quantum paraelectric and its ferroelectric instabilities are weaker than $SrTiO_3$.[132] They also predicted a strong anisotropy in the dielectric response of $La_{0.5}Na_{0.5}TiO_3$. Investigations on the structural and dielectric properties of $La_{0.5}Na_{0.5}TiO_3$ using X-ray and neutron diffraction experiments and density functional calculation revealed the high temperature paraelectric character of it dielectric constant.[133] The chemical disorder in the A site of $La_{0.5}Na_{0.5}TiO_3$ decrease the magnitude of the structural distortion and lowers the dielectric response. Low ferroelectricity and quantum paraelectric nature is due to the weak ferroelectric instabilities observed in the $La_{0.5}Na_{0.5}TiO_3$. Inaguma *et al* observed that the dielectric constant of $La_{0.5}Na_{0.5}TiO_3$ is independent of frequency in the range 5-600 kHz and for T < 30 K the dielectric constant is independent of temperature which proves the quantum mechanical stabilization of the paraelectric phase below 30 K.[133]

Different compositions of the solid solution series (1-x)$Bi_{0.5}Na_{0.5}TiO_3$–$xLa_{0.5}Na_{0.5}TiO_3$ ($0 \leq x \leq 0.4$) are synthesized and the structural changes probed. Dielectric properties, density and microstructure are studied and correlated with the structural changes.

6.2. Synthesis

Different compositions in the (1-x)$Bi_{0.5}Na_{0.5}TiO_3$–$xLa_{0.5}Na_{0.5}TiO_3$ ($0 \leq x \leq 0.04$) solid solutions were prepared by the citrate-gel method, where x = 0, 0.1, 0.2, 0.3, and 0.4.

Table 6.1: Compositions in the (1-x)$Bi_{0.5}Na_{0.5}TiO_3$–$xLa_{0.5}Na_{0.5}TiO_3$ series and the corresponding sample codes.

x	**Composition** **(1-*x*)$Bi_{0.5}Na_{0.5}TiO_3$–*x*$La_{0.5}Na_{0.5}TiO_3$** **(1-*x*)BNT–*x*LNT**	**Sample code**
0	BNT	BNT
0.1	0.9BNT–0.1LNT	0.1LNT
0.2	0.8BNT–0.2LNT	0.2LNT
0.3	0.6BNT–0.3LNT	0.3LNT
0.4	0.8BNT–0.4LNT	0.4LNT

Solutions of stoichiometric amounts of bismuth nitrate ($Bi(NO_3)_3.5H_2O$), sodium nitrate ($NaNO_3$) and lanthanum nitrate ($LaNO_3.6H_2O$) were made separately by dissolving bismuth nitrate in dilute nitric acid and the nitrates of sodium and lanthanum in distilled water and mixed together. Stoichiometric amount of titanium isopropoxide ($Ti[OCH(CH_3)_2]_4$) was dissolved in isopropyl alcohol and citric acid was dissolved in this solution with continuous stirring. The ratio of citric acid to total metal ion was taken as 3:1. The mixed metal nitrate solution was added to the titanium isopropoxide solution with constant stirring and then evaporated at 60 ^oC on a hot plate until a transparent viscous gel was obtained. A foam was obtained after heating the dried gel overnight at 150 ^oC. The foam was then crushed using a mortar to fine powder. This powder was initially calcined at 400 ^oC, and then at 850 ^oC and 1000 ^oC with intermediate grindings. The powder samples obtained were uniaxially pressed into circular discs (10 mm diameter x 3 mm height) at a pressure of 8 MPa and sintered at 1200 ^oC for 2 hours. All the samples were sintered

under identical conditions at heating and cooling rates of 5 ^oC/min. The sintered pellets were crushed in to fine powder and used for XRD, Raman spectroscopy and solid-state NMR studies. The synthesized compositions and the corresponding sample codes are listed in Table 6.1.

6.3. Powder X-ray diffraction

All the samples are initially characterized by powder XRD to verify formation of single phase compositions. Figure 6.1 shows the powder XRD patterns of all the compositions and the simulated pattern of BNT using the structural parameters of the monoclinic Cc space group.[105] All peaks in the XRD patterns of the different compositions match very well with the simulated pattern of BNT, without any additional peaks, indicating formation of single phase compositions.

Table 6.2: Lattice parameters, reduced χ^2 and R_p values of (1-*x*)BNT–*x*LNT obtained from Rietveld analysis.

Sample	**Cc**				χ^2	R_p (%)
	a (Å)	**b (Å)**	**c (Å)**	**β (degrees)**		
BNT	9.5261	5.4832	5.5089	125.42	2.065	5.18
0.1LNT	9.5102	5.4907	5.4911	125.26	2.959	5.46
0.2LNT	9.509	5.484	5.495	125.30	2.765	5.28
0.3LNT	9.5142	5.4857	5.4847	125.25	2.336	5.04
0.4LNT	9.5098	5.4843	5.4838	125.21	2.399	5.15

Detailed structural analysis has been carried out by Rietveld refinement of the XRD patterns of all the compositions of the BNT–LNT series. Reasonable agreement is obtained with the experimental and simulated patterns, with low reduced χ^2 and R_p values as shown in Table 6.1, using the monoclinic Cc space group of BNT. Figure 6.2 shows the results of the Rietveld refinement analysis of all the studied compositions in the (1-*x*)BNT–*x*LNT series. The refinement results confirmed the formation of all the compositions under the monoclinic Cc space group. Aparna *et al* reported a phase transition at x~0.075 in the BNT-LNT solid solution and observed an anomaly in the dielectric constant in this region.[129] Cheah *et al* observed that the crystal symmetry of BNT changed from hexagonal to tetragonal with La substitution in the cation deficient compositions $(Bi_{50}.Na_{0.5})_{(1-1.5x)}La_xTiO_3$.[126] The authors reported that the solubility of La

in the BNT lattice reached its limit at 10 mol% and a secondary phase of $Bi_2Ti_2O_7$ formed at higher La compositions.

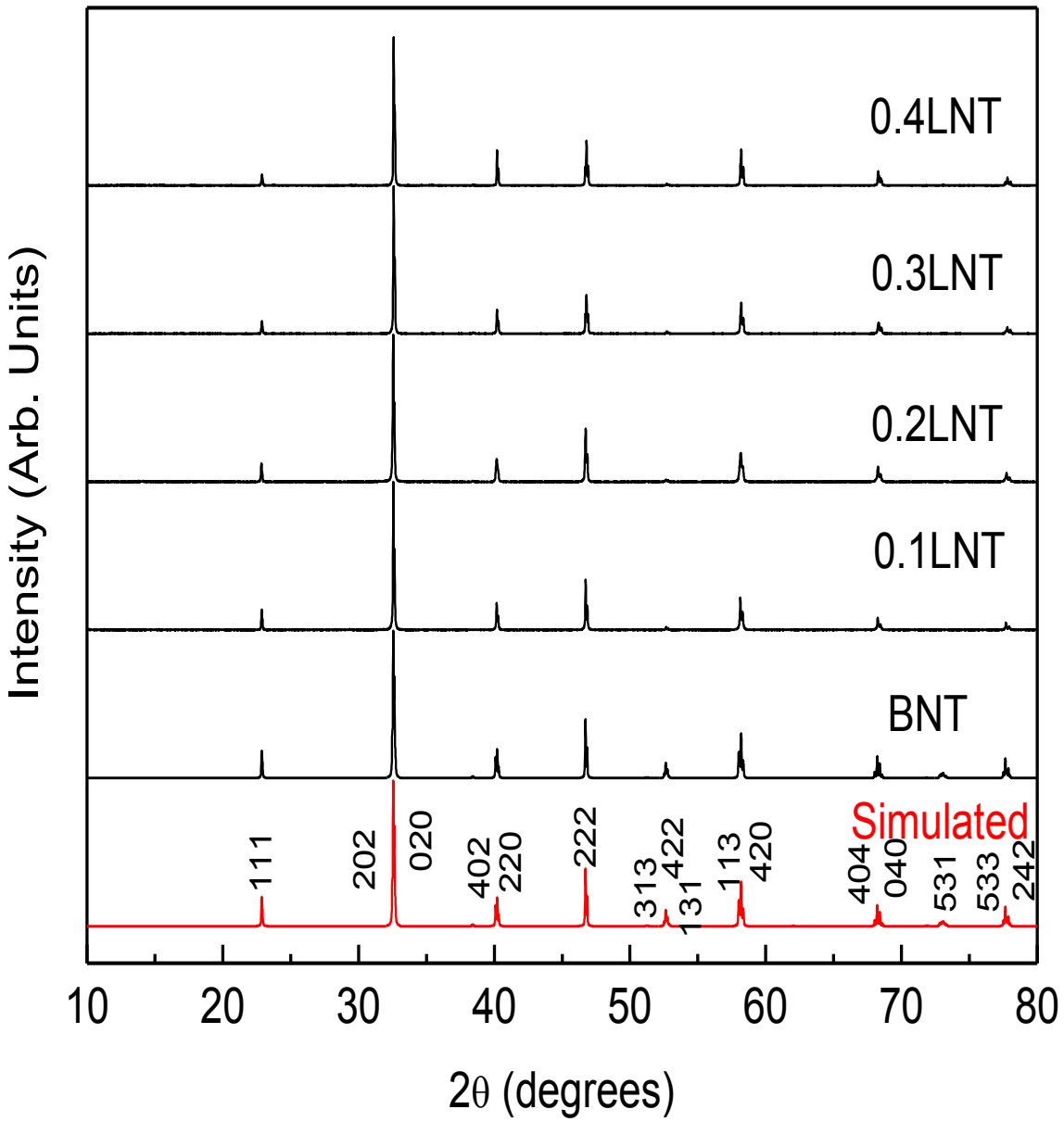

Figure 6.1: Powder XRD patterns of different compositions in (1-x)BNT–xLNT solid solution series. Simulated pattern of BNT is shown at the bottom for comparison.

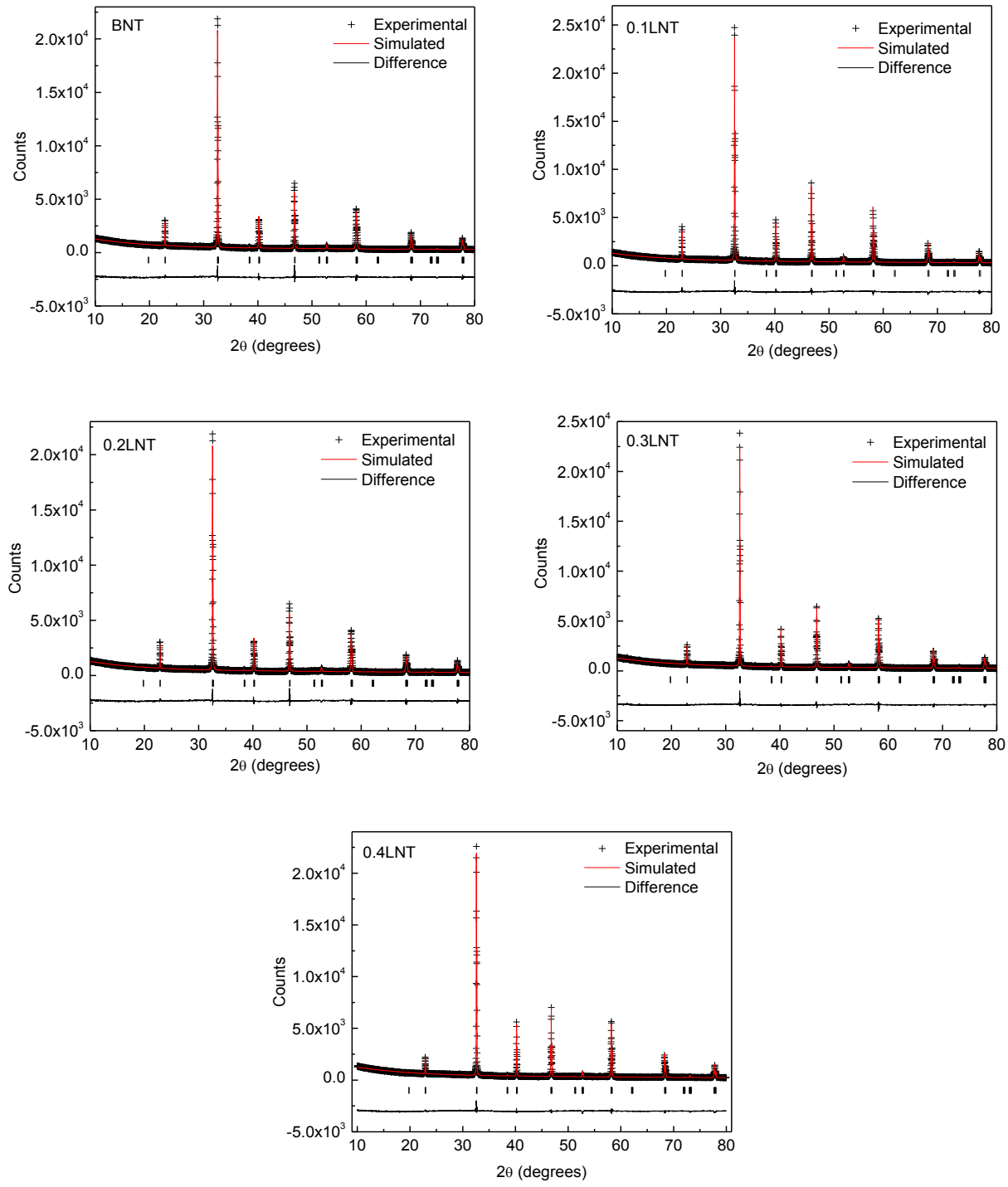

Figure 6.2: Results of the Rietveld refinement of (1-x)BNT–xLNT using monoclinic Cc space group, for BNT, 0.1LNT, 0.2LNT, 0.3LNT, 0.4LNT.

The present study on the stoichiometric compositions (1-x)$Bi_{0.5}Na_{0.5}TiO_3$–$xLa_{0.5}Na_{0.5}TiO_3$ shows that single phase compositions are obtained in the entire

compositional range, with monoclinic structure and without any structural phase transition. This is expected because of the comparable ionic sizes of Bi^{3+} and La^{3+}.

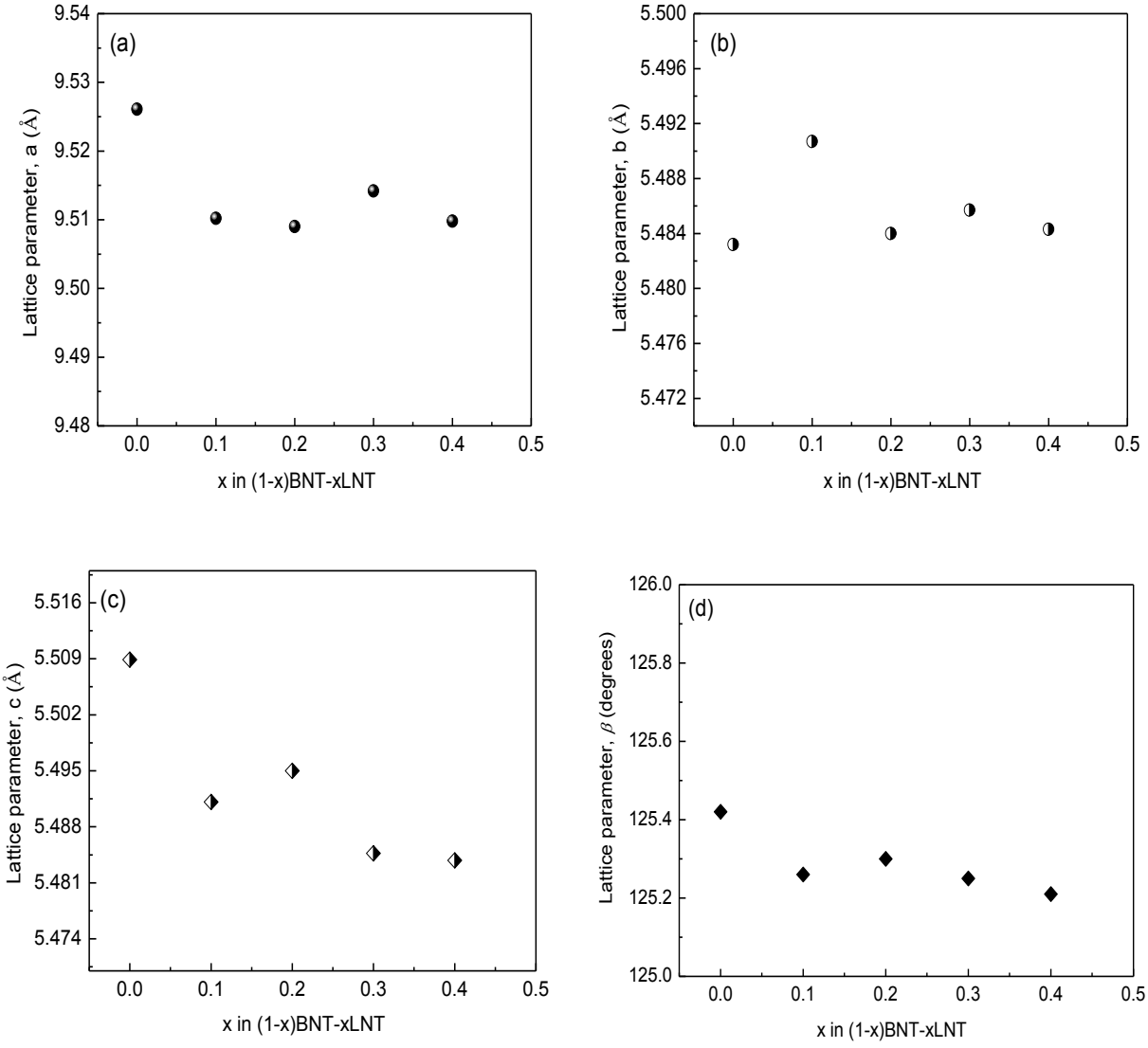

Figure 6.3: Variation of monoclinic lattice parameters (a) '*a'*, (b) '*b'*, (c) '*c'* and (d) angle β of (1-x)BNT–xLNT solid solution as a function of x.

The variations of the lattice parameters '*a'*, '*b'*, '*c'* and the monoclinic angle β obtained from the Rietveld refinement analysis, as a function of La^{3+} concentration in (1-x)BNT–xLNT, are shown in Figure 6.3.Very small decrease in all the lattice parameters and unit cell volume are observed. This is due to the minor difference in the ionic sizes of Bi^{3+} and La^{3+} as well as the reduced contribution from the $6s^2$ lone pair in the Bi^{3+} ion which is absent in the La^{3+} ion.

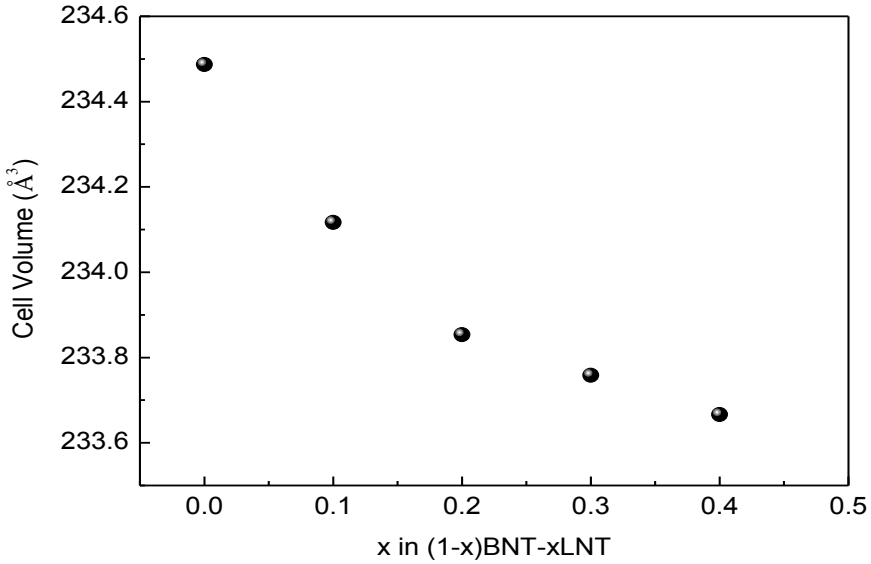

Figure 6.4: Variation of unit cell volume of (1-x)BNT–xLNT solid solution series as a function of x.

6.4. Raman spectroscopy

Raman spectra of different compositions of (1-x)BNT–xLNT are shown in Figure 6.5. As the concentration of La increased, the band below 180 cm^{-1} has broadened. The bands in the 200–400 cm^{-1} and 400–700 cm^{-1} regions also show changes with substitution. A notable change is the decrease in broadening and increase in the intensity of the latter band with La-substitution.

Raman spectra of all the compositions of (1-x)BNT–xLNT are deconvoluted to Gaussian peaks and the Raman parameters are extracted. The Raman spectrum of BNT is deconvoluted to 7 Gaussian peaks, as discussed in chapter 3 (section 3.4). The band below 180 cm^{-1} is fitted with one peak. The 200–400 cm^{-1} region is deconvoluted to 3 peaks and the 400–700 cm^{-1} region also is deconvoluted in to 3 peaks. The band below 180 cm^{-1} in the Raman spectra of x = 0.1, 0.2, 0.3 and 0.4 could be deconvoluted into two peaks and for the corresponding compositions, the band in the 200–400 cm^{-1} region could be deconvoluted in to two peaks. Thus, one of the peaks in the 200–400 cm^{-1} region in the spectra of BNT is shifted to lower frequencies, due to the substitution of Bi by La. It has been reported that in the Raman spectra of $La_{0.5}Na_{0.5}TiO_3$ and $La_{2/3-x}Na_xTiO_3$,[134,130] three main phonons are present in the band below 180 cm^{-1} in which two peaks are due to the Ti displacement and the third one belongs to the A-site displacement.

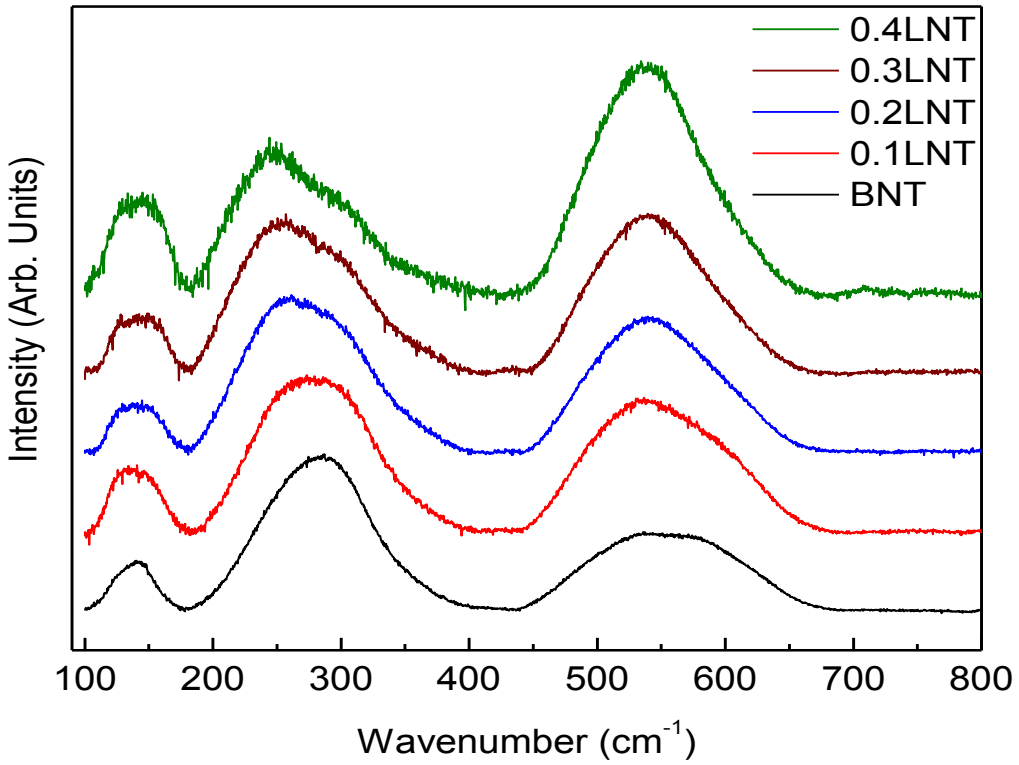

Figure 6.5: Raman spectra of different compositions of (1-x)BNT–xLNT.

The phonon in the 200–400 cm^{-1} region is associated with the A-site cation displacement. The high frequency region (400–700 cm^{-1}) belongs to the oxygen movements in the TiO_6 octahedra. Thus, the additional peak in the band below 200 cm^{-1} is likely to be due to the contribution from Ti-O vibrations, caused by the presence of La in the structure. It is possible that one of the contributions from the Ti-O vibrations is shifted to lower frequencies so that the band in the 200–400 cm^{-1} region consists of only two peaks. The deconvoluted Raman spectra of all the compositions are shown in Figure 6.6. The changes in the Raman spectra of BNT on substitution of La could be due to the local symmetry changes caused by the reduced effect of $6s^2$ lone pair with La substitution and the large difference in the atomic mass of Bi and La.

Due to the high mass of bismuth, the Bi-O vibrations are expected in the low frequency region.[70] Hence, the band below 180 cm^{-1} is due to the La/Na-O vibrations. In BNT, this band is deconvoluted to one peak which belongs to the Na-O vibrations whereas in La substituted compositions (x = 0.1, 0.2, 0.3, 0.4), this band is deconvoluted into two peaks.

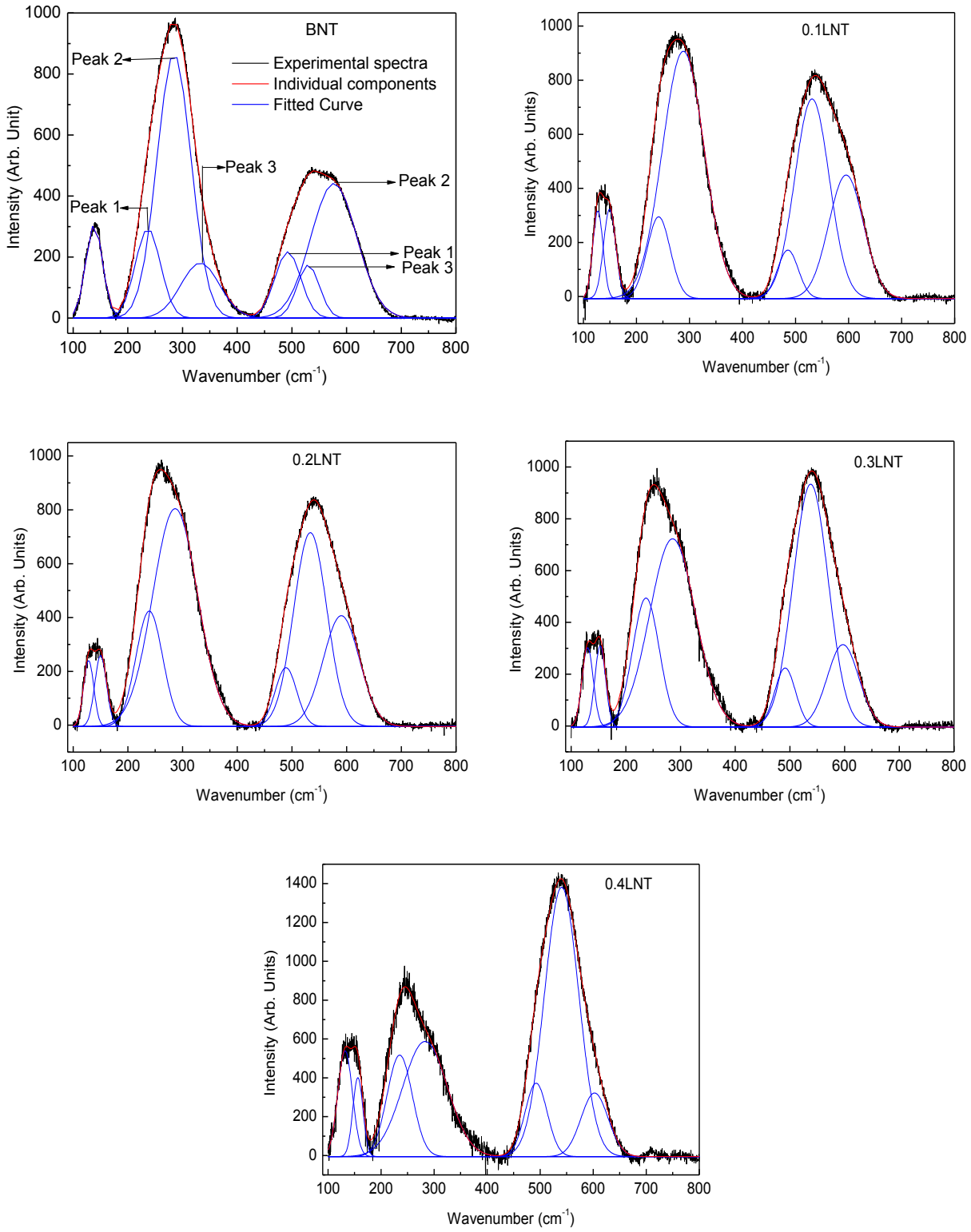

Figure 6.6: Deconvoluted Raman spectra of BNT, 0.1LNT, 0.2LNT, 0.3LNT, and 0.4LNT in (1-x)BNT–xLNT. The black, red and blue curves correspond to experimental spectra, fitted curves and the individual components, respectively.

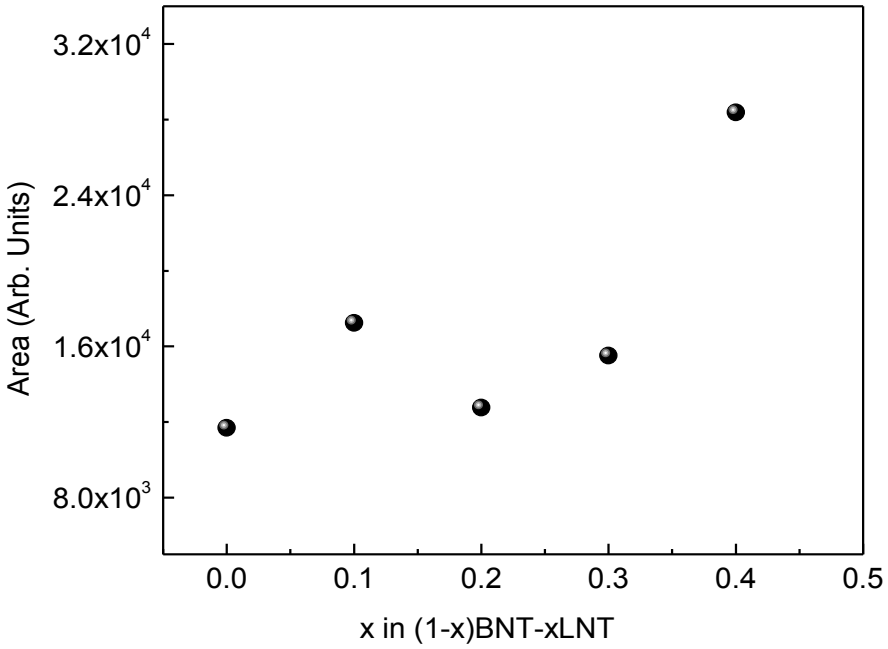

Figure 6.7: Changes in the area under the curve of the band below 180 cm^{-1} in the Raman spectra as a function of x in (1-x)BNT–xLNT.

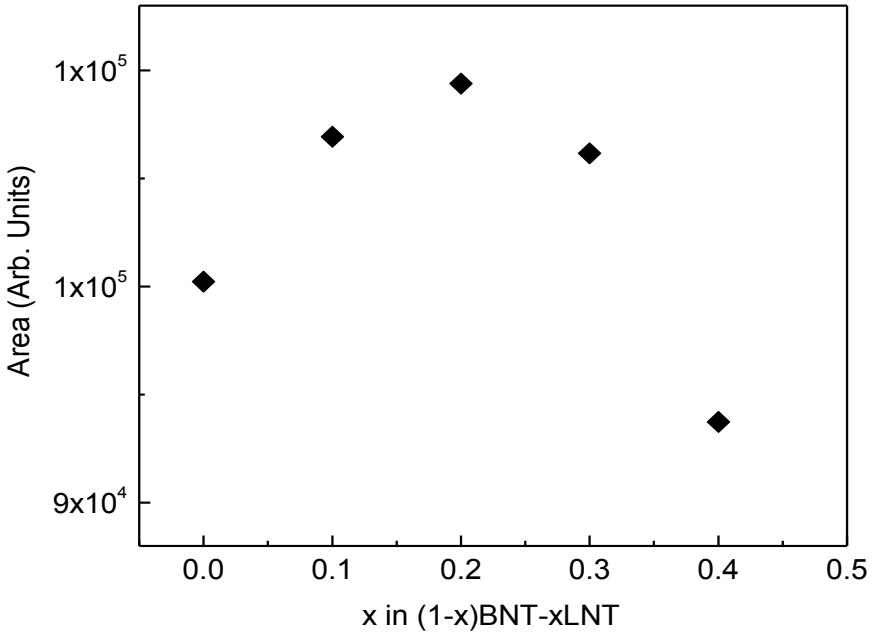

Figure 6.8: Changes in the area under the 200–400 cm^{-1} band in the Raman spectra as a function of x in (1-x)BNT–xLNT.

The additional modes observed in the region below 180 cm^{-1} of the La-substituted compositions could be due to the La-O/Ti-O vibrations and also due to the local symmetry changes resulting from the $6s^2$ lone pair. As the concentration of La increased effect of $6s^2$ decreased, this led to local symmetry changes and changes in the A-O vibrations. In the case of LNT, the distortion contributed by the $6s^2$ lone pair is zero which leads to a low frequency shift of the Ti-O band below 180 cm^{-1}. The area under the band below 180 cm^{-1} is plotted against La concentration and shown in Figure 6.7. The area is increased with La-substitution.

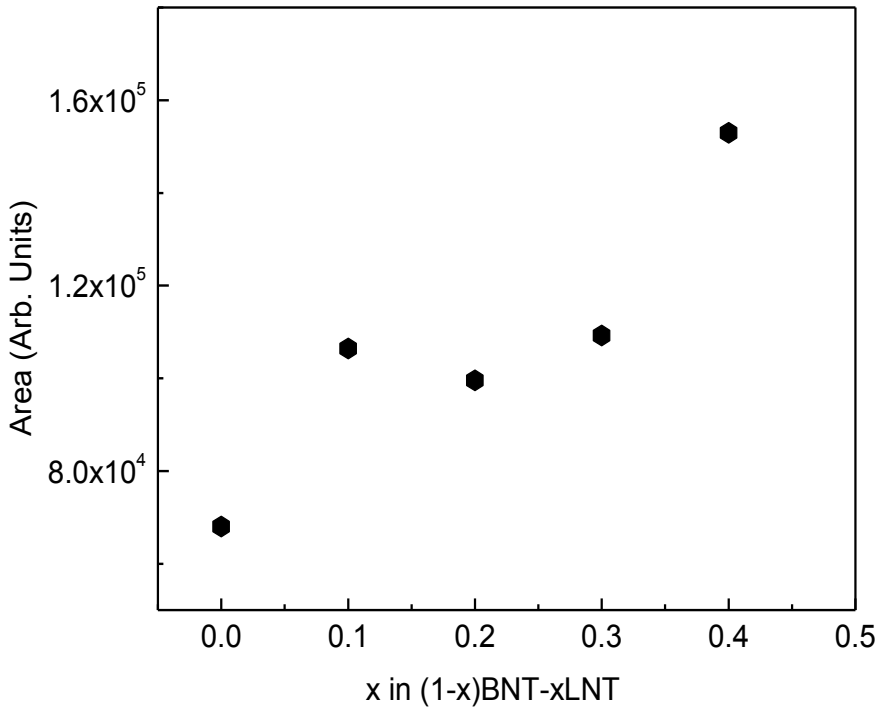

Figure 6.9: Changes in the area under the 400-700 cm^{-1} band in the Raman spectra as a function of x in (1-x)BNT–xLNT.

The Raman band in the 200–400 cm^{-1} region also showed changes with substitution. In unsubstituted BNT, this region consists of three peaks whereas in the La substituted compositions (x =0.1, 0.2, 0.3, 0.4), this band is deconvoluted to two peaks. Since 200–400 cm^{-1} region belongs to the Ti-O vibrations in BNT, changes in this region with La-substitution indicate changes in the Ti-O bond. The change in the area under the band in the 200–400 cm^{-1} region is shown in Figure 6.8. The area is initially increased up to x = 0.2 and then decreased with increasing La content, suggesting minor structural changes.

The 400–700 cm^{-1} region of the Raman spectra belongs to the TiO_6 octahedra. In BNT and La substituted compositions (x = 0.1, 0.2, 0.3, 0.4), this region is deconvoluted to three Raman modes, as observed in the case of K- and Li-substituted compositions, as discussed in the previous chapters. The changes in the area under the band in the 400–700 cm^{-1} region as function of x is shown in Figure 6.9. The area increased with increasing La concentration, suggesting minor changes in the TiO_6 octahedra on substitution of La for Bi in BNT.

6.5. Solid-state NMR spectroscopy

In (1-x)BNT–xLNT, all the nuclei are NMR active. Out of them, two quadrupolar nuclei, ^{23}Na and ^{139}La are most sensitive and SSNMR of these two nuclei are carried out to obtain insights into the local structural changes in the solid solution series with La concentration.

6.5.1. ^{23}Na NMR

^{23}Na MAS NMR spectra of different compositions of (1-x)BNT–xLNT are shown in Figure 6.10 (a) and Figure 6.10 (b) shows the zoomed part of the central region of the spectra. It is observed that all the spectra have line shapes characteristic of the systems which have a distribution in quadrupolar coupling constant (Section 2.3.2.3). The ^{23}Na NMR parameters are extracted from the ^{23}Na MAS NMR spectra of the different compositions of BNT–LNT using the DMFIT program. The 'Czjzek' model in the DMFIT program, which includes the Gaussian isotropic model (GIM), is used for generation of the lineshape since the experimental spectra of all the compositions showed a lineshape typical to a system which has a distribution of quadrupolar coupling constant, as discussed in Chapter 3 (Section 3.5).[90] The NMR parameters extracted from the ^{23}Na MAS spectra are shown in Table 6.2. The experimental and simulated ^{23}Na spectra of selected compositions of BNT–LNT are shown in Figure 6.11. For all compositions, the simulated spectra match exactly with the experimental data.

Figure 6.12 shows the variation of the quadrupolar coupling (C_Q^*) with La substitution. It is observed that the C_Q^* initially increased from x = 0 to x = 0.1 and then decreased almost linearly with increasing La concentration. Since the C_Q^* is related to the crystal symmetry of the material, materials having higher crystal symmetry possess low values for C_Q^* and materials with low crystal symmetry possess higher values for C_Q^*.[91]

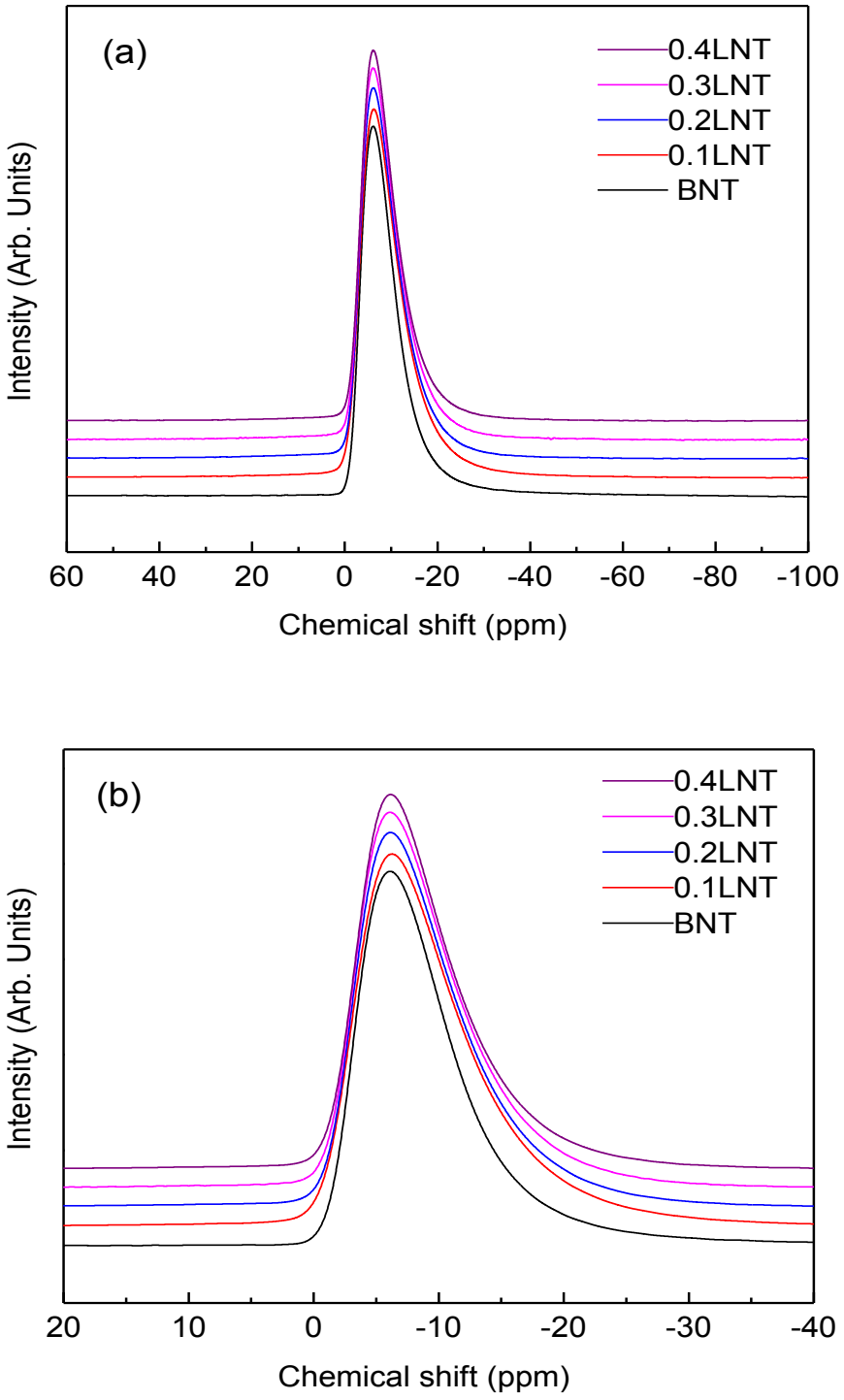

Figure 6.10: (a) ^{23}Na NMR spectra of the different compositions in the (1-x)BNT–xLNT series, (b) Zoomed view of the central region.

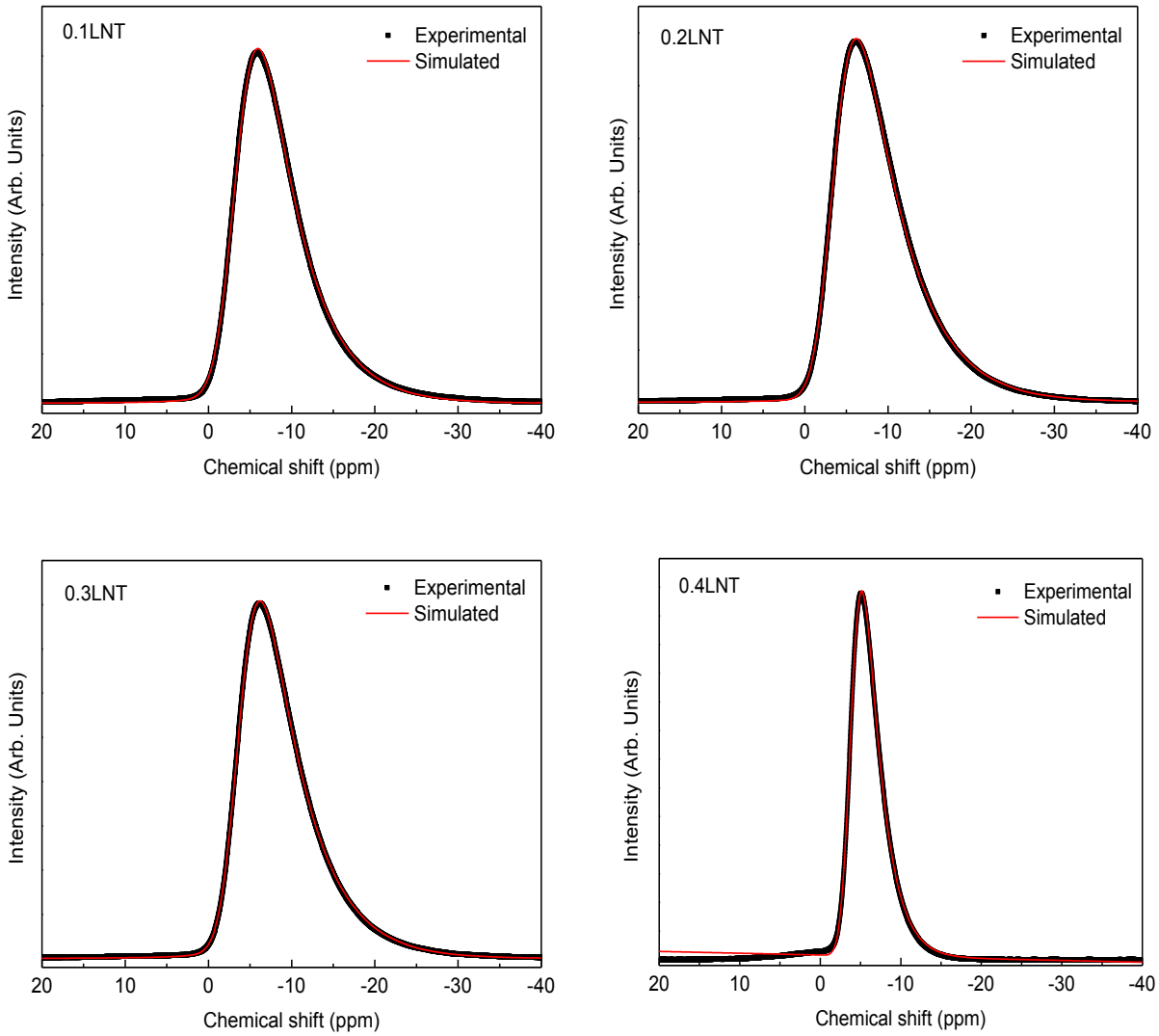

Figure 6.11: Comparison of the experimental and simulated ^{23}Na MAS NMR spectra of selected compositions (0.1LNT, 0.2LNT, 0.3LNT, 0.4LNT) of (1-x)BNT–xLNT.

The decrease of C_Q^* with La concentration for x > 0.1 indicate the increased crystal symmetry of the material. As the substituted concentration of the La^{3+} ions increases, the effect of $6s^2$ lone pair in the crystal symmetry decreases resulting in a decrease in the distortion of the unit cell. The relatively larger C_Q^* of x = 0.1 is probably due to the local inhomogeneous distribution of La^{3+} in the BNT lattice, leading to larger distortion of the crystal lattice.

Table 6.3: Parameters extracted from ^{23}Na MAS NMR spectra.

Sample	δ_{iso} (ppm)	C_Q^*(kHz)	Δ_{CS} (ppm)
BNT	-3.02	1058	4.36
0.1LNT	-3.06	1152	4.37
0.2LNT	-3.08	1126	4.15
0.3LNT	-3.11	1111	4.14
0.4LNT	-3.32	1079	3.92

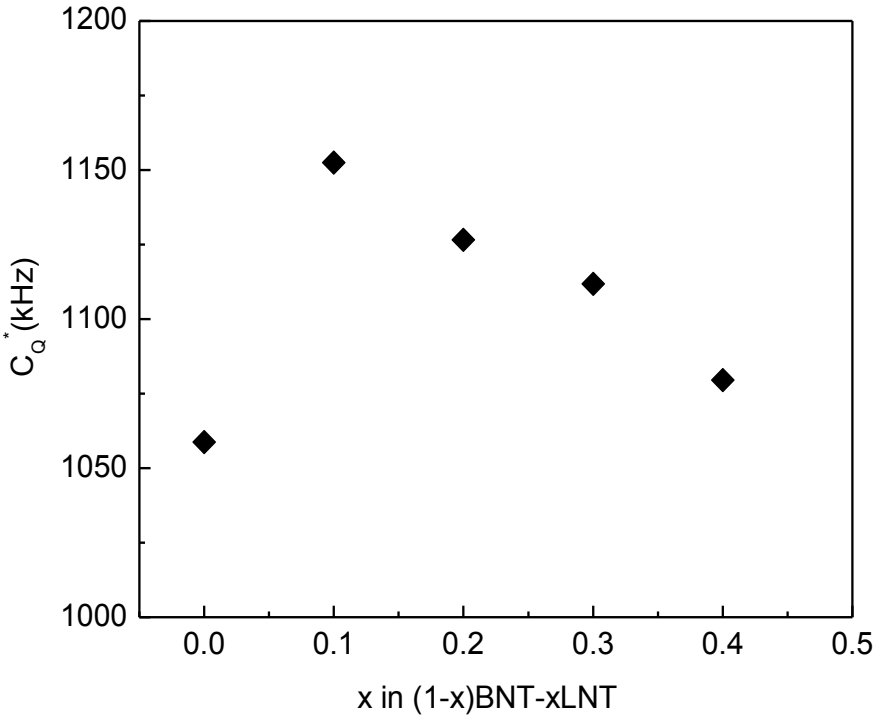

Figure 6.12: Variation of the ^{23}Na C_Q^* of (1-*x*)BNT–*x*LNT as a function of *x*.

6.5.2. ^{139}La NMR

Figure 6.13 (a) shows the ^{139}La MAS NMR spectra of all the compositions of BNT–LNT solid solution series and Figure 6.13 (b) shows the enlarged plot. It is observed that the lineshape of ^{139}La is characteristic of systems which have a distribution of quadrupolar coupling constant as described in chapter 2 (section 2.4.2.3.) and it can also be seen that these are systems with very large quadrupolar coupling since the line width are very large (~ 30 kHz)

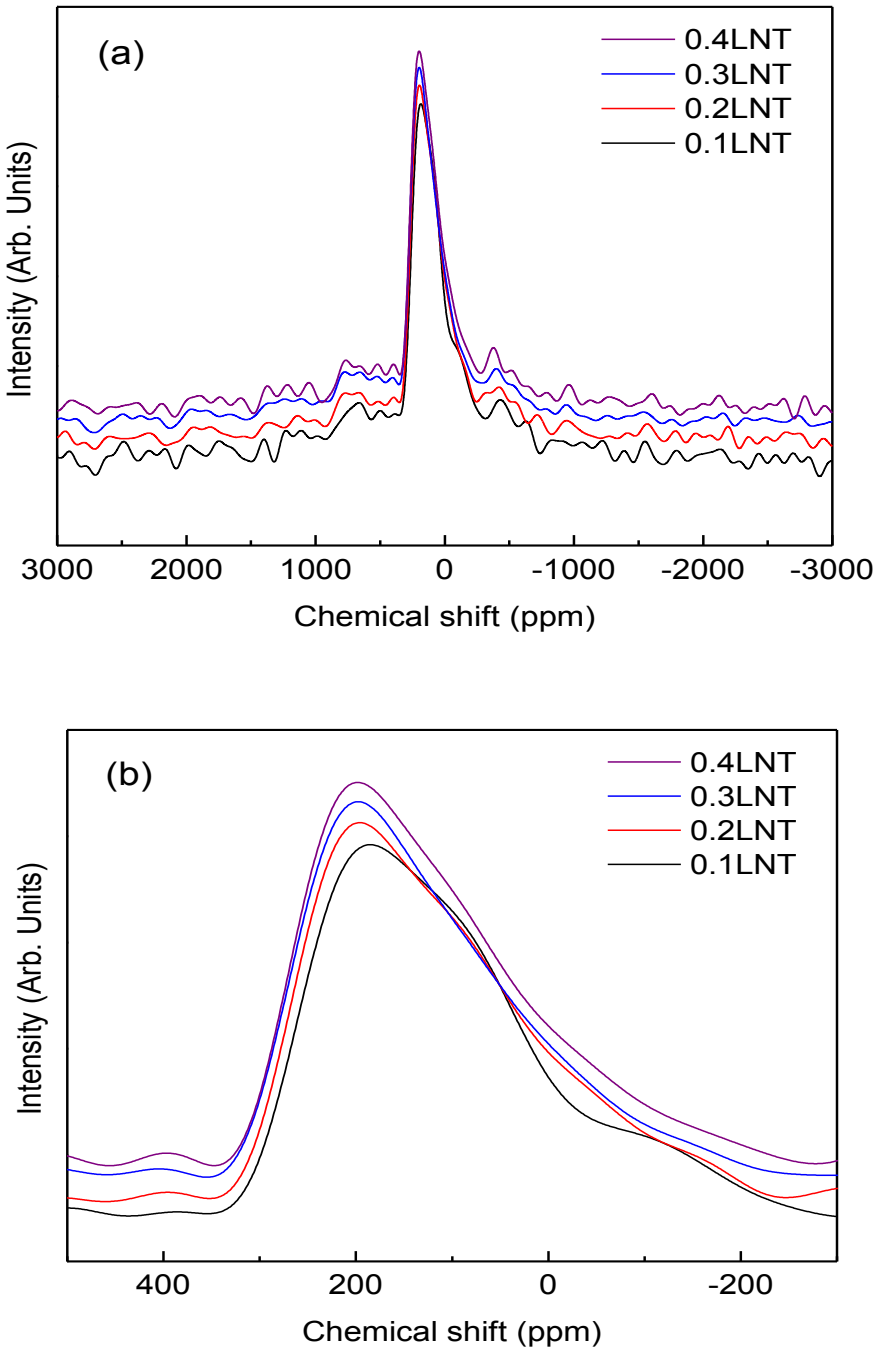

Figure 6.13: (a) ^{139}La NMR spectra of the different compositions in the (1-x)BNT–xLNT series, (b) Zoomed view of the central region.

The ^{139}La NMR parameters are extracted from the MAS spectra for all the compositions of (1-x)BNT–xLNT using the DMFIT program. The 'Czjzek' model in the DMFIT program, which includes the Gaussian isotropic model (GIM), was used for generation of the lineshape

since the experimental spectra of all the compositions showed a quadrupolar frequency distribution. The NMR parameters extracted from the ^{139}La MAS spectra are shown in Table 6.3. The experimental and simulated ^{139}La spectra of different compositions of BNT–LNT are shown in Figure 6.14. For all compositions, the simulated spectra match exactly with the experimental data.

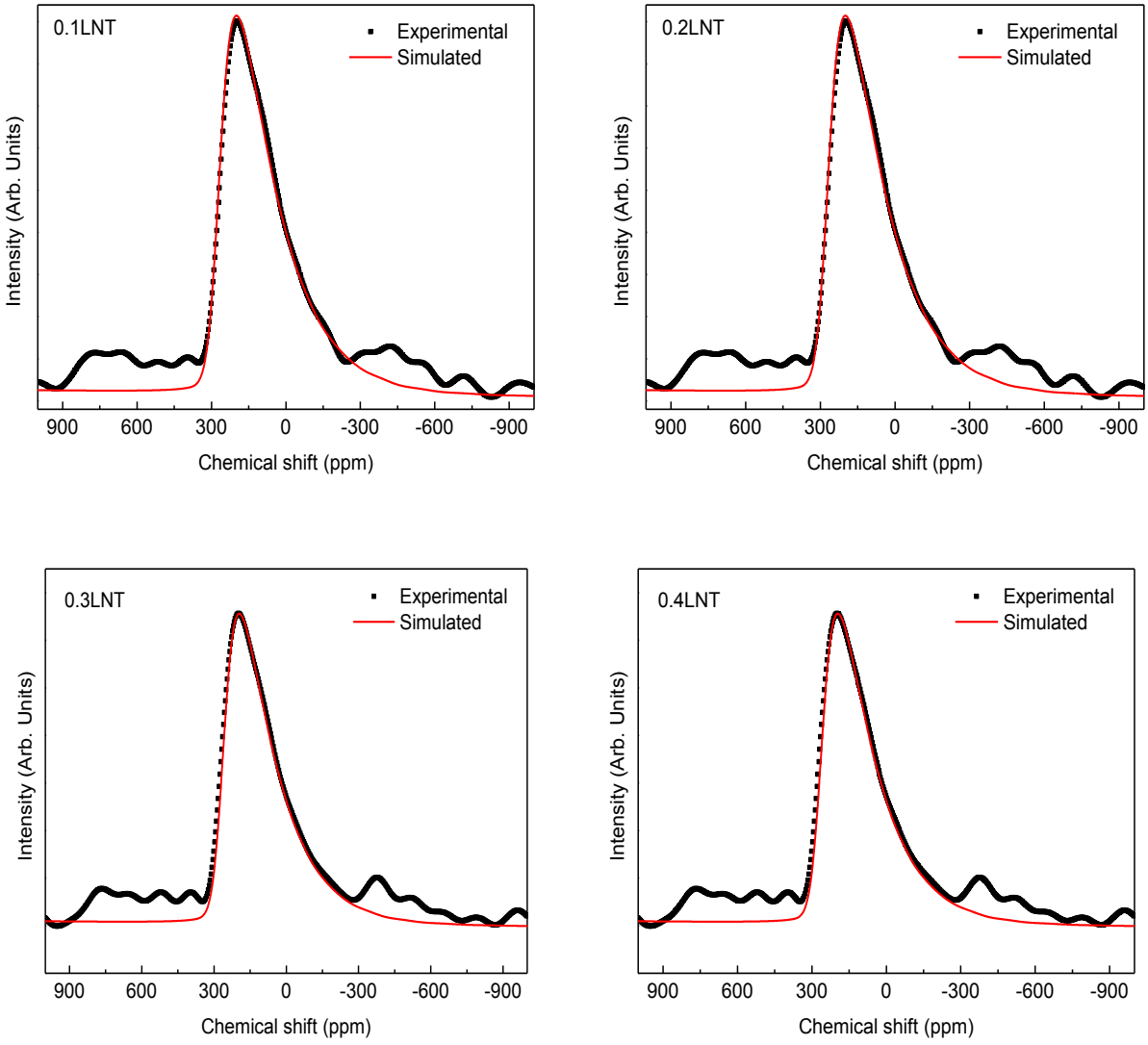

Figure 6.14: Comparison of the experimental and simulated ^{139}La MAS NMR spectra of selected compositions (0.1LNT, 0.2LNT, 0.3LNT, 0.4LNT) of (1-x)BNT–xLNT.

Table 6.4: Parameters extracted from ^{139}La MAS NMR spectra.

Sample	δ_{iso} (ppm)	C_Q^*(MHz)	Δ_{CS} (ppm)
0.1LNT	278.40	26.77	85.01
0.2LNT	278.37	24.66	78.07
0.3LNT	276.00	23.69	81.95
0.4LNT	269.57	23.76	75.07

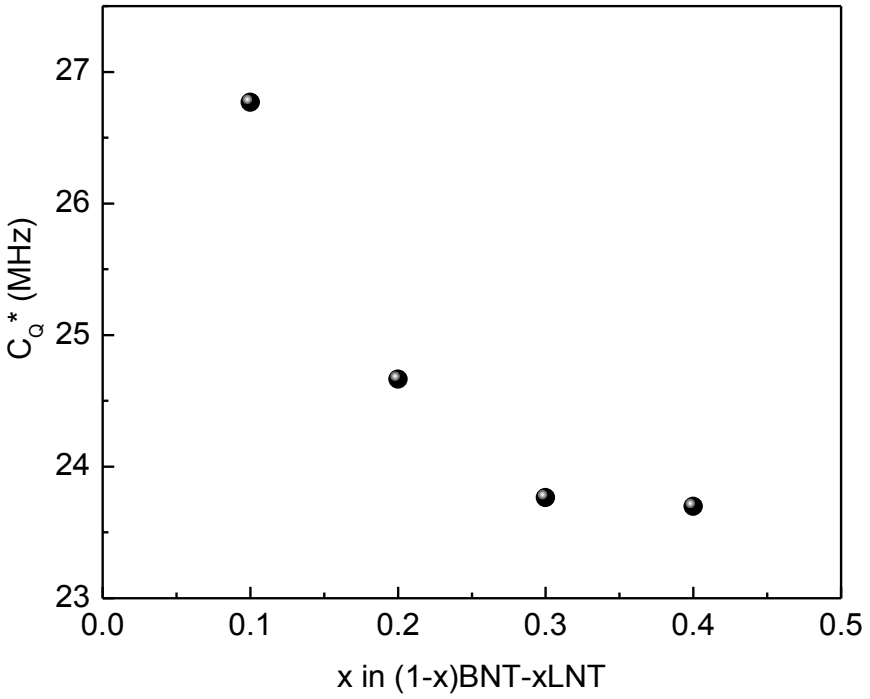

Figure 6.15: Variation of the ^{139}La C_Q^* of (1-*x*)BNT–*x*LNT as a function of *x*.

The changes in quadrupolar coupling (C_Q^*) with La substitution are shown in Figure 6.15. The quadrupolar coupling of BNT–LNT decreased with increasing La concentration which indicates the increase in the symmetry on substitution. The C_Q^* of ^{23}Na and ^{139}La extracted from the MAS NMR spectra decrease with increasing La concentration. These results substantiate that the system experiences lesser distortion and increased symmetry with higher La concentration.

6.6. Scanning electron microscopy

SEM images of all the compositions of BNT–LNT solid solution are shown in Figure 6.16. It is clearly visible that the microstructure of the ceramics changed with the substitution of La^{3+} ions.

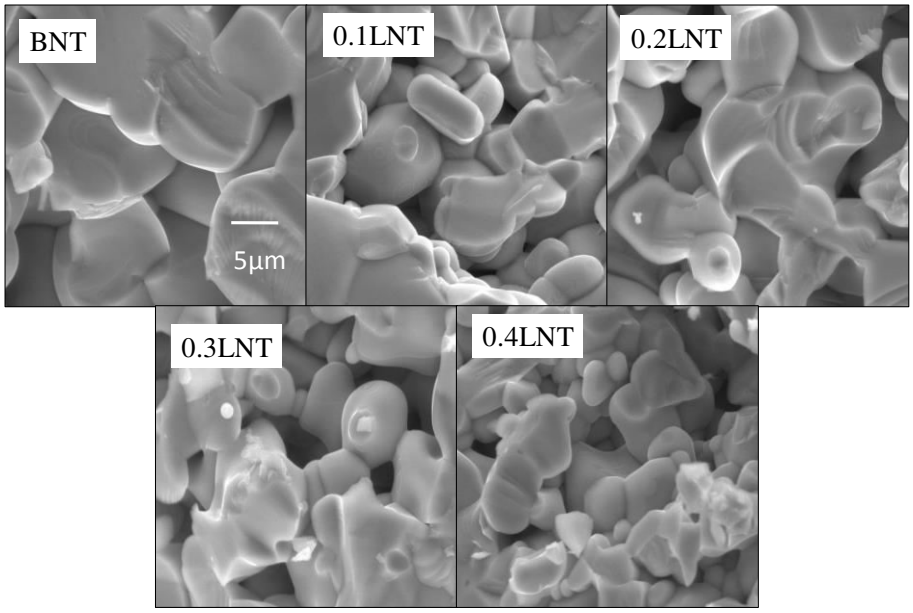

Figure 6.16: SEM micrographs of different compositions in the (1-x)BNT–xLNT series. The scale shown is common for all images.

Table 6.5: Density and grain size of different compositions in the (1-x)BNT–xLNT series.

Sample	**Grain size (µm)**	**Measured density (g/cm^3)**	**Theoretical density (g/cm^3)**
BNT	11.8	4.69	5.96
0.1LNT	9.7	4.79	5.91
0.2LNT	7.9	4.03	5.81
0.3LNT	6.5	3.98	5.72
0.4LNT	5.3	3.93	5.62

As the concentration of La^{3+} ions are increased in the compositions, grain size of the ceramics is decreased along with increasing number of pores. The average grain size of the ceramics is compared with the measured density in Table 6.4. Large grains of size ~12 μm are observed for BNT. The larger grain size observed for BNT in the BNT–LNT solid solution series compared to the grain size of BNT in the BNT–BKT (Figure 3.20), BNT–BLT (Figure 4.21) and BNT–BLT–BKT (Figure 5.18) solid solutions is due to the relatively higher sintering temperature (1200 ^oC) in the present case. The grain size of the ceramics decreased with La^{3+}substitution.

6.7. Density

Figure 6.17 shows the variation of the density of the BNT–LNT compositions with La concentration. There is an initial increase in the density for x = 0.1 compared to the density of BNT and the density further decreases with increasing La concentration. A large drop in the density is observed between x = 0.1 and 0.2.

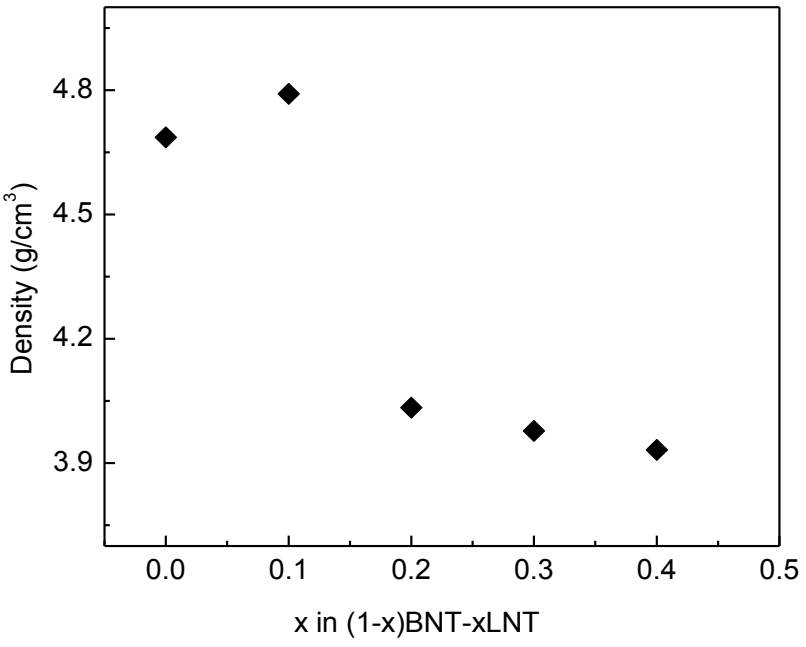

Figure 6.17: Variation of the sintered density of (1-x)BNT–xLNT as a function of x.

It is observed from the SEM images that as the La-substitution is increased, the grain size has decreased with increasing porosity. Thus, the changes in the density with increasing La content in the compositions are well correlated with the microstructure. The theoretical and measured densities of the ceramics are compared in Table 6.4. The measured density is~70 % of the theoretical density whereas in the reported studies ~92 % of the theoretical density is obtained. This is probably due to the difference in synthesis method, processing conditions, compaction pressure and sintering temperature. For example Aparna *et al*[129] reported ~90 % of the theoretical density for samples synthesized by solid state reaction and for powders compacted at a pressure of 5 ton/cm^2 (~100 MPa) and a sintering temperature of 1100 ^oC, compared to the compaction pressure of 8 MPa used in the present work.

6.8. Dielectric constant

Dielectric constant of all the compositions of the (1-x)BNT–xLNT solid solution series is measured at 1 kHz. Figure 6.18 shows the variation of the dielectric constant with La concentration. The dielectric constant values are comparable to that reported in the literature.[129]

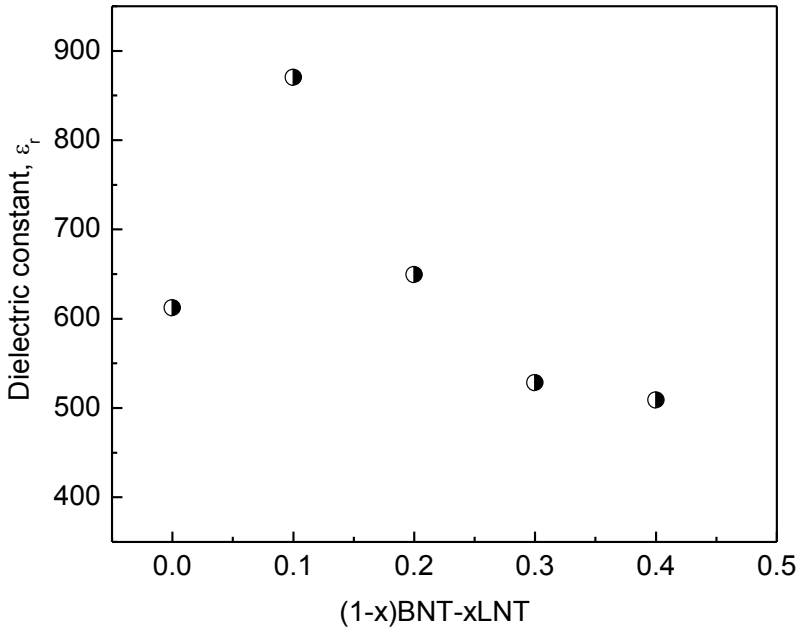

Figure 6.18: Variation of the dielectric constant of (1-x)BNT–xLNT as a function of x.

The dielectric constant of $x = 0.1$ is larger than that of BNT. On further increasing the La concentration, the dielectric constant has decreased. All the compositions, except $x = 0.1$, show lower dielectric constant than that of BNT. Variation of the dielectric constant is very well correlated with the changes in the structural parameters as well as the microstructure and density. Both La^{3+} and Bi^{3+} ions have almost the same size and charge, hence the variation in the lattice parameters is due to the effect of $6s^2$ lone pair present in the Bi^{3+} ions. $6s^2$ lone pair causes more distortion and polarization in the crystal lattice. As the concentration of La^{3+} ions is increased, the effect of $6s^2$ lone pair is reduced, and hence the polarization in the crystal lattice has decreased. As a result, the dielectric constant of the ceramics is reduced with La-substitution. The relatively larger dielectric constant of the composition with $x = 0.1$ could be due to the local inhomogeneous distribution of La atoms in BNT crystal lattice, as well as due to the relatively larger density of this composition

6.9. Structure-property correlations

The present studies on (1-x)$Bi_{0.5}Na_{0.5}TiO_3$–$xLa_{0.5}Na_{0.5}TiO_3$ solid solutions showed a close correlation between the structural parameters and the properties of the system. Similar trends are observed in the changes of some of the Raman and NMR spectral parameters as well as the properties of the solid solution on La-substitution.

Figure 6.19 compares the changes in C_Q^* of ^{139}La and the unit cell volume with La concentration. Both the parameters showed similar variations with substitution. Figure 6.20 compares the changes in the ^{23}Na quadrupole coupling (C_Q^*), area under the Raman band in the 200-400 cm^{-1} region, dielectric constant and density of the solid solutions. All the four parameters show similar trend in the variation with La-substitution. All the parameters showed a small increase from $x = 0$ to $x = 0.1$ and then decreased with increasing degree of La-substitution. Even the area under the Raman bands below 200 cm^{-1} and in the 400–700 cm^{-1} regions showed some anomaly for $x = 0.1$, indicating some local structural changes on substitution.

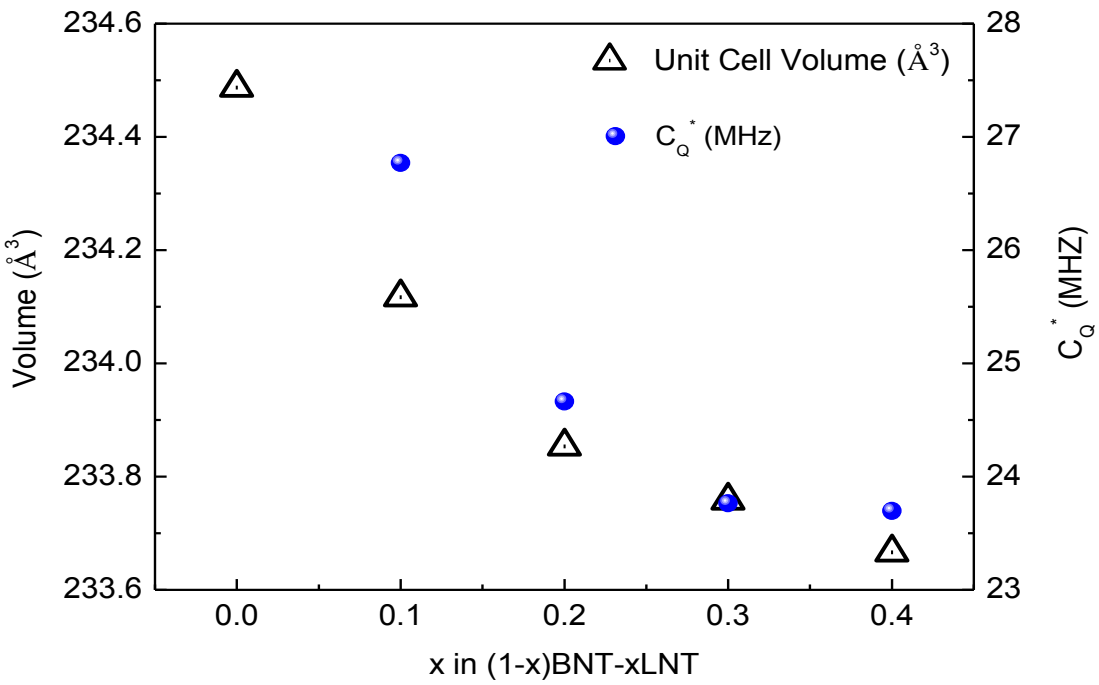

Figure 6.19: Comparison of the changes in the ^{139}La NMR quadrupolar coupling (C_Q^*) and the unit cell volume as a function of x in (1-x)BNT–xLNT.

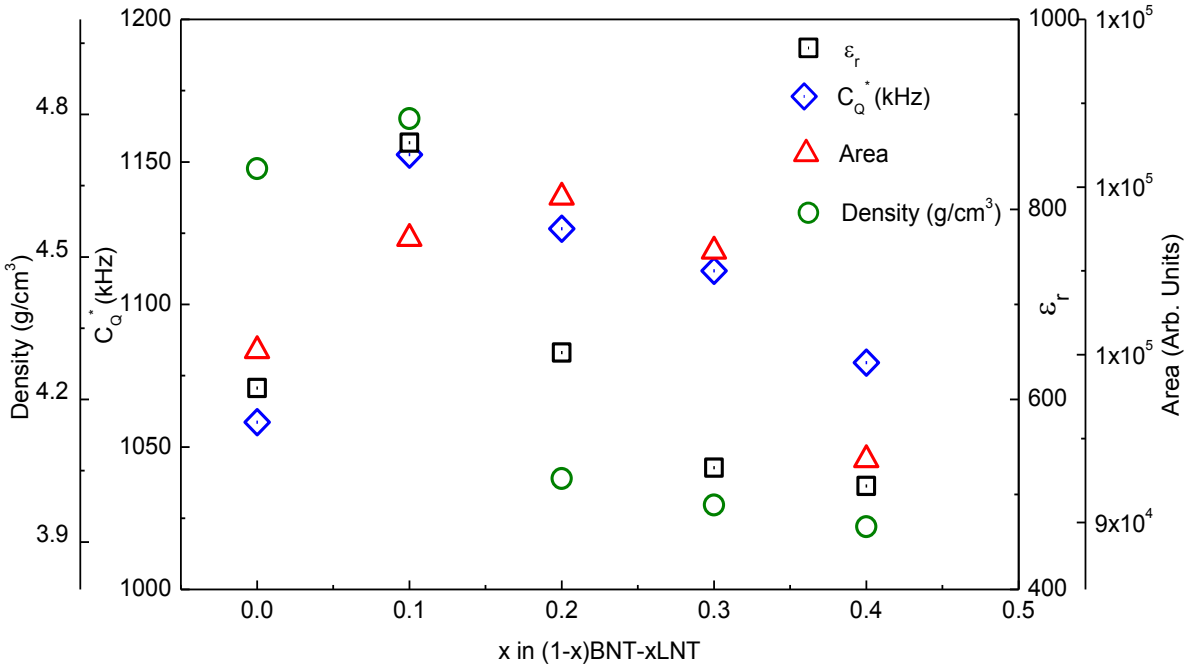

Figure 6.20: Comparison of the changes in the ^{23}Na NMR quadrupolar coupling (C_Q^*), dielectric constant (ε_r), density and the area under the band in the 200-400 cm^{-1} region in the Raman spectra, as a function of x in (1-x)BNT–xLNT.

Since the Raman and NMR spectral parameters are related to local symmetry changes, the results indicate that the local symmetry changes greatly influence the dielectric constant and density of BNT–LNT. The Raman band in the 200-400 cm^{-1} region is associated with Ti-O vibration. The changes in area under this band indicate changes in the Ti-O bond with substitution. The decrease in the C_Q^* of ^{23}Na MAS spectra with La-substitution indicates increase in local symmetry with substitution. The changes in the Ti-O bond with La-substitution alter the symmetry of the system which affects the polarization that contributed to the dielectric constant.

6.10. Conclusions

Detailed structural analysis of (1-x)$Bi_{0.5}Na_{0.5}TiO_3$–$xLa_{0.5}Na_{0.5}TiO_3$ solid solutions, for $0 \leq x \leq 0.4$, has been carried out by Rietveld analysis of powder XRD patterns as well as Raman and NMR spectroscopy. Rietveld analysis confirmed the formation of all the compositions under monoclinic structure with Cc space group without any phase transition. Solid state NMR studies showed that the quadrupolar coupling obtained from both ^{23}Na and ^{139}La spectra decrease with increasing La concentration, indicating higher symmetry for La-rich compositions. Raman and NMR studies indicated anomalous values for the derived parameters around $x = 0.1$. Similar changes around this composition are observed in the dielectric constant and density. On increasing the La concentration, the dielectric constant and density are found to decrease, along with increased porosity. The decrease in the dielectric constant and density is due to the less polarization due to the reduced distortion of the Bi-O and La-O polyhedra, as evidenced from NMR studies. The studies on (1-x)BNT–xLNT solid solutions clearly showed the effect of Bi^{3+} $6s^2$ lone pair in deciding the structure and properties. From the present studies, it is concluded that contribution to the ferroelectric properties of BNT is not only from the distorted TiO_6 octahedra but also from the Bi^{3+} $6s^2$ lone pairs.

Chapter 7

Conclusions and Future perspectives

7.1. Conclusions

The widely used high performance piezoelectric ceramics, lead zirconatetitanate, $PbZr_{1-x}Ti_xO_3$, have been excluded from many commercial applications due to the toxic effect of lead. Studies have been carried out to develop an effective alternate for $PbZr_{1-x}Ti_xO_3$. Bismuth sodium titanate, $Bi_{0.5}Na_{0.5}TiO_3$ based solid solutions are lead free piezoelectric material with properties comparable to that of $PbZr_{1-x}Ti_xO_3$. Understanding of structure-property correlation will help to improve the physical properties of $Bi_{0.5}Na_{0.5}TiO_3$ based solid solutions. This work is an attempt to study the changes in the local structure and symmetry and to correlate these changes with the properties of $Bi_{0.5}Na_{0.5}TiO_3$ (BNT) based solid solutions. Structure-property correlations of the solid solutions of $Bi_{0.5}Na_{0.5}TiO_3$–$Bi_{0.5}K_{0.5}TiO_3$ (BNT–BKT), $Bi_{0.5}Na_{0.5}TiO_3$–$Bi_{0.5}Li_{0.5}TiO_3$ (BNT–BLT), $Bi_{0.5}Na_{0.5}TiO_3$–$Bi_{0.5}Li_{0.5}TiO_3$–$Bi_{0.5}K_{0.5}TiO_3$ (BNT–BKT–BLT), and $Bi_{0.5}Na_{0.5}TiO_3$–$La_{0.5}Na_{0.5}TiO_3$ (BNT–LNT) have been studied. The structural parameters are studied using powder XRD and Raman spectroscopy, and local structural variations are studied using solid-state NMR. The microstructure as well as density and dielectric properties of the solid solutions are correlated with the structural changes.

The main motivation to choose A-site substitution in the ABO_3 perovskite structure of $Bi_{0.5}Na_{0.5}TiO_3$with alkali metal ions (substitution of Na^+ by Li^+ and K^+) is based on the reported improvement in the piezoelectric properties in the $Bi_{0.5}Na_{0.5}TiO_3$–$Bi_{0.5}K_{0.5}TiO_3$ solid solution series. The solid solution formed between $Bi_{0.5}Na_{0.5}TiO_3$ and $Bi_{0.5}K_{0.5}TiO_3$ could overcome some of the drawbacks of $Bi_{0.5}Na_{0.5}TiO_3$ such as high conductivity and large coercive field. A high performance region is observed in a certain compositional region in the $Bi_{0.5}Na_{0.5}TiO_3$–$Bi_{0.5}K_{0.5}TiO_3$ solid solution. There are various differing reports on the $Bi_{0.5}Na_{0.5}TiO_3$–$Bi_{0.5}K_{0.5}TiO_3$ solid solution, related to its crystal structure, structural phase transition, existence of the morphotropic phase boundary (MPB) region and the compositional range of the MPB region. Hence to understand the changes in the structure and properties, a detailed analysis of the solid solutions of $(1-x)Bi_{0.5}Na_{0.5}TiO_3$–$xBi_{0.5}K_{0.5}TiO_3$ in the compositional range $0 \leq x \leq 0.36$, with close compositions, is carried out in this work. Similarly, since the ionic radius of K^+ (1.64 Å) is larger than that of Na^+ (1.39 Å) , the role of cation size on the structure and properties of $Bi_{0.5}Na_{0.5}TiO_3$–$Bi_{0.5}K_{0.5}TiO_3$ solid solution is studied by substituting Na^+ (1.39 Å) by a smaller ion Li^+ (0.92 Å) in the $(1-x)Bi_{0.5}Na_{0.5}TiO_3$–$xBi_{0.5}Li_{0.5}TiO_3$ solid solutions in the range $0 \leq x \leq 0.20$ and the co-substitution of Li^+ and K^+ in the $(1-x)Bi_{0.5}Na_{0.5}TiO_3$–$(x/2)Bi_{0.5}Li_{0.5}TiO_3$–$(x/2)Bi_{0.5}K_{0.5}TiO_3$ (where the average size of

Li^+ and K^+ is comparable to that of Na^+). The structure and properties of the different solid solutions are analysed and the changes in the structure and local symmetry are correlated with the dielectric properties of the solid solutions. Similarly, the effect of bismuth 6s lone pair of electrons on the ferroelectric properties of $Bi_{0.5}Na_{0.5}TiO_3$ is investigated by substituting Bi^{3+} with La^{3+} (both ions having comparable ionic size) in the $Bi_{0.5}Na_{0.5}TiO_3$–$La_{0.5}Na_{0.5}TiO_3$ solid solution series. A detailed structure property analysis of $(1-x)Bi_{0.5}Na_{0.5}TiO_3$–$xLa_{0.5}Na_{0.5}TiO_3$ series is carried out and the effect of bismuth lone pair on the properties is investigated.

Both rhombohedral structure with R3c space group and monoclinic structure with Cc space group are reported for $Bi_{0.5}Na_{0.5}TiO_3$. From the Rietveld refinement analysis of the XRD pattern of $Bi_{0.5}Na_{0.5}TiO_3$ using rhombohedral R3c and monoclinic Cc, The Rietveld refinement analysis using the monoclinic Cc space group gave a reasonable agreement with the simulated pattern with relatively low values of reduced χ^2 and R_P, suggesting that the correct space group of $Bi_{0.5}Na_{0.5}TiO_3$ is monoclinic Cc.

The crystal structures of different close compositions of $(1-x)Bi_{0.5}Na_{0.5}TiO_3$–$xBi_{0.5}K_{0.5}TiO_3$ in the range $0 \leq x \leq 0.36$ are investigated using the Rietveld refinement of XRD patterns, Raman spectroscopy and solid-state NMR. The Rietveld refinement of XRD patterns showed that single phase compositions with monoclinic Cc space group are formed below $x < 0.18$. A biphasic MPB region with monoclinic Cc and tetragonal P4bm structures is observed in the compositional region with $0.18 \leq x \leq 0.36$. The Raman analysis of the $(1-x)Bi_{0.5}Na_{0.5}TiO_3$–$xBi_{0.5}K_{0.5}TiO_3$ solid solution series showed major structural changes for $x > 0.18$. An additional band observed in the 200-400 cm^{-1} region in the spectra for $x > 0.18$ indicated structural changes and changes in the Ti-O bonds. Moreover, for $x > 0.18$, a drastic downward frequency shift in the position of the band below 180 cm^{-1} and an upward frequency shift of individual components of the band in the 400-700 cm^{-1} region are observed which specify the structural changes above $x = 0.18$. Thus, the results obtained from both the powder XRD and the Raman analysis showed major structural changes above $x = 0.18$ in the $Bi_{0.5}Na_{0.5}TiO_3$–$Bi_{0.5}K_{0.5}TiO_3$ solid solution. ^{23}Na MQMAS NMR experiments indicated that only one sodium site is present in the $Bi_{0.5}Na_{0.5}TiO_3$–$Bi_{0.5}K_{0.5}TiO_3$ solid solution series in the range $0 \leq x \leq 0.36$. ^{23}Na solid-state NMR studies also showed that the quadrupolar coupling (C_Q^*) decreases up to $x = 0.15$, increases above this composition up to $x = 0.22$ and then decreases again at higher compositions. The microstructure analysis showed that fused and less porous grains is formed in the MPB region. Some of the Raman spectral parameters also showed deviation at above $x = 0.15$. These results suggested that the onset of the MPB region

is likely to be $x = 0.15$, due to local symmetry changes on substitution, and the MPB region corresponds to $0.15 \leq x \leq 0.24$. Maximum density, polarization and dielectric constant are observed for the $Bi_{0.5}Na_{0.5}TiO_3$–$Bi_{0.5}K_{0.5}TiO_3$ solid solution in the MPB region. Thus, the present studies gave detailed information on the onset and compositional range of the MPB region in the $Bi_{0.5}Na_{0.5}TiO_3$–$Bi_{0.5}K_{0.5}TiO_3$ solid solution series and the close correlations between the structure, microstructure, density and dielectric constant.

Changes in structure and properties on substitution of Li^+ for Na^+ in the solid solution series $(1\text{-}x)Bi_{0.5}Na_{0.5}TiO_3$–$xBi_{0.5}Li_{0.5}TiO_3$ in the compositional range $0 \leq x \leq 0.20$ are studied. Rietveld refinement analysis of the XRD patterns showed that all the compositions are formed under the monoclinic Cc space group as that of $Bi_{0.5}Na_{0.5}TiO_3$, suggesting the absence of any phase transition and MPB region. The distortion in the $Bi_{0.5}Na_{0.5}TiO_3$ crystal lattice due to the substitution of the smaller ion Li^+ is less compared to the distortion caused by substitution of the larger K^+ ion. Though no phase transformation is detected, changes in the lattice parameters indicated minor structural distortion and local symmetry changes in the $Bi_{0.5}Na_{0.5}TiO_3$ lattice with Li substitution. Raman analysis also supported the results obtained from the XRD studies. Compared to the BNT–BKT series, increase in the ^{23}Na quadrupolar coupling (C_Q^*) with Li substitution indicated increasing local symmetry. The Lorentzian component in the ^7Li NMR spectra increased with Li substitution. This showed the increased mobility of the Li^+ ions in the crystal lattice with increasing $Bi_{0.5}Li_{0.5}TiO_3$ concentration. The downward frequency shift of the Raman band below 180 cm^{-1} also indicated the increased Li^+ mobility in the $Bi_{0.5}Na_{0.5}TiO_3$ lattice. Thus, XRD, Raman and NMR parameters showed similar trends in the changes with increasing $Bi_{0.5}Li_{0.5}TiO_3$ concentration. All the three parameters showed deviation above $x = 0.1$, evidencing local symmetry changes and small distortion at this composition. The variations in the microstructure, density and dielectric constant of the $Bi_{0.5}Na_{0.5}TiO_3$–$Bi_{0.5}Li_{0.5}TiO_3$ solid solution series also showed similar trends, suggesting close correlation between the structure and properties.

Phase transition and MPB region are not observed in the Li^+ and K^+ co-substituted $(1\text{-}x)Bi_{0.5}Na_{0.5}TiO_3$–$(x/2)Bi_{0.5}Li_{0.5}TiO_3$–$(x/2)Bi_{0.5}K_{0.5}TiO_3$ solid solution series. All the compositions are formed under the monoclinic Cc space group. The lattice parameters and cell volume of the solid solutions changed a little with substitution, indicating distortions in the crystal lattice. Raman spectroscopy analysis supported the results from XRD studies, where the effect of substitution is found to be reflected in the variations of the Raman spectral parameters. Evidence for increased mobility of Li^+ ions in the $Bi_{0.5}Na_{0.5}TiO_3$ lattice is also

obtained from the Raman studies. This observation is also supported by the ^{7}Li SSNMR results where the Lorentzian component showed increase with substitution. A small increase in the quadrupolar coupling (C_Q^*) of ^{23}Na NMR suggested local symmetry changes. The microstructure of the solid solutions changed with substitution which is reflected in the density. A small increase in the dielectric constant is observed with increasing substitution, suggesting the role of minor structural changes due to the comparable size of the co-substituted ions with that of Na.

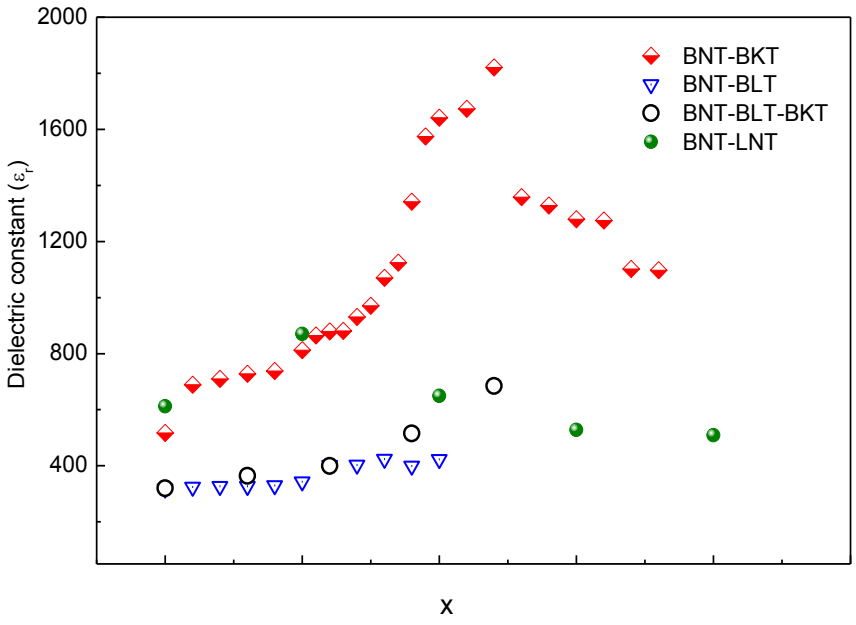

Figure 7.1: Comparison of the variation of dielectric constants of $Bi_{0.5}Na_{0.5}TiO_3$–$Bi_{0.5}K_{0.5}TiO_3$ (BNT–BKT), $Bi_{0.5}Na_{0.5}TiO_3$–$Bi_{0.5}Li_{0.5}TiO_3$ (BNT–BLT), $Bi_{0.5}Na_{0.5}TiO_3$–$Bi_{0.5}Li_{0.5}TiO_3$–$Bi_{0.5}K_{0.5}TiO_3$ (BNT–BLT–BKT) and $Bi_{0.5}Na_{0.5}TiO_3$–$La_{0.5}Na_{0.5}TiO_3$ (BNT–LNT) solid solutions.

A detailed structural analysis of $(1\text{-}x)Bi_{0.5}Na_{0.5}TiO_3$–$xLa_{0.5}Na_{0.5}TiO_3$ solid solution series for $0 \leq x \leq 0.4$ has been carried out, where Bi^{3+} and La^{3+} have comparable ionic sizes. Rietveld refinement analysis of the XRD patterns of all the compositions showed that they are formed under the monoclinic Cc space group without any phase transformation. The ^{23}Na and ^{139}La SSNMR studies showed that the local symmetry increased with La substitution that indicated the reduced effect of $6s^2$ lone pair contribution to the crystal lattice. The Raman and NMR parameters showed deviations around $x = 0.1$. Density and dielectric constant of the ceramics also showed similar deviations around $x = 0.1$. The decrease in the dielectric constant indicated decrease in the polarization. From the studies on the $Bi_{0.5}Na_{0.5}TiO_3$–$La_{0.5}Na_{0.5}TiO_3$ solid solution series, it is concluded that the distortion in the crystal lattice decreased due to the decreased effect of Bi $6s^2$ lone pair with La concentration.

The variations of the dielectric constant with composition of the different $Bi_{0.5}Na_{0.5}TiO_3$ based solid solutions are compared in Figure 7.1. A large increase in the dielectric constant is observed for $Bi_{0.5}Na_{0.5}TiO_3$–$Bi_{0.5}K_{0.5}TiO_3$ with K^+ substitution, compared to the other solid solutions. Larger dielectric constant is observed in the MPB region. The highest dielectric constant observed in the MPB region is almost four times that of the unsubstituted composition (BNT). The difference in the magnitude of the dielectric constant of BNT in the different substituted compositions is due to the difference in the sintering temperature. $Bi_{0.5}Na_{0.5}TiO_3$–$La_{0.5}Na_{0.5}TiO_3$ solid solution series showed a decrease in the dielectric constant with increasing La^{3+} due to the decreased contribution from the $6s^2$ lone pair contribution from Bi.

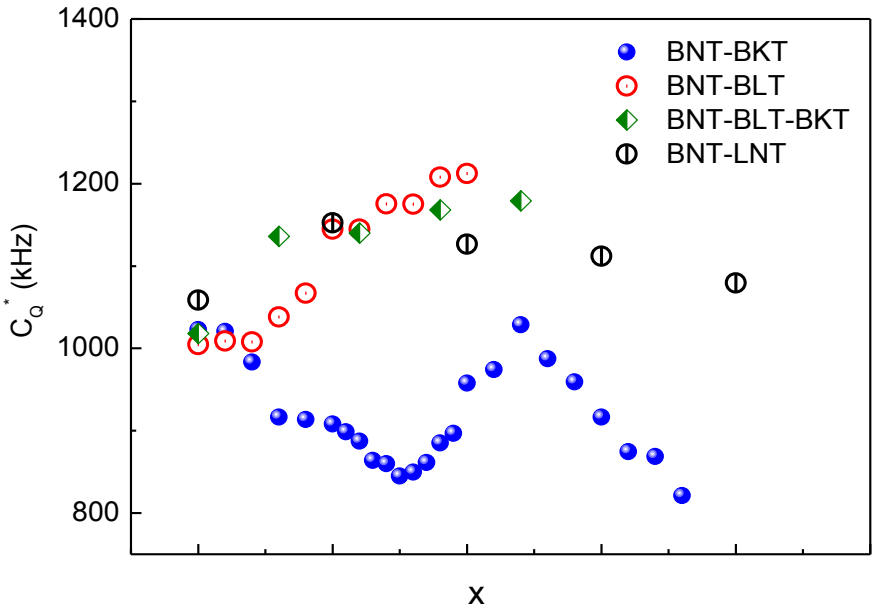

Figure 7.2: Comparison of the ^{23}Na quadrupolar coupling constant (C_Q^*) of $Bi_{0.5}Na_{0.5}TiO_3$–$Bi_{0.5}K_{0.5}TiO_3$ (BNT–BKT), $Bi_{0.5}Na_{0.5}TiO_3$–$Bi_{0.5}Li_{0.5}TiO_3$ (BNT–BLT), $Bi_{0.5}Na_{0.5}TiO_3$–$Bi_{0.5}Li_{0.5}TiO_3$–$Bi_{0.5}K_{0.5}TiO_3$ (BNT–BLT–BKT) and $Bi_{0.5}Na_{0.5}TiO_3$–$La_{0.5}Na_{0.5}TiO_3$ (BNT–LNT) solid solutions.

Comparison of the ^{23}Na quadrupolar coupling constant of $Bi_{0.5}Na_{0.5}TiO_3$–$Bi_{0.5}K_{0.5}TiO_3$, $Bi_{0.5}Na_{0.5}TiO_3$–$Bi_{0.5}Li_{0.5}TiO_3$, $Bi_{0.5}Na_{0.5}TiO_3$–$Bi_{0.5}Li_{0.5}TiO_3$–$Bi_{0.5}K_{0.5}TiO_3$ and $Bi_{0.5}Na_{0.5}TiO_3$–$La_{0.5}Na_{0.5}TiO_3$ solid solutions is shown in Figure 7.2. In the $Bi_{0.5}Na_{0.5}TiO_3$–$Bi_{0.5}K_{0.5}TiO_3$ series, the quadrupolar coupling (C_Q^*) showed an initial decrease and then an increase to a maximum indicating the changes the in local symmetry with K^+ substitution. However, for the other substituted compositions, $Bi_{0.5}Na_{0.5}TiO_3$–$Bi_{0.5}Li_{0.5}TiO_3$ and $Bi_{0.5}Na_{0.5}TiO_3$–$Bi_{0.5}Li_{0.5}TiO_3$–$Bi_{0.5}K_{0.5}TiO_3$, the quadrupolar coupling (C_Q^*) increased with substitution whereas for the $Bi_{0.5}Na_{0.5}TiO_3$–$La_{0.5}Na_{0.5}TiO_3$ solid solution series, the

quadrupolar coupling (C_Q^*) decreased with substitution. This shows that the effects of local symmetry variation with substitution of K^+, Li^+, La^{3+} and the co-substitution of Li^+ and K^+ are different that are reflected in the changes in quadrupolar coupling. This is probably due to the difference in the ionic sizes of the substituted ions, which affect the local symmetry in different ways. In the case of $Bi_{0.5}Na_{0.5}TiO_3$–$La_{0.5}Na_{0.5}TiO_3$, the role of the $6s^2$ lone pair of Bi^{3+} is very important.

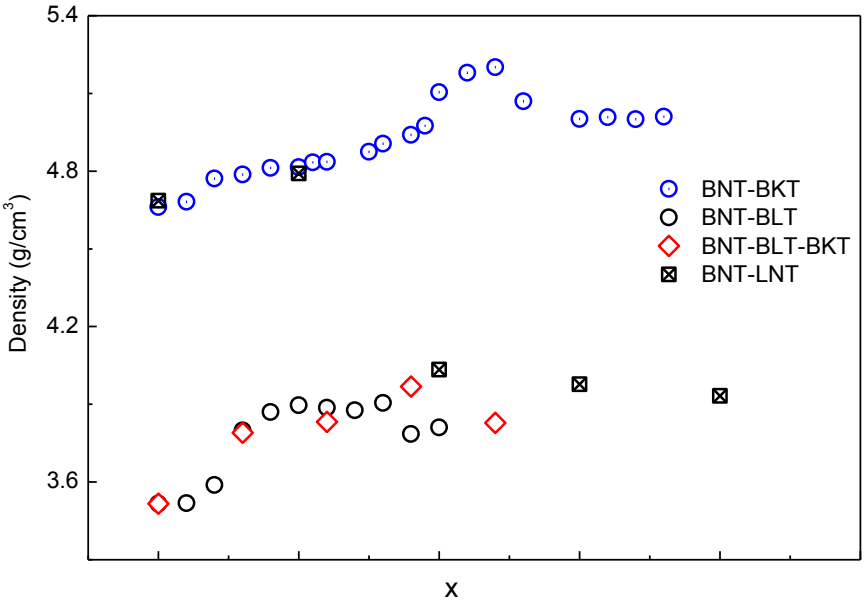

Figure 7.3: Comparison of the density of $Bi_{0.5}Na_{0.5}TiO_3$–$Bi_{0.5}K_{0.5}TiO_3$ (BNT–BKT), $Bi_{0.5}Na_{0.5}TiO_3$–$Bi_{0.5}Li_{0.5}TiO_3$ (BNT–BLT), $Bi_{0.5}Na_{0.5}TiO_3$–$Bi_{0.5}Li_{0.5}TiO_3$–$Bi_{0.5}K_{0.5}TiO_3$ (BNT–BLT–BKT) and $Bi_{0.5}Na_{0.5}TiO_3$–$La_{0.5}Na_{0.5}TiO_3$(BNT–LNT) solid solutions.

The variation of the densities of $Bi_{0.5}Na_{0.5}TiO_3$–$Bi_{0.5}K_{0.5}TiO_3$, $Bi_{0.5}Na_{0.5}TiO_3$–$Bi_{0.5}Li_{0.5}TiO_3$, $Bi_{0.5}Na_{0.5}TiO_3$–$Bi_{0.5}Li_{0.5}TiO_3$–$Bi_{0.5}K_{0.5}TiO_3$ and $Bi_{0.5}Na_{0.5}TiO_3$–$La_{0.5}Na_{0.5}TiO_3$ solid solution series are compared in Figure 7.3. The large difference in the densities of BNT in the different series is due to the difference in the sintering temperature. The density of $Bi_{0.5}Na_{0.5}TiO_3$–$Bi_{0.5}K_{0.5}TiO_3$ solid solution increased to a maximum with K^+ substitution and then decreased. The maximum density obtained is 5.3 g/cm^3. $Bi_{0.5}Na_{0.5}TiO_3$–$Bi_{0.5}Li_{0.5}TiO_3$, $Bi_{0.5}Na_{0.5}TiO_3$–$Bi_{0.5}Li_{0.5}TiO_3$–$Bi_{0.5}K_{0.5}TiO_3$ solid solution series showed initial increase in the density with substitution but relatively low values are observed when compared to $Bi_{0.5}Na_{0.5}TiO_3$–$Bi_{0.5}K_{0.5}TiO_3$ solid solution. Density of $Bi_{0.5}Na_{0.5}TiO_3$–$La_{0.5}Na_{0.5}TiO_3$solid solution decreased with La^{3+} substitution.

From the results of the different studies carried out in this thesis, it may be concluded that structural phase transition and MPB region exist only in the $Bi_{0.5}Na_{0.5}TiO_3$–$Bi_{0.5}K_{0.5}TiO_3$

solid solution series and relatively higher density and dielectric constants are observed in the MPB region in $Bi_{0.5}Na_{0.5}TiO_3$–$Bi_{0.5}K_{0.5}TiO_3$ solid solution. All the four solid solution series that were studied showed a deviation around $x = 0.1$ in the quadrupolar coupling, density and dielectric constant, indicating the role of local symmetry changes, which is evidenced from NMR studies. Thus, it can be concluded that solid state NMR studies on the ferroelectric compositions can give convincing and important information on the correlation between structural changes and properties of the compositions.

7.2. Future perspectives

The changes in the structure and some of the properties of the $Bi_{0.5}Na_{0.5}TiO_3$ and Li^+, Na^+, K^+, La^{3+} substituted $Bi_{0.5}Na_{0.5}TiO_3$ solid solution are studied in the present work. However, the ferroelectric properties such as P-E hysteresis loop measurements, piezoelectric properties such as piezoelectric constant and electromechanical coupling constant and the temperature dependence of dielectric constant of these ceramics are not measured and analysed. The P-E hysteresis loop measurements of $Bi_{0.5}Na_{0.5}TiO_3$–$Bi_{0.5}K_{0.5}TiO_3$ solid solution are limited to ± 2 kV only, where the polarization is not saturated and hence only the minor loops are traced. It is expected that detailed studies on ferroelectric polarization of all the solid solutions, at high fields, will give a clear picture of the correlation between the local structural changes and the ferroelectric properties as well as the extent of polarization in the solid solutions. Similarly, measurements of the piezoelectric constant and electromechanical coupling constant of all the solid solutions are need to be studied to get detailed information on the correlation between these values and the local structural variations. Temperature dependent dielectric constant studies of the ceramics will give more information on the phase transition temperatures and the temperature limit of the materials for practical applications. All the compositions in the present study are having very low densities, due to the low compaction pressure used for making the pellets. Densities close to the theoretical values are required for practical applications. Hence, detailed studies on high density ceramics may shed more light on the structure-property correlations.

The studies in this thesis are limited to a single sintering temperature. The effect of sintering temperature and conditions such as heating/cooling rate, sintering time, etc, on the structure and properties of the solid solution are not examined. Hence, the present work can be extended to ceramics synthesized and processed under different conditions to optimize higher values of density and ferroelectric parameters for practical applications.

Although the quadrupolar nuclei Na^+, Li^+ and La^{3+} are probed and their NMR spectral characteristics are analysed, $^{47/49}$Ti NMR and the Li relaxation studies are not carried out. Since the ferroelectric characteristics are related to the changes in the TiO_6 octahedra in the perovskite lattice, more structural information are expected from $^{47/49}$Ti NMR studies using a high field spectrometer. Such studies can identify the minor distortions and symmetry changes in the TiO_6 octahedra of $Bi_{0.5}Na_{0.5}TiO_3$ based solid solutions with Bi- and Na-site substitutions. Temperature dependent relaxation studies on Li^+ nuclei can provide more information on the nature of Li^+ migration in the crystal lattice.

Thus, the preliminary results on the correlation between local structural variations and the dielectric constant, based on the solid state NMR studies reported in this thesis, are only an indication and it is expected that more detailed studies as mentioned may shed more light on the various aspects of the ferroelectric compositions studied in the present thesis.

List of Publications

1. K. Anjali, T.G. Ajithkumar and P. A. Joy, "Correlations between structure, microstructure, density and dielectric properties of the lead-free ferroelectrics $Bi_{0.5}(Na,K)_{0.5}TiO_3$," *J. Adv. Dielectr.,* **5**[**4**] 1550028 (2015)

Reference

1. M. Borowski, *Perovskites: Structure, Properties And Uses*, Nova Science Publishers, (2010)
2. N. W. Thomas, *Acta Cryst. B,* **45** 337-344 (1989)
3. A.S. Bhalla, R. Guo and R. Roy, *Mat. Res. Innovat.,* **4** 3-26 (2000)
4. M. A. Green, A. Ho-Baillie and H. J. Snaith, *Nat. Photon.,* **8** 506-514 (2014)
5. A. F. Wells, *Structural Inorganic Chemistry*, Oxford Science publications, (1995)
6. U. Müller, *Inorganic Structural Chemistry*, Wiley & Sons Ltd, (1993)
7. Inorganic Crystallographic Structure Database (ICSD), Copyright © 2005 by FIZ Karlsruhe, Germany.
8. O. Muller and R. Roy, *The Major Ternary Structural Families*, Springer-Verlag, (1974)
9. E. V. Antipov, A. M. Abakumov and S. Y. Istomin, *Inorg. Chem.,* **47** 8543-8552 (2008)
10. M. Johnsson and P. Lemmens, *Crystallography And Chemistry of Perovskites*, eprintarXiv:cond-mat/0506606, (2005)
11. F. Hao, C. C. Stoumpos, D. H. Cao, R. P. H. Chang and M. G. Kanatzidis, *Nat. Photon.,* **8** 489-494 (2014)
12. A. R. West, *Solid State Chemistry And Its Applications*, John Wiley and Sons, (1984)
13. K. Y. Gufan, *Phys. Solid State,* **47** 459-465 (2005)
14. M. Faraday, *Phil. Trans.,* **128** 1-40 (1837)
15. A. Asamitsu, Y. Moritomo, Y. Tomioka, T. Arima and Y. Tokura, *Nature,* **373** 407-409 (1995)
16. C. B. Sawyer and C. H. Tower, *Phys. Rev.,* **35** 269-273 (1930)
17. G. H. Haertling, *J. Am. Ceram. Soc.,* **82** 797-818 (1999)
18. F. S. Galasso, *Structure, Properties And Preparation Of Perovskite-Type Compounds*, Pergamon Press Inc, (1969)
19. H. Thurnauer and J. Deaderick, USA Patent no. 2429588 (1947)
20. A. V. Hippel, R. G. Breckenridge, F. G. Chesley and L. Tisza, *Ind. Eng. Chem.,* **38** 1097-1109 (1946)
21. D. Fu and M. Itoh, Role of Ca off-Centering in Tuning Ferroelectric Phase Transitions in $Ba(Zr,Ti)O_3$ System, *Ferroelectric Materials - Synthesis and Characterization*, (2015)
22. A. R. West, *Basic Solid State Chemistry*, John Wiley & Sons Ltd., (1999)
23. H. F. Kay and P. Vousden, *Phil. Mag. Series 7,* **40** 1019-1040 (1949)
24. A. A. Bokov and Z-. G. Ye, *J. Mater. Sci.,* **41** 31-52 (2006)

25. G. A. Samara and E. L. Venturini, *Phase Transit.,***79** 21-40 (2006)
26. Z-. G. Ye, *Key Eng. Mat.,* **155** 81-82 (1998)
27. L. E. Cross, *Ferroelectrics,***76** 241-267 (1987)
28. G. A. Smolensky, *J. Phys. Soc. Jpn.,* **28** 26 (1970)
29. A. -B. M. A. Ibrahim, J. Osman, M. K. A. Rahman and R. Murgan, *Morphotropic Phase Boundary In Ferroelectric Materials*, :INTECH Open Access Publisher
30. B. Jaffe B, J. W. J. Crook and H. L. Jaffe, *Piezoelectric Ceramics*, Academic Press, (1971)
31. Z-. G. Ye, Y. Bing, J. Gao, A. A. Bokov, P. Stephens, B. Noheda and G. Shirane, *Phys. Rev. B,* **67** 104104 (2003)
32. O. Bidault, E. Husson and P. Gaucher , *J. Phys. III France,* **7** 1163-1172 (1997)
33. B. Noheda, J. A. Gonzalo, L. E. Cross, R. Guo, S. E. Park, D. E. Cox and G. Shirane, *Phys. Rev. B,* **61** 8687-8695 (2000)
34. H. H. Rogers, *Technical Report - Massachusetts Inst. Tech. Lab. Insulation Res* (1952)
35. G. Shirane and S. Hoshino, *J. Phys. Soc. Jap.,* **6** 265-270 (1950)
36. S. Roberts, *J. Am. Ceram. Soc.,* **33** 63-66 (1950)
37. G. Shirane and A. Takeda, *J. Phys. Soc. Jap.,* **7** 5-11 (1952)
38. G. Shirane and K. Suzuki, *J. Phys. Soc. Jap.,* **7** 12-18 (1952)
39. E. Sawaguchi, *J. Phys. Soc. Jap.,* **8** 615 (1953)
40. B. Noheda, J. A. Gonzalo, A. C. Caballero, C. Moure, D. E. Cox and G. Shirane, *Ferroelectrics,* **237** 541-548 (2000)
41. R. Guo, L. E. Cross, S. E. Park, B. Noheda, D. E. Cox and G. Shirane, *Phys. Rev. Lett.,* **84** 5423-5426 (2000)
42. X. H. Du, J. H. Zheng, U. Belegundu and K. Uchino, *Appl. Phys. Lett.,* **72** 2421-2423 (1998)
43. R. Guo, L. E. Cross, S. E. Park, B. Noheda, D. E. Cox and G. Shirane, *Phys. Rev. Lett.,* **84** 5423-5426 (2000)
44. M. Ahart, M. Somayazulu, R. E. Cohen, P. Ganesh, P. Dera, H.-k. Mao, R. J. Hemley, Y. Ren, P. Liermann and Z. Wu, *Nature,* **451** 545-548 (2008)
45. D. A. Berlincourt, C. Cmolik and H. Jaffe, *Proc. IRE,* **48** 220-229 (1960)
46. S. Ahmad, R. K. Panda and V. F. Janas, *Ferroelectric Ceramics: Processing, Properties & Applications*, http://www.rci.rutgers.edu/~ecerg/projects/ferroelectric.html.(2006)
47. S. E. E. Park and W. Hackenberger, *Curr. Opin. Solid State Mater. Sci.,* **6** 11-18 (2002)
48. L. Yi, K. Moon and C. P. Wong, *Science,* **308** 1419–1420 (2005)

49. P. K. Panda, *J. Mater. Sci.,* **44** 5049-5062 (2009)
50. E. Ringgaard, T. Wurlitzer and W. W. Wolny, *Ferroelectrics,* **319** 323-333 (2005)
51. T. Takenaka and H. Nagata, *J. Euro. Ceram. Soc.,* **25** 2693–2700 (2005)
52. W. Liu and X. Ren, *Phy. Rev. Lett.,* **103** 257602 (2009)
53. P. Wang, Y. Li and Y. Lu, *J. Euro. Ceram. Soc.,* **31** 2005–2012 (2011)
54. T. Karaki, K. Yan, T. Miyamoto and M. Adachi, *Jpn. J. Appl. Phy.,* **46** L97–L98 (2007)
55. R. Bechmann, *J. Acoust. Soc. Am.,* **28** 347-350 (1956)
56. H. Nagata, T. Shynya, Y. Hiruma and T. Takenaka, *Ceram. Trans.,* **167** 213-221 (2004)
57. Y. Hiruma, R. Aoyagi, H. Nagata and T. Takenaka, *Jpn. J. Appl. Phys. Part 1,* **44** 5040–5044 (2005)
58. Z. Yang, B. Liu, L. Wei and Y. Hou, *Mater. Res. Bull. ,* **43** 81-89 (2008)
59. Y.-R. Zhang, J. –F. Li and B.-P. Zhang, *J. Am. Ceram. Soc.,* **91** 2716-2719 (2008)
60. H. Y. Tian, K. W. Kwok, H. L. W. Chan and C. E. Buckley, *J. Mater. Sci.,* **42** 9750–9755 (2007)
61. H. Hu, M. Zhu, F. Xie, N. Lei, J. Chen, Y. Hou, and H. Yan, *J. Am. Ceram. Soc.,* **92** 2039–2045 (2009)
62. D. Lin and K. W. Kwok, *J. Mater. Sci. ,* **44** 4953–4958 (2009)
63. D. Q. Xiao, D. M. Lin, J. G. Zhu and P. Yu, *J. Electro. Ceram.,* **16** 271–275 (2006)
64. D. Lin, Q. Zheng, C. Xu and K. W. Kwok, *Appl. Phys. A,* **93** 549–558 (2008)
65. S. H. Choy, X. X. Wang, H. L. W. Chan and C. L. Choy, *Appl. Phys. A,* **89** 775–781 (2007)
66. G. A. Smolenskii, V.A. Isupv, A.I. Agranovskaya and N.N. Krainik, *Sov. Phys. Solid State,* **2** 2584 (1961)
67. P. Popper, S. N. Ruddlesden and T. A. Ingles, *Trans. Br. Ceram. Soc.,* **56** 356-365 (1957)
68. O. Elkechai, M. Manier and J. P. Mercurio, *Phys. Status Solidi A,* **157** 499-506 (1996)
69. S. Gorfman and P. A. Thomas, *J. Appl. Crystallogr.,* **43** 1409-1414 (2010)
70. J. Kreisel, A. M. Glazer, G. Jones, P. A. Thomas, L. Abello, and G. Lucazeau, *J. Phys. Conden. Mat.,* **12** 3267 (2000)
71. M. Izumi, K. Yamamoto, M. Suzuki, Y. Noguchi and M. Miyayama, *Appl. Phys. Lett.,* **93** 242903 (2008)
72. A. Sasaki, T. Chiba, Y. Mamiya and E. Otsuki, *Jpn. J. of Appl. Phys. 1,* **38** 5564-5567 (1999)
73. P.-Y. Chen. C.-C. Chou, T. -Y. Tseng and H. H. D. Chen, *Ferroelectrics,* **381** 196-200 (2009)

74. H. Xie, L. Jin, D. Shen, X. Wang, and G. Shen, *J. Cryst. Growth,* **311** 3626-3630 (2009)
75. J. M. Honig and C. N. R. Rao, *Preparation And Characterization Of Materials*, Academic Press, (1981)
76. D. Segal, *Chemical Synthesis Of Advanced Ceramic Materials*, Cambridge University Press, (1991)
77. C. N. R. Rao, *Chemical Approaches To The Synthesis Of Inorganic Materials*, Wiley Eastern Ltd, (1994)
78. J. P. Jolivet, M. Henry and J. Livage, *Metal Oxide Chemistry And Synthesis: From Solution To Solid State*, John Wiley & Sons, (2000)
79. S. T. Aruna and A. S. Mukasyan, *Curr. Opin. Solid State Mater. Sci.,* **12** 44-50 (2008)
80. A. K. Tyagi, *Combustion Synthesis: A Soft-Chemical Route For Functional Nano-Ceramics*, BARC newsletter, (2006)
81. H. P. Klug and L. E. Alexander, *X-Ray Diffraction Procedures*, Wiley, (1954)
82. B. D. Cullity and S. R. Stock, *Elements Of X-Ray Diffraction*, Prentice Hall, (2001)
83. W. Kraus and G. Nolze, Powder Cell for Windows (PCW), version 2.4 (The software is freely available from http://www.ccp14.ac.uk.)
84. H. M. Rietveld, *Acta. Crystallogr.,* **22** 151-152 (1967)
85. H. M. Rietveld, *J. Appl. Crystallogr.,* **2** 65-71 (1969)
86. R. A. Young, *The Rietveld Method*, Oxford University Press, (1995)
87. B. Toby, *J. Appl. Crystallogr.,* **34** 210-213 (2001)
88. M. H. Levitt, *Spin Dynamics: Basics Of Nuclear Magnetic Resonance*, Wiley, (2008)
89. M. J. Duer, *Solid-State NMR Spectroscopy Principles And Applications*, John Wiley & Sons, (2002)
90. D. Massiot, F. Fayon, M. Capron, I. King, S. L. Calve, B. Alonso, J.-O. Durand, B. Bujoli, Z. Gan and G. Hoatson, *Magn. Reson. Chem.,* **40** 70-76 (2002)
91. K. J. D. MacKenzie and M. E. Smith, *Multinuclear Solid-State Nuclear Magnetic Resonance Of Inorganic Materials*, Pergamon, (2002)
92. G. Czjzek, J. Fink, F. Götz, H. Schmidt, J. M. D. Coey, J.-P. Rebouillat and A. Liénard, *Phys. Rev. B,* **23** 2513–2530 (1981)
93. C. N. Banwell and E. M. McCash, *Fundamentals Of Molecular Spectroscopy*, McGraw-Hill, (1994)
94. J. R. Ferraro, *Introductory Raman Spectroscopy*, Academic press, (2003)

95. W. G. Fateley, F.R. Dollish, N. T. McDevitt and F. Bentley, *Infrared And Raman Selection Rules For Molecular And Lattice Vibrations: The Correlation Method*, John Willey and Sons, (1972)

96. W. Zhou, R. Apkarian, Z. L. Wang and D. Joy, *Fundamentals Of Scanning Electron Microscopy (SEM)*, Springer, (2007)

97. D. A. Huerta, V. Sosa, M. C. Vargas and J. C. Ruiz-Suarez, *Phy. Rev. E,* **72** 031307 (2005)

98. A. Kumar and S. Sharma, *Prog. Electromagn. Res.*, **69** 47-54 (2007)

99. M. Stewart, M.G. Cain and D. A. Hall, *NPL Report CMMT(A),* **152** (1999)

100. M.-S. Zhang, J. F. Scott and J. A. Zvirgzds, *Ferroelectrics Lett.,* **6** 147-152 (1986)

101. I. G. Siny, E. Husson, J. M. Beny, S. G. Lushnikov, E. A. Rogacheva, and P. P. Syrnikov, *Ferroelectrics,* **248** 57-78 (2000)

102. I. G. Siny, T. A. Smirnova and T. V. Kruzina, *Ferroelectrics,* **124** 207-212 (1991)

103. A. Medek, J. S. Harwood and L. Frydman, *J. Am. Chem. Soc.,* **117** 12779-12787 (1995)

104. G. O. Jones and P. A. Thomas, *Acta Crystallogr. B,* **58** 168-178 (2002)

105. E. Aksel, J. S. Forrester, J. L. Jones, P. A. Thomas, K. Page and M. R. Suchomel, *Appl. Phys. Lett.,* **98** 152901 (2011)

106. E. Kroumova, M. I. Aroyo, J. M. P. -Mato, A. Kirov, C. Capillas , S. Ivantchev and H. Wondratschek, *Phase. Transit.,***76** 155-170 (2015)

107. G. Marcano, C. Rincon, S.A. López, G. Sánchez Pérez, J. L. H. -Pérez, J.G. Mendoza-Alvarez and P. Rodríguez, *Solid state commun.,* **151** 84-86 (2011)

108. H. R. Xia, H. Yu, H. Yang, K. X. Wang, B. Y. Zhao, J. Q. Wei, J. Y. Wang and Y. G. Liu, *Phys. Rev. B,* **55** 14892 (1997)

109. K. Samanta, A. K. Arora, T. R. Ravindran, S. Ganesamoorthy, K. Kitamura and S. Takekawa, *Vib. Spectrosc.,* **62** 273-278 (2012)

110. D. Schutz, M. Deluca, W. Krauss, A. Feteira, T. Jackson and K. Reichmann, *Adv. Funct. Mater.,* **22** 2285-2294 (2012)

111. A. Medek, J.S. Harwood and L. Frydman, *J. Am. Chem. Soc.,* **117** 12779-12787 (1995)

112. M. Otonicar, S. D. Skapin, M. Spreitzer, and D. Suvorov, *J. Eur. Ceram. Soc.,* **30** 971-979 (2010)

113. W. Lu, G. Fan, X. Wang and F. Liang, *Jpn. J. Appl. Phys.,* **45** 8763–8765 (2006)

114. S. Said and M. E. Maaoui, *J. Electroceram.,* **35** 90-97 (2015)

115. D. Lin, D. Xiao, J. Zhu, P. Yu, H. Yan and L. Li, *Mater. Lett.,* **58** 615-618 (2004)

116. W. Lu, Y. Wang, G. Fan, X. Wang and F. Liang, *J. Alloys. Compd.,* **509** 2738–2744 (2011)

117. D. Lin, Q. Zheng, C. Xu and K.W. Kwok, *Appl. Phys. A,* **93** 549-558 (2008)

118. B.-Q. Ming, J.-F. Wang and G.-Z. Zang, *Chin. Phys. Lett.,* **25** 3776 (2008)

119. R. D. Shannon, *Acta Cryst.* A, **32** 77671 (1976)

120. J. Karger and P. Heitjans, *Diffusion In Condensed Matter: Method, Material, Models*, Springer-Verlag Berlin, (2001)

121. A. Kuhn, M. Kunze, P. Sreeraj, H. D. Wiemhofer, V. Thangadurai, M. Wilkening, and P. Heitjans, *Solid State Nucl. Mag.,* **42** 2-8 (2012)

122. J. Frantti, *Phys. Chem. B,* **112** 6521-6535 (2008)

123. G. Catalan and J. F. Scott, *Adv. Mater.,* **21** 2463–2485 (2009)

124. D. Lebeugle, D. Colson, A. Forget, and M. Viret, *Appl. Phys. Lett.,* **91** 022907 (2007)

125. Y. Hiruma, Y. Watanabe, H. Nagata and T. Takenaka, *Key Eng. Mater.,* **350** 93-96 (2007)

126. M. Cheah, K. A. Razak and C. Y. Ng, *Adv. Mater. Res.,* **858** 141-146 (2014)

127. J. Y. Yi, J. -K. Lee and K.-S. Hong, *J. Am. Ceram. Soc.,* **85** 3004-3010 (2002)

128. M. Aparna, G. Prasad and G. S. Kumar, *Ferroelectrics,* **324** 63-69 (2005)

129. M. Aparana, T. Bhimasankaram, G. S. Kumar and G. Prasad, *Mod. Phys. Lett. B,***16** 1007-1019 (2002)

130. F. Borodavka, E. Simon, I. Gregora, S. Kamba, R. Haumont and J. Hlinka, *J. Phys. Condens. Matter.,* **25** 085901 (2013)

131. Y. Li, S. Qin and F. Seifert, *J. Solid State Chem.,* **180** 824-33 (2007)

132. G. Geneste, J-M. Kiat and C. Malibert, *Phys. Rev. B,* **77**, 052106 (2008)

133. Y. Inaguma, J-H. Sohn, I.-S. Kim, M. Itoh and T. Nakamura, *J. Phys. Soc. Jpn.,* 61 3831- 3832 (1992)

134. M. -Y. Chen, C. Y. Chiu, C. -T. Chia, J. F. Lee, and J. J. Bian, *J. Eur. Ceram. Soc.,* **30** 335-339 (2010)